Multiferroic Properties and Magnetization Reversal in Perovskite Oxides

A Thesis

Submitted for the Degree of

DOCTOR OF PHILOSOPHY

by

PRANAB MANDAL

CHEMISTRY AND PHYSICS OF MATERIALS UNIT
JAWAHARLAL NEHRU CENTRE FOR ADVANCED SCIENTIFIC RESEARCH
(A Deemed University)
Bangalore – 560 064

MARCH 2012

DECLARATION

I hereby declare that the matter embodied in the thesis entitled "**Multiferroic Properties and Magnetization Reversal in Perovskite Oxides**" is the result of investigations carried out by me at the Chemistry and Physics of Materials Unit, Jawaharlal Nehru Centre for Advanced Scientific Research, Bangalore, India under the supervision of Prof. A. Sundaresan and it has not been submitted elsewhere for the award of any degree or diploma.

In keeping with the general practice in reporting scientific observations, due acknowledgment has been made whenever the work described is based on the findings of other investigators.

Pranab Mandal

CERTIFICATE

I hereby certify that the matter embodied in this thesis entitled "**Multiferroic Properties and Magnetization Reversal in Perovskite Oxides**" has been carried out by Mr. Pranab Mandal at the Chemistry and Physics of Materials Unit, Jawaharlal Nehru Centre for Advanced Scientific Research, Bangalore, India under my supervision and it has not been submitted elsewhere for the award of any degree or diploma.

Prof. A. Sundaresan
(Research Supervisor)

Acknowledgments

Firstly, I sincerely thank Prof. A. Sundaresan for providing an opportunity to work under his guidance. I thank him for providing me interesting research problems and enough time to understand them. He has treated me as a family member and friend and has been a great support and source of motivation during ups and downs of my PhD life.

Prof. C. N. R. Rao, FRS has been a great source of inspiration during my doctoral work. I would like to sincerely thank him for suggestions in various problems and providing us all the experimental facilities.

I thank Dr. A. Iyo and Dr. Y. Tanaka for high pressure synthesis facility and hospitality at AIST, Tsukuba, Japan during my stay. I also thank for fruitful collaboration with Mr. Venkata Srinu Bhadram, Prof. Chandrabhas, Mr. N. M. Dasari, Dr. Raja and Prof. Raveau.

My sincere thank to past and present CPMU chairmen, Prof. C. N. R. Rao, Prof. G. U. Kulkarani and Prof. Balasubramanian for providing all the experimental facilities.

I thank my past and present lab mates, Dr. Vengadesh, Madhu, Shipra, Nitesh, Dr. Sundarayya, Rana, Bharath and Somnath for their help and fruitful atmosphere in the lab.

I thank Dr. Shekhar, Dr. Kaushik and Dr. Ajay for teaching different experimental techniques.

I thank Prof. Chandrabhas, Prof. Sundaresan, Prof. Eswaramoorthy, Prof.

Waghmare, Prof. T. N. Guru Row and Prof. S. Ranganathan for their wonderful courses. I thank all faculties in CPMU and TSU for their kind words.

I would like to sincerely thank Dr. Achintya Chatterjee (Malda College, WB) for motivating me towards research. I thank all my teachers for their support.

I thank Anil and Gurusamy (Bruker Corp.), Selvi, Basavaraj (FESEM), Sreenath, Vasu, Srinivasa Rao and Mr. Arakinathan for various technical help in experiments. I thank Moorthy, Sunil and Balaraju for their assistance.

I sincerely thank Academic Section and Administration for all the official help. I also thank Complab for computational and printing facilities. I thank JNCASR family for all the support and care in lab and students residence.

I greatly acknowledge Department of Science and Technology (DST) for research fellowship, JST-DST project for sponsoring transport and stay in Japan and Prof. C. N. R. Rao for awarding Sheik Saud RAK-CAM Junior Fellowship.

I thank all my friends at JNCASR and IISc for their encouragement, inspiration and criticism. I also thank all my friends in JNU and Malda College for their love and support.

I thank all my relatives for their love and blessings. I express my gratitude to Mr. Baidyanath Mandal and Mrs. Mitali Mandal for growing me as their own child. I thank my mother, brother and wife Sangita for selfless love that has kept me alive. Finally, I want to thank GOD for this life.

I am dedicating this thesis to my father Late Pradip K. Mandal.

Preface

The thesis presents study of multiferroic properties in perovskite oxides where ferroelectricity and magnetism (ferro- or antiferromagnetism) can coexist. The thesis is focused on bismuth and yttrium based perovskite oxides that exhibit multiferroic properties and temperature induced magnetization reversal.

Chapter 1 gives an introduction to multiferroic materials and various mechanisms that induce ferroelectricity.

Chapter 2 describes experimental details of material synthesis and physical property measurements followed in the thesis.

Chapter 3 deals with non-magnetic ion substitution at the Fe-site of $BiFeO_3$. $BiFeO_3$ is a room temperature ferroelectric and antiferromagnetic (G-type). A spiral magnetic ordering present below T_N , cancels any finite magnetization arising from spin canting. Substitution of Al and Sc at the Fe-site suppresses the spiral magnetic ordering and induces finite magnetization. The Sc substituted compounds show an improved dielectric and ferroelectric properties compared to that of Al.

Chapter 4 discusses structural, magnetic and dielectric properties of high pressure synthesized $BiCr_{0.5}Mn_{0.5}O_3$. A glassy magnetic behavior is observed below Néel temperature. The compound crystallizes in a centrosymmetric structure (C2/*c*) and exhibits unusually high dielectric constant ($\sim 10^4$) near room temperature. The behavior is explained in terms of Maxwell-Wagner relaxation due to grain boundary polarization as revealed from impedance and dielectric spectroscopic study.

Chapter 5 deals with the observation of temperature induced magnetization re-

versal in high pressure synthesized $BiFe_{0.5}Mn_{0.5}O_3$. The compound has an orthorhombic structure (P$n2_1m$). It orders antiferromagnetically at 270 K and shows negative magnetization below a compensation temperature T^* (208 K at 50 Oe), down to the lowest temperature measured. Substitution by Sr and La at the Bi-site stabilizes the compound in rhombohedral structure at ambient pressure. The absence of magnetization reversal in these compounds indicates important role of structure.

Chapter 6 is focused on magnetization reversal study of ambient pressure synthesized $YFe_{1-x}M_xO_3$ ($0 \leq x \leq 1.0$ for M = Cr and $0 \leq x \leq 0.45$ for M = Mn). These compounds crystallize in orthorhombic structure (P*nma*) and undergo a first-order spin reorientation transition below Néel temperature. Negative magnetization is observed in compounds near the equal mixing of Fe and Mn/Cr. The reversal is understood in terms of interplay of magnetic anisotropy and Dzyaloshinskii-Moriya interactions on the different superexchange interactions.

Chapter 7 presents the discovery of magneto(di)electric effect in the centrosymmetric $YFe_{1-x}Mn_xO_3$ perovskites. These compounds exhibit magnetodielectric effect at magnetic transitions whereas ferroelectricity appears at lower temperatures. A large magnetocapacitance of 18% is found near the spin-reorientation transition (320 K) for the compound with x = 0.4. Further, electric polarization could be increased by magnetic field confirming the material to be a new magnetoelectric multiferroic. Magnetodielectric effect is attributed to the spin-phonon coupling at the magnetic transitions whereas the polar state may arise either due to complex magnetic ordering or spin-disorder which requires further investigation.

Publications

1. Dielectric and impedance studies on the double perovskite Ba_2BiTaO_6, **P. Mandal** and A. Sundaresan, *Solid State Sci.* **11**, 861 – 864 (2009).

2. Structure, magnetism and giant dielectric constant of $BiCr_{0.5}Mn_{0.5}O_3$ synthesized at high pressures, **P. Mandal**, A. Iyo, Y. Tanaka, A. Sundaresan and C. N. R. Rao, *J. Mater. Chem.* **20**, 1646 – 1650 (2010).

3. Temperature-induced magnetization reversal in $BiFe_{0.5}Mn_{0.5}O_3$ synthesized at high pressure, **P. Mandal**, A. Sundaresan, C. N. R. Rao, A. Iyo, P. M. Shirage, Y. Tanaka, C. Simon, V. Pralong, O. Lebedev, V. Caignaert and B. Raveau, *Phys. Rev. B* **82R**, 100416 (2010).

4. Spin-Reorientation, Ferroelectricity, and Magnetodielectric Effect in $YFe_{1-x}Mn_xO_3$ ($0.1 \leq x \leq 0.40$), **P. Mandal**, V. S. Bhadram, Y. Sundarayya, C. Narayana, A. Sundaresan and C. N. R. Rao, *Phys. Rev. Lett.* **107**, 137202 (2011).

5. Structure and complex magnetic behavior of disordered perovskite $(Bi_{0.5}Sr_{0.5})(Fe_{0.5}Mn_{0.5})O_3$, **P. Mandal**, S. R. Bhat, Y. Sundarayya, A. Sundaresan and C. N. R. Rao, *RSC Adv.* **2**, 292 (2012).

6. Tunable inverse and normal magnetocaloric effects and the magnetization reversal in $YFe_{1-x}Mn_xO_3$, **P. Mandal**, C. R. Serrao, A. Sundaresan, C. N. R. Rao, *Communicated*.

7. Weak ferromagnetism and magnetization reversal in $YFe_{1-x}Cr_xO_3$, **P. Mandal**,

A. Sundaresan, N. M. Dasari and N. S. Vidhyadhiraja, *Communicated*.

8. Effect of Non-magnetic Ion Substitution on the Multiferroic Properties of $BiFeO_3$, **P. Mandal**, A. Iyo, P. M. Shirage, Y. Tanaka, A. Sundaresan, C. N. R. Rao, *Communicated*.

Other miscellaneous publications:

1. Ferroelectricity in ordered perovskite $BaBi^{3+}_{0.5}Bi^{5+}_{0.2}Nb^{5+}_{0.3}O_3$ with Bi^{3+}:$6s^2$ lone pair at the B-site, R. V. K. Mangalam, **P. Mandal**, E. Suard and A. Sundaresan, *Chem. Mater.* **19**, 4114 (2007).

2. HollowSpheres to Nanocups: Tuning the Morphology and Magnetic Properties of Single-Crystalline Fe_2O_3 Nanostructures, D. Jagadeesan, U. Mansoori, **P. Mandal**, A. Sundaresan and M. Eswaramoorthy, *Angew. Chem. Int. Ed.* **47**, 7685 (2008).

3. Magnetocapacitive $La_{0.6}Sr_{0.4}MnO_3$/0.7Pb($Mg_{1/3}Nb_{2/3}$)O_3 – 0.3$PbTiO_3$ epitaxial heterostructure, A. R. Chaudhuri, **P. Mandal**, S. B. Krupanidhi and A. Sundaresan, *Solid State Commun.* **148**, 566 – 569 (2008).

4. Investigation of biferroic properties in $La_{0.6}Sr_{0.4}MnO_3$/0.7Pb($Mg_{1/3}Nb_{2/3}$)O_3 epitaxial bilayered heterostructures, A. R. Chaudhuri, S. B. Krupanidhi, **P. Mandal** and A. Sundaresan, *J. Appl. Phys.* **106**, 054103 (2009).

5. Zero magnetization in a disordered ($La_{1-x/2}Bi_{x/2}$)($Fe_{0.5}Cr_{0.5}$)O_3 uncompensated weak ferromagnet, K. Vijayanandhini, C. Simon, V. Pralong, Y. Brard, V. Caignaert, B. Raveau, **P. Mandal**, A Sundaresan and C. N. Rao, *J. Phys. Cond. Matt.* **21**, 486002 (2009).

6. Multiferroic and magnetodielectric properties of the $Al_{1-x}Ga_xFeO_3$ family of oxides, Ajmala Shireen, Rana Saha, **P. Mandal**, A. Sundaresan and C. N. R. Rao, *J. Mater. Chem.* **21**, 57 (2011).

7. Tuning of dielectric properties and magnetism of $SrTiO_3$ by site-specific doping of Mn, D. Choudhury, S. Mukherjee, **P. Mandal**, A. Sundaresan, Satadeep Bhattacharya, R. Mathieu, P. Lazor, Olle Eriksson, B. Sanyal, P. Nordblad, A. Negi, S. V. Bhat, O. Karis, D. D. Sarma *Phys. Rev. B* **84**, 125124 (2011).

8. Mössbauer spectroscopic study of spin reorientation in Mn-substituted yttrium orthoferrite, Y. Sundarayya, **P. Mandal**, A. Sundaresan and C. N. R. Rao, *J. Phys. Cond. Matter* **23**, 436001 – 436006 (2011).

Contents

1 Introduction to Multiferroics: Materials and Mechanism 1

1.1 Ferroelectricity 2

1.2 Ferromagnetism 6

1.3 Magnetoelectric materials 8

1.3.1 ME effect in single phase materials 10

1.3.2 ME effect in composites 10

1.4 Magnetoelectric multiferroics 12

1.5 Classification of multiferroics 14

1.5.1 Proper ferroelectrics 14

1.5.1.1 Lone pair effect 15

1.5.2 Improper ferroelectrics 16

1.5.2.1 Geometric frustration 16

1.5.2.2 Charge ordering 17

1.5.2.3 Complex magnetic ordering 18

1.5.3 Application of magnetoelectric multiferroic materials 23

1.5.4 Cross-coupling and temperature factor 24

1.6 Motivation of present work 25

2 Experimental Techniques **27**

2.1 Materials preparation 27

2.1.1 Solid state reaction 27

2.1.2 High pressure apparatus 28

2.2 Structure and Physical properties 30

2.2.1 Structure 30

2.2.1.1 Powder X-ray diffraction 30

2.2.1.2 Powder neutron diffraction 31

2.2.1.3 Rietveld refinement 31

2.2.2 Ferroelectric measurement 33

2.2.2.1 P-E loop measurement 33

2.2.2.2 Pyroelectric current measurement 34

2.2.3 Dielectric measurement 35

2.2.3.1 Capacitance and loss measurements 35

2.2.3.2 Experimental set-up for low temperature measurements 38

2.2.4 Magnetic properties 39

2.2.4.1 DC magnetization 40

2.2.4.2 AC susceptibility 41

3 Effect of Non-magnetic Ion Substitution on the Multiferroic Properties of $BiFeO_3$ **43**

3.1 Introduction 43

3.2 Experimental 46

3.3 Results and discussions 47

3.3.1 Structure . . . 47
3.3.2 Magnetic properties . . . 49
3.3.3 Dielectric properties . . . 51
3.3.4 Ferroelectric properties . . . 56
3.4 Conclusions . . . 58

4 Structure, Magnetism and Giant Dielectric Constant of $BiCr_{0.5}Mn_{0.5}O_3$ Synthesized at High Pressures 59

4.1 Introduction . . . 59
4.2 Experimental . . . 62
4.3 Results and discussion . . . 63
4.3.1 Structure . . . 63
4.3.1.1 High temperature X-ray diffraction . . . 64
4.3.2 Magnetic properties . . . 67
4.3.2.1 DC magnetization . . . 67
4.3.2.2 AC susceptibility . . . 69
4.3.3 Dielectric properties . . . 70
4.3.3.1 Maxwell-Wagner relaxation . . . 72
4.3.3.2 AC conductivity . . . 75
4.3.3.3 Impedance spectroscopy . . . 76
4.4 Conclusions . . . 79

5 Temperature–induced Magnetization Reversal and Complex Magnetic Behavior in $Bi_{1-x}A_xFe_{0.5}Mn_{0.5}O_3$ (x = 0, 0.5 and A = La, Sr) 81

5.1 Introduction 81
5.2 Experimental 83
5.3 Results and discussion 84
5.3.1 Structure 84
5.3.2 Magnetic properties 86
5.3.2.1 Temperature-induced magnetization reversal 88
5.3.2.2 Pole reversal 91
5.3.2.3 Zero field cooled measurements: Role of remnant magnetic field 92
5.3.2.4 Origin of magnetization reversal 94
5.3.3 Structure and complex magnetic behavior of $Bi_{0.5}A_{0.5}Fe_{0.5}Mn_{0.5}O_3$; A = Sr, La 96
5.3.3.1 Crystal and magnetic structure 97
5.3.3.2 Valence states 100
5.3.3.3 Cluster and spin-glass behavior in BSFMO 102
5.4 Conclusions 107

6 Magnetization Reversal in $YFe_{1-x}M_xO_3$ (M = Cr and Mn) 109

6.1 Introduction 109
6.2 Experiments 111
6.3 Result and discussion 111
6.3.1 Structure and Magnetic Properties of $YFe_{1-x}Cr_xO_3$ 112
6.3.1.1 Structure 112

6.3.1.2 Weak ferromagnetism and spin-reorientation in $YFe_{1-x}Cr_xO_3$ . . . 114
6.3.1.3 Temperature induced magnetization reversal . . . 116
6.3.1.4 Neutron diffraction study on $YFe_{0.5}Cr_{0.5}O_3$ . . . 119
6.3.1.5 Reversal mechanism . . . 126
6.3.2 Structure and magnetic properties of $YFe_{1-x}Mn_xO_3$ . . . 130
6.3.2.1 Structure of $YFe_{1-x}Mn_xO_3$ . . . 130
6.3.2.2 Weak ferromagnetism and spin-reorientation in $YFe_{1-x}Mn_xO_3$ . . . 132
6.3.2.3 Magnetization reversal . . . 134
6.3.2.4 Neutron diffraction studies on $YFe_{0.6}Mn_{0.4}O_3$ . . . 135
6.3.2.5 Origin of magnetization reversal in $YFe_{1-x}Mn_xO_3$ . . 140
6.3.2.6 Magnetocaloric effect in $YFe_{1-x}Mn_xO_3$ . . . 142
6.4 Conclusions . . . 144

7 Ferroelectricity and Magneto(di)electric Effect in Centrosymmetric $YFe_{1-x}Mn_xO_3$ 147

7.1 Introduction . . . 147
7.2 Experiments . . . 149
7.3 Result and discussions . . . 150
7.3.1 Magnetodielectric effect . . . 150
7.3.2 Maxwell-Wagner relaxation and intrinsic magnetocapacitance . 153
7.3.3 Ferroelectricity and magnetoelectric coupling . . . 156
7.3.4 Origin of ferroelectricity and magneto(di)electric effect . . . 160

7.3.4.1 Spin-phonon Coupling 160

7.3.4.2 Spin disorder 161

7.4 Conclusion 163

8 Summary **165**

CHAPTER 1

Introduction to Multiferroics: Materials and Mechanism

Present day leisure and basic needs of our daily life has triggered an exponential increase in technical advances. This has enforced scientists and engineers to discover new compounds and develop technologies. At present, this is reflected in all technologies involving metals, ceramics, semiconductors, polymers, composites, biomaterials and other exotic materials. Not only these have commercial value but are also of fundamental interest. In last century, there have been several breakthrough inventions such as superconductivity, metal-oxide-silicon (MOS) transistors, optical storage materials, giant magnetoresistance, semiconductor lasers, optical fibers, liquid crystals, nanomaterials etc. These discoveries have greatly influenced the advances in medical science, telecommunications, storage devices and other branches of science. Miniaturization is another objective for integration and higher performance of present day's devices.

Multifunctional materials provide a way to combine various functionalities in a single compound. Such advanced materials with coexisting superior properties can be good candidates for application in various fields mentioned above. Progress in materials design, instruments and microscopic understanding has further helped to discover these exotic phenomenon. Superconductivity which was discovered 100 years ago, is still being widely studied to find materials with zero electrical resistance at room temperature. Superconductivity and magnetism though closely related but coexistence is

rather difficult to achieve. It has also been observed that coexistence of two mutually exclusive properties mostly gives rise to exotic phenomena which can be useful for better control of the functionalities. Multiferroic is one such example where the mutually exclusive ferroic properties coexist in a single material.

In a ferroic material, the order parameter spontaneously appears below a characteristic transition temperature and that can be switched by external force or field [1, 2]. Ferroics can be classified mainly into three categories namely ferroelastic, ferroelectric and ferromagnetic where the corresponding order parameters are strain, polarization and magnetization respectively. The ferroelastic materials possess spontaneous deformation or strain below a transition temperature. When a stress (force per unit area) is applied, the strain can be switched hysteretically. Here, we have focused our primarily on ferroelectricity and ferromagnetism as discussed below in detail.

1.1 Ferroelectricity

An electric dipole consist of a positive and a negative charge, q separated by a distance d. The dipole moment is defined as the product of charge and the distance. The dipole moment per unit volume is known as polarization ($\mathbf{P}$). In materials, where the dipoles can be polarized with an electric field are called electrically polarizable as shown schematically by an elliptic box in figure 1.1. In the paraelectric phase of $BaTiO_3$ which has cubic structure, centers of the positive charges Ba^{2+}, Ti^{4+} and negative charges of O^{2-} lies at the center of the cube. Thus, non-centrosymmetric structure is an essential condition for a compound to be polar.

Ferroelectricity is a phenomenon where a spontaneous electric polarization exist be-

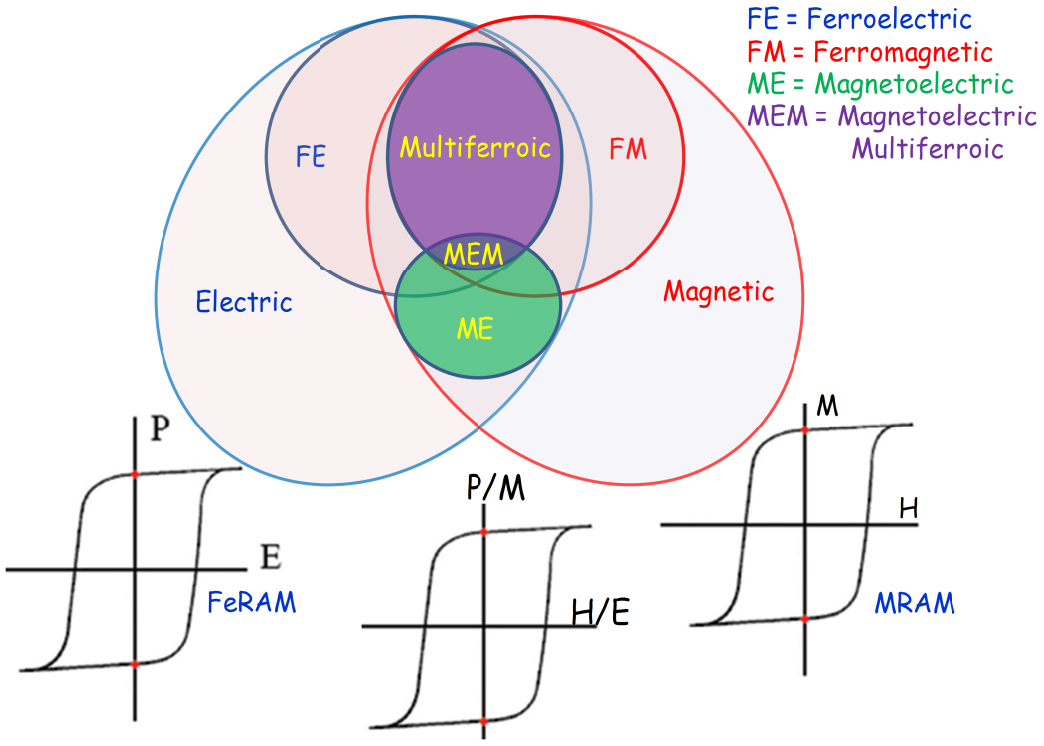

Figure 1.1: Electrically and magnetically polarizable materials are shown as elliptic region. Ferromagnets and Ferroelectrics which are subset of these are shown as circular regions. The materials in the overlapped region (violet) are multiferroic i.e., both ferroelectric and ferromagnetic. Magnetoelectric (ME) effect which need not, arise in any of the materials that are both magnetically and electrically polarizable is shown by green circular region. The materials belonging to the region MEM are magnetoelectric multiferroic.

low Curie temperature (T_{CE}) even in absence of any field and that can be switched with an external electric field. This forms a subset of electrically polarizable materials as represented by a circle (FE) in figure 1.1. As ferroelectricity is deeply related to symmetry, the crystal with non-centrosymmetric structure only can show the polar nature. Antiferrolectrics are the other class of electrically polarizable materials where the spontaneous dipole moment is zero due to centrosymmetric structure. In fact, ferroelectricity is subgroup of pyroelectric and piezoelectric class of compounds. Piezoelectricity is the effect where spontaneous polarization appears when a stress is applied and vice versa i.e.,

there is a strain induced under an electric field. Below Curie point, a pyroelectric crystal has a spontaneous polarization which may or may not be switchable. This classification can be understood in terms of symmetry. There are 32 point groups which can be classified into two classes based on the symmetry. The point groups which possess center of symmetry are known as centrosymmetric and thus can not be polar. Out of 32 point groups 11 are non-polar i.e., centrosymmetric. In the remaining 21 point groups, 20 (except the point group 432) are non-centrosymmetric and show piezoelectricity. These non-centrosymmetric structures can have one or more crystallographically unique direction (polar axes) along which the piezoelectric effect is observed. Particularly, polar crystals with one of the ten point groups (1, 2, m, mm2, 4, 4mm, 3, m , 3m, 6 and 6mm) have only one unique polar axis and can show spontaneous polarization. Such compounds are known as pyroelectric. It is not always possible to switch the spontaneous polarization in all the pyroelectric crystals possibly due to very high coercive field [2]. Ferroelectrics are those pyroelectric compounds where the spontaneous polarization is switchable.

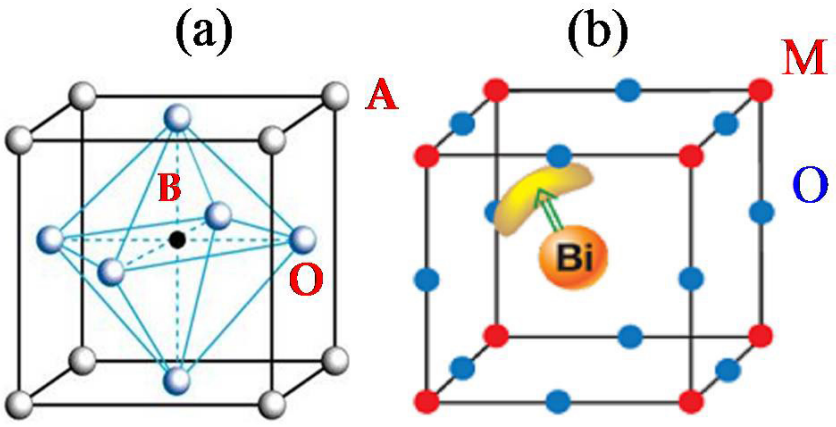

Figure 1.2: (a) Perovskite structure ABO_3 with BO_6 octahedra. (b) Bi perovskite oxide ($BiMO_3$) showing 6s lone pairs

In 1921, ferroelectricity was discovered in Rochelle salt, $KNa(C_4H_4O_6).4H_2O$ [3]. This compound was first prepared by Elie Seignette in mid 1600 in La Rochelle, France and thus the effect is also known as Seignette effect. Later ferroelectricity was observed in perovskite $BaTiO_3$ which has very high dielectric constant ($\sim$1200) near the Curie temperature (T_{CE}) 393 K [4, 5]. Perovskites are cubic type structure represented as ABO_3, where A ions are present at the corners, B ions at the centre of the cube and oxygen occupies centre of each face as shown schematically in figure 1.2. $BaTiO_3$ undergoes structural transition from paraelectric cubic to noncentrosymmetric tetragonal at Curie temperature and successive transitions to orthorhombic and rhombohedral phases at further low temperatures. Incidentally, the most studied ferroelectrics such as $PbTiO_3$, $PbZr_{1-x}Ti_xO_3$, $PbMg_{2/3}Nb_{1/3}O_3$, $K_xNa_{1-x}NbO_3$ etc. also possess perovskite structure.

Based on the mechanism of transition from paraelectric (centrosymmetric) to ferroelectric (non-centrosymmetric) phase, ferroelectrics are divided into order-disorder and displacive types. Order-disorder type of transition is observed in compounds typically with Hydrogen (H) bond such as KH_2PO_4 where below T_C the ordered H-bonds give rise to a net dipole moment. Above T_C, these bonds are disordered giving a paraelectric phase. In the displacive ferroelectrics, the ions are displaced about the polar center below Curie temperature. The ionic crystals belong to this class. In $BaTiO_3$, the Ba^{2+} and Ti^{4+} ions are displaced relative to O^{2-} ions developing a net dipole moment below the Curie temperature. As ferroelectrics are electrically insulating, they are also good candidate for dielectric materials.

In normal ferroelectric such as $BaTiO_3$, the dielectric constant shows a sharp tran-

sition with a weak frequency dependence at the Curie temperature. The lead based compounds of the type $Pb(B_1,B_2)O_3$ (B_1, B_2 are cations with different valences), such as $PbZr_{1-x}Ti_xO_3$ and $PbMg_{2/3}Nb_{1/3}O_3$ show a broad diffused transition with a large frequency dispersion. This kind of materials are known as relaxor ferroelectrics.

1.2 Ferromagnetism

Ferromagnetism can be considered as the magnetic analog of ferroelectricity. Below Curie temperature (T_C), the ferromagnetic compounds possess spontaneous magnetic moment which is reversibly switchable with external magnetic field as shown in figure 1.1. In these compounds, the spins or the magnetic moments align parallel to each other. There exist two more types of magnetic ordering known as antiferromagnetic and ferrimagnetic. In antiferromagnetic compounds, the neighbouring spins align antiparallel to each other, thus resulting a net zero magnetic moment below the transition temperature known as Néel temperature, T_N. In ferrimagnetic compounds, spins with different magnetic moments couple antiferromagnetically resulting finite magnetic moments.

The magnetic ordering is understood in terms of an internal molecular field which tends to align the spins in parallel or antiparallel. The concept of molecular field was proposed by Weiss about a century ago [6]. The origin of molecular field is now understood to be a quantum mechanical exchange energy as proposed by Heisenberg and Dirac [7, 8]. This is the energy gained for parallel or antiparallel arrangement between two spins S_i and S_j and expressed as $-2J\mathbf{S}_i \cdot \mathbf{S}_j$. The positive sign of J favors parallel arrangement while the negative sign prefers antiparallel arrangement between the spins. The internal field is so strong that compounds show spontaneous magnetic mo-

ment below TC even in the absence of external field. At Curie temperature, the thermal energy (k_BT) destroys the magnetic ordering and results in random arrangement of spins. Above, $T_{C/N}$, the magnetic susceptibility ($\chi = M/H$) follows Curie - Weiss law,

$$\chi = \frac{C}{T - \theta} \tag{1.1}$$

where C is the Curie constant and θ is Weiss temperature. For ferromagnetic interaction θ is positive whereas antiferromagnetic interaction leads to a negative value of θ. The Curie constant is related to the effective magnetic moment by

$$\mu_{\text{eff}} = 2.83 \times \sqrt{C} \tag{1.2}$$

From the fit of paramagnetic susceptibility to Curie - Weiss law, number of free electrons contributing to the effective magnetic moment can be calculated. For example, if the magnetic ions has *n* unpaired electrons, the spin only theoretical value is given by

$$\mu_{\text{SO}} = \frac{g}{2}\sqrt{n(n+2)} \tag{1.3}$$

In oxides, the interactions between the magnetic ions are mediated by the nonmagnetic oxygen ion. The magnetic interaction can be either superexchange or double exchange. In this 180 ° superexchange interaction, the exchange interaction occurs through the virtual transfer of electrons to the neighbouring magnetic ions via oxygen [9]. The ground magnetic state can be ferromagnetic or antiferromagnetic predicted following the Goodenough - Kanamori rule which states that the superexchange interactions are antiferromagnetic where the virtual electron transfer is between overlapping orbitals that are each half-filled, but they are ferromagnetic where the virtual electron

transfer is from a half-filled to an empty orbital or from a filled to a half-filled orbital [10, 11]. On the other hand, double exchange interaction occurs in compounds mixed valent ions where electron is exchanged from one to another magnetic ion mediated by oxygen.

1.3 Magnetoelectric materials

The coupling between the electric and magnetic properties are known for more than century now. Magnetoelectric effect (ME) is a phenomenon where electric dipole moment can be induced by an external magnetic field and vice/versa [12, 13]. This effect can directly be obtained by coupling between the order parameters i.e., polarization and magnetization or indirectly also via strain. In Landau theory, this effect is treated by expressing the free energy F of a homogeneous and stress free system in terms of magnetic field (H) and electric field (E) as

$$\begin{aligned} F(\vec{E},\vec{H}) = F_0 - P_i^S E_i - M_i^S H_i \\ -\frac{1}{2}\epsilon_0\epsilon_{ij}E_iE_j - \frac{1}{2}\mu_0\mu_{ij}H_iH_j - \alpha_{ij}E_iH_j \\ -\frac{1}{2}\beta_{ijk}E_iH_jH_k - \frac{1}{2}\gamma_{ijk}H_iE_jE_k - \cdots \end{aligned} \tag{1.4}$$

where P_S and M_S denotes the spontaneous polarization and magnetization with ϵ and μ as electric and magnetic susceptibilities. The polarization ($P = -\delta F/\delta E$) and magnetization ($M = -\delta F/\delta H$) are obtained by differentiating the free energy with respect to

the electric and magnetic fields respectively and can be written as:

$$P_i(\vec{E},\vec{H}) = P_i^S + \epsilon_0\epsilon_{ij}\,E_j + \alpha_{ij}\,H_j + \frac{1}{2}\beta_{ijk}\,H_j\,H_k + \frac{1}{2}\gamma_{ijk}\,H_i\,E_j - \cdots \tag{1.5}$$

$$M_i(\vec{E},\vec{H}) = M_i^S + \mu_0\mu_{ij}\,H_j + \alpha_{ij}\,E_i + \beta_{ijk}\,E_i\,H_j + \frac{1}{2}\gamma_{ijk}\,E_j\,E_k - \cdots \tag{1.6}$$

As clear from the equations 1.5 and 1.6, in case of pure magnetic or electric systems only the first two terms are non-zero. The third term in these equations stands for the induced polarization or magnetization which is linear to the magnetic or electric field. The coupling constant α is a tensor and known as linear magnetoelectric coefficient whereas the higher order terms $\hat{\beta}$ and $\hat{\gamma}$ signify the nonlinear ME coupling. In materials where magnetoelectric effect is absent the terms containing these coefficients vanishes and are purely magnetic or electric. Also, neglecting the higher order ME coefficient, the linear coefficient can be related to the magnetic and electric susceptibilities by following relation,

$$\alpha_{ij}^2 \leq \epsilon_0\mu_0\epsilon_{ij}\mu_{ij} \tag{1.7}$$

Thus, it follows from the equation that a magnetoelectric system need not be either ferroelectric or ferromagnetic as shown schematically (ME) in figure 1.1. But the magnetoelectric coupling coefficient is high when the material is ferromagnetic as well as ferroelectric as the large relative electric and magnetic susceptibilities (ϵ and μ) will give rise to a large magnetoelectric effect according to equation 1.7. Experimentally, either the induced magnetization or the polarization is measured when the compound

is subjected to an electric or a magnetic field. In the linear ME effect, the coefficient is typically specified in units of mV cm^{-1} Oe^{-1} or ps cm^{-1}.

1.3.1 ME effect in single phase materials

The ME effect was first indicated in an experiment by Röntgen in 1888 where a moving dielectric, placed in an electric field was found to be magnetized [14]. Later, in 1894 Curie suggested the possibility of magnetoelectric effect from symmetry grounds [15]. It must be pointed out that magnetoelectric effect breaks the time reversal symmetry. In 1959, the effect was first established by Dzyaloshinskii based on the time reversal symmetry breaking in an antiferromagnetic Cr_2O_3 which later was soon confirmed experimentally by Astrov in 1960 [16, 17]. The induction of magnetization by an electric field and the reverse effect i.e., inducing polarization by magnetic field was demonstrated in Cr_2O_3 [17–19]. In Cr_2O_3, the maximum magnetoelectric coefficient (α_{zz}) was found to be 4.1 ps m^{-1} near the Néel temperature 307 K above which it vanishes. This was followed by observation in single phase materials such as Ti_2O_3, $GaFeO_3$, boracite and phosphate compounds, antiferromagnetic Gd_2CuO_4, Sm_2CuO_4, solid solutions like $PbFe_{0.5}Nb_{0.5}O_3$, garnet films, multiferroic $BiFeO_3$ etc [12, 13]. Among the single phase compounds, the largest value of magnetoelectric coefficient observed in $TbPO_4$ (36.7 ps m^{-1}). Magnetoelectric effect in various single phase as well as in two phase systems are well summarized in few review articles [12, 13, 20, 21].

1.3.2 ME effect in composites

As mentioned before, the ME effect can indirectly be induced by strain. In fact the coupling has been observed in two phase systems such as composites, laminates and

epitaxial heterostructure of ferroelectric and ferromagnetic materials where the strain is mediated by magnetostrictive and electrostrictive properties [12, 13]. As mentioned, ferroelectric compounds are also piezoelectric and most of the manganites and ferrites are magnetostrictive. Thus, a composite system of ferroelectric and ferromagnetic is expected to show a large magnetoelectric effect. This was demonstrated first by van Suchtelen, van den Boomgard *et al* on the unidirectionally solidified two phase structure of ferroelectric/piezoelectric $BaTiO_3$ and ferromagnetic/piezomagnetic $CoFe_2O_4$ mixtures which showed a very high ME voltage of 130 $mVcm^{-1}Oe^{-1}$. This value corresponds to 720 ps m^{-1} much larger than the observed values for single phase compounds [22, 23]. Later, many other materials such as $PbZr_{1-x}Ti_xO_3$ (PZT, d_{33} = 250 pm V^{-1}), $Bi_4Ti_3O_{12}$, $PbMg_{1/3}Nb_{2/3}O_3$ - $PbTiO_3$ (PMN - PT) etc. were used as piezoelectric and $Tb_{1-x}Dy_xFe_2$ alloys (Terfenol-D), perovskite manganites, yttrium iron garnets etc. were chosen as magnetostrictive to study magnetoelectric composites [12].

The magnetoelectric effect in composites was further improved using laminated structure consisting of piezoelectric and magnetostrictive elements sandwiched between magnetostrictive component and therefore causing a macroscopic separation. This has helped to avoid several drawbacks which so far had restricted the ME coupling in composites such as chemical diffusion, ineffective poling due to low resistivity of magnetostrictive component, defects etc. Ryu *et al* reported that laminated composite structure of PZT (piezoelectric) disc sandwiched between $Tb_{1-x}Dy_xFe_2$ (magnetostrictive) discs showed an enormously high ME voltage of 4680 mV cm^{-1} Oe^{-1} [24]. This procedure adopted for thick films of $NiFe_2O_4$ - PZT bilayer and multilayers showed ME voltage up to 1500 mV cm^{-1} Oe^{-1} [25]. Surprisingly, it was observed for the multilayer composite

systems, that the output voltage is dependent on the frequency of the AC magnetic field. The output voltage was seen to increase at a resonance frequency which is dependent on magnetic, electric or mechanical eigenmodes of the system. The maximum ME effect observed till date is on a trilayer structure of Permendur (an alloy consisting of 49% Fe, 49% Co and 2% V) - PZT - Permendur and is 90000 $\mathrm{mV\,cm^{-1}\,Oe^{-1}}$ [26]. The magnetoelectric effect has also been found in the nanocomposites in the form of epitaxial heterostructure and also in assembled nanostructure [27, 28]

The first experimental set up to study magnetoelectric effect (electric field induced) was measured was designed by Astrov [17]. At present, the ME effect is studied mainly by three methods namely i) static method, ii) quasi-static method and iii) dynamic method. Prior to the measurement, the sample is poled electrically as well as magnetically. In the first method, the output voltage is measured while increasing the magnetic field. Later, to avoid the accumulated charges arising due to electrical, poling quasi dynamic and dynamic methods are used. An AC magnetic field is used in dynamic method and the output voltage is measured in a time varying DC magnetic field [29, 30].

1.4 Magnetoelectric multiferroics

Multiferroics, as the term suggests, are the materials where multiple ferroic properties can coexist. As shown in figure 1.1, there is common region (Multiferroic) where the materials possess both the ferroic properties. The coexistence often leads to a cross coupling between the order parameters. Also, there is a small region in the diagram where there is an overlap between magnetoelectric and multiferroic properties. Materials of these class are known as magnetoelectric multiferroics. Our main interest here is on

the coexistence of ferroelectricity and ferromagnetism and possible coupling between them. Since ferromagnetic insulators are rare, often the ferroelectricity is combined with antiferromagnetism. According to the mechanism of classical ferroelectrics, it is hard to combine ferroelectricity and ferromagnetism in the same phase. The outer orbital (*d* or *f*) of a ferromagnet or antiferromagnet is required to be partially filled. On the other hand, in ferroelectric $BaTiO_3$, the Ti^{4+} has no electrons at the outer shell (d^0) and the system is ferroelectric but not ferromagnetic. The strong hybridization between the O-2p and Ti-3d states was proven to essential for ferroelectricity [31]. Thus, in a classical system, d^0-ness seems to be crucial for ferroelectricity whereas d^n for ferromagnetism. This brings a conflict to design a single phase multiferroic material. However, several alternative methods have been adopted to obtain multiferroics as summarized in review articles [13, 32–36]. The very first indication of coexistence of these ferroic properties known as ferroelectromagnets were by Smolensky and Venevtsev in 1959 [32, 37, 38]. Although these materials are known from 1960, the field became more exciting for the scientific community in the last decade after reinvestigation of multiferroicity in $BiFeO_3$ and $TbMnO_3$. At present the number of such materials are large and have been observed not only in oxides but also in fluorides and oxyfluorides [39].

In the context of ferroics, it is important to discuss symmetry rules. Ferroelastics are invariant under time or spatial inversion symmetry. The ferroelectric materials break spatial inversion symmetry whereas ferromagnet breaks time reversal symmetry. The multiferroics in fact breaks both the symmetries.

1.5 Classification of multiferroics

As discussed before the ferroelectricity and ferro- or antiferromagnetism are mutually exclusive in classical ferroelectric materials, therefore several alternative methods have been attempted by scientific community to achieve ferroelectricity in a magnetic material. Multiferroic materials can be classified based either on mechanisms or materials. Depending on the origin of ferroelectricity the magnetic ferroelectrics are classified mainly into two groups namely, proper and improper ferroelectrics. In the proper ferroelectricity, the structural transformation or instability is responsible for the polar state whereas a more complex lattice distortion arising from a secondary ordering induces improper ferroelectricity. This will be discussed with examples in the following sections.

1.5.1 Proper ferroelectrics

The well known compounds such as $BaTiO_3$, $PbTiO_3$ etc. belong to this class of ferroelectrics. At the ferroelectric Curie temperature these compounds undergo a structural transition from centrosymmetric (non-polar) to a non-centrosymmetric (polar) structure. As shown by Cohen in his famous article that the hybridization between the B-site element (d^0) with oxygen ions ($2p$) is essential to sustain a ferroelectric distortion [31]. This ferroelectric distortion in this compounds normally gives rise to a large ferroelectric polarization ($4 - 300\,\mu\,C/cm^2$).

1.5.1.1 Lone pair effect

Other than the hybridization between unoccupied transition metal and the oxygen ions, ferroelectric distortion has been observed due to stereochemical activity of lone pair electrons. Despite the compounds $BaTiO_3$ and $PbTiO_3$ are having similar properties such as unit cell volumes, tetragonal structure below the Curie temperature, the ferroelectric behaviors in them are quite different. The former compound has a *c/a* strain of 1 % whereas the later compound $PbTiO_3$ has rather large strain of 6 %. This difference is attributed to the 6s lone pair of lead where hybridization of lead and oxygen states leads to a large distortion in contrast to ionic nature of Ba and O interaction in $BaTiO_3$ [31]. The trivalent Bi ion has identical electronic state ($6s^2$) and several perovskite oxides are found to have polar or noncentrosymmetric structure. This provides an opportunity to design multiferroic compound having a formula $BiMO_3$ or $PbMO_3$ where M is transition metal ion having unpaired *d* or *f* electrons can lead to (anti-)ferromagnetic ground states via superexchange interaction. The very first multiferroic compounds reported in this family are $Pb(Fe_{2/3}W_{1/3})O_3$ and $BiFeO_3$ [32]. Although, the lead based ferroelectrics are superior compared to the other classes of ferroelectrics, researchers are avoiding the use of lead due to its toxicity. On the other hand, bismuth based perovskites remains a better choice. Using first principles calculations, it was shown that the 6*s* lone pair of Bi (figure 1.2) drives the off center distortion and is responsible for ferroelectricity in Bi based perovskites [40]. It must be noted that $BiAlO_3$ and $BiFeO_3$ are the only compounds in $BiMO_3$ family which are ferroelectric while other are non-polar. Except $BiFeO_3$, all the $BiMO_3$ perovskite compounds are stabilized under high pressure ($\sim$ 4 - 6 GPa). Perovskites of the type $Bi_2MM'O_6$ known as double perovskite

opens up a possibility to a have ferromagnetic ground with proper choice of M and M′ according to Goodenough-Kanamori rule.

1.5.2 Improper ferroelectrics

In this class of ferroelectrics, the polarization appears from a secondary transition and thus the order parameter considered in phenomenological Landau theory is not polarization but a different physical parameter relating to such transitions [41]. Dielectric behaviors in this system are quite different and mostly do not follow the Curie-Weiss law above the phase transition. Also, as the ferroelectricity is secondary, the dielectric constant is comparatively lower. Following by theoretical prediction, this type of ferroelectricity was first observed in gadolinium molybdate, $Gd_2(MoO_4)_3$ where the polarization arises from an elastic instability [42]. At present ferroelectricity in large number of multiferroics are improper and induced from complex ordering of charge, spin, bond etc as discussed below in detail.

1.5.2.1 Geometric frustration

In hexagonal manganite $RMnO_3$ the ferroelectricity is observed due to geometric frustration for small rare earth ions (R) [43]. For example, $YMnO_3$ is ferroelectric below 950 K whereas the antiferromagnetic ordering is observed at 77 K [44]. The ferroelectric phase of $YMnO_3$ has a hexagonal structure (space group $P6_3cm$) which transforms to a centrosymmetric structure $P6_3/mmc$ above the ferroelectric Curie temperature [45]. In the noncentrosymmetric phase, the Mn^{3+} ions are not located in octahedra but in a five fold coordination. Also, the rare earth ion is located in a seven fold coordination. Origin of ferroelectricity in such systems has been described in terms of buckling of

layered MnO_5 polyhedra and an unusual displacements of Y ions resulting a net polarization [46].

1.5.2.2 Charge ordering

Charge ordering of magnetic ions has been demonstrated to result in ferroelectricity. For example, $LuFe_2O_4$ is ferrimagnetic below 250 K and the polar state is observed below charge ordering temperature of Fe^{2+} and Fe^{3+}. In this compound, the Lu, Fe and O are stacked alternatively in the triangular lattice and the ordering of Fe^{2+} and Fe^{3+} results in a ferroelectric state below 330 K. Another example of ferroelectricity induced from a charge ordered state is in Fe_3O_4. Below the metal insulator transition at 125 K, a complex of charge ordering occurs which induces electric polarization [47, 48]. In the colossal magnetoresistive oxides $R_{1-x}Ca_xMnO_3$ (R = rare earth), manganese exists in both trivalent and tetravalent states. At low temperature, Mn^{3+} and Mn^{4+} are ordered (site centered) at low temperature which give rise to a robust charge ordered insulating state for x = 0.5. As Mn^{3+} is Jahn-Teller active, an orbital ordering is also observed in this half doped manganites. It has been shown in manganites close to $x \sim 0.4$, there exist a charge ordered state which is not only site centered but also bond centered. The coexistence of these two types of charge ordering can lead to ferroelectric state as suggested by Efremov *et al* [49]. Dielectric anomalies observed across the charge order and magnetic transitions with a magnetocapacitance effect was suggested to arise from the coupling between electric and magnetic orders [50].

1.5.2.3 Complex magnetic ordering

In many magnetic ferroelectrics, the center of inversion symmetry is broken due to complex magnetic ordering [34–36]. In these compounds, ferroelectricity is observed due to the appearance of certain type of spin structure. Such spin structures can be either collinear or noncollinear. Figure 1.3 illustrates the sinusoidal, screw, cycloidal and conical spin structures.

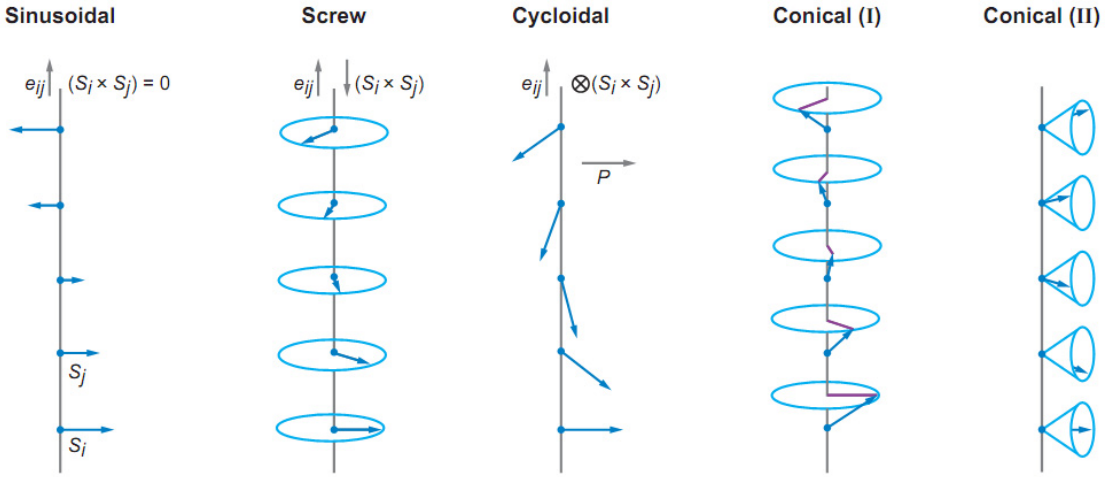

Figure 1.3: Possible collinear and non-collinear magnetic structure.

1.5.2.3.1 Cycloidal ordering

Among the non-collinear spin structures, only cycloidal and conical ordering breaks the inversion symmetry as discussed below. The perovskite manganites $RMnO_3$ (R = Tb, Dy, $Eu_{1-x}Y_x$ etc.), have a centrosymmetric orthorhombic structure (P*nma*/P*bnm*) and order antiferromagnetically at low temperatures (< 50 K). Below T_N, these compounds undergo a transverse spiral (cycloidal) spin ordering accompanied by ferroelectric transition. In $TbMnO_3$, the sinusoidal antiferromagnetic ordering occurs at 42 K and cycloidal magnetic ordering appears below 27 K [51]. Incidentally, the ferroelectric polarization also arises at the onset of the cycloidal magnetic ordering. Ferroelectricity

induced from cycloidal ordering has also been observed in several other materials such as $Ni_3V_2O_8$, CuO, $MnWO_4$, $LiCu_2O_2$, $LiCuVO_4$ etc [52–55].

1.5.2.3.2 Conical ordering

Under weak magnetic field, the screw or the cycloidal type of spin ordering can be transformed into conical spin structures as shown in figure 1.3. Ferroelectricity in the ferrimagnetic compound $CoCr_2O_4$ which orders at 93 K, originates from a conical spin states realized below 26 K. Upon cooling the compound in presence of both magnetic field (along [001]) and electric field (along [$\bar{1}$10]), the induced electric polarization could be reversed with external magnetic field [56, 57]. Later, similar magnetically induced ferroelectricity was reported in several other helimagnets $ZnCr_2Se_4$, $Ba_{0.5}Sr_{1.5}Zn_2Fe_{12}O_{22}$ and $Ba_2Mg_2Fe_{12}O_{22}$ [58–60]. The compounds $CuFeO_2$ and $ACrO_2$ (A = Cu and Ag) have centrosymmetric crystal structure ($R\bar{3}m$) where the elements Cu/A, Fe and O forms a triangular sublattice and stacks along *c*-axis. These compounds posses a 120 ° spin structure below the antiferromagnetic transition. This particular spin structure was shown to break center of inversion symmetry and induce polarization [61, 62].

1.5.2.3.3 Spin-current model

Microscopically, the ferroelectricity induced by the non-collinear magnetic structure discussed above is understood in terms of spin-current model or the inverse Dzyaloshinskii-Moriya model. In this scenario, the adjacent spin (S_i and S_j) pair produce a local polarization and thus net polarization can be expressed as

$$\mathbf{P} = a \sum_{<i,j>} \mathbf{e}_{ij} \times (\mathbf{S}_i \times \mathbf{S}_j)$$

where, $\mathbf{e}_{ij}$ is unit vector along the direction connecting the adjacent spins and a is a constant involving spinorbit and spin-exchange interactions as well as the possible spin-lattice coupling terms [63–65]. As the polarization contains cross product of two spins,

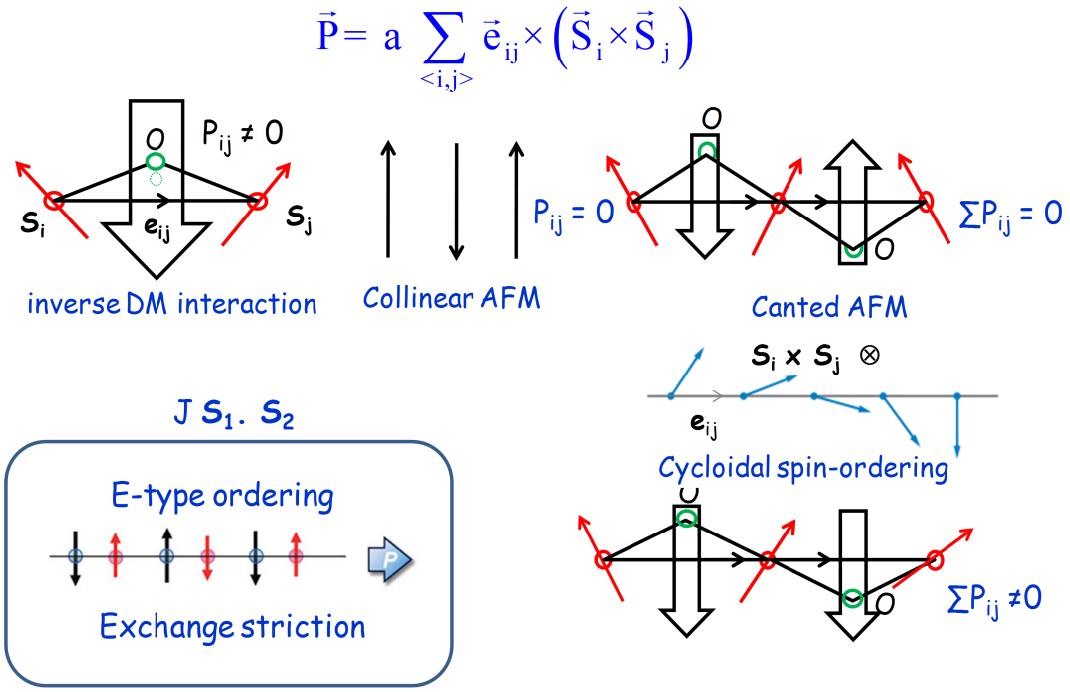

Figure 1.4: Ferroelectricity induced from complex magnetic ordering in terms of spin-current model and exchange striction.

this mechanism is also known as antisymmetric $\mathbf{S}_i \times \mathbf{S}_j$ coupling. It is clear from the expression, a collinear antiferromagnet will have no local or net polarization. Ferroelectricity in perovskite manganites $RMnO_3$ can be understood in the following way. In orthorhombically distorted structure, the Mn – O – Mn angle is less than 180 ° and oxygen ion bridging the manganese ions are not at the center of inversion symmetry as shown in figure 1.4. Moreover, the spin structure can further cant due to spin frustration arising from cycloidal or conical ordering. For a normal canted antiferromagnet, polarization is produced locally between two adjacent spins but next neighbour spins also gives a polarization which is in opposite direction and thus the net resultant po-

larization is zero. In cycloidal spin ordering, the spin rotation axis is perpendicular to the propagation direction of the spiral. As the adjacent spin pairs are not identical, the net polarization does not get cancelled out and results in a finite polarization. In figure 1.4, as shown for the cycloidal ordering, the polarization due to adjacent spin pairs appears in the same direction and thus adds up to result in a finite polarization. The same explanation holds for the ferroelectricity appearing in conical spin structures.

$CaMn_7O_{12}$ with incommensurate helical magnetic structure, were found to exhibit the largest polarization $\sim$ 3000 $\mu C/m^2$ which could not be explained by the spin-current model. In these new class of compounds, a ferroaxial coupling mechanism was proposed to explain the ferroelectric behavior [66, 67].

1.5.2.3.4 Collinear E-type ordering

The orthorhombic manganites $RMnO_3$ (R = Ho - Lu and Y) with a collinear E-type magnetic ordering was predicted to exhibit 100 times larger polarization [64, 68, 69]. Experimentally, ferroelectricity and magnetoelectric effect was observed in manganites with magnetic as well as non-magnetic rare earth ions. A similar E-type ordering induced ferroelectricity has also been observed in RMn_2O_5 and perovskite $RNiO_3$ [34, 70]. The inversion symmetry breaks due to symmetric exchange-striction of Mn - Mn of the type $S_i.S_j$. Unlike in non-collinear magnetic ordering, this mechanism does not include any spin-orbit coupling. In particular, this is understood by up - up - down - down ($\uparrow\uparrow\downarrow\downarrow$) spin chain model where nearest neighour coupling is ferromagnetic and next nearest interaction is antiferromagnetic [64]. Due to the exchange striction effect, the bond length between parallel spin shortens whereas between antiparallel bond it increases. This leads to a net polarization along the spin chain as shown in figure

1.4. $RNiO_3$ is an interesting case where $Ni^{3+\delta}$ and $Ni^{3-\delta}$ are ordered in up - up - down - down configuration and thus polar behavior arises due to both site centered as well as E-type of ordering [70]. In orthorhombic manganites ($RMnO_3$) showing an E-type ordering where the Mn spins form zigzag chains in the *ab* plane which stacks antiferromagnetically (+ - + -) along *c* direction. This configuration leads to a polarization along *a* axis. In RMn_2O_5, the Mn ions form loops with five spins as Mn^{4+} - Mn^{3+} - Mn^{3+} - Mn^{4+} -Mn^{3+} with nearest neighour coupled antiferromagnetically. As these spins are in loop, it causes a frustration leading to a complex structure. The electric polarization is induced by $\uparrow\uparrow\downarrow$ or $\downarrow\downarrow\uparrow$ spin ordering along the *b* axis [35].

1.5.2.3.5 Disorder induced ferroelectricity

Very recently, ferroelectricity has been observed in disordered canted antiferromagnetic perovskites ($ABB'O_3$) at the Néel temperature [71]. In these oxides where A is non-magnetic and B, B′ are two magnetic ions disordered at the B-site of the perovskite. Following inverse DM model, the canted antiferromagnetic structure of ABO_3 and $AB'O_3$ would give no macroscopic polarization. This situation is still valid when B and B′ are perfectly ordered. However, when Band B′ are randomly disordered a polar state can be realized.

In a recent report on canted antiferromagnetic $SmFeO_3$, ferroelectricity appearing at Néel temperature was explained from inverse DM interaction acting on the non-equivalent Fe ions at the crystallographic 4*b* position [72]. In this report the interaction of Fe and the rare earth was not considered. Bharath *et al* demonstrated that the rare earth orthoferrite or orthochromite systems RMO_3 exhibits a polar behavior when R is magnetic such as Gd, Sm etc [73].

1.5.3 Application of magnetoelectric multiferroic materials

The coupled order parameters in ME materials has opened up the possibility of employing an extra degree of freedom in device applications. In 1973, Wood and Austin suggested various possible applications in devices involving i) modulation of amplitudes, polarizations and phases of optical waves, ii) ME data storage and switching, iii) optical diodes, iv) spin-wave generation, v) amplification and vi) frequency conversion [74]. These probabilities were far from realization due to the weak coupling in single phase materials. Later, the large ME effect arising from the resonance effect in composite materials indicated it to be a promising candidate for transducers which can convert the microwave magnetic field into a microwave electric field and also attenuators or phase shifters where the resonance frequency are tunable with respect to electric or magnetic field strength [75]. The ME materials have also been suggested to be used in sensing a magnetic field as small as 1 nT [12]. In few multiferroics, the magnetoelectric effect has found to be robust and magnetoelectric switching in these compounds are promising candidates for memory device related applications. The ideal application would perhaps be a memory device made of a magnetoelectric multiferroic where the polarization or magnetization can be switched by magnetic or electric field. In a magnetic random access memory (MRAM) device, writing bits is a challenge at high density, whereas in a ferroelectric random access memory (FeRAM), reading the bit is a challenge. In a robust multiferroic, this problem can be avoided by ferroelectric writing and magnetic reading. The other application includes in microelectronics, spintronics and sensor technique [76]. Such a magnetoelectric switching has been demonstrated in years ago in magnetoelectric boracite $Ni_3B_7O_{13}I$. The ME signal or polarization was

demonstrated to switch below 60 K [77]. Using an exchange interaction at the interface between a multiferroic and a ferromagnet was shown to be useful for local control of ferromagnetism using an electric field [78, 79]. Ramesh's group recently demonstrated a room temperature multiferroic switch using a p-n junction of calcium-doped bismuth ferrite film [80].

1.5.4 Cross-coupling and temperature factor

As discussed so far, the ferroelectricity in a magnetic system is induced either from magnetic origin or other kind of ordering such as charge ordering, lone pair effect or geometric frustration. It can be easily pointed out that where the origin is not magnetism related, the ferroelectric and magnetic transition transitions are well separated. Mostly, the ferroelectric ordering occurs at temperature well above the magnetic transitions. As the mechanisms behind magnetism and ferroelectricity are different, this leads to a rather weak coupling between the two orders. The magnetically induced multiferroic systems on the other hand shows a large coupling between the two order parameters as the origin of ferroelectricity is directly involved with magnetic structure. Unfortunately, most of these compounds order much below the room temperature with low polarization values ($\sim 0.02\mu C/cm^2$). This inhibits any room temperature applications related to memory device. It has therefore become important to find new mechanisms or new materials which can demonstrate multiferroic properties at room temperature with large polarization and strong magnetoelectric coupling.

1.6 Motivation of present work

The thesis work is aimed to discover new magnetoelectric multiferroics having a large magnetoelectric coupling at room temperature. The ordered perovskite La_2NiMnO_6 is ferromagnetic with high Curie temperature (T_C = 280 K) because of the superexchange interaction between Ni^{2+} ($t_{2g}^6 e_g^2$) and Mn^{4+} ($t_{2g}^3 e_g^0$) according to Goodenough - Kanamori rule [81, 82]. Based on this mechanism, we selected bismuth based perovskite with different magnetic ions at the B-site for possible multiferroic properties with ferromagnetic ground state.

CHAPTER 2

Experimental Techniques

The details of sample preparation and physical properties of perovskite oxides investigated in this thesis are described.

2.1 Materials preparation

All the compounds presented here are polycrystalline and were prepared by solid state reaction at high temperatures and at ambient or high pressures. The first three chapters deals with bismuth based perovskites which can not be prepared at ambient pressure and thus a high-pressure technique was adopted. For the compounds discussed in the later chapters, samples were prepared by solid state route at the ambient conditions.

2.1.1 Solid state reaction

The most widely used method for the preparation of polycrystalline solids is the solid state reaction where precursor materials (oxides or carbonates) are mixed and heated at high temperatures. The energy required for reaction is provided by the thermal energy. The temperature of reaction controls the thermodynamic and kinetic factors of the reaction. Box furnaces and tube furnaces (ELITE) capable of heating up to 1500 °C were used for sample preparation at ambient pressure.

2.1.2 High pressure apparatus

For the sample preparation at high pressures, a cubic anvil type apparatus having six pistons (RIKEN CAP 07) arranged in a cubic fashion was used and the picture of the apparatus is shown in figure 2.1. A homogeneous pressure is achieved for the sample by using this technique when the equal pressures applied from six directions. Using this instrument, samples can be prepared with maximum pressure of 5.5 GPa (450 tonnes) and maximum temperature of 1350°C.

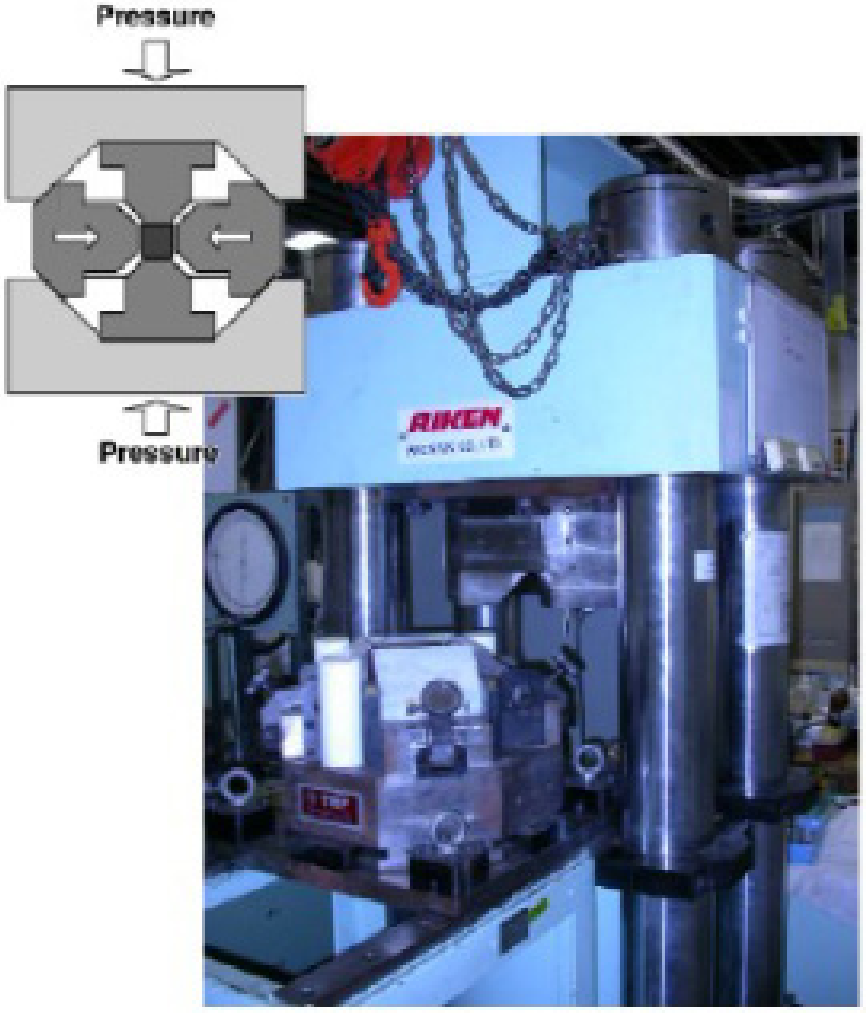

Figure 2.1: Cubic anvil type apparatus.

Figure 2.2 shows the schematic diagram of the sample preparation procedure using

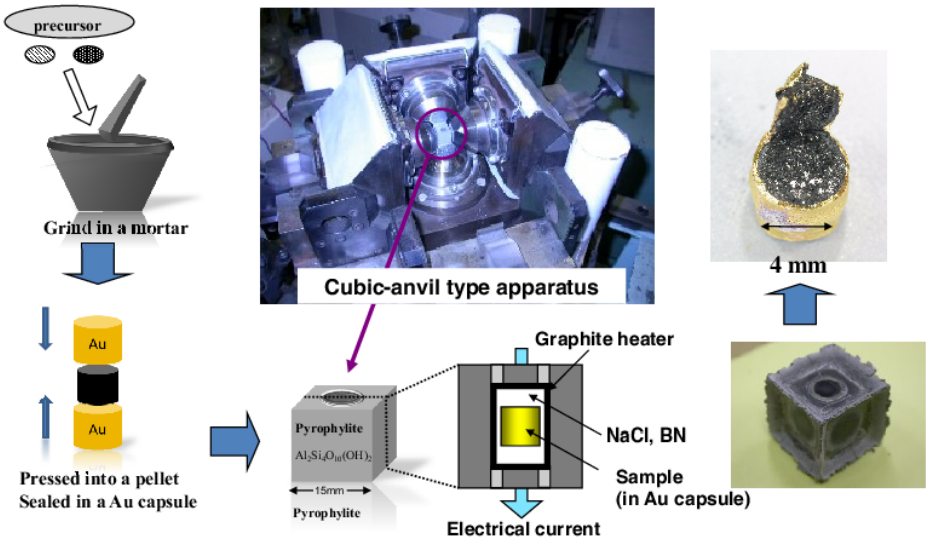

Figure 2.2: Procedure for sample preparation.

this technique. The precursor oxides weighed in stoichiometric proportions are mixed and pelletized and then capsulated with gold. The gold capsule is then covered with a cylinder made using NaCl with 20 % ZrO_2. This cylinder is inserted in a graphite cylinder and kept inside a Pyrophyllite ($Al_2Si_4O_{10}(OH)_2$) cell through the cylindrical hole. After placing the graphite cylinder at the center, both sides of the hole are covered with molybdenum plate and stainless steel ring (figure 2.2). The pyrophyllite cell is placed in the high pressure apparatus. The cell is subjected to the required pressure and then heated for two hours. After 2 hours, the heater is switched off and the pressure is reduced slowly. The solid sample was removed from the Au capsule. In this method, 300 mg of sample can be prepared. In the cell, Pyrophyllite acts as a gasket, graphite is used as heater and NaCl is a good thermal conductor and at same time provides electrical insulation. The gold capsule is provided to avoid the reaction of the sample with the cell materials. The advantages of this method are very short reaction time

and control of oxygen stoichiometry. The main disadvantage of this procedure is small quantity of sample obtained in a single attempt.

2.2 Structure and Physical properties

2.2.1 Structure

The structural characterization were performed by X-ray and neutron diffraction techniques. For X-ray diffraction, laboratory X-ray machine D8 Advance (Bruker Inc.) was used with zero background sample holder and the neutron diffraction measurements were performed at D2b instrument at ILL (The Institut Laue-Langevin).

2.2.1.1 Powder X-ray diffraction

X-ray diffraction technique provides a way to identify and completely describe the structure. A crystalline solid has a periodic arrangements of ions or atoms separated by a distance of few Å. An electromagnetic wave of suitable wavelength can diffract when pass through the solid. Since X-rays are waves of electromagnetic radiation, atoms can scatter X-ray waves through the atom's electrons. The scattered X-ray interfere constructively when the Bragg's condition is obeyed.

$$2d \sin\theta = n\lambda \tag{2.1}$$

where *d* is an interplanar distance, θ, Bragg angle, λ, wavelength of the X-ray used and n is an integer. In polycrystalline compound or powder sample, the grains are oriented in all possible direction and thus gives constructive diffraction for all the interplanar distances accounted in the measured angle θ. The intensity of the diffracted light is

proportional to square of the structure factor F,

$$F_{hkl} = \sum_j N_j f_j \, e^{[2\,\pi\, i(hx_j + ky_j + lz_j)]} \tag{2.2}$$

In this expression, f is the atomic scattering factor defined as,

$$|f|^2 = f_0 e^{-\frac{B \sin^2\theta}{\lambda}} \tag{2.3}$$

In this expression B is the Debye-Waller temperature factor ($B = 8\pi^2\, U^2$) which is proportional to the mean square amplitude of the thermal vibration (U).

2.2.1.2 Powder neutron diffraction

Neutron diffraction technique is similar to the X-ray diffraction though neutrons interact with matter differently. While X-rays interact primarily with the electron cloud surrounding each atom, neutrons interact directly with the nucleus of the atom. The scattering length of neutron do not change linearly with the atomic number unlike in X-ray diffraction. Another key advantage over X-ray diffraction is that light elements (low Z such as O) atoms also contribute strongly to the diffracted intensity even in the presence of large atoms. Moreover, as the neutrons carry a spin (-1.91 nuclear magneton), it interacts with the magnetic moments. Neutron diffraction is widely used to solve crystal as well as magnetic structure.

2.2.1.3 Rietveld refinement

Rietveld refinement is a technique devised by Hugo Rietveld for use in the characterization of crystalline materials [83]. The neutron and X-ray diffraction of powder samples

results in a diffraction pattern characterized by peak position and the intensity. The Rietveld method uses a least squares approach to refine a theoretical line profile until it matches the measured profile.

The calculated at a point *i* is given by,

$$y_{ci} = s \sum_{K} L_K |F_K|^2 \, S(2\theta_i - 2\theta_K) \, P_K \, A + y_{bi} \tag{2.4}$$

where, s is scale factor, K represents Miller indices, L_K contains Lorenz, polarization and multiplicity factors, S is the profile shape function, P_K is preferred orientation function, A is absorption function and F_K is the structure factor as defined earlier and y_{bi} is the background intensity.

The shape function can be a complex function containing both Lorentzian (L) and and Gaussian (G). The much used pseudo-Voigt (pV) or modified pseudo-Voigt (mod pV) are complex function are described as

$$pV = \eta \, L + (1 - \eta) G \tag{2.5}$$

where η is a function of 2θ containing refinable parameters U, V, W, X, Y and Z.

In the Rietveld method, the scale factor, cell parameters, atomic positions, isothermal parameters and other parameters are refined to minimize a function M which represents the difference between a calculated profile (y_i) and the observed data (y_{ci}).

$$M_y = \sum_{i} w_i \left\{ y_i - y_{ci} \right\}^2 \tag{2.6}$$

where w_i is the statistical weight $w_i = \frac{1}{y_i}$

2.2.2 Ferroelectric measurement

A ferroelectric compound is characterized a spontaneous polarization below T_C. Experimentally, the ferroelectricity can be confirmed by measuring P-E hysteresis loop.

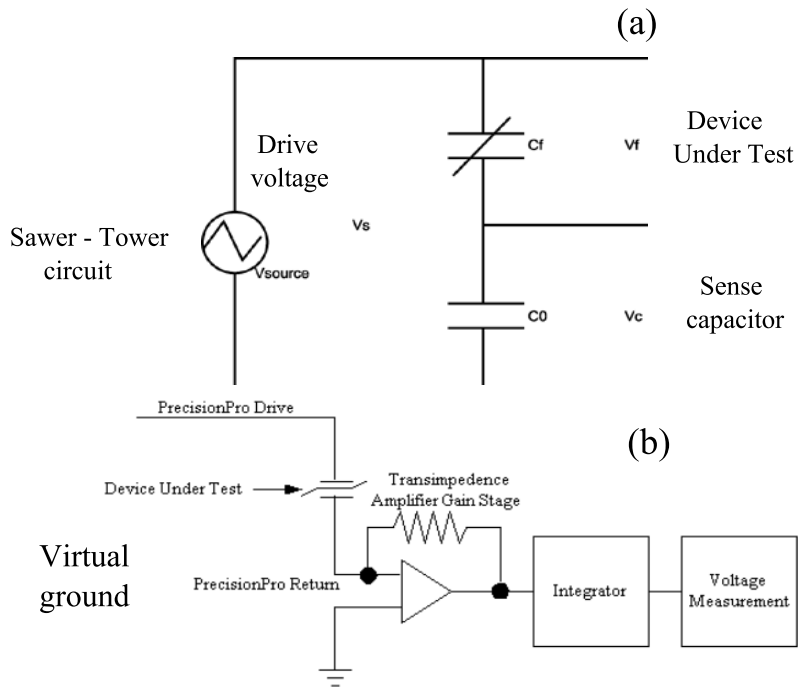

Figure 2.3: (a) Standard Sawyer - Tower circuit, (b) Sawyer - Tower circuit empoying virtual ground.

2.2.2.1 P-E loop measurement

The ferroelectric measurements have been carried out using Radiant Technologies Precision Workstation. A Sawyer-Tower circuit is a standard procedure to measure ferroelectric samples as shown in figure 2.3a. The sample to be measured (device under test) is placed in series with a standard capacitor (sense capacitor). As both the capacitor acquires same charge upon applied voltage, the polarization can be calculated using the relation below. In Sawyer Tower circuit is modified to avoid back voltage and parasitic capacitance by introducing a virtual ground circuit as shown in figure 2.3b. In this mea-

surement, a triangular voltage waveform is applied to the sample in a series of voltage steps. At each voltage step, the current induced in the sample by the voltage step is integrated and the integral value is captured and converted into polarization (μC/cm^2)

$$\frac{\mu C}{cm^2} = \frac{Q}{Area} = \frac{CV}{Area} = \frac{Integrator\ Volts \times Sense\ Capacitor}{Sample\ Area} \tag{2.7}$$

The ferroelectric tester used here, could be employed for measurements up to voltage (V) of 4 kV and maximum frequency of 1 kHz. The cylindrical ceramic pellets were painted with silver or gold sputtered to from a capacitor. While measuring the P-E loop, the following facts have been considered. In some compounds, the coercive field can be as high as 150 kV/cm. As there is a restriction in the upper limit, the capacitor thickness (t) is reduced to 150 - 300 μm to reach a high field (E = V/t). Also, at low frequency the conductive contribution will have significant contribution and hence a higher frequency ($\sim$ 1 kHz) is preferred. If the experiments are conducted in air, the air molecule breaks down at high field resulting a spark between the electrodes. To prevent this, the capacitor is immersed into an oil bath (silicon oil).

2.2.2.2 Pyroelectric current measurement

In improper ferroelectrics where the polarization value is small, conventional P-E loop measurements are not effective. For all the improper ferroelectrics, pyroelectric measurement is widely used. In this measurement, the compound is cooled below the ferroelectric transition by applying a electric voltage. At the lowest temperature, the capacitor is shorted for a long time to remove the stray charges. The pyroelectric current is then measured against time and temperature. The polarization is calculated using

expression,

$$P = \frac{\int I\, dt}{A} \tag{2.8}$$

2.2.3 Dielectric measurement

In ferroelectric compounds, the dielectric constant shows an anomaly and above T_{CE} follow Curie law. Thus dielectric measurement is a complimentary to the PE loop measurements. Other than ferroelectric compounds, the thesis presents detailed dielectric behavior of few compounds.

2.2.3.1 Capacitance and loss measurements

By definition, dielectric is an insulator which can be polarized by an electric field. As it is an insulator, no current can flow when charged with a DC voltage. The charge stored in a capacitor is expressed as $Q = C \times V$. For a parallel plate capacitor with area A and thickness d, the capacitance is written as

$$C = \frac{\epsilon_0\, \epsilon_r\, A}{d} \tag{2.9}$$

where, ϵ_0 and ϵ_r are the permittivity of vacuum and relative permittivity. The induced polarization can be expressed as,

$$\mathbf{P} = \epsilon_\mathbf{0}(\epsilon_\mathbf{r} - \mathbf{1})\mathbf{E} \tag{2.10}$$

As the AC measurements gives a complex dielectric constant (ϵ_r^*) in terms $|\epsilon_r^*|$ and

loss ($\tan\delta$), the real ($\epsilon_r^{'}$) and imaginary parts ($\epsilon_r^{''}$) are calculated from the relations,

$$\epsilon_r^* = \epsilon_r^{'} - j\,\epsilon_r^{''}$$

$$and \tag{2.11}$$

$$\tan\theta = \frac{\epsilon_r^{''}}{\epsilon_r^{'}}$$

Dielectric systems are studied by measuring, dielectric constant (C) and loss ($\tan\delta$) as a function of temperature and frequency. When an AC signal ($v_0\,\sin\omega\,t$) is applied, the parameters v_0 and measurement frequency f ($\omega/2\pi$) can be varied. As the stimulus is AC, it results in real and imaginary parts of dielectric constants. While the real part signifies the amount of energy stored, the imaginary part represents the energy lost. The frequency dependence of dielectric constant and loss is of particular interest to identify the nature of phase transition or relaxation behavior.

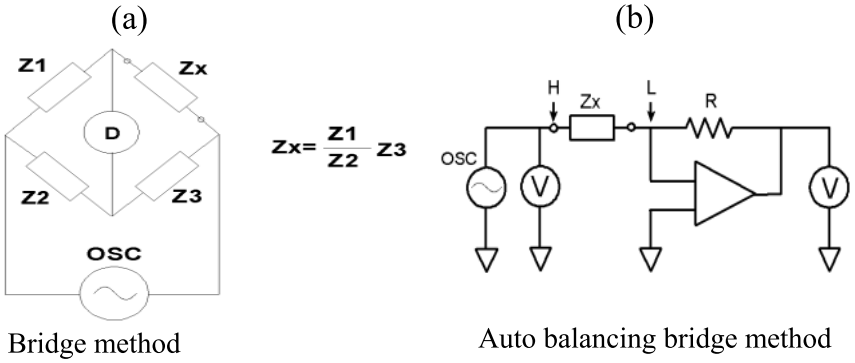

Figure 2.4: Bridge method and auto balancing bridge for dielectric capacitance measurements.

The capacitance is obtained indirectly by measuring impedance ($Z = 1/j\omega\,C$; $j = \sqrt{-1}$) which is the AC analog of DC resistance. The simplest method to measure impedance (Z_x) is bridge method as shown in figure 2.4a. Most commercially available

instruments (Agrement products) uses an auto balancing bridge (figure 2.4b) which maintains a virtual ground at a point L. The impedance Z_x is calculated using voltage measurements at High terminal H and that across R.

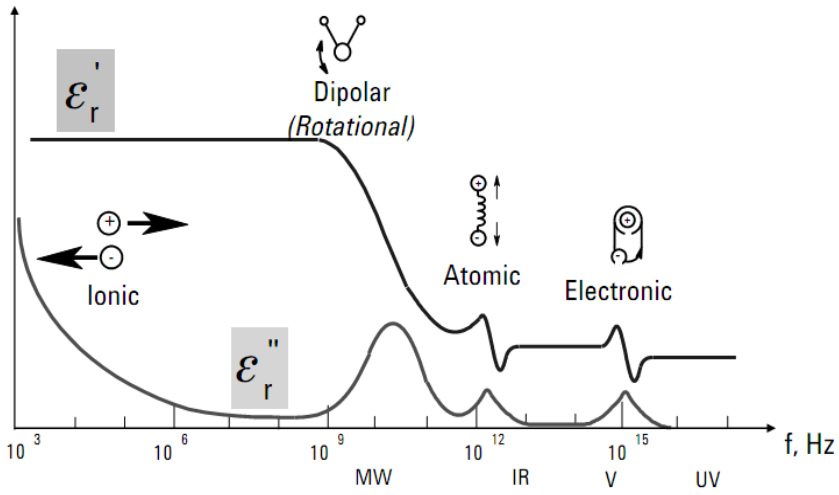

Figure 2.5: Frequency response of dielectric mechanisms.

Dielectric relaxation is another aspect which is widely used to characterize a dielectric material. When an AC signal is applied, the dipoles try to follow the polarity of the signal. Although, at low frequency dipoles can follow the signal, at high enough frequency ($f > f_c$) it can not and thus relaxes. Above relaxation frequency f_c, the dielectric constant value decreases with a corresponding peak in the loss part. If the system is homogeneous having same relaxation times for all the dipoles, the real and imaginary constant follows Debye law.

$$\epsilon(\omega) = \epsilon_\infty + \frac{\epsilon_0 - \epsilon_\infty}{1 + j\omega\tau} \tag{2.12}$$

where, ϵ_0 and ϵ_∞ are the dielectric constant at zero and infinite frequency and τ is relaxation time.

Microscopically, four types of of mechanisms can contribute to the dielectric feature namely, ionic, dipolar, atomic and electronic. The frequency dependence of these contribution is shown in figure 2.5. In the working frequency range (40 - 110 MHz) of Agilent 4294A Impedance analyzer, all the four mechanisms contribute to the dielectric behavior.

2.2.3.2 Experimental set-up for low temperature measurements

To probe a dielectric or ferroelectric transition, it is essential to record temperature dependence of dielectric constant or polarization. Temperature dependence of dielectric

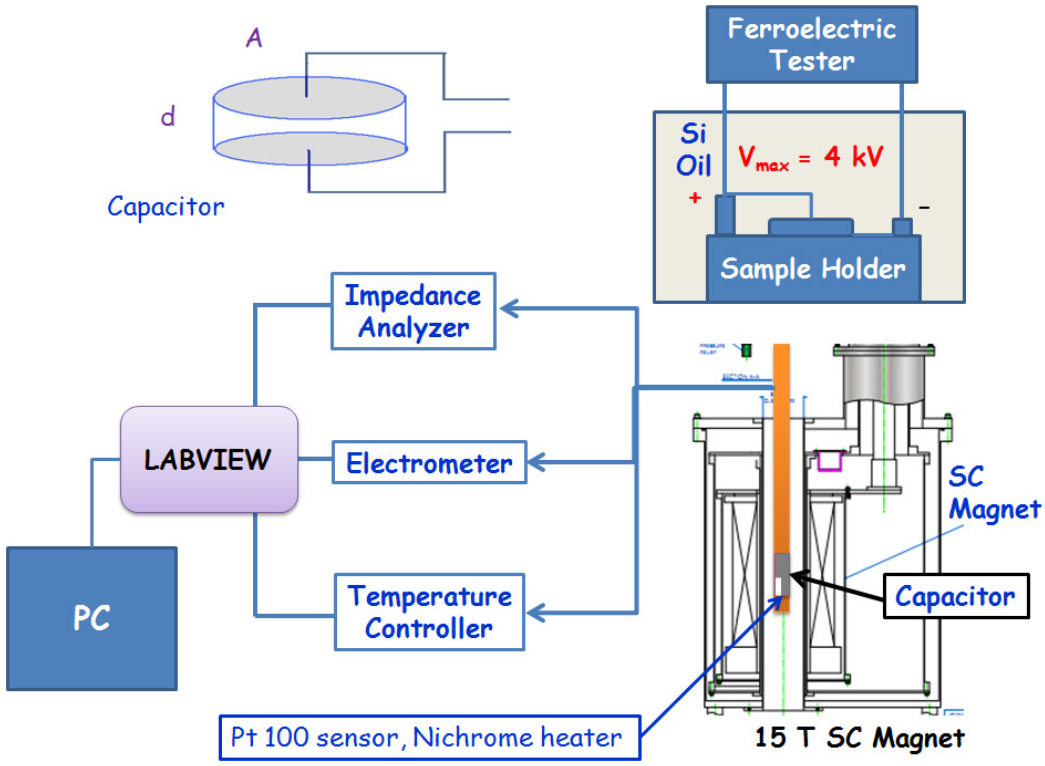

Figure 2.6: The 14T magnet system for low temperature high magnetic field measurements.

constant with frequency dependence can give a microscopic insight of the material. Also, to study cross coupling of order parameters in multiferroic compounds, dielectric

or ferroelectric measurements are required to measure under a magnetic field. For this purpose we have made a set-up which can be used in the temperature range 10 - 400 K and at high magnetic field up to 15 Tesla. In a custom made sample probe assembly, Pt100 temperature sensor and cartridge heater (Lakeshore Cryogenics) were installed in a rectangular copper block. For dielectric measurements, good quality coaxial cable was used for connections from sample probe assembly to the Impedance analyzer or electrometer. For dielectric measurements, a 4TP (four terminal pair) to 2 TP (two terminal pair) configuration is used. To monitor and control temperature, sensor and heater were connected to Lakeshore 330 temperature controller. Finally, the impedance analyzer and temperature controller were interfaced using LABVIEW to collect data with computer control. The arrangements are schematically shown in figure 2.6. To subtract the cable capacitance, open and close loop corrections were performed before the measurement.

For pyroelectric measurement, the electrometer Keithley 6517A was used to measure the pyrocurrent. This meter is capable of measuring very high resistance and low current (2 pA). The electrometer is interfaced with the temperature controller to collect pyroelectric current against time and temperature simultaneously. Prior to the measurement, the stray current due to cable are nullified. As the measured current is very small ($\sim 10^{-12} Amps$), the sample holder should be well shielded.

2.2.4 Magnetic properties

Magnetic properties were studied by DC as well as AC magnetization measurements. The basic principle of magnetic measurements follow Faraday's law. As the second law

states that the change of magnetic flux ($\phi = \mathbf{B} \cdot \mathbf{A}$) with time would generate a voltage (e) which is proportional to rate of change of flux.

$$e \propto -\frac{d\phi}{dt} \propto -\frac{d(\mathbf{B} \cdot \mathbf{A})}{dt} \tag{2.13}$$

where B is magnetic field and A is the area.

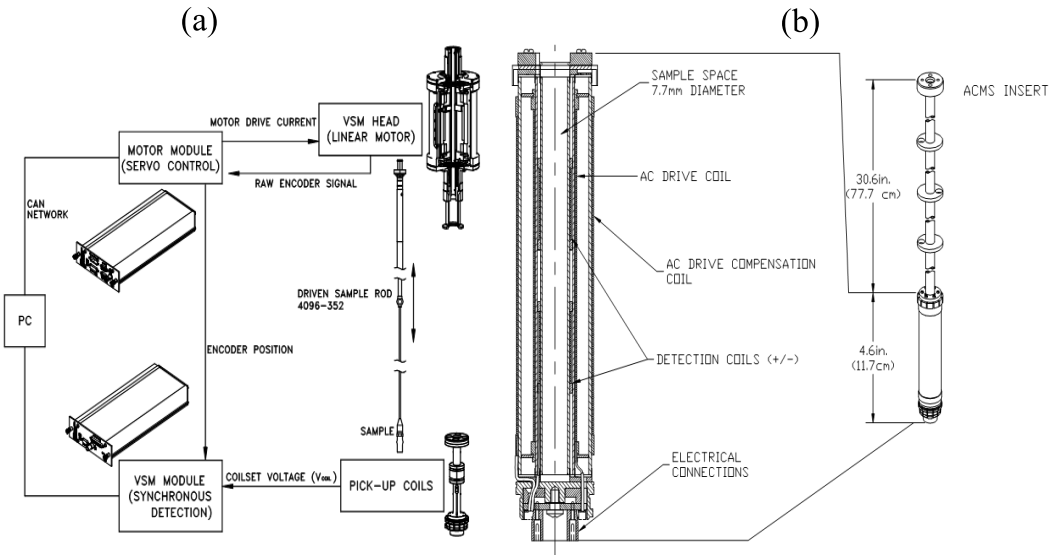

Figure 2.7: Schematic diagram for (a) DC magnetization and (b) AC susceptibility measurements in physical property measurement system.

2.2.4.1 DC magnetization

DC magnetization measurements have been carried out in a vibrating sample magnetometer (VSM). As the name suggest, sample vibrates inside a pickup coil with a defined amplitude (A) and frequency (f) in a static magnetic field (H). The block diagram is shown in figure 2.7a. The voltage V_{Coil} induced in the pick up can be rewritten mod-

ifying equation 2.13 as,

$$\begin{aligned} V_{Coil} &= \frac{d\phi}{dt} \\ &= (\frac{d\phi}{dz})(\frac{dz}{dt}) \end{aligned} \tag{2.14}$$

For a sinusoidally oscillating sample, the voltage is given by,

$$V_{\text{Coil}} = 2\pi\, fCmA \sin(2\pi\, ft) \tag{2.15}$$

where m is the magnetic moment of the sample and C is a coupling constant.

2.2.4.2 AC susceptibility

The AC susceptibility measurements are performed in presence or absence of a static magnetic field while the sample position is kept fixed. Instead an AC magnetic field ($H = H_0 \sin \omega\, t$) is applied. The AC susceptibility can be defined as,

$$\begin{aligned} \chi &= \frac{dM}{dH} \\ \chi &= \chi' + j\chi'' \end{aligned} \tag{2.16}$$

As in the case of DC measurements, susceptibility is defined as $\chi = M/H$, the AC susceptibility can be considered as the slope of the M-H hysteresis loop.

An AC-susceptometer consists of three coils, a primary coil, and two secondary coils. The sample is placed at the centre of one of the secondary coil. The coils are wound in such way that in absence of sample, signal generated from both the secondary coils cancel each other. The primary coil which surrounds (in most cases), produces an AC magnetic field. The two components of susceptibility (χ' and χ'') are extracted using a circuit consisting of lock-in amplifier.

In the Physical Property Measurement System, the signal detection and analyzing technique is slightly different. The sample undergoes a five point measurement process. The sample is successively moved to center of bottom detection coil, center of top detection coil and again center of bottom detection coil. The signals are modified and digitized by an analog to digital (A/D) converter and then saved as response waveform. After these measurements, two more reading are obtained with sample placed at the center between the two coil arrays with opposite polarities of the calibration coil detection circuit. The real and imaginary parts are calculated for each response waveform by fitting and comparing to the driving signal. The schematic diagram is shown in figure 2.7b

Similar to dielectric measurements, the susceptibility is recorded as a function of temperature and frequency. In complex glassy systems, both DC and AC susceptibility are complementary to each other for complete understanding.

CHAPTER 3

Effect of Non-magnetic Ion Substitution on the Multiferroic Properties of $BiFeO_3$ *

3.1 Introduction

In the context of magnetoelectric multiferroics, lone pair effect in bismuth and lead based perovskite oxides has been exploited to induce ferroelectricity [13, 33, 84, 85]. Particularly, bismuth perovskites ($BiMO_3$ where M is transition metal ion) have been preferred over the lead compounds because of increasing health concern due to toxicity. In these compounds, stereo-chemically active 6s lone pair electrons do not take part in any bonding and have been shown theoretically to be responsible for non-centrosymmetric structure [40]. Depending on whether the M^{3+} ion has unpaired electrons or not, $BiMO_3$ can be magnetic or non-magnetic. It is interesting to note that few of these have non-centrosymmetric structure which often lead to a polar state. In the case where M^{3+} has no unpaired electron, a ferroelectric or piezoelectric behavior is observed whereas with M^{3+} having unpaired electrons, the compound can be both ferroelectric and ferromagnetic.

Perhaps, the most studied compound in the multiferroic $BiMO_3$ family is $BiFeO_3$. The crystal structure is reported to be rhombohedral with space group (R3*c*) [86]. It is not only a room temperature multiferroic i.e., ferroelectric (T_C = 1103 K) and antiferro-

*Based on this work, a manuscript has been submitted. P. Mandal, P. M. Shirage, A. Iyo, Y. Tanaka, A. Sundaresan and C. N. R. Rao *Communicated*

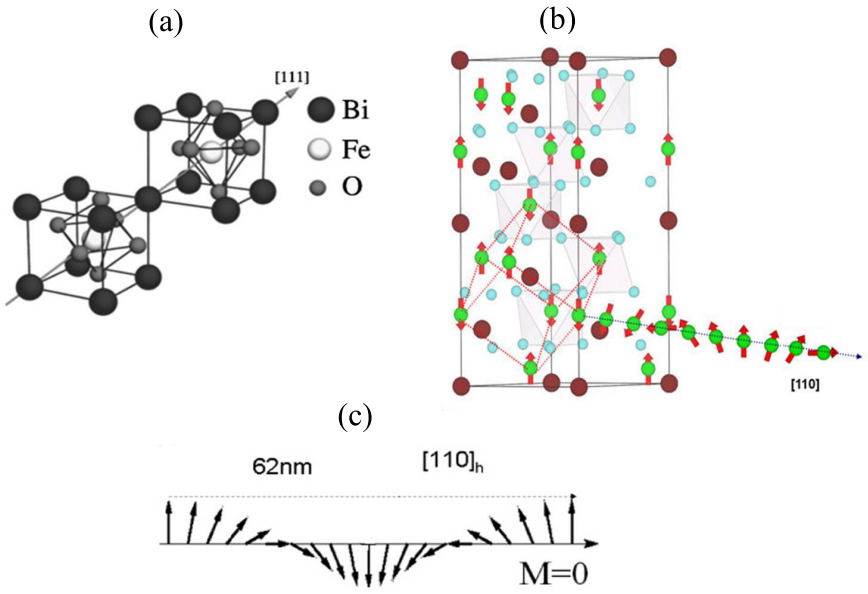

Figure 3.1: (a) Rhombohedral unit cell of $BiFeO_3$ showing the polarization vector towards [111] direction. (b) Magnetic structure in a hexagonal unit cell showing spiral magnetic ordering. (c) Cancelation of magnetic moment due to spiral magnetic ordering.

magnetic (T_N = 640 K) but also the only member in this family which can be synthesized at ambient pressure [32]. Single crystal studies in $BiFeO_3$ showed an electric polarization value of 3.5 μC/cm^2 along the [001] direction of the rhombohedral cell [87]. Later, epitaxial thin films showed much higher value of polarization of 50 - 60 μC/cm^2 at room temperature along the [001] direction as reported by Wang *et al* [88]. The highest value of polarization (158 μC/cm^2 at 90 K) has been reported in polycrystalline thin film of $BiFeO_3$ on $Pt/TiO_2/SiO_2/Si$ substrate exceeding the theoretically predicted values of 90 - 100 μC/cm^2 [89, 90]. Below the Néel temperature, a G-type antiferromagnetic ordering is known to exist where the Fe^{3+} (S = 5/2) moments are coupled ferromagnetically in the pseudocubic (111) planes and antiferromagnetically between the adjacent planes [91]. Theoretically, it has been predicted that if the magnetic moments are oriented perpendicular to [111] direction, a net magnetization of 0.05 μ_B/Fe can arise from

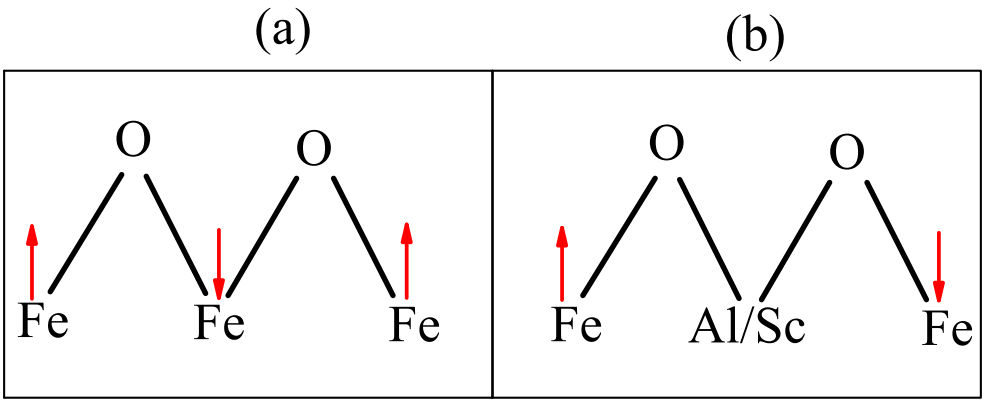

Figure 3.2: (a) Antiferromagnetic superexchange interaction between Fe moments. Substitution by a non-magnetic ions will increase the distance between Fe moments affecting the exchange interaction.

spin canting due to Dzyaloshinskii-Moriya interaction [92]. In contrast, a linear magnetic hysteresis loop is observed in polycrystalline samples. Neutron diffraction studies showed a spiral magnetic ordering with an incommensurate long wavelength of 620 Å along $[110]_h$ to exist below the Néel temperature which cancels out any net magnetization (figure 3.1) and also suppresses linear magnetoelectric effect [93, 94]. There have been several efforts to suppress or destroy the spiral magnetic ordering in $BiFeO_3$ which would give rise to a finite magnetization and linear magnetoelectric effect as predicted from first principles [95]. Canonical substitution at the A or B-site in $BiFeO_3$, epitaxial strain or application of high magnetic field can suppress such spiral magnetic ordering and improve the magnetic and magnetoelectric properties [88, 96–103]. Our aim in this study was to suppress the spiral magnetic ordering and induce finite magnetization by means of non-magnetic ion substitutions at the Fe-site of $BiFeO_3$. We chose trivalent Al and Sc with ionic radii of 0.53 Å and 0.74 Å respectively, which are smaller and greater than the ionic radii of Fe^{3+} ion (0.64 Å) in six coordination [104]. As shown

schematically in figure 3.2, the superexchange path Fe – O – Fe in $BiFeO_3$ is changed to Fe - O - Al/Sc - O - Fe which would affect the spiral magnetic ordering. Due to large difference between the sizes of Fe and Al/Sc, solid state route at ambient pressure results in impurity phases. This may also be due to the fact that $BiScO_3$ and $BiAlO_3$ are high pressure phases [105, 106]. In this chapter, we present synthesis and multiferroic properties of high pressure synthesized $BiFe_{1-x}M_xO_3$ where M = Al, Sc. Solid solution is obtained up to x = 0.3 for Al and x = 0.2 for Sc. A significant improvement in the magnetic property is observed for Al and Sc substitution. A Maxwell-Wagner relaxation behavior with high dielectric loss is observed in the Al substituted compounds whereas Sc substitution showed a low loss and exhibited ferroelectric hysteresis. This study demonstrates that multiferroic properties of $BiFeO_3$ can be improved by possible suppression of spiral magnetic ordering.

3.2 Experimental

As discussed previously, $BiFeO_3$ can be synthesized at ambient pressure by rapid liquid phase sintering or by quenching method [107, 108]. As $BiAlO_3$ and $BiScO_3$ are high pressure phases, attempt of ambient pressure synthesis by solid state route resulted in large amount of impurity phases. Thus, we have synthesized all the compounds using high pressure technique in a cubic anvil type apparatus (RIKEN CAP - 07). The precursor oxides Bi_2O_3, Fe_2O_3, Al_2O_3 and Sc_2O_3 were mixed in stoichiometric amounts and subjected to high pressure of 4.5 GPa and heated at temperatures 1023 - 1123 K for 2 hours. Phase purity were confirmed by X-ray diffraction in a Bruker D8 Advance diffractometer and the profile refinements were carried out using Fullprof soft-

ware package [109]. Magnetization behavior was studied by a vibrating sample magnetometer (VSM) in a physical property measurement system (PPMS). For electrical measurement, silver paint was applied on both sides of the cylindrical pellets. Ferroelectric hysteresis loop (PE) was recorded in the Radiant ferroelectric tester (RT66). The sample holder was immersed inside an oil bath which helped to use maximum voltage of 4 kV of the amplifier. For dielectric measurement, the capacitor was mounted in a custom made sample probe assembly and inserted in a 15 T cryo-cooled magnet system to collect temperature dependent capacitance and loss data. Agilent 4294A impedance analyzer was used to study dielectric behavior in the frequency range 100 Hz to 1 MHz by applying an AC bias.

3.3 Results and discussions

3.3.1 Structure

Room temperature X-ray diffraction data collected for the compounds indicated that the solid solution exist up to x = 0.3 for Al and x = 0.2 for Sc substitution. The profile refinements confirmed rhombohedral structure (Space group R3c) at room temperature, similar to the parent compound $BiFeO_3$. Beyond these limits, substitution of Al and Sc results in the formation of excess impurity phases such as $Bi_{24}Al_2O_{40}$, $Bi_2Al_4O_9$, $Bi_{25}FeO_{40}$, $Bi_2Fe_4O_9$ etc. Figure 3.3 shows profile refinement for the compounds $BiFe_{0.9}Al_{0.1}O_3$ and $BiFe_{0.9}Sc_{0.1}O_3$. The lattice parameters obtained from the refinements are plotted in figure 3.4 and are found to vary linearly with concentration following Vegard's law. As the ionic radius of Fe^{3+} is greater than Al^{3+} and smaller than Sc^{3+}, the lattice parameters a and c decreases for Al and increases for Sc substi-

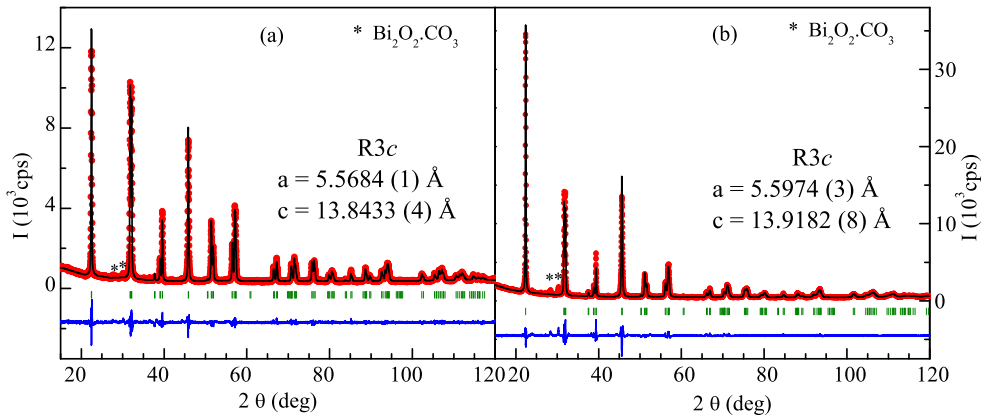

Figure 3.3: profile refinements of (a) $BiFe_{0.9}Al_{0.1}O_3$ and (b) $BiFe_{0.9}Sc_{0.1}O_3$ at room temperature. Asterisk indicates presence of a non-magnetic impurity phase of $Bi_2O_2.CO_3$.

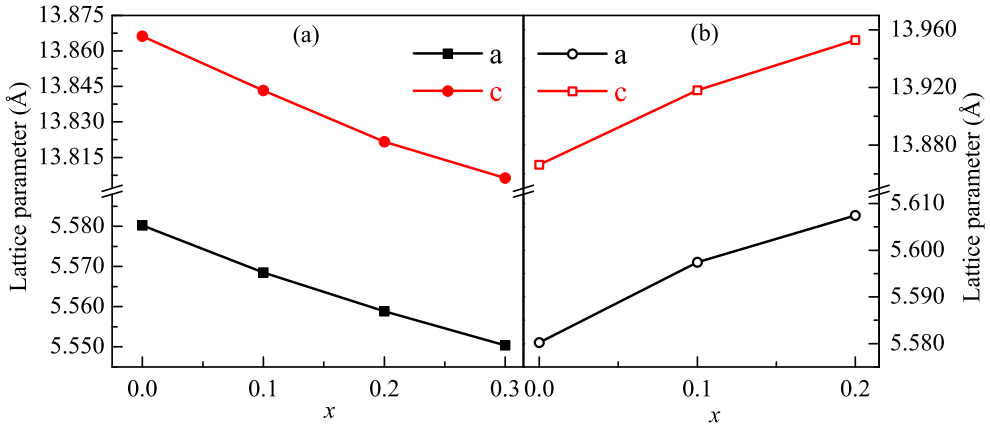

Figure 3.4: Variation of lattice parameters with (a) Al and (b) Sc concentration in BFAO and BFSO respectively.

tuted compounds. The fact that $BiFeO_3$ and $BiScO_3$ possess different structures, above $x = 0.2$ the compounds $BiFe_{1-x}Sc_xO_3$ forms with mixed phase of rhombohedral (Space group R3c) and monoclinic (Space group C2/c) structures. Although, the end members of $BiFe_{1-x}Al_xO_3$ are isostructural (Space group R3c), the solid solution do not form in complete range due to large difference in size between Fe^{3+} and Al^{3+} ions. It is im-

portant to mention that the isostructural compounds Fe_2O_3 and Al_2O_3 do not even form solid solution but rather results in $AlFeO_3$ which is structurally different (space group P$na2_1$) [110].

3.3.2 Magnetic properties

Figure 3.5 shows the field cooled magnetization curves for $BiFe_{1-x}Al_xO_3$ compounds collected under a magnetic field of 1000 Oe. As shown by arrows in figure 3.5, field cooled magnetization data of the parent compound $BiFeO_3$ shows three anomalies at 50, 200 and 250 K. Presence of these anomalies are consistent with the earlier reports [111]. Bifurcation of ZFC (not shown) and FC curves starts below 250 K which is attributed to glassy feature in the system [111]. The 200 K anomaly is attributed to be due to spin reorientation transition which is a common feature in rare earth orthoferrites [112]. At further low temperature, a spin-glass state occurs (T_{SG} = 29.4 K) which is indicated by an anomaly near 50 K in the DC magnetization data. With increase in the Al concentration, the high temperature anomalies at 200 and 250 K gets suppressed and disappear for the compound with x = 0.2. In $BiFe_{0.7}Al_{0.3}O_3$, none of the anomalies are present and magnetization increases below 250 K to a plateau and further increases below 50 K.

In contrast to Al substituted compounds, the Sc substituted compounds not not show spin reorientation transition as can be seen in figure 3.6. The magnetization values below 300 K, initially decrease for x = 0.1 whereas for x = 0.2 it increases. It should be mentioned that these measurements are not actual field cooled measurements due to the fact that the field was applied at 400 K whereas the Néel temperature is well

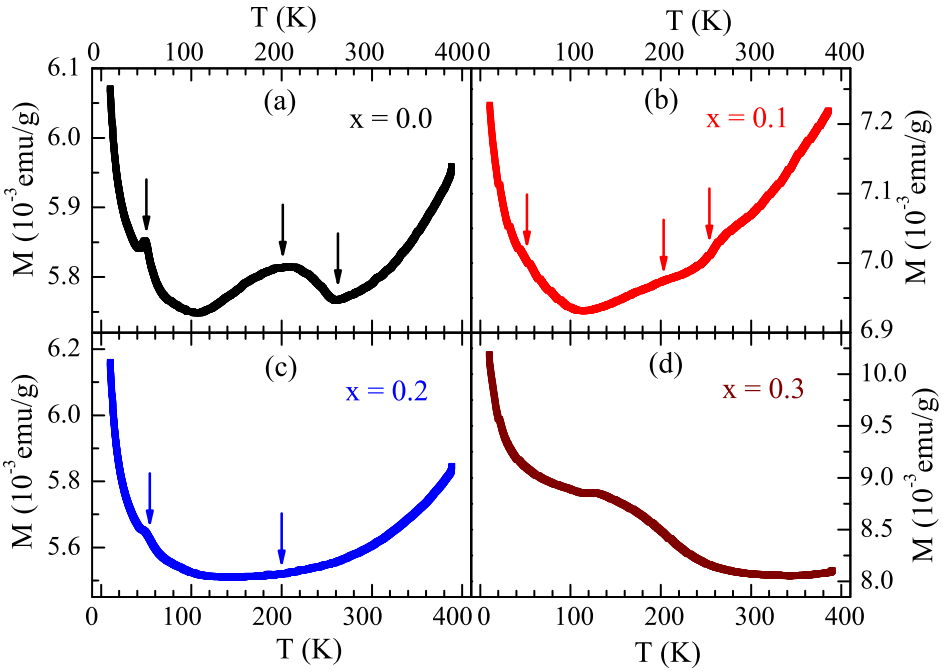

Figure 3.5: Field cooled magnetization curves of $BiFe_{1-x}Al_xO_3$ under a magnetic field of 1 kOe.

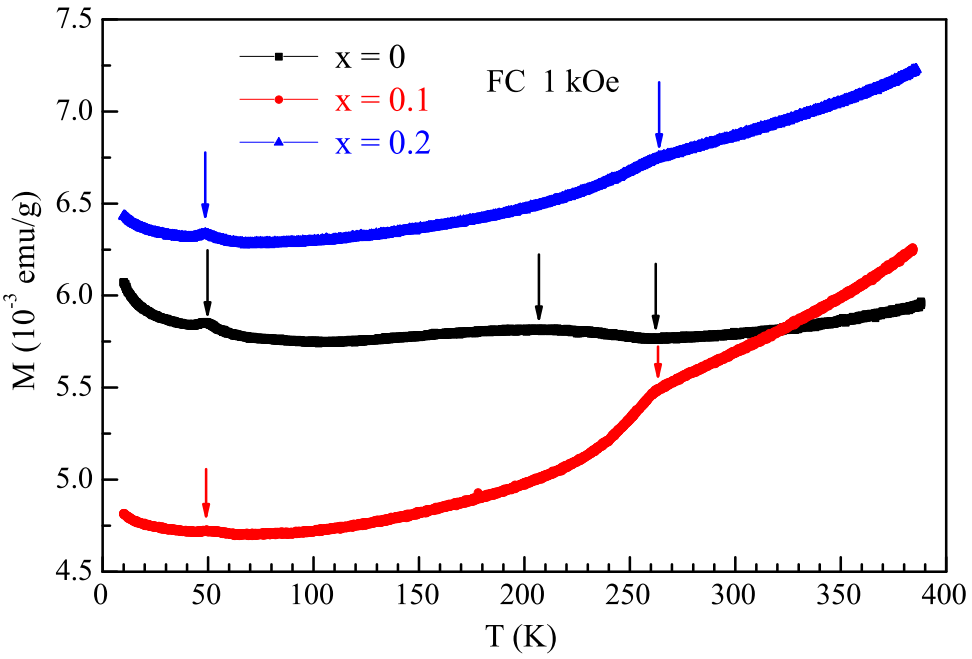

Figure 3.6: Field cooled magnetization curves of $BiFe_{1-x}Sc_xO_3$ under a magnetic field of 1 kOe.

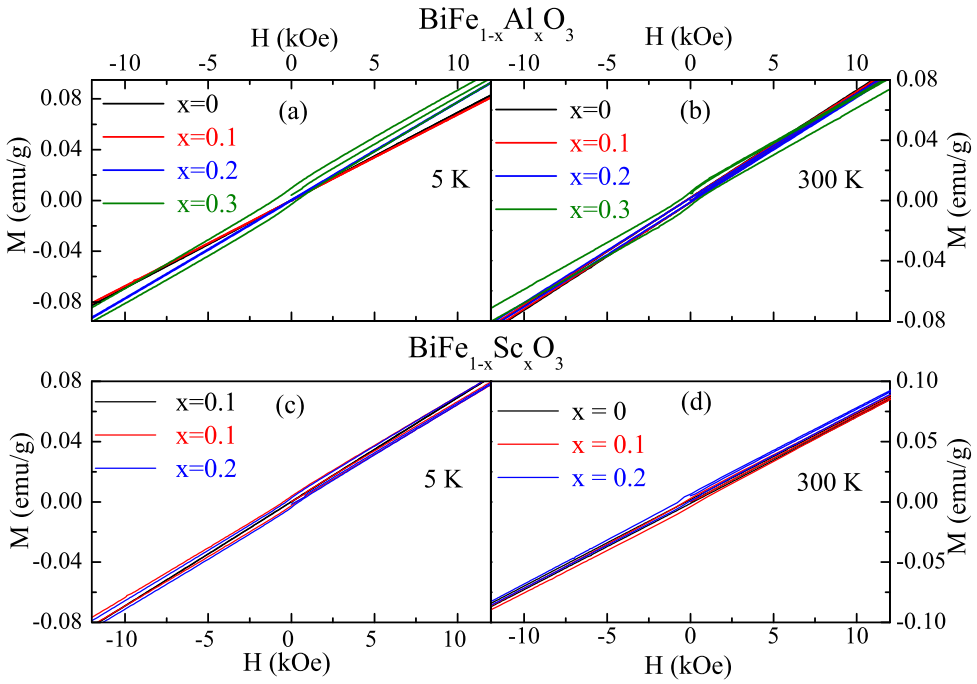

Figure 3.7: Magnetic isotherms of (a - b) $BiFe_{1-x}Al_xO_3$ and (c - d) $BiFe_{1-x}Sc_xO_3$ collected at 5 and 300 K.

above 400 K. Magnetic isotherms data collected at 5 and 300 K are shown in figure 3.7 (a - b) for Al and (c - d) for Sc substituted compounds. It is clear from the plot, that the parent compound shows a linear hysteresis behavior which is expected for spiral magnetic ordering. Substitution of either Al and Sc induces a finite magnetization at low temperature as well as at room temperature. With increasing Al and Sc concentration, the magnetization value increases. These results suggest suppression of spiral magnetic ordering and thus inducing finite magnetization.

3.3.3 Dielectric properties

Before discussing ferroelectric properties we examine the dielectric features in these compounds. All the $BiFe_{1-x}Al_xO_3$ compounds show a step like increase in dielectric constant value above 200 K. The corresponding loss data show peaks at temperatures

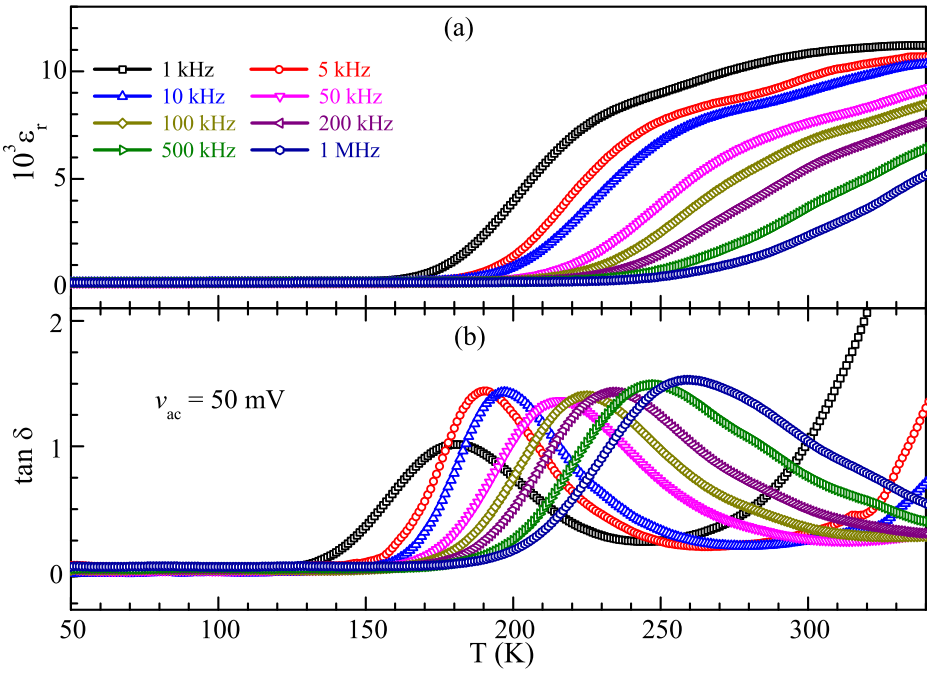

Figure 3.8: Temperature dependence of (a) dielectric constant (ϵ_r)and (b) loss (tan δ) of $BiFe_{0.9}Al_{0.1}O_3$

.

slightly below the dielectric constant step. Both dielectric constant and loss values are highly frequency dependent and dielectric constant value decreases with increasing frequency. Due to the lossy behavior, AC bias of 50 mV was used for the dielectric measurements. As all three compounds show similar feature, the temperature dependence of dielectric constant and loss is shown only for $BiFe_{0.9}Al_{0.1}O_3$ (figure 3.8). Above 200 K, a large dielectric constant ($\sim 10^4$) is observed which is high compared to intrinsic dielectric constant (50 - 100) value. This indicates the presence of extrinsic effects which contribute to such a high dielectric constant values. Also, in the temperature range 50 - 340 K, only one relaxation is observed as seen in figure 3.8 which shows no anomaly but a giant increase in the dielectric constant with a single peak in the corresponding tan δ data. These features indicate a Debye-like relaxation process which is common

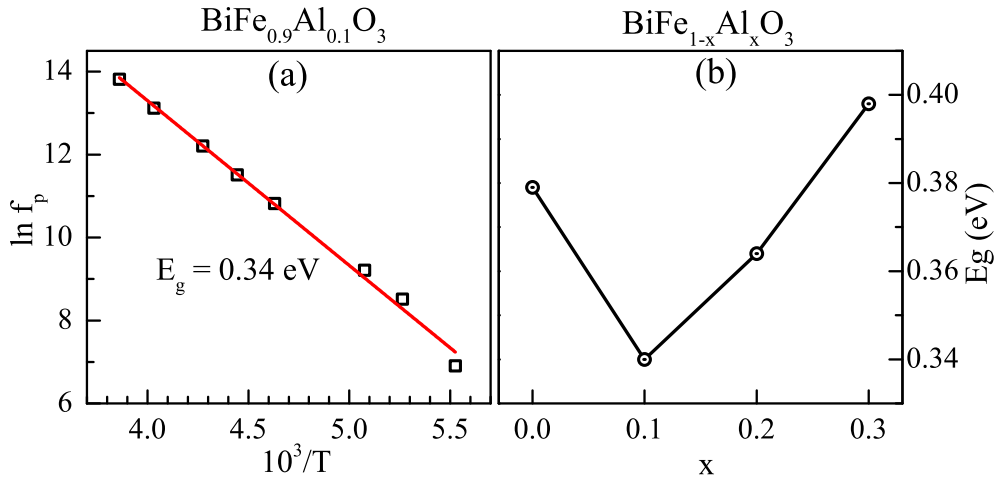

Figure 3.9: (a) Activation energy calculated from the loss data fitted to Arrhenius equation for $BiFe_{0.9}Al_{0.1}O_3$. (b) Activation energy as a function of Al concentration.

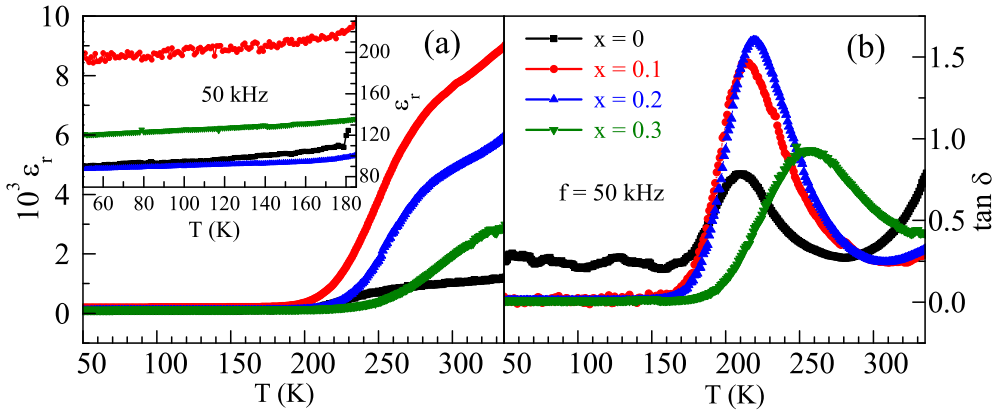

Figure 3.10: Dielectric constant and loss features in $BiFe_{1-x}Al_xO_3$. The inset shows dielectric constant at low temperatures.

in many lossy oxide materials known as the Maxwell-Wagner relaxation. In polycrystalline samples, this behavior can arise due to polarization at the grain boundary - material and/or electrode-material interfaces [113, 114]. Usually in this temperature and frequency regime, grain boundary polarization is responsible for the Maxwell-Wagner effect. This will be discussed in more detail in the next chapter.

The loss peaks in figure 3.8 denotes the dielectric relaxation frequency. As the

relaxation process is thermally activated, the relaxation time ($\tau = 1/f$) follows Arrhenius equation. The activation energy E_g for this relaxation has been calculated from the equation $f = f_0 e^{-\frac{E_g}{k_B T}}$ where f is the relaxation frequency, f_0 is prefactor and k_B is Boltzmann constant 8.617×10^{-5} eV/K. The linear fit results in an activation energy of 0.34 eV for the compound $BiFe_{0.9}Al_{0.1}O_3$ as shown in figure 3.9 (a). With Al substitution, activation energy initially decreases for x = 0.1 and then increases linearly. Dielectric features have been compared at a fixed frequency of 50 kHz as shown in figure 3.10 (a-b). At room temperature, the dielectric constant values decreases with Al concentration above x = 0.1. Similar feature is also observed at low temperatures as shown in the inset of figure 3.10.

Figure 3.11 and 3.12 show the temperature dependence of dielectric constant and loss for Sc substituted samples. Unlike the $BiFe_{1-x}Al_xO_3$ compounds, the dielectric constant as well as the loss values in Sc compounds are significantly less and do not exhibit a step like increase. The ϵ_r and $tan\delta$ values increase with temperature and shows a frequency dispersion. This may indicate a Maxwell-Wagner relaxation at higher temperature. Coinciding with the dielectric constant increase, a loss anomaly is visible near 250 K in $BiFe_{0.9}Sc_{0.1}O_3$. Room temperature frequency dependence of dielectric constant and loss in $BiFe_{1-x}Sc_xO_3$ is depicted in figure 3.13 where dielectric constant is plotted in the left axis whereas loss values are shown in the right axis. In the frequency region of 100 to 1 MHz, dielectric constant values vary between 140 to 80 and also the corresponding loss values vary between 0.1 to 0.03. It can be clearly observed that at high frequency region where the dipoles contributing to Maxwell-Wagner effect do not respond, the dielectric constant value is higher in the compound with x = 0.1. Compared

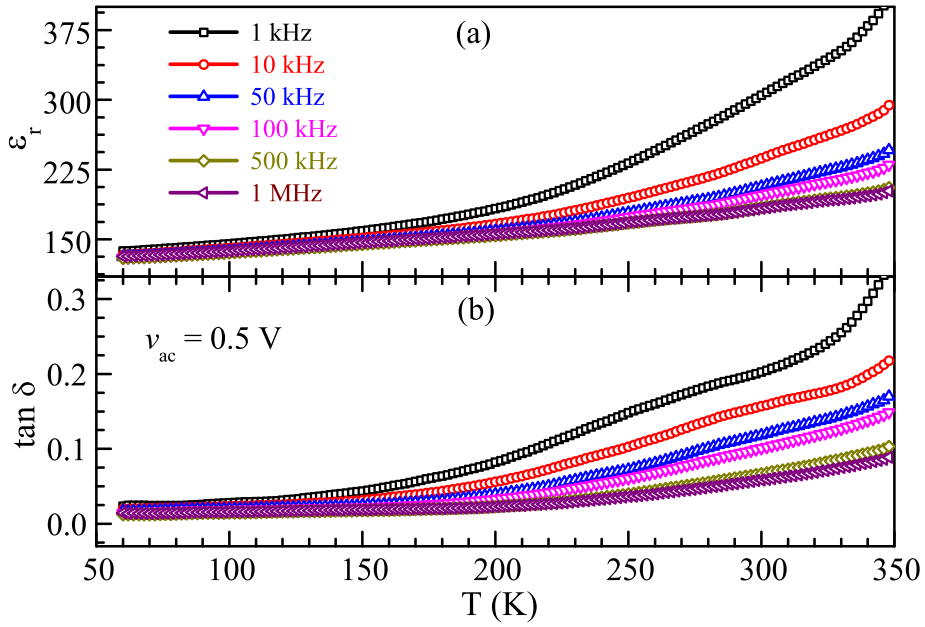

Figure 3.11: Temperature dependencies of (a) dielectric constant (ϵ_r) and (b) loss ($tan\delta$) of $BiFe_{0.9}Sc_{0.1}O_3$ plotted at different frequencies.

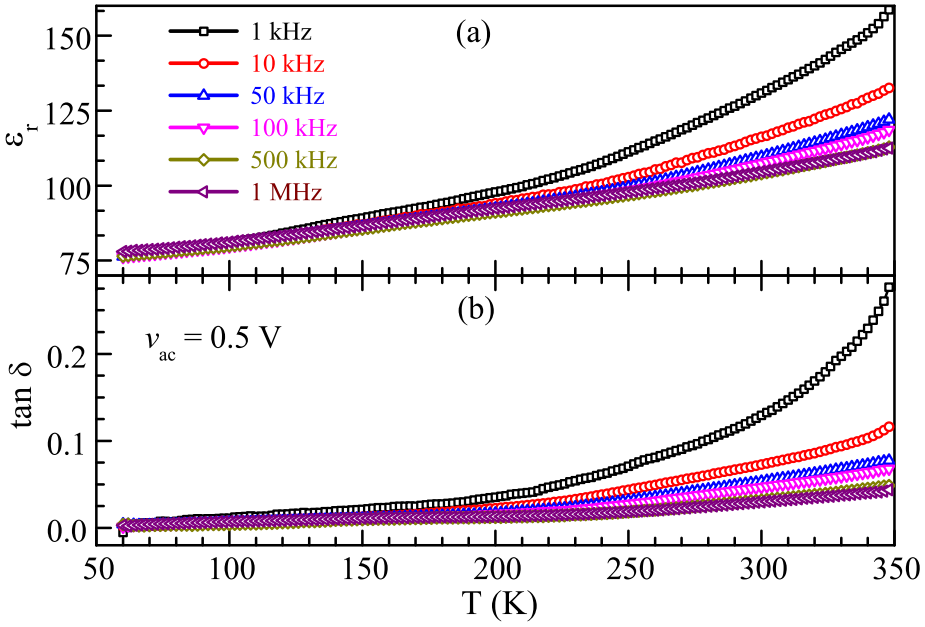

Figure 3.12: (a) Dielectric constant (ϵ_r) and (b) loss ($tan\delta$) against temperature of $BiFe_{0.8}Sc_{0.2}O_3$ plotted at different frequencies.

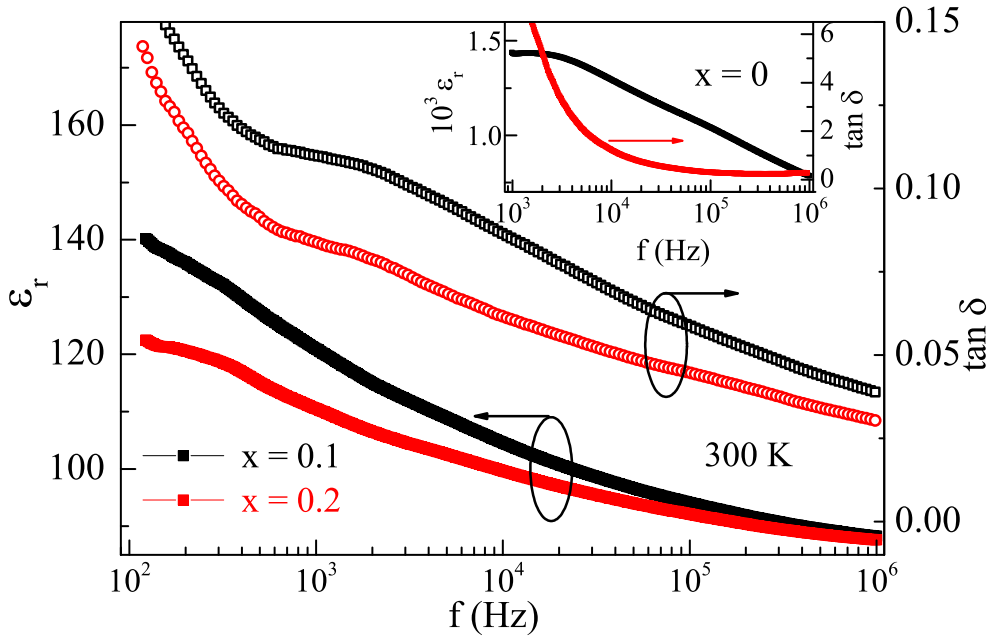

Figure 3.13: Room temperature dielectric constant and loss behavior of $BiFe_{1-x}Sc_xO_3$. The data of $BiFeO_3$ is shown in inset for comparison.

to the parent compound $BiFeO_3$, dielectric constant are nearly ten times higher whereas the loss values are 100 times lower at low frequency. Thus, Sc substituted compounds show improved dielectric properties compared to $BiFeO_3$ and $BiFe_{1-x}Al_xO_3$.

3.3.4 Ferroelectric properties

In $BiFe_{1-x}Al_xO_3$ samples, we could not measure PE loop due to high DC conductivity as also indicated from the dielectric measurements. On the other hand, $BiFe_{1-x}Sc_xO_3$ which showed improved dielectric features, the PE loops are shown in figure 3.14a and b. At lower voltages, the PE loops do not saturate and rather appears to be leaky. When the loop was measured at relatively high voltage and at high frequency of 1 kHz, a nearly saturated loop is obtained for $BiFe_{0.9}Sc_{0.1}O_3$ compound. The maximum polarization value obtained is P_S = 3.7 μC/cm^2 with remnant polarization of 2.37 μC/cm^2 and a

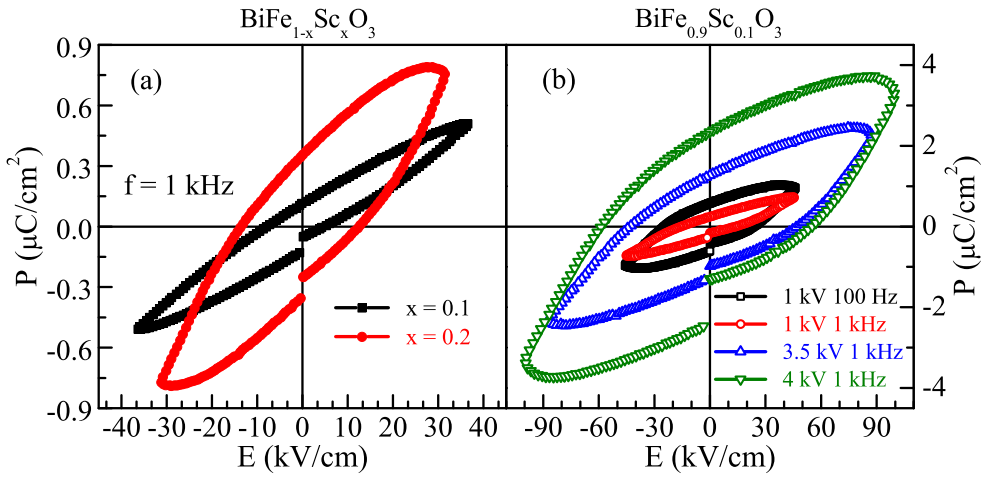

Figure 3.14: PE hysteresis loop in (a) $BiFe_{1-x}Al_xO_3$ and (b) $BiFe_{0.9}Al_{0.1}O_3$

.

coercive field of 57 kV/cm. As thickness of the pellet could not be reduced below 400 μm and the maximum voltage is restricted to 4 kV, we could not obtain a saturated loop. It can be easily observed that when the measurement frequency is varied, the loop shape changes significantly as shown in figure 3.14b. This also indicates the contribution from dielectric loss or the DC conduction. In a ferroelectric capacitor of area A having a finite conductivity σ, the measured or switched charge (Q) in time t can be represented as,

$$Q = 2P_rA + \sigma EAt \tag{3.1}$$

where, the first term is the polar contribution and the second term arises from the finite DC conduction or loss. It is important to mention that this lossy contribution can be avoided at very high frequency where the dipoles can not follow the measurement frequency. We could not employ this technique due to our instrument limitation where above 1kHz frequency the number of data points become significantly less. Room temperature saturated ferroelectric P-E loop, has been reported in high quality epitaxial

thin films and also in polycrystalline samples of $BiFeO_3$ [88, 108]. In ceramic samples, ferroelectric measurements are mostly hindered by loss or leakage current which arises due to oxygen defects. In $BiFeO_3$, leaky hysteresis behavior arises from finite DC conduction due to presence of Fe^{2+} ions which consequently leads to oxygen vacancies [115, 116]. Quality of precursor Fe_2O_3 and synthesis route have been observed to dramatically affect the phase purity and thus ferroelectric properties of $BiFeO_3$ [117]. However, several preparation methods such as rapid liquid phase sintering or quenching have been employed to avoid these issues [107, 108]. High pressure synthesis at 6 GPa has also been shown to be effective to control the stoichiometry and obtaining a saturated PE hysteresis [118]. In the present case although high pressure technique was adapted, the compounds were prepared at relatively low pressures (4.5 GPa).

3.4 Conclusions

$BiFe_{1-x}Al_xO_3$ and $BiFe_{1-x}Sc_xO_3$ have been synthesized using high pressure technique. Solid solution with a rhombohedral structure (R3*c*) could be obtained up to x = 0.2 and 0.3 for Al and Sc substitutions respectively. Finite magnetization observed at room temperature suggest suppression of the spiral magnetic ordering. The Al substituted $BiFeO_3$ compounds exhibits Maxwell-Wagner relaxation whereas the Sc compounds showed improved dielectric and ferroelectric properties.

CHAPTER 4

Structure, Magnetism and Giant Dielectric Constant of $BiCr_{0.5}Mn_{0.5}O_3$ Synthesized at High Pressures[†]

4.1 Introduction

In the context of multiferroic materials [13, 33, 84, 119], there has been wide interest in the study of bismuth-based transition metal oxides of the type $BiMO_3$ (M= 3d transition metal) because of their structural peculiarities as well as promising physical properties [51, 88, 120–122]. For example, though both La^{3+} and Bi^{3+} ions have similar ionic radii (1.16 Å and 1.17 Å respectively in nine-fold coordination) [104], $LaFeO_3$ crystallizes in a centrosymmetric orthorhombic structure (space group P*nma*) while $BiFeO_3$ has a noncentrosymmetric rhombohedral structure (R3*c*) [86, 123]. Origin of the noncentrosymmetric distortion is attributed to the stereochemical activity of 6s lone pair electrons of Bi^{3+} ions [40]. Thus, $BiFeO_3$ is multiferroic where the ferroelectricity (T_{CE} = 1100 K) originates from the Bi^{3+} ions and antiferromagnetism (T_N = 650 K) appears due to ordering of Fe^{3+} (S=5/2) moments [32, 88]. Among the $BiMO_3$ (M = transition metal) series, $BiMnO_3$ has also been extensively studied with respect to structure, magnetism and ferroelectric properties because it is the only material reported to be ferromagnetic with a T_C of 105 K [51, 124]. Although there was an indication of ferroelectricity in multiphasic sample of $BiMnO_3$ [125], later investigations

[†]This work has appeared in *J. Mater. Chem.*, **20**, 1646 (2010)

on bulk samples as well as thin films have not confirmed ferroelectricity unambiguously. Unlike $LaMnO_3$, which has the orthorhombic structure (P*nma*), an early neutron diffraction study showed $BiMnO_3$ to possess a highly distorted noncentrosymmetric monoclinic structure (C2) [126]. Recent studies based on convergent beam electron diffraction, however, show the presence of a centre of inversion symmetry [127, 128]. Theoretical calculations also suggest a centrosymmetric space group (C2/*c*) for ideal $BiMnO_3$ [129]. Very recently, selected area electron diffraction studies have revealed the presence of a long-range ordered structure with C2 symmetry and short range ordered structure with P2 or $P2_1$ symmetry [128]. Oxygen nonstoichiometry has also been reported to have a great influence on the structure and magnetism of $BiMnO_3$ [130, 131]. On the other hand, $BiCrO_3$ has a centrosymmetric monoclinic structure (C2/*c*) and undergoes a long range G−type antiferromagnetic ordering at $T_N = 109$ K with a weak ferromagnetic component [121, 122, 132]. These isostructural compounds differ on their monoclinic angles which are 110.66 ° and 108.56 ° for $BiMnO_3$ and $BiCrO_3$ respectively [122, 127]. It is worth noting that $BiAlO_3$ is ferroelectric and has non-centrosymmetric structure similar to $BiFeO_3$ [106, 133] whereas $BiGaO_3$ and $BiScO_3$ possess centrosymmetric structure [105, 128]. It, therefore, appears that the Bi^{3+} ion with the 6s lone pair does not always cause a noncentrosymmetric structure. It is noteworthy that except $BiFeO_3$, which is a room temperature ferroelectric and antiferromagnetic compound, all the other bismuth-based $BiMO_3$ compounds (M= Sc, Cr, Mn, Co and Ni) require high pressures to stabilize them in the perovskite structure [51, 105, 120, 121, 134].

Bismuth-based oxides with two different magnetic ions at the B−site can show

interesting magnetic properties due to various exchange couplings arising from their differing magnetic moments and symmetry of the orbital involved. For example, the ordered oxide, Bi_2NiMnO_6, is a ferromagnet with a high Curie temperature (T_C = 140 K) according to the Goodenough-Kanamori (GK) rules and ferroelectric (T_{CE} = 485 K) due to Bi^{3+} ions [135, 136]. It was theoretically predicted that the compound Bi_2FeCrO_6 would be an ordered perovskite where Fe^{3+} and Cr^{3+} would order along the cubic (111) direction to give a rock-salt type ordering with a high ferrimagnetic transition temperature [92]. However, experimental results on polycrystalline samples have shown that Fe and Cr ions are disordered at the B-site of the rhombohedral (R3*c*) structure with a collective magnetic ordering at 130 K likely to be due to frustration arising from Fe^{3+} – O – Fe^{3+}, Cr^{3+} – O – Cr^{3+} and Fe^{3+} – O – Cr^{3+} magnetic interactions [137]. Later, ordering of trivalent Fe and Cr ions was confirmed in epitaxial thin films [138, 139]. A checkerboard type of ordering between Fe and Mn ions was in Bi_2FeMnO_6 while experimentally a double zigzag type of ordering has been indicated in high pressure synthesized compounds [140, 141]. This motivated us to synthesize and study the structure, magnetism, multiferroic properties of Bi_2CrMnO_6. The combination of transition metals was chosen because certain oxidation states of Cr and Mn (Cr^{3+} and Mn^{3+}: d^3 and d^4) can be expected to exhibit a ferromagnetic ground state on ordering at the B-site. Contrary to this expectation, $BiCr_{0.5}Mn_{0.5}O_3$ is not an ordered compound and adopts the $BiCrO_3$ structure (C2/*c*) with a monoclinic angle of $108.140(2)^\circ$, undergoing a phase transition around 650 K. Owing to the disordered structure the compound orders antiferromagnetically at 96 K and below T_N shows a frustrated magnetic behavior. The compound interestingly exhibits a giant dielectric constant over a broad temperature

and frequency range similar to $CaCu_3Ti_4O_{12}$ and related materials. This is explained in terms of extrinsic contribution from grain boundary and electrode – material interface due to Maxwell – Wagner relaxation.

4.2 Experimental

As mentioned previously, except $BiFeO_3$, other $BiMO_3$ requires high pressure to stabilize. Attempt of ambient pressure synthesis of Bi_2CrMnO_6 by solid state route resulted formation of impurity phases. Polycrystalline Bi_2CrMnO_6 was synthesized under high pressure and high temperature employing a cubic anvil type apparatus (RIKEN CAP-07) as described in 2. Stoichiometric amounts of preheated Bi_2O_3, Mn_2O_3 and Cr_2O_3 were mixed, ground well inside a glove box and pressed into a cylindrical shaped pellet. The pellet was placed inside a gold capsule and reacted at a temperature of 1073 K and a pressure of 4.5 GPa. Phase purity was confirmed by Bruker D8 Advance X-ray diffractometer. A software package Fullprof [109] was used to analyze the structural data and perform Rietveld refinement. Differential scanning calorimetry data were collected on Q2000 system (TA instruments). Magnetic properties were characterized by DC and AC susceptibility measurement in a Physical Property Measurement System (PPMS, Quantum Design, USA). Dielectric measurements were carried out with an Impedance Analyzer (Agilent 4294A) using coaxial cable wire in a 4TP – 2T configuration. Silver paint or sputtered gold was used as electrode and the sample was placed in a custom made sample holder which is inserted into the sample chamber of a cryo – cooled 15 tesla superconducting magnet system (Cryo Industries of America Inc.). At high temperature ($>$ 300 K), dielectric properties were measured by depositing gold on either

side of the pellet and using a spring loaded sample holder.

4.3 Results and discussion

4.3.1 Structure

In figure 4.1, Rietveld refinement on the room temperature X-ray diffraction (XRD) pattern of $BiCr_{0.5}Mn_{0.5}O_3$ is shown based on the centrosymmetric monoclinic structure with space group (C2/*c*). The structural parameters of $BiCrO_3$ and $BiMnO_3$ were used as initial parameters for the refinement in space groups C2 and C2/*c*. The centrosymmetric space group C2/*c* was found to fit better than the non-centrosymmetric space group C2. The refined lattice parameters obtained from the Rietveld refinement are a= 9.4590(3) Å, b= 5.5531(2) Å, c= 9.6465(3) Å and β = 108.149(2)°. The observed monoclinic angle is very close to that reported for $BiCrO_3$. The other structural parameters obtained from the refinement are given in Table 4.1. Because of the presence of extra peaks due to unknown impurity phases the χ^2 value is slightly higher but the parameters with standard errors are quite acceptable. As we could not identify the nature of impurity phase, the extra peaks are excluded in the refinement. There are two crystallographic sites for the transition metals in the space group C2/*c*. Since it is difficult to determine the distribution of Cr and Mn ions over the sites 4*d* and 4*e* using laboratory X-rays, we distributed these ions equally among the two sites. This reflects that though we anticipated ordering between Cr and Mn ions, these ions are disordered at the B-sites. Selected bond lengths and angles are given in Table 4.2. The Bi-O and average Cr/Mn-O bond lengths are comparable to those observed in $BiCrO_3$ and $BiMnO_3$. Bond valence sum (BVS) calculated from the bond lengths are consistent with the trivalent

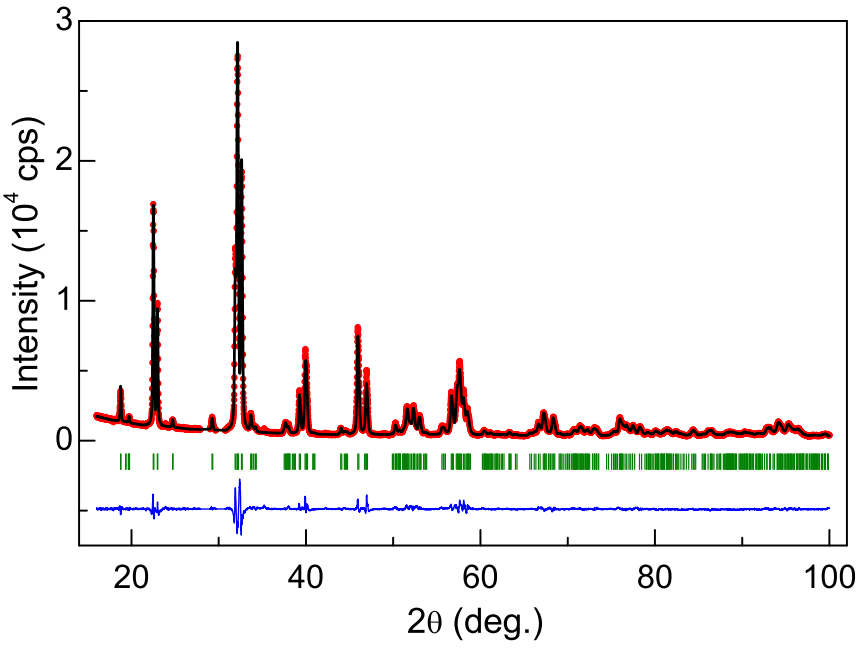

Figure 4.1: Rietveld refinement on the room temperature X-ray diffraction data. Observed (dots) and calculated (line) X-ray diffraction pattern of $BiCr_{0.5}Mn_{0.5}O_3$ at room temperature. The bottom curve shows the difference pattern and the vertical marks are the symmetry allowed Bragg reflections.

states of Bi, Cr and Mn ions. The absence of long-range ordering of the transition metal ions is further supported by the magnetic properties where we do not see ferromagnetic ordering expected from the presence of $Cr^{3+}(d^3)$ and $Mn^{3+}(d^4)$ ions.

4.3.1.1 High temperature X-ray diffraction

Structural change from low symmetry to a higher symmetry has commonly been observed in the related materials. For example, the compounds $BiMnO_3$ and $BiCrO_3$ are reported to show a structural change from monoclinic (C2/*c* or C2) to orthorhombic (P*nma*) at high temperatures. This transition from low to a high symmetry was attributed to ferroelectric to paraelectric transition [51, 132]. Though, so far there is no clear indication of ferroelectricity in these compounds and it is believed that ferroelec-

Table 4.1: Crystallographic data of $BiCr_{0.5}Mn_{0.5}O_3$ at room temperature

Atom	Wyck. Position	Oxidation	*x*	*y*	*z*	B_{iso}	Occ.
Bi	8f	+3	0.1328(1)	0.2172(2)	0.1287(2)	0.68(2)	0.952(3)
Cr1	4e	+3	0.0000	0.2303(8)	0.75	0.82(6)	0.25
Mn1	4e	+3	0.0000	0.2303(8)	0.75	0.82(6)	0.25
Cr2	4d	+3	0.25	0.25	0.50	0.82(6)	0.25
Mn2	4d	+3	0.25	0.25	0.50	0.82(6)	0.25
O1	8f	-2	0.089(1)	0.205(2)	0.584(1)	1.000	1.00
O2	8f	-2	0.149(2)	0.557(2)	0.378(2)	1.000	1.00
O3	8f	-2	0.351(2)	0.541(2)	0.164(1)	1.000	1.00

a= 9.4662(3) Å; *b*= 5.5577(2) Å; *c*= 9.6538(4) Å; β = 108.140(1)°;
χ^2 = 6.11; R_p = 10.6; R_{wp} = 10.6; R_P = 11.7;
R_{Bragg} = 10.6 ; RF factor= 4.34

Table 4.2: Selected bond lengths (Å), angles (°) and bond valence sum (BVS) of $BiCr_{0.5}Mn_{0.5}O_3$ at room temperature

Bond length(Å)/Angle°				
Bi - O1	2.44(2)	2.40(2)	3.20(2)	
Bi - O2	2.27(3)	2.80(3)	3.00(3)	
Bi - O3	2.19(3)	2.68(2)	2.96(2)	3.22(3)
Cr1/Mn1 - O1		2.03(2) x 2		
Cr1/Mn1 - O2		1.94(2) x 2		
Cr1/Mn1 - O3		2.06(2) x 2		
Cr2/Mn2 - O1		1.96(2) x 2		
Cr2/Mn2 - O2		2.13(2) x 2		
Cr2/Mn2 - O3		1.95(2) x 2		
BVS Bi		2.90 (1)		
BVS Cr1/Cr2		2.94 (7)		
BVS Mn1/Mn2		3.23 (8)		

tricity is forbidden owing to the centrosymmetric structure. High temperature X-ray diffraction data reveal the occurrence of a structural change from the monoclinic (C2/*c*) to an orthorhombic (P*nma*) phase as shown in figure 4.2. The monoclinic-orthorhombic transition is complete at 873 K, but we observe coexistence of the two phases in the XRD patterns collected at 673 and 773 K. At these temperatures, a better fit was ob-

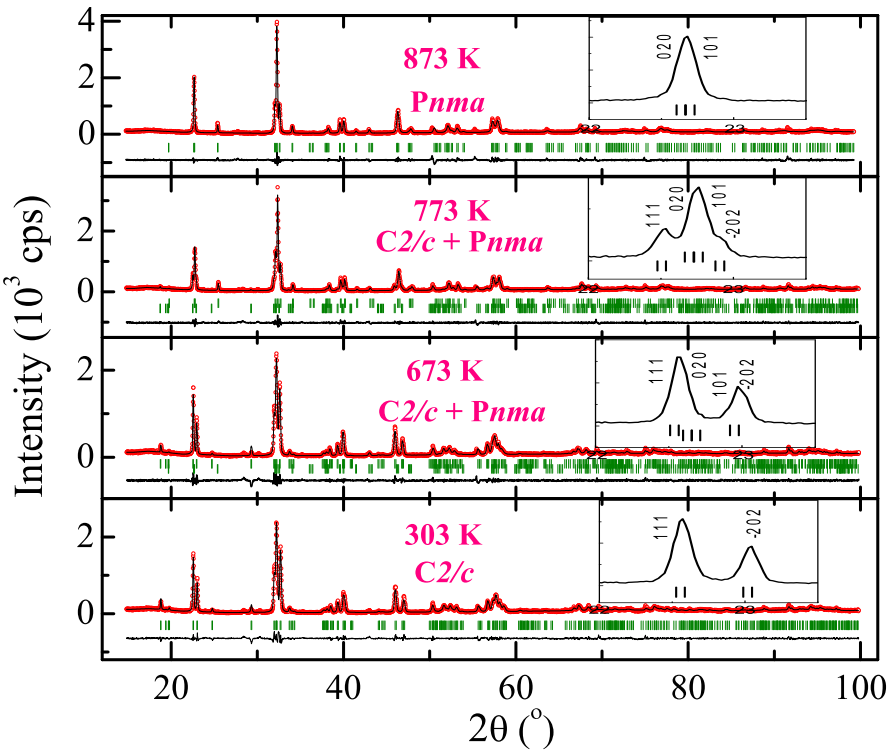

Figure 4.2: X-ray diffraction patterns at high temperatures showing monoclinic to orthorhombic transition.

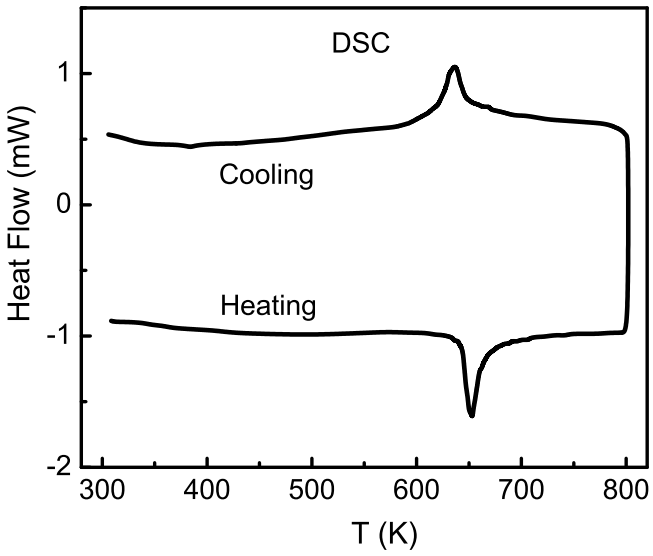

Figure 4.3: Differential scanning calorimetry curves show that the monoclinic to orthorhombic transition is reversible.

tained for a mixture of C2/*c* and P*nma* phases. Coexistence of the two phases is consistent with the first order nature of the phase transition. An endothermic peak at 650 K in differential scanning calorimetry (DSC) confirms the occurrence of the phase transition and its first-order nature. The DSC curves in figure 4.3, show the peaks at different temperatures while heating and cooling as expected of a first-order transition. Interestingly, the transition temperature of $BiCr_{0.5}Mn_{0.5}O_3$ is between that of $BiMnO_3$ ($\sim$770 K) and $BiCrO_3$ ($\sim$440 K) [51, 132]. At 873 K, the refined lattice parameters obtained from profile fit for the P*nma* space group are $a = 5.5878$ (4) Å, $b = 7.8606$ (7) Å and $c = 5.4979$ (4) Å.

4.3.2 Magnetic properties

4.3.2.1 DC magnetization

Figure 4.4 shows the variation of the molar susceptibility under zero field-cooled (ZFC) and field – cooled (FC) conditions measured under a magnetic field of 100 Oe. Three clear anomalies are observed at 25, 53 and 96 K which disappear on applying a high magnetic field of 10 kOe (see inset (a) in figure 4.4). Furthermore, the ZFC-FC curves coincide in the entire temperature range accompanied by a rise in susceptibility below 100 K. Above 100 K, the low field susceptibility follows Curie-Weiss behavior. The data is fitted to the Curie-Weiss law, $\chi = C/(T - \theta)$ where C is the Curie constant and θ is Weiss temperature. From the fit, we obtain the effective magnetic moment $\mu_{eff} = 4.16\,\mu_B$ and the Weiss constant θ = +59 K. The value of μ_{eff} is close to the spin only value of 4.42 μ_B expected for $Cr^{3+} - Mn^{3+}$ configuration. The Weiss constant for $BiCrO_3$ is negative (– 359 K) whereas it is positive (126 K) for $BiMnO_3$ indicating the

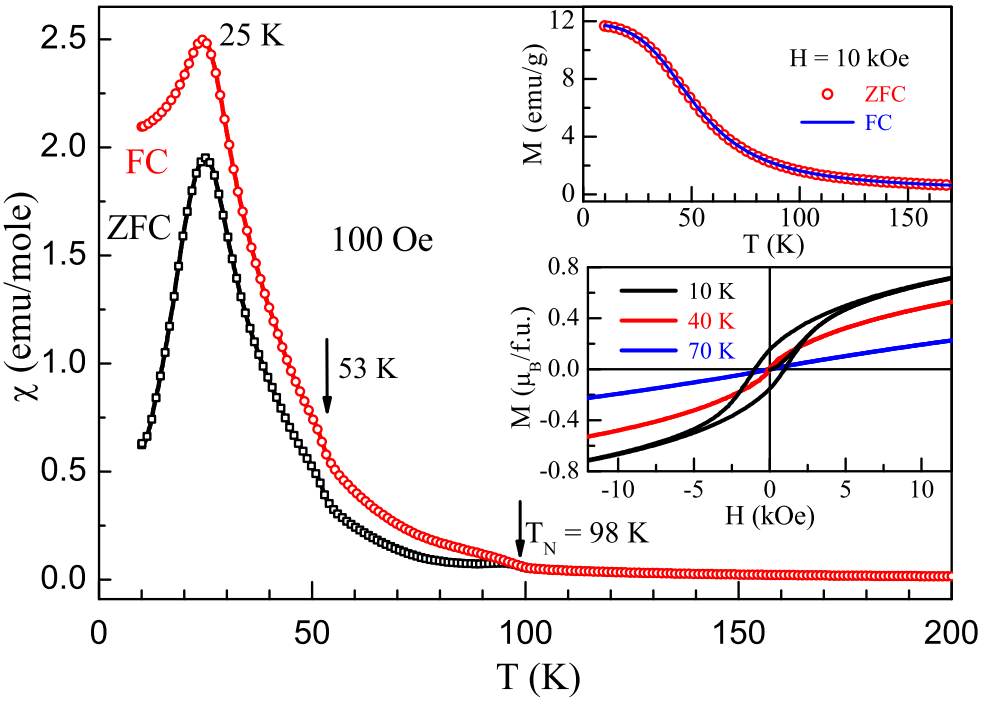

Figure 4.4: Molar susceptibility versus temperature curves showing three anomalies at 25, 50 and 97 K. The irreversibility between ZFC and FC curves below 97 K indicates the canting of magnetic moments. Inset (a) shows the temperature dependence of magnetization at 10 kOe and (b) shows the magnetization versus field at various temperatures.

change in the nature of magnetic interaction from antiferromagnetic to ferromagnetic in the parent compounds [51, 132]. The positive intermediate value of $\theta = 59$ K in $BiCr_{0.5}Mn_{0.5}O_3$ is reasonable considering that both the end members have the monoclinic structure.

The magnetic behavior of $BiCr_{0.5}Mn_{0.5}O_3$ is similar to the parent compound $BiCrO_3$ which shows three anomalies at slightly higher temperatures (40, 70 and 109 K) in the DC magnetization data [121]. The decrease in the magnetic transition temperatures in the former can arise due to the dilution of the Cr^{3+} ions in $BiCrO_3$ lattice with Mn^{3+} ions. As in the case of $BiCrO_3$, where the low-temperature anomaly at 40 K disappears

upon applying high fields, all the three anomalies in $BiCr_{0.5}Mn_{0.5}O_3$ disappear as seen in inset (a) of figure 4.4. Inset (b) in figure 4.4 shows the magnetic isotherms at 10, 40 and 70 K. At 10 K, the compound shows a hysteresis behavior without saturation indicating a weak ferromagnetic behavior at low temperatures. This is consistent with the fact that Cr^{3+} and Mn^{3+} ions are disordered at the B – site. The M-H loop becomes feeble with increase in temperature and at 70 K it becomes almost linear.

4.3.2.2 AC susceptibility

Ac susceptibility data of $BiCr_{0.5}Mn_{0.5}O_3$ were collected at different frequencies from 100 Hz to 10 kHz under an applied AC field of 5 Oe. The real and imaginary parts of the AC susceptibility show three anomalies in agreement with the DC magnetization data.

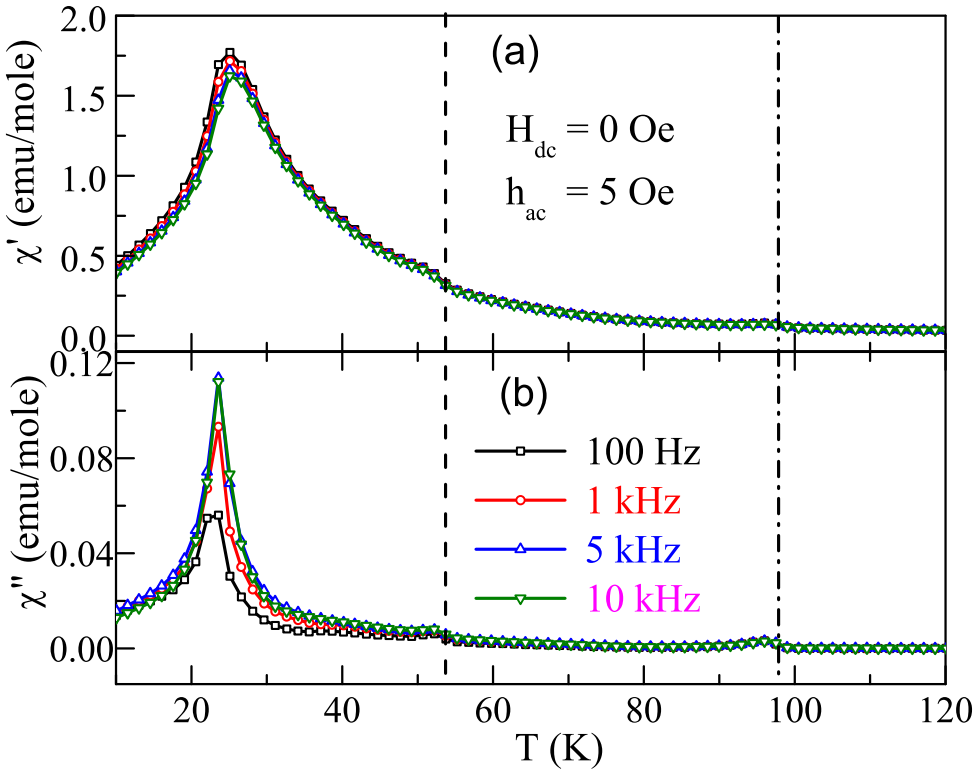

Figure 4.5: AC susceptibility data plotted against temperature at different frequencies.

The real part χ' shows a small frequency dispersion below the first anomaly at 25 K whereas the imaginary part χ'' shows a frequency dispersion between the first and third anomalies. The peak positions do not shift near the anomaly at 70 and 110 K. Though, there is a weak frequency dependence in χ' and χ'' data near 25 K anomaly where peak in real parts shift towards higher temperature and in imaginary part peak anomaly shifts towards lower temperature. This feature is close to the parent compound $BiCrO_3$ [121].

4.3.3 Dielectric properties

As the room temperature structure is centrosymmetric, we do not expect ferroelectricity in this compound. This is confirmed by measuring P – E hysteresis loop which showed a linear curve. Though this material is not ferroelectric, dielectric properties can still be interesting and important for various applications such as capacitors, sensors, actuators, resonators, filters and memory devices [142]. Figure 4.6 depicts the dielectric constant (ϵ_r) and loss tangent (tanδ) behavior at different frequencies in the temperature range 20 – 400 K (applied AC bias of 0.5 Volt). This compound exhibits a high dielectric constant ($\sim$14000 at 1 kHz) and loss ($\sim$ 0.95) at room temperature. Starting from a low value ($\sim$ 100), the dielectric constant increases rapidly above 200 K to unusually high values ($\sim 10^4$) with an anomaly around 300 K as shown in figure 4.6a. This behavior is frequency-dependent and the peaks shift towards high temperature with increasing frequency. The loss data in figure 4.6 show frequency-dependent peaks corresponding to the dielectric constant peaks. In this temperature range, the loss peaks due to the second anomaly is visibile only at lower frequencies. Interestingly, the loss peak corresponding to the first anomaly appear at lower temperatures than the dielectric constant

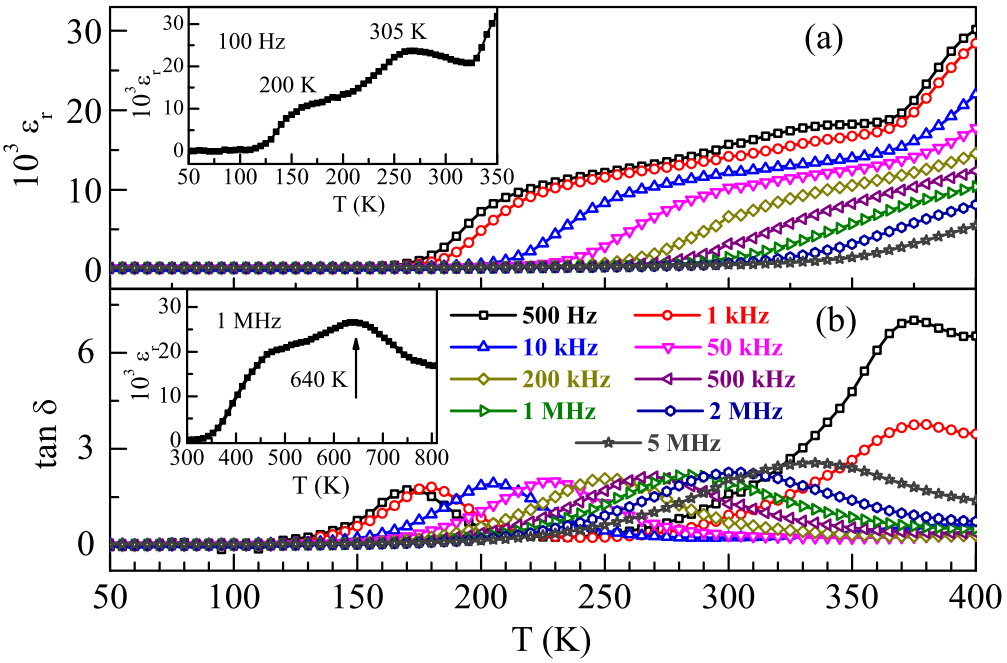

Figure 4.6: Temperature dependence of (a) relative dielectric constant (ϵ_r) and (b) loss (tanδ) showing a giant dielectric constant at room temperature and two dielectric anomalies. Inset (a) shows two clear anomalies at low frequency (100 Hz) dielectric constant data. The dielectric anomaly at 650 K as shown in the inset of figure (b) is associated with the structural phase transition.

peak whereas it appears at a slightly higher temperature in case of second anomaly. Two relaxation processes seems to be associated with the dielectric anomalies below 400 K. This becomes evident from the dielectric constant data at 100 Hz shown as an inset (a) in figure 4.6 and the loss data in figure 4.6b. The first anomaly may be related to Maxwell-Wagner relaxation due to the interfacial polarization at the grain boundaries. This phenomenon is common in heterogeneous systems where there is a difference between the grain and grain boundary conductivities due to which surface charges pile up at the interface, giving rise to a Debye-like relaxation on application of AC bias [143, 144]. As there is no structural transition around the second dielectric

anomaly (300 K), we assign it to possible hopping of electrons among the transition metal ions. Detailed analysis show that the second relaxation is due to conduction process as discussed below. In addition to these two anomalies, the dielectric constant at high frequency (1 MHz) shows an anomaly near 640 K as shown in inset of figure 4.6(b). This anomaly is related to the structural phase transition from monoclinic to the orthorhombic phase. The shoulder around 450 K correspond to the second relaxation process observed in the low-temperature dielectric data.

4.3.3.1 Maxwell-Wagner relaxation

For practical applications, a material with high dielectric constant, low loss and constant value over broad temperature and frequency range is desirable. Very few materials satisfy all these criteria and the number of such materials useful for device application is not therefore large. Mostly, high values of dielectric constant are observed in ferroelectric materials near the ferroelectric to paraelectric transition in a narrow temperature range. In past few years, giant dielectric response has been reported in non-ferroelectric materials such as $CaCu_3Ti_4O_{12}$ (CCTO) [145, 146], certain Fe-based compounds [143, 147] and in other materials [113, 144, 148] in a broad temperature and frequency range. Earlier studies on polycrystalline CCTO samples showed that the origin of giant dielectric constant was due to intrinsic effect arising from slowing down of highly polarizable relaxational modes [145] or slowing down of dipolar fluctuations in nanosize domains [146]. Later, detailed studies on polycrystalline as well as on single crystalline samples have confirmed the contributions from extrinsic effects [113, 149] and moreover the mechanism is believed to be different in ceramic and single crystals

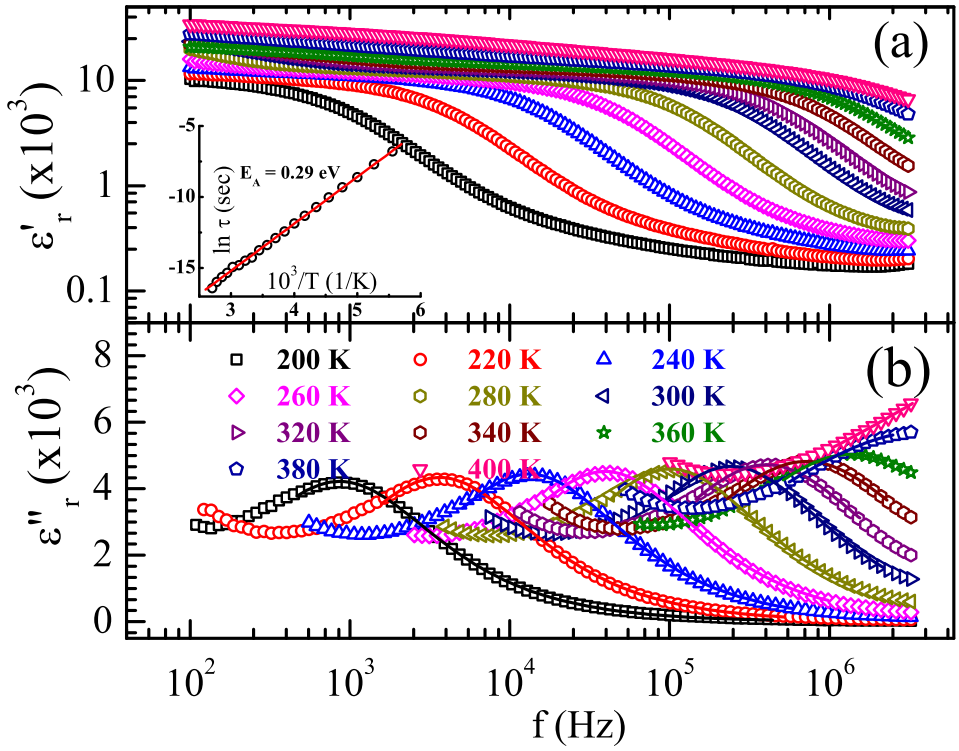

Figure 4.7: Variation of (a) real ($\epsilon_r^{'}$) and (b) imaginary ($\epsilon_r^{''}$) parts of dielectric constant as a function of frequency at different temperatures. Data has been plotted in limited range for clarity. Solid lines in (b) represent fits to modified Debye relation (see text). Inset shows relaxation time (τ) which follows Arrhenius equation for activated process.

[150, 151]. Maxwell-Wagner type relaxation either due to depletion layers at the grain boundaries or at the electrode-material interface have also been suggested to explain the behavior [113]. In some systems, internal barrier layer capacitance (IBLC) effect due to Schottky barriers formation at the grain boundaries best explains the giant dielectric constant in ceramics [114, 152]. In single crystal of CCTO, rather a different mechanism, electrode polarization effect at the metal-semiconductor junction is believed to be responsible for such dielectric behavior [113, 150]. In few other materials, where the colossal dielectric response is believed to be intrinsic, the origin is attributed to electronic polarization [147, 148]. From application point of view, such high values of

dielectric constant should persist up to the gigahertz region but most of these materials show a fall in the megahertz frequency.

Figure 4.7 shows real and imaginary parts of dielectric constant plotted against frequency at different temperatures. At low frequency, real part shows a plateau and then decreases dramatically to a constant low value of $\epsilon_r \sim 500$ at high frequencies. It should be noted that this constant value of dielectric constant at high frequency is much higher than the intrinsic dielectric constant of a material. The step like behavior of ϵ_r with a coinciding peak in the loss spectra (figure 4.7) is typical of a Debye-like relaxation process. However, we found that the behavior deviates from the ideal Debye relaxation which assumes a single relaxation time (τ) [153]. Rather, the behavior was found to follow a modified Debye relation which includes a distribution of relaxation times defined by a parameter α [154]. The dielectric constant was fitted with equation

$$\epsilon^*(\omega) = \epsilon_\infty + \frac{(\epsilon_0 - \epsilon_\infty)}{(1 + (i\,\omega\,\tau)^{1-\alpha})} \tag{4.1}$$

where ϵ_0 and ϵ_∞ are the low and high frequency dielectric constants and $\alpha = 0$ gives the ideal Debye relaxation behavior. In figure 4.7b, solid lines through the points show fits to the $\epsilon_r^{''}$ using equation 4.1. From the fitting, obtained value of α vary from 0.13 to 0.58 with temperature. The most probable relaxation times, extracted from the fit, follows Arrhenius law

$$\tau = \tau_0 e^{\frac{E_A}{k_B T}}$$

with an activation energy of 0.29 eV.

4.3.3.2 AC conductivity

To understand high temperature relaxation process, AC conductivity ($\vec{\sigma} = j\,\vec{\epsilon}\,\vec{\omega}$), calculated from the dielectric data, was analyzed in the temperature range 300 – 400 K. Figure 4.8 shows real part of conductivity ($\sigma' = \omega\,\epsilon_0\,\epsilon''$) plotted against frequency at different temperatures. At higher temperatures, AC conductivity values become independent in low frequency region. This excludes the possibility of pure ionic conduction in the material. Values of DC conductivity were extracted at each temperature by extrapolating AC conductivity (σ') to zero frequency. The obtained DC conductivity (Figure 4.8 inset) follows Arrhenius behavior with activation energy of 0.30 eV. This value is

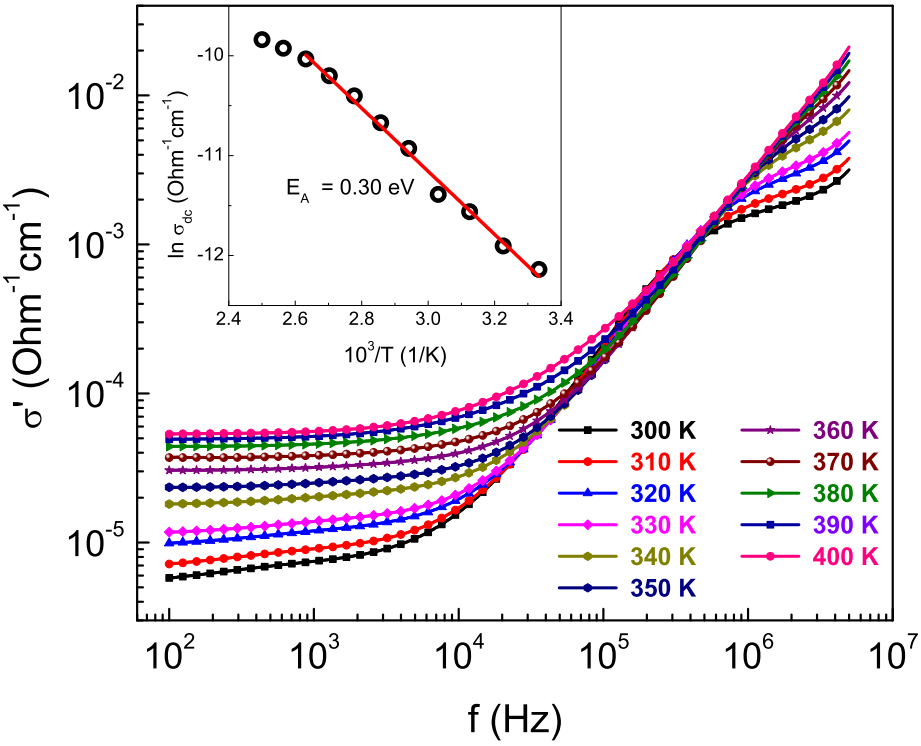

Figure 4.8: Real part of AC conductivity (σ') against frequency shown at different temperatures. Inset shows DC conductivity, derived from AC conductivity plot, following Arrhenius equation.

comparable to the activation energy associated with the DC conduction in mixed valent Mn compounds [155, 156]. Dielectric relaxation around this temperature is thus related to conduction process possibly due to mixed valence of transition metal ions arising from oxygen non-stoichiometry.

4.3.3.3 Impedance spectroscopy

Impedance study is helpful to relate electrical properties of a material to its microstructure and also to separate out the contributions from different electro-active regions [157, 158]. Figure 4.9 shows the Nyquist or Z^* ($Z^{''}$ vs. $Z^{'}$) plot at 250 K where parts of two semicircular arcs indicate that the electrical response is dominated by mainly two contributions, each of which can be represented by a parallel capacitance (C) – resistance (R) component. The intercept of a semicircle to the real axis gives R value whereas C can be calculated using the relation $\omega_m \tau = 1$, where ω_m is the angular frequency at the arc maxima and $\tau = CR$ is the time constant of the circuit [157]. Capacitance values extracted from Z^* plots in the high and low frequency arcs are of order of pF and nF which correspond to grain and grain boundary values [157]. Both grain and grain boundary resistance values extracted from the circular fit were found to follow Arrhenius law with close activation energies of 0.27 eV. This may indicate that the grain boundary response is associated with the constriction resistance which occurs due to necking of grains possibly due to low pellet density which gives rise to similar behavior of grain and grain boundary resistances. This activation energy is also close to that of the low temperature dielectric relaxation. Above 270 K, the low frequency arc (grain boundary contribution) slightly deviates from the semicircular shape which

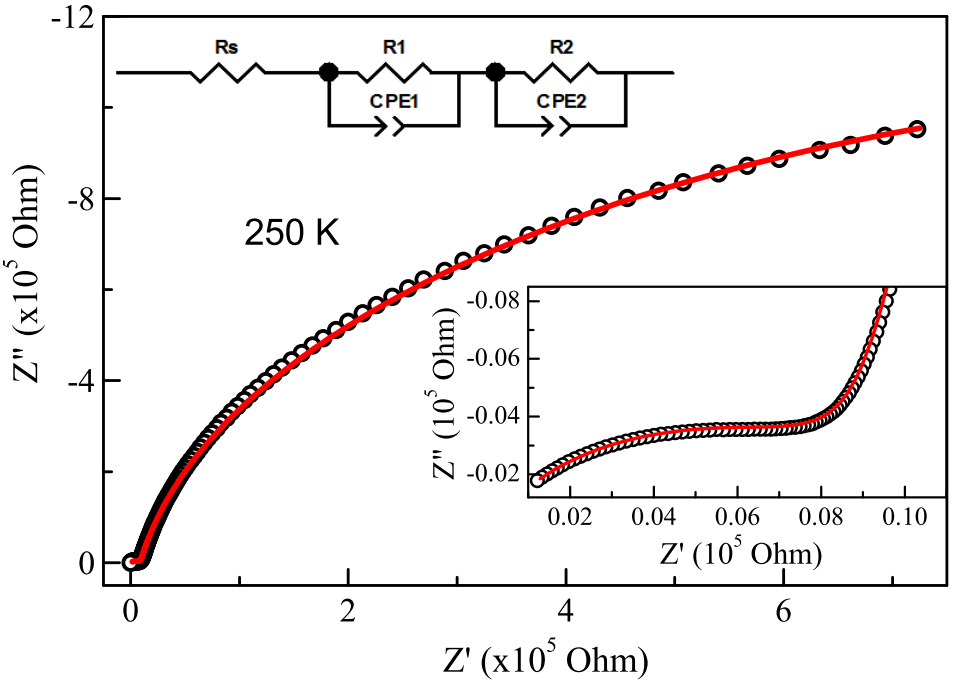

Figure 4.9: Nyquist plot at 250 K (open circle) and simulated data (solid line) using equivalent circuit as shown in figure. Inset shows the low frequency region zoomed for clarity.

may indicate appearance of extrinsic contributions. This was confirmed by measuring dielectric constant with different thicknesses (400 to 275 μm) and changing electrode from sputtered gold to silver paint as shown in inset of figure 4.10. The dielectric constant values are different at the low frequency region but they merge at high frequencies which suggest contributions from extrinsic factors such as interfacial polarization or electrode polarization effect [114]. Electrode contribution seems to play a significant role only at high temperature as Nyquist plot shows grain and grain boundary contributions at lower temperature. Based on the following observations, an equivalent circuit is used to model the data at low temperature as shown in inset (a) of figure 4.9. The resistance R_S is assigned to account for non-zero intercept of high frequency arc to the

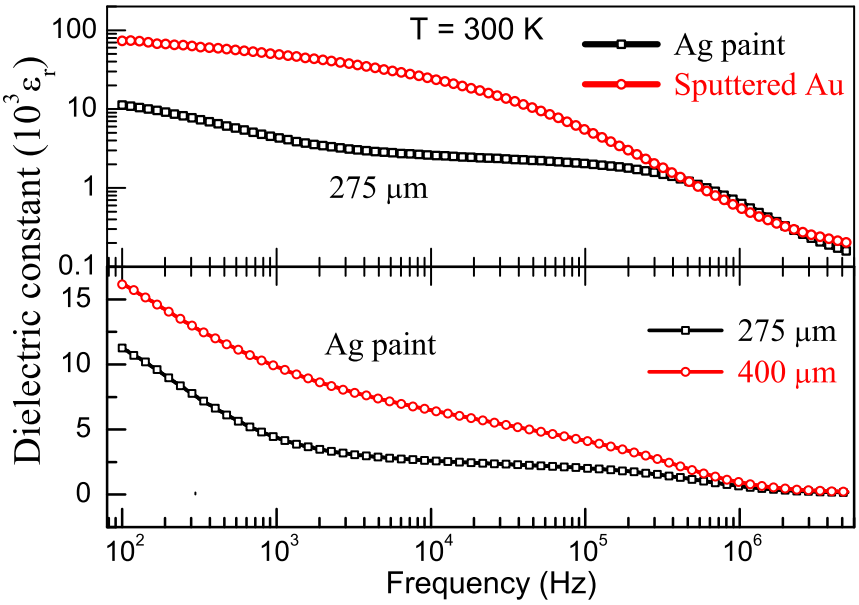

Figure 4.10: Extrinsic contribution as reflected in dielectric behavior in different electrodes (upper panel) and thickness variation (lower panel).

real axis and capacitance is replaced with a constant phase element CPE

$$Z_{CPE} = \frac{1}{C_{\mathrm{N}}(i\,\omega)^n} \tag{4.2}$$

where C_N is frequency independent term which acts like capacitance value and n signifies the deviation from the ideal capacitor behavior [158]. Simulated data (shown by solid lines) at 250 K using the above mentioned equivalent circuit shows good agreement with the experimental data. Inset (b) shows the same result zoomed at high frequency region. The value of n obtained for low and high frequency arcs are 0.76 and 0.93 respectively. As expeted, the high frequency value of n is close to unity which reflects the relaxation due to grain region.

4.4 Conclusions

$BiCr_{0.5}Mn_{0.5}O_3$ has been prepared at high pressure and high temperature. The material crystallizes in the centrosymmetric monoclinic structure (C2/*c*) similar to $BiCrO_3$ and undergoes a phase transformation to orthorhombic phase (P*nma*) around 640 K. The compound orders antiferromagnetically at 98 K below which two more anomalies are observed. Surprisingly, the material exhibits a giant dielectric constant at room temperature and two relaxation processes below 400 K. Low temperature relaxation process and giant dielectric constant is resulted from Maxwell-Wagner polarization at grain boundary whereas the relaxation at high temperature is attributed to conduction arising from oxygen defects. Impedance studies show that at low temperature dielectric response is dominated from grain and grain boundary whereas at higher temperatures electrode effects appears in the low frequency region. A good agreement was obtained between experimental and simulated data using a equivalent circuit consisting of two parallel C – R circuits connected in series.

CHAPTER 5

Temperature–induced Magnetization Reversal and Complex Magnetic Behavior in $Bi_{1-x}A_xFe_{0.5}Mn_{0.5}O_3$ (x = 0, 0.5 and A = La, Sr)[‡]

5.1 Introduction

Among the bismuth based transition metal oxides, $BiFeO_3$ received much attention because of its multiferroic properties with coupled ferroelectricity (T_{CE} = 1103 K) and magnetism (T_N = 640 K). However, below Néel temperature the compounds possess a spiral spin structure with wavelength of 620 Å which inhibits any macroscopic magnetization [93]. For strong magnetoelectric coupling, the coexistence of ferromagnetism and ferroelectricity is essential. One way to achieve ferromagnetism in theses oxides would be to design an ordered perovskite $Bi_2MM'O_6$ with two magnetic ions M and M′ at the B-site. With suitable choice, the rock-salt ordering of M and M′ ions can lead to ferromagnetic behavior according to Goodenough-Kanamori rule whereas stereochemical activity of $6s^2$ lone pair of Bi^{3+} ionss can induce ferroelectricity [10, 11, 40]. For example, Bi_2NiMnO_6 is ferroelectric as well as ferromagnetic where the rock-salt type of ordering between Ni^{2+} and Mn^{4+} gives a ferromagnetic behavior below 140 K and ferroelectricity appears due to Bi^{3+} lone pair below 485 K [135, 136]. Also, the ambient pressure synthesized $Bi_2Ni_{2/3}Mn_{4/3}O_6$, though disordered, was found to be polar [159]. An essential condition to form double perovskite is to have charge dif-

[‡]Work has appeared in *Phys. Rev. B.*, 82, 100416R (2010) and *RSC Adv.* 2, 292 (2012).

ference of 2 - 6 and/or size difference between the B-site cations [160, 161]. Despite close ionic radii, an ordered structure has been stabilized between Fe^{3+} – Mn^{3+} and Fe^{3+} – Cr^{3+} ions using epitaxial constrain. Ueda *et. al.* have reported ordering between Fe^{3+} and Cr^{3+}/Mn^{3+} in $LaFeO_3$ – $LaCrO_3$ superlattices and epitaxial thin film of $LaFe_{0.5}Mn_{0.5}O_3$ [162, 163]. Ordering of trivalent Fe and Cr ions was also confirmed in epitaxial thin films of multiferroic Bi_2FeCrO_6 as predicted from first principle calculations [92, 138, 139].

In this work, we have chosen two most studied multiferroic perovskite of $BiFeO_3$ and $BiMnO_3$ to form an ordered perovskite. As mentioned previously, $BiFeO_3$ can be synthesized at ambient pressure and posses a rhombohedral structure ($R\bar{3}c$). The compound is ferroelectric (T_{CE} = 1103 K) and antiferromagnetic (T_N = 643 K) at room temperature. The high pressure monoclinic phase of $BiMnO_3$ is ferromagnetic at low temperature (T_C = 105 K) whereas ferroelectricity is still controversial. Our aim in thus study to prepare an ordered compound Bi_2FeMnO_6 where lone pair effect of Bi ion can induce ferroelectricity and superexchange interaction between Fe^{3+} and Mn^{3+} would give rise to a ferromagnetic behavior following Goodenough-Kanamori rule.

The compound $BiFe_{0.5}Mn_{0.5}O_3$ is found to be crystallized in orthorhombic structure with a possible space group $Pn2_1m$. Contrary to our anticipation, the trivalent Fe and Mn ions do not order in a rock-salt manner but rather a double zig-zag type of ordering is indicated from electron diffraction studies. Although our aim in this study was to design a multiferroic material but most surprisingly we observed negative magnetization below a compensation temperature (T^*). More importantly, magnetic switching behavior can be observed below T^* implying possible applications in memory related devices.

Absence of rock-salt type ordering between the B-site cations leads to the presence of Fe – O – Fe, Fe - O - Mn and Mn - O - Mn superexchange interactions. The antiferromagnetically coupled canted moments of Fe - Fe and Fe - Mn give rise to a ferrimagnetic like ground state and the competition between these results in negative magnetization. When La or Sr is substituted at the Bi-site of $BiFe_{0.5}Mn_{0.5}O_3$, the structure changes to rhombohedral (space group $R\bar{3}c$). None of these compounds exhibits negative magnetization indicating important role of orthorhombic distortion. $Bi_{0.5}Sr_{0.5}Fe_{0.5}Mn_{0.5}O_3$ (BSFMO) shows a complex magnetic behavior below Néel temperature (T_N = 226 K) whereas $Bi_{0.5}La_{0.5}Fe_{0.5}Mn_{0.5}O_3$ (BLFMO) is a canted antiferromagnet (T_N = 220 K).

5.2 Experimental

As $BiMnO_3$ is a high pressure phase, attempt to prepare $BiFe_{0.5}Mn_{0.5}O_3$ at ambient pressure was not successful and thus high pressure technique was adopted. Polycrystalline samples were prepared at high pressure and high temperature using cubic anvil type apparatus (RIKEN CAP 07) as discussed in chapter 2. The starting oxides Bi_2O_3, Fe_2O_3, MnO and MnO_2 were mixed in stoichiometric amounts and loaded in a gold capsule. The pressed gold capsule was subjected to 4.5 GPa pressure and heated to 1073 K for 2 hours and slowly cooled down to room temperature and thereafter the pressure was released slowly. Polycrystalline samples of BSFMO and BLFMO have been prepared using solid state reaction route at ambient pressure. Stoichiometric amounts of Bi_2O_3, $SrCO_3$, Fe_2O_3 and Mn_2O_3 were mixed and ground intimately and then heated between 1073 and 1273 K in air with several intermittent grindings. At the final stage, the powder was pelletized and sintered at 1373 K for 12 hours and cooled slowly at a

rate of 3 deg/min. BLFMO was prepared using La_2O_3 preheated at 1223 K and final sintering was done at 1173 K for 12 hrs. Room temperature X – ray data were collected with a Bruker D8 Advance diffractometer. Neutron data for BSFMO and BLFMO were collected at various temperatures with the high resolution powder diffractometer D2B at ILL using wavelength of 1.594 Å. Rietveld refinements were carried out from the X – ray and neutron data using a software package Fullprof [109]. Transmission electron microscopy (TEM) has been carried out using a Tecnai G2 30 UT microscope operated at 300 kV and having point resolution 0.17 nm. For TEM study, the samples were crushed in n-butanol and deposited on a holey carbon membrane supported by a copper grid. Mössbauer spectra were recorded in transmission mode using ^{57}Co γ -ray source in a Rhodium matrix and multi – channel analyzer. The sample thickness was adjusted to obtain Fe content of $\sim$10 mg/cm^2. The calibrations for velocity and isomer shift were performed using iron (Fe) foil. The Mössbauer spectra were analyzed using SITE and DIST options in WinNormos-for-Igor software package. The magnetic properties were studied using a vibrating sample magnetometer (VSM) in Physical Property Measurement System (PPMS), Quantum Design, USA.

5.3 Results and discussion

5.3.1 Structure

Analysis of powder X – ray diffraction (PXRD) pattern of the powder sample showed that the major phase is a perovskite. Profile fit on the room temperature data is shown in figure 5.1 (top panel). The presence of small amount (< 5 %) of secondary phase was detected and identified to be one of the oxygen non – stoichiometric phases of $BiMnO_3$.

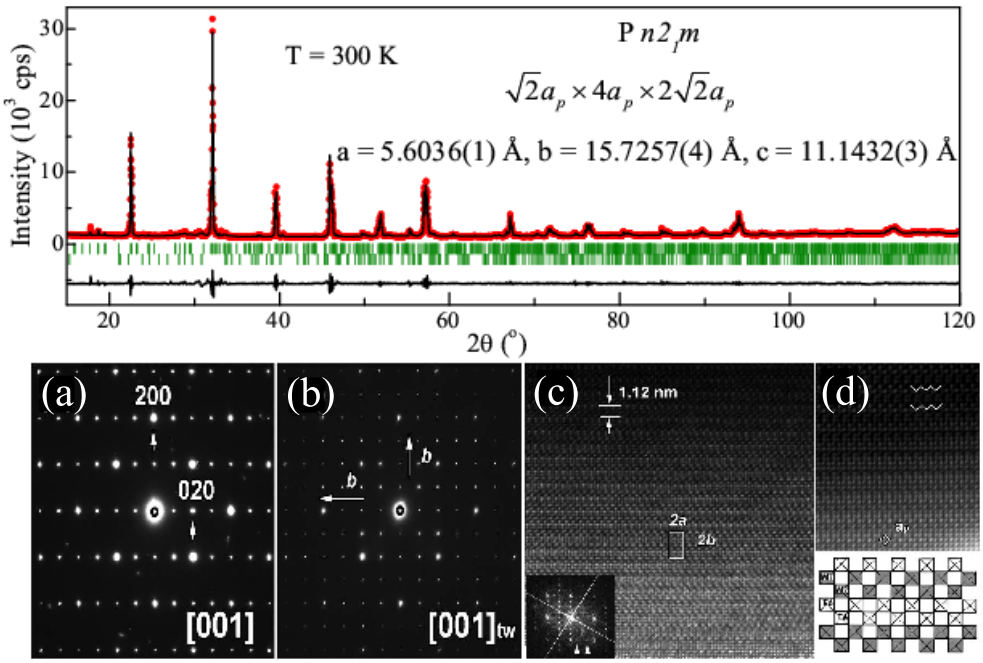

Figure 5.1: (Top panel) Profile fit of room temperature X-ray diffraction data of $BiFe_{0.5}Mn_{0.5}O_3$. Filled circles are the experimental points, solid line represents the calculated pattern, vertical ticks represent the Bragg positions and the difference between experimental and calculated curves is shown by line below the Bragg positions. (Lower panel) ED pattern (a) untwined and (b) permutation twinned, (c) High Resolution TEM image along [001] and corresponding FT pattern. Note the white arrows which point spots due to twinning. (d) Enlargement of the image: double zigzag rows of bright dots alternate with darker double rows, interpreted as ordering of double rows of MnO_6 and FeO_6 octahedra.

It should be mentioned that the samples prepared using Mn_2O_3 as starting material had higher amount of impurity phase and thus MnO and MnO_2 were used [130]. In the perovskite structure, Fe and Mn ions at the B – site can either be disordered or arranged in a rock – salt/layered configuration to form a double perovskite. Mössbauer experiments at room temperature revealed that iron is present in Fe^{3+} state, which requires manganese also be present in Mn^{3+} state assuming that the compound is oxygen sto-

ichiometric. Energy dispersive spectroscopy (EDS) analysis performed on numerous micro – crystals of the perovskite shows that the cationic composition does not vary from one crystal to the other and is close to the nominal composition of the sample, i.e. '$Bi_{1.09}Fe_{0.46}Mn_{0.45}$'. The profile fit confirms that the major phase can be indexed by an orthorhombic cell, with the lattice parameters of the type of $\sqrt{2}a_P \times 2\sqrt{2}a_P \times 4a_P$ (a_P = cubic lattice constant) as reported in $Bi_2Mn_{4/3}Ni_{2/3}O_6$ [159] and $BiFe_{1-x}Mn_xO_3$, x= 0.2 – 0.6 [164]. Lattice parameters obtained from the refinement are a = 5.562(2) Å, b= 11.191(2) Å and c= 7.845(2) Å consistent with a previous report [164]. The electron diffraction study confirms the perovskite sub – cell and the two lattice parameters $a \approx \sqrt{2}\, a_p$, $b = 2\sqrt{2}\, a_p$, as shown from the [001] ED pattern of this phase (figure 5.1 a). The corresponding [001] HRTEM image (figure5.1 c) suggests that the Mn^{3+} and Fe^{3+} cations are not distributed at random in the structure but may form double zigzag rows (figure 5.1 d), running along b axis. Such an arrangement of these cations with same charge may be due to Jahn – Teller distortion associated with Mn^{3+} ions that results in distortion of MnO_6 octahedra which is different from FeO_6 octahedra. Nevertheless, multitwinning phenomena take place in the crystal (figure 5.1 b) and prevent the c parameter to be established with certainty and this oxide does not show a 1:1 ordering of Mn^{3+} and Fe^{3+} classically observed in double perovskite [160, 161].

5.3.2 Magnetic properties

Figure 5.2 shows a plot of magnetization against temperature under field – cooled (FC) conditions at an applied field of ±50 Oe. It is clearly seen from the bottom inset of this figure that the magnetic ordering occurs at 270 K in both positive and negative applied

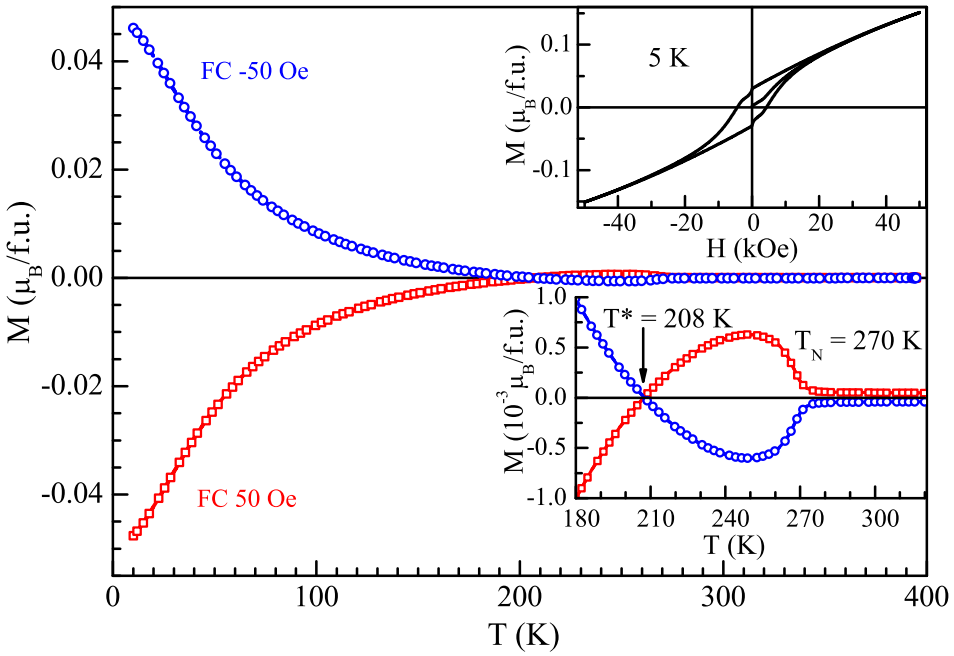

Figure 5.2: Magnetization as a function of temperature recorded at ±50 Oe under field-cooled (FC) process exhibiting magnetization reversal. Insets show the magnetic ordering temperature (lower panel) and a weak ferromagnetic hysteresis at 5 K (upper panel).

fields. The magnetization value expressed in μ_B/f.u. suggests an antiferromagnetic ground state with spin canting. This is consistent with the fact that Fe^{3+} and Mn^{3+} ions are not ordered and thus would result in antiferromagnetic ordering. If these B – site ions were ordered as rock – salt type, one would expect a ferromagnetic ordering according to the Goodenough – Kanamori rule as in the case of La_2NiMnO_6 (T_C = 280 K) [81, 165]. In order to further understand the magnetic ground state, isothermal magnetization M(H) data were recorded at 5 K and the result is shown in the upper inset of figure 5.2. As can be seen that M(H) data exhibits a hysteresis loop with a low value of remnant polarization of 0.03 μ_B/f.u. and a coercive field of 4.3 kOe. Further, the magnetization does not saturate even at 50 kOe field and the unsaturated magnetization

obtained by extrapolating the linear magnetization to the ordinate is 0.05 μ_B/f.u. This value is much lower than that expected for a ferromagnetic ordering of Fe^{3+} (S = 5/2) and Mn^{3+} ions (S = 2) through the Fe^{3+} – O – Mn^{3+} superexchange interaction but rather close to weak ferromagnetic or canted antiferromagnetic behavior. As Fe^{3+} and Mn^{3+} ions are not ordered in a rock-salt manner, we expect Fe – O – Fe, Mn – O – Mn and Fe – O – Mn superexchange interactions to be present in this system. Since this compound contains equal proportion of Fe and Mn ions, one would expect a dominant Fe – O – Mn interaction. In such a disordered system, the Fe - Fe and Mn - Mn would act as a impurity cluster present in the host matrix of Fe - Mn. The impurity clusters of Fe - Fe or Mn - Mn would would retain the magnetic behavior of its parent compounds $BiFeO_3$ and $BiMnO_3$ in the structure of host matrix of Fe - Mn [166]. Above the magnetic ordering, the susceptibility could be fitted with the Curie – Weiss law and effective paramagnetic moment obtained from the fit is 4.01 μ_B, which is lower than the expected spin only value of 5.43 μ_B. The value of Weiss temperature was found to be positive ($\theta_P = +106$ K). This is in conflict with the antiferromagnetic ground state and reflects a dominant ferromagnetic Fe – O – Mn superexchange interaction [167].

5.3.2.1 Temperature-induced magnetization reversal

The most noteworthy observation is that the sign of magnetization becomes negative below a compensation temperature (T^* = 208 K) under an applied field of +50 Oe while it is positive under -50 Oe. The two magnetization curves exhibit a mirror like behavior (figure 5.2). This phenomenon is known as temperature – induced magnetization reversal or negative magnetization. With increasing (positive) magnetic field, T^* decreases

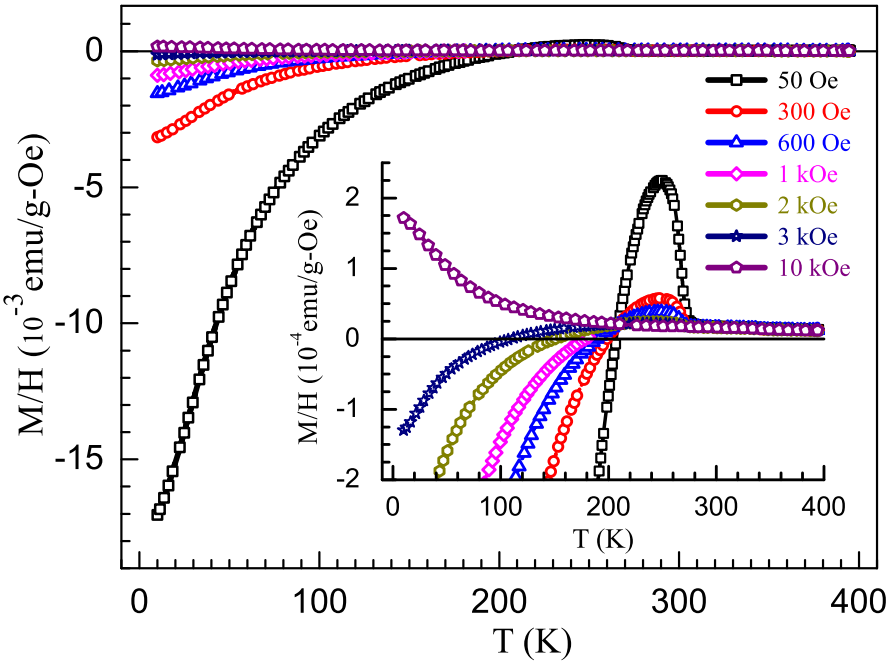

Figure 5.3: Magnetization versus temperature measured at different magnetic fields showing the decrease of T^* with increasing magnetic field. At 10 kOe, the magnetization switches to positive value.

and the magnetization changes from negative to positive value at high enough fields as shown in figure 5.3. This suggests that below T^*, the net magnetic moment initially aligned against the applied magnetic field is oriented along the applied direction at high magnetic fields.

The phenomenon of magnetization reversal or negative magnetization is known for more than five decades [141, 168–178]. Negative magnetization implies that the magnetic moments are aligned opposite to the applied field which is normally associated with high energy compared to the parallel alignment of magnetic moments. As early as 1948, Néel predicted that certain ferrimagnetic materials such as spinel oxides can exhibit negative magnetization due to different temperature dependence of sublattice

magnetization arising from different molecular fields acting on the magnetic ions in two different crystallographic sites [179]. As a result, it is possible that the magnetizations of different sublattices cancel each other, rendering the material to exhibit a net zero magnetization at a characteristic temperature called compensation temperature (T^*). Above and below this temperature, magnetization is dominated by one type of sublattice and the sign of the magnetization changes from positive to negative or vice versa. This behavior was experimentally observed in lithium chromium ferrite, cobalt vanadate and some garnets [168–170]. Few molecular ferrimagnets which are analogs of Prussian – blue, show negative magnetization with one or two compensation temperatures depending on the number of magnetic elements mixed at various crystallographic sites [174, 175]. Using neutron diffraction study, Yusuf *et al* gave a microscopic model and demonstrated that these molecular ferrimagnets can be promising for practical applications [180, 181]. In a weak ferrimagnetic compound nickel format dehydrate $Ni(HCOO)_2.2H_2O$, the non-equivalent Ni ions constitute two canted antiferromagnetic sublattices and competition of which gives rise to magnetization reversal [176, 177].

The ferromagnetic Laves – phase $SmAl_2$ with the cubic structure shows zero magnetization due to the large orbital magnetic moment of Sm^{3+} ions aligned anti – parallel to the spin moment [182]. Since then this phenomenon has been observed in other classes of materials where the mechanism proposed is different from that suggested for ferrimagnetic systems. Antiferromagnetic orthovanadates, RVO_3 (R = La, Ce, Nd, Sm etc.) are reported to show negative magnetization even though all the V^{3+} ions occupy only one crystallographic site and thereby cannot be classified into Néel's model for ferrite spinels [172, 173, 183–186]. Various explanations have been offered for the behavior

of rare – earth orthovanadates. For example, in $LaVO_3$, it is suggested that the canted spin moment reverses upon crossing the first – order structural transition at 138 K below which the orbital angular moment is maximized [173]. In YVO_3, multiple temperature induced magnetization reversal is reported, the origin of magnetization reversal being considered to arise from the competition between single ion magnetic anisotropy and antisymmetric Dzyaloshinskii – Moriya (DM) interaction [186, 187]. In antiferromagnetic chromites, such as $GdCrO_3$, $La_{1-x}Pr_xCrO_3$ and $La_{0.75}Nd_{0.25}CrO_3$, negative magnetization is attributed to the polarization of paramagnetic rare – earth moments opposite to the canted Cr^{3+} moments [188–190]. Recently, in $(La_{1-x/2}Bi_{x/2})(Fe_{0.5}Cr_{0.5})O_3$, where the magnetic ions Fe^{3+} and Cr^{3+} occupy single crystallographic site, shows negative magnetization at high temperatures [191].

5.3.2.2 Pole reversal

In order to demonstrate spin reversal phenomenon, magnetic switching experiments have been performed at few temperatures below T^* and the results at 175 K are shown in figure 5.4. In this experiment, the sample was first cooled to a particular temperature under 50 Oe field and then the field was increased to 1725 Oe in order to switch the magnetization to an equivalent and a positive value. This process was cycled several times to examine reproducibility of the switching behavior. It is clear from the figure that the magnetization can be switched between a positive and a negative value reversibly by just increasing the field to a nominally large field. In contrast to a ferromagnetic system, where two stable polar states are switched by changing the direction of the applied field, in the present case the polarity can be switched to any value by changing the field

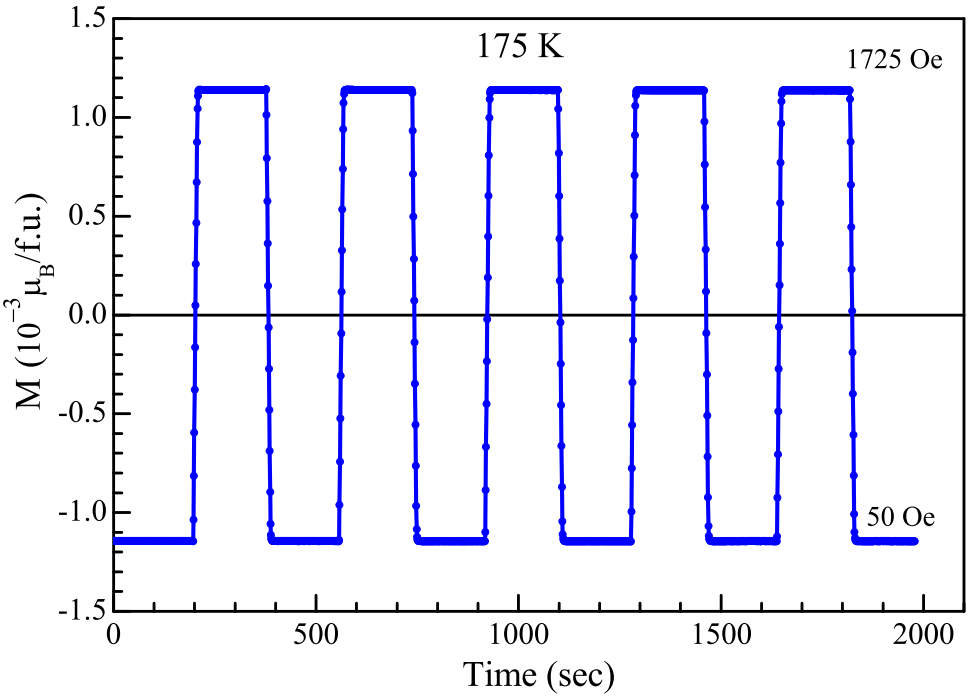

Figure 5.4: Magnetization versus time showing the reversal of magnetization with change in magnetic fields at 175 K.

in the same direction. It is important to explore whether such a phenomenon would be useful in device applications. A similar demonstration of spin reversal has recently been shown in a Prussian blue molecular magnet by Yusuf *et al* [181].

5.3.2.3 Zero field cooled measurements: Role of remnant magnetic field

It should be mentioned that the observation of magnetization reversal in this material is intrinsic as these measurements are carried out under field-cooled condition. However, care must be taken while performing zero-field-cooled measurements where a negative remnant field present in the superconducting magnet can result in negative magnetization [192]. At this point it is important to address the non-equilibrium zero-field-cooled

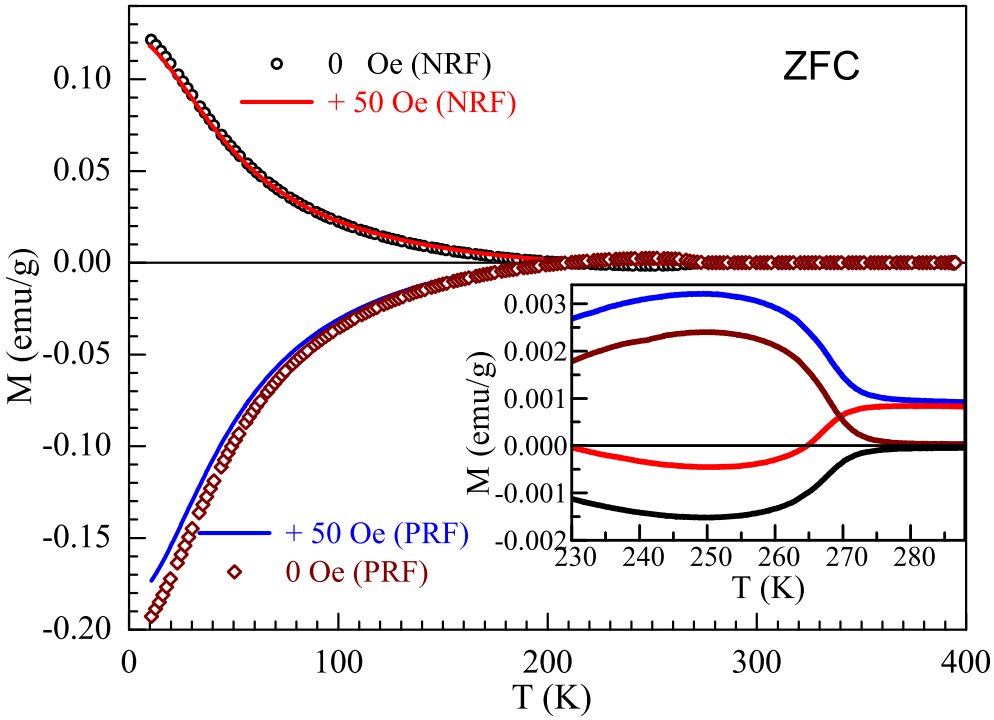

Figure 5.5: Zero field cooled magnetization curves under ± 50 Oe at showing remnant field effect of superconducting magnet. Inset shows the same zoomed for clarity in the paramagnetic state. Please note that the magnitude of moment in the paramagnetic state indicates the sign of the remnant field.

(ZFC) magnetization of $BiFe_{0.5}Mn_{0.5}O_3$ to demonstrate that the reversal of magnetization is true and not a measurement field (NRF) and a positive remnant field (PRF) in presence as well as in the absence of an applied field as shown in figure 5.5. It can be seen that the data obtained under a PRF and a PRF with an applied field of +50 Oe exhibit negative magnetization similar to that is seen in the case of FC measurement under +50 Oe (figure 5.2). In the case of the ZFC magnetization measured under a NRF, the presence of a NRF is obvious from the inset of the figure 5.5 where the magnetization is negative above the magnetic ordering temperature. The overall magnetization is, therefore similar to that of the FC magnetization measured under -50 Oe (figure 5.2). In the

present case, the ZFC magnetization measured under +50 Oe but cooled under a NRF shows a similar behavior exhibited for NRF (figure 5.5) and -50 Oe (figure 5.2) except above the magnetic ordering temperature or in the paramagnetic state where the magnetization is positive. We therefore confirm that the ZFC magnetization data measured under a zero applied field (0 Oe) and +50 Oe with the sample cooled under a NRF are not intrinsic to the sample. In order to avoid this issue, prior to each ZFC measurement the field should be oscillated to from a negative value (30 kOe). It may be mentioned here, for a FC measurement under applied fields much larger than the remnant field, the sign of the remnant field does not matter except that the exact field value would be lower or higher than the applied field by a value equivalent to the remnant field.

5.3.2.4 Origin of magnetization reversal

To understand the origin of negative magnetization in $BiFe_{0.5}Mn_{0.5}O_3$, first of all, it is essential to know the crystallographic arrangement of magnetic ions. As discussed above, iron and manganese ions are not 1:1 ordered and both of these ions occupy a single crystallographic site 8*d* which is consistent with the antiferromagnetic ground state. These facts rule out the mechanism proposed by Néel for ferrimagnetic systems involving two or more different crystallographic sites. The present compound is similar to recently reported cation disordered perovskite $(La_{1-x/2}Bi_{x/2})(Fe_{0.5}Cr_{0.5})O_3$ where the magnetization reversal was explained based on clusters of canted antiferromagnetic $La_{1-x}Bi_xFeO_3$ and $La_{1-x}Bi_xCrO_3$ which are coupled antiferromagnetically through dipolar interaction [191]. These clusters with different magnetization vary independently with temperature and results in compensation. This model may not be

applicable to the present compound because one of the end members, $BiFeO_3$ is antiferromagnetic ($T_N \sim 640$ K) with a rhombohedral structure while the other end member, $BiMnO_3$ is ferromagnetic ($T_C \sim 105$ K) with a highly distorted monoclinic structure. Previously, we argued that the reversal origin is similar to that of suggested for single crystalline YVO_3 and $Y(Fe,Cr)O_3$ both possessing orthorhombic (P*nma*) structure [171, 186]. In these oxides magnetization reversal was explained in terms of competing single ion magnetic anisotropy and antisymmetric DM interactions [186, 193, 194].

The parent compound $BiFeO_3$ is a canted antiferromagnet due to the antisymmetric DM interaction [95]. The Mn substitution at the Fe site not only changes the structure from rhombohedral to orthorhombic where the oxygen octahedra are highly distorted but also introduces large magnetic anisotropy [195, 196]. Also, as mentioned previously, absence of B-site ordering gives rise to Fe - Fe, Fe - Mn and Mn - Mn superexchange interactions which would order at the Néel temperature of respective parent compounds $BiFeO_3$, $BiFe_{0.5}Mn_{0.5}O_3$ and $BiMnO_3$ [166]. The Fe - Fe orders at very high temperature (T_N=640 K) whereas Mn - Mn orders at low temperature (T_C = 105 K for $BiMnO_3$ and T_N = 42 K for o-$YMnO_3$) [124, 197, 198]. Since the Mn - Mn ordering occurs at very low temperature ($\sim$ 100 K), the compensation is believed to occur due to antiferromagnetic coupling of canted Fe - Fe and Fe - Mn moments. These two canted moments act as two sublattice magnetizations and results in a ferrimagnetic like ground state. This will be discussed in more detail in the next chapter in context of magnetization reversal in $YFe_{1-x}Cr_xO_3$ and $YFe_{1-x}Mn_xO_3$ [166, 199]. In fact, it will be demonstrated that the magnetization reversal is a common phenomenon in many perovskites with magnetic ions with different magnetic anisotropy disordered

at the B-site. It has also been observed that all these canted antiferromagnetic oxides exhibiting reversal phenomenon have orthorhombic structure [191, 199–201]. To probe the role of structure, we have extended this study and synthesized the present compound at ambient pressure by A-site substitutions with La and Sr as discussed in the next section.

5.3.3 Structure and complex magnetic behavior of $Bi_{0.5}A_{0.5}Fe_{0.5}Mn_{0.5}O_3$; A = Sr, La

The high pressure phases of Bi perovskite can sometime be stabilized at ambient pressure by A or B-site modification. For example La or Sr substitution at the Bi-site of $BiMnO_3$ or $BiCrO_3$ could be synthesized by solid state route at ambient pressure [202–204]. In order to support the role of anisotropy and structure in magnetization reversal, we have chosen two closely related compound $Bi_{0.5}A_{0.5}Fe_{0.5}Mn_{0.5}O_3$ where A = Sr and La. While in La substituted compound, both Fe and Mn ions are expected to be in trivalent states, in case Sr substitution Fe and Mn ions would to be present in trivalent and tetravalent states respectively. Thus, it would be interesting to study and compare the systems $Bi^{3+}_{0.5}Sr^{2+}_{0.5}Fe^{3+}_{0.5}Mn^{4+}_{0.5}O_3$ (BSFMO) and $Bi^{3+}_{0.5}La^{3+}_{0.5}Fe^{3+}_{0.5}Mn^{3+}_{0.5}O_3$ (BLFMO) having the spin configurations d^5 - d^3 and d^5 - d^4 respectively. The compound BLFMO with an an orthorhombic structure (SG P*nma*) was reported to have and show multiferroic properties at low temperature whereas BSFMO is known to have rhombohedral structure[205, 206]. The physical properties of BSFMO in particular are discussed in detail.

5.3.3.1 Crystal and magnetic structure

Indexing of room temperature powder X-ray data of BSFMO and BLFMO suggested a rhombohedral symmetry though earlier studies based on X-ray diffraction showed BLFMO to have an orthorhombic structure [205]. We performed Rietveld refinements on the room temperature X-ray data with R3c and R$\bar{3}c$ space groups. A slightly better χ^2 and low values of estimated error in the refined parameters were obtained for the centrosymmetric space group R$\bar{3}c$ for both the compounds which is consistent with a previous report on BSFMO [206]. The lattice parameters and the atomic positions obtained from X-ray data were used as initial parameters for the Rietveld refinement on the neutron data. The rhombohedral phase R$\bar{3}c$ in BSFMO persists over a wide temperature range (100 to 923 K) as confirmed from low and high temperature X-ray data (not shown).

The absence of super-lattice reflection in X-ray and neutron diffraction patterns suggests no A-site ordering between Bi and Sr cations or B-site ordering between Fe and Mn ions. A weak broad peak around $2\theta \sim 20^\circ$, where there is no nuclear Bragg reflection, could be seen in neutron data at 300 K for both compounds which develops into a clear reflection with increased intensity at low temperatures as shown in figures 5.6 and 5.7. Presence of a broad peak at 300 K might be due to short range magnetic interactions of Fe - Fe which orders at quite high temperature [166]. Our attempt to refine site occupancies of Bi^{3+} and Sr^{2+} ions gave unrealistic values with large errors which may be due to the close neutron scattering lengths of 8.53 and 7.02 fm respectively. Further, Rietveld refinement on room temperature X-ray data showed site occupancies of Bi and Sr to be close to 1:1 ratio and therefore site occupancies of Bi and Sr (La) were fixed

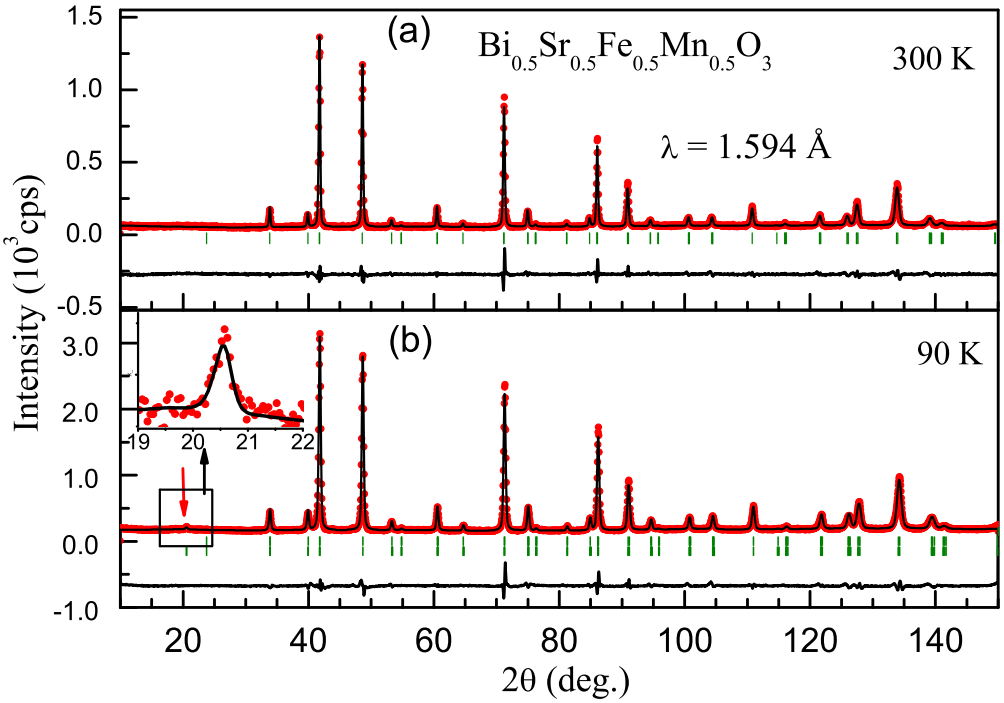

Figure 5.6: Rietveld refinement on the neutron data of $(Bi_{0.5}Sr_{0.5})(Fe_{0.5}Mn_{0.5})O_3$ collected at 300 and 90 K.

Table 5.1: Lattice parameters, atomic positions and other parameters of $Bi_{0.5}Sr_{0.5}Fe_{0.5}Mn_{0.5}O_3$ and $Bi_{0.5}La_{0.5}Fe_{0.5}Mn_{0.5}O_3$ obtained from Rietveld refinements of powder neutron (NPD) diffraction data at 300 K and low temperatures. Bi/Sr(La) occupy 6*a* (0,0,0.25) and Fe/Mn occupy 6*b* (0, 0, 0) positions whereas O takes the general position 18*e* (x, 0, 0.25)

Parameter	$Bi_{0.5}Sr_{0.5}Fe_{0.5}Mn_{0.5}O_3$		$Bi_{0.5}La_{0.5}Fe_{0.5}Mn_{0.5}O_3$	
a (Å)	5.4817(2)	5.4810(1)	5.5275(1)	5.5206(1)
c (Å)	13.4107(5)	13.4029(3)	13.5006(3)	13.4808(2)
x_O	0.4693(2)	0.4652(2)	0.4537(3)	0.5462(2)
B_{iso} Bi/Sr(La)	2.05(5)	1.79(3)	2.27(5)	1.89(4)
B_{iso} Fe/Mn	0.31(10)	0.10(70)	0.86(9)	0.20(6)
B_{iso} O	1.59(3)	1.42(2)	2.19(4)	1.90(2)
χ^2	3.99	6.80	8.36	9.61
R_p	25.4	16.4	24.4	21.7
R_{wp}	18.7	13.2	19.0	18.0
R_B	7.01	5.06	11.0	9.90
R_f factor	6.76	4.69	9.50	7.49

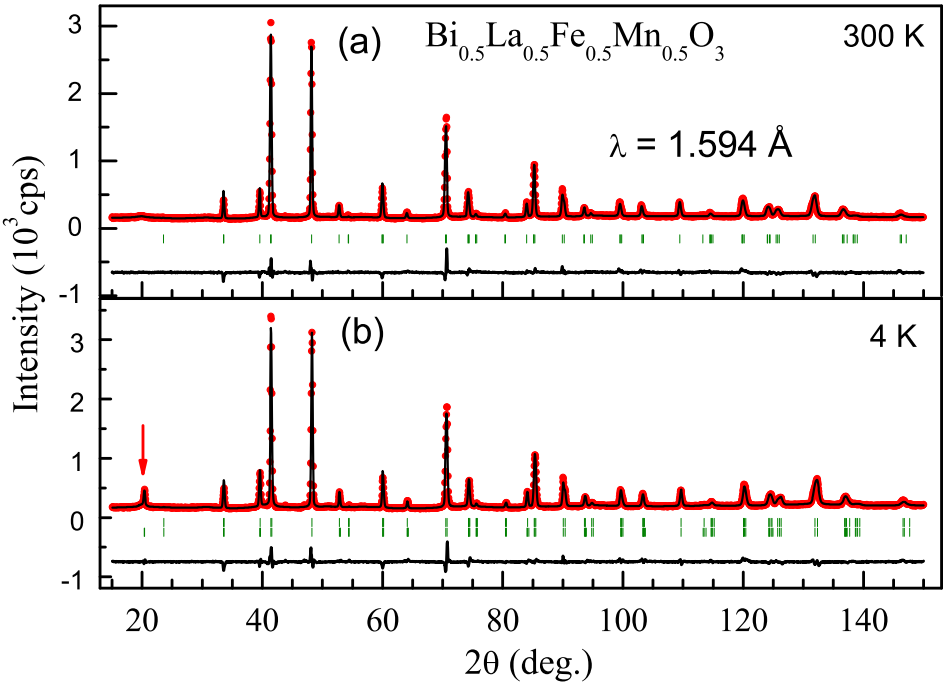

Figure 5.7: Rietveld refinement on the neutron data of $(Bi_{0.5}La_{0.5})(Fe_{0.5}Mn_{0.5})O_3$ collected at 300 and 4 K.

Table 5.2: Selected bond lengths (Å) and angles (°) of BSFMO and BLFMO

Parameter	BSFMO		BLFMO	
	300 K	90 K	300 K	4 K
Bi/Sr(La) - O	2.909(1)×3 2.573(2)×3 2.744(8)×6	2.931(1)×3 2.550(2)×3 2.744(1)×3	2.508(2)×3 2.770(2)×6	2.506(1)×3 2.766(1)×6
Fe/Mn - O	1.945(1)×6	1.946(2)×6	1.969(1)×6	1.966(1)×6
Fe/Mn-O-Fe/Mn	170.071(10)×4	168.744(2)×4	165.064(9)×4	165.13(1)×4

whereas the occupancies of Fe and Mn sites were refined and found to be stoichiometric. These facts are in accordance with energy-dispersive X-ray spectroscopy (EDX) data collected at various spots. Also, the refinement of oxygen occupancy does not deviate significantly from the stoichiometric value and therefore was kept fixed. Figure 5.6b and 5.7b shows the Rietveld refinements on the neutron data for BSFMO

and BLFMO collected at 90 and 4 K, respectively. In figure 5.6b, the magnetic reflection near $2\theta \sim 20^{\circ}$ has been zoomed in for clarity. This reflection is rather weak which may be due to the fact that the data was collected at relatively higher temperature (90 K). The magnetic reflections in the low temperature neutron diffraction patterns (shown by arrows) were modelled by G-type antiferromagnetic coupling of disordered Fe/Mn moments aligned along the c-axis of the hexagonal lattice. Though the magnitudes of the magnetic moments associated with Fe^{3+} (S=5/2) and Mn^{4+} or Mn^{3+} (S=3/2 or S=2) ions are different, due to the fact that these ions are distributed randomly, it is difficult to determine finite magnetization, if any, using thermal neutrons. The average magnetic moments of Fe/Mn in BSFMO (90 K) and BLFMO (4 K) are 1.11(8) μ_B and 1.30(3) μ_B respectively which are much lower than their respective theoretical values. Results from Rietveld refinement of neutron diffraction data have been summarized in table 5.1 and 5.2.

5.3.3.2 Valence states

It is important to verify the valence state of the B-site cations as it plays a significant role in determining properties particularly in compounds containing manganese. In $LaMnO_3$, the valence state of the manganese ions depends on the synthesis conditions which determine stoichiometry of the compound [207]. While the valence state of manganese in stoichiometric $LaMnO_3$ is +3, the cation and/or oxygen non-stoichiometry leads to a mixed valence of Mn^{3+}/Mn^{4+} [208]. In order to examine the valence state of state of Fe, we performed Mössbauer experiments at room temperature and the results are shown in figure 5.8. Mössbauer spectra plotted with velocity along the *x*-axis

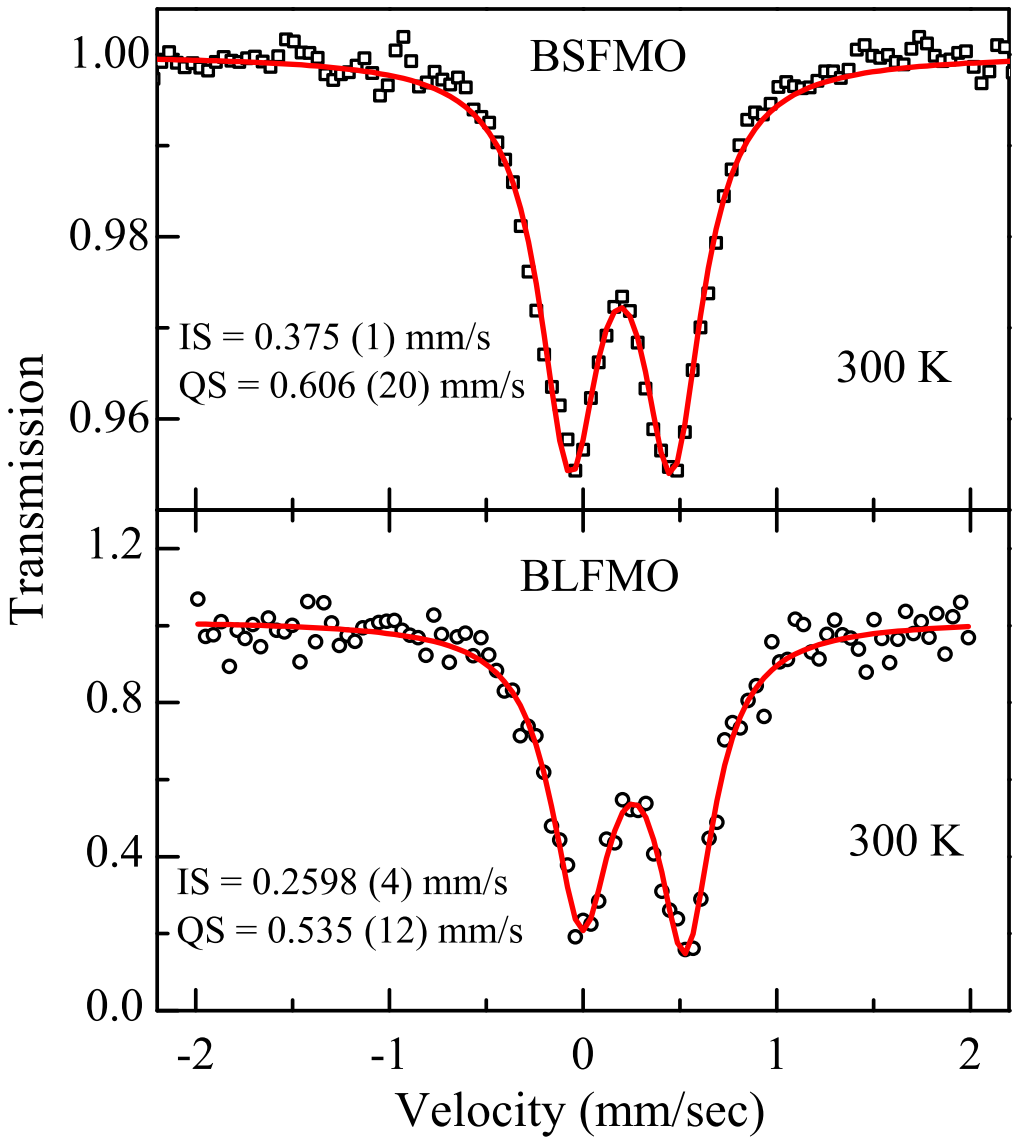

Figure 5.8: Room temperature Mössbauer spectra of (a) $Bi_{0.5}Sr_{0.5})(Fe_{0.5}Mn_{0.5})O_3$ and (a) $Bi_{0.5}La_{0.5})(Fe_{0.5}Mn_{0.5})O_3$

and relative transmission of the γ-rays along the y-axis. In order to obtain the values of isomer shifts (IS or δ) and quadrupole splitting (QS or Δ), the spectra were fitted to a doublet consisting of a pair of Lorentzians, the fit has been shown as a thick line passing through the open symbols. The fit results δ = 0.375 (1) mm/sec and Δ = 0.61 (2) mm/sec for BSFMO. Similar analysis carried out for BLFMO has resulted

in the IS and QS values as δ = 0.259 (1) mm/sec and Δ = 0.54 (1) mm/sec. These values are consistent with those reported for similar compounds in the literature and thus confirm the presence of Fe^{3+} ions in paramagnetic state [209]. The valence state of manganese in the present compound can indirectly be inferred from the inspection of average Fe/Mn-O bond lengths in BSFMO and BLFMO (table 5.2). It can be noticed that the average Fe/Mn-O bond length in the former (1.945(1) Å) is smaller than that in the latter (1.969(1) Å). Since Fe ions are present in trivalent in both the compounds, the smaller average Fe/Mn-O bond length suggests that Mn ions are present in the tetravalent state in BSFMO and in the trivalent state in BLMFO.

5.3.3.3 Cluster and spin-glass behavior in BSFMO

DC magnetization data of the compound BSFMO were collected in zero field cooled (ZFC) and field cooled (FC) modes. In ZFC mode, the sample was cooled in absence of magnetic field whereas a field was applied while cooling in the FC mode and data were recorded while warming up in both the cases. The ZFC-FC data under a magnetic field of 100 Oe is shown in figure 5.9. Three anomalies are observed at 30, 114 and 226 K in the ZFC data. The antiferromagnetic ordering of Fe^{3+} and Mn^{4+} takes place below T_N = 226 K. In should be mentioned here that the magnetic properties are highly dependent on the sample preparation. The cooling rate at the final stage of sintering was 3 deg/min and when this rate changed to higher or lower value, Curie-Weiss behavior is not observed above T_N similar to a previous report [206]. As can be seen from the figure, ZFC-FC shows a large irreversibility which might indicate a glassy state below T_N. Moreover, as the field is increased, the anomalies below T_N shift towards lower

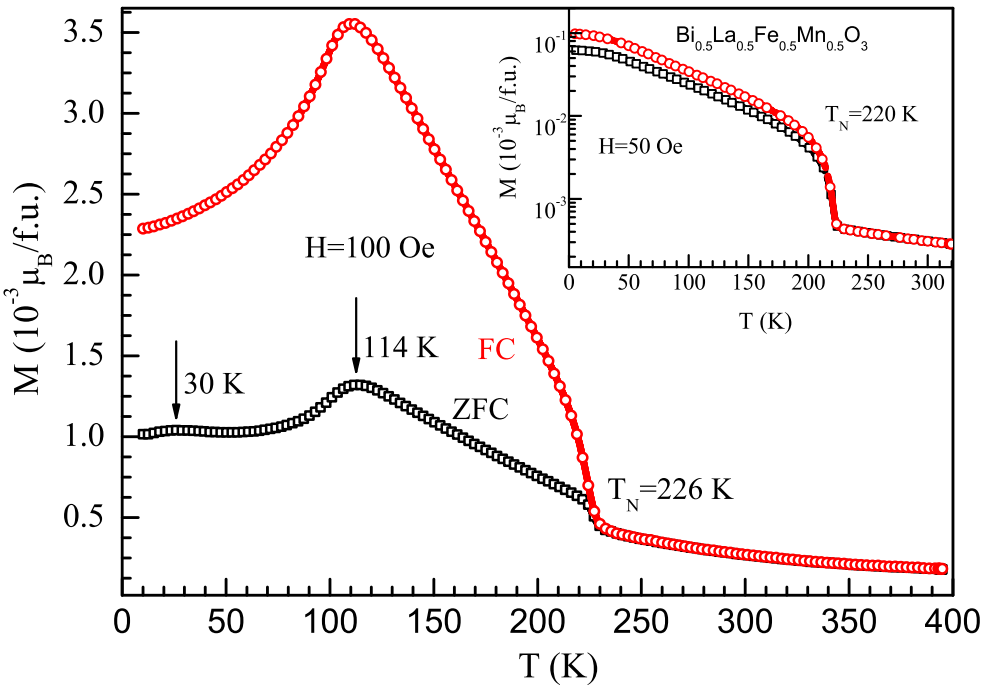

Figure 5.9: ZFC-FC curves under magnetic field of 100 Oe for $(Bi_{0.5}Sr_{0.5})(Fe_{0.5}Mn_{0.5})O_3$ showing magnetic anomalies at 30, 114 and 226 K. Inset shows ZFC-FC curves for $(Bi_{0.5}La_{0.5})(Fe_{0.5}Mn_{0.5})O_3$ at 50 Oe.

temperature. At very high field (20 kOe), low temperature anomalies smear out and only the anomaly at T_N is observed (not shown). This is a further indication of glassy state and when such a high field is applied, all the moments could orient along the field direction consistent with the disappearance of low temperature anomalies in the ZFC data. Above T_N, the magnetic susceptibility (100 Oe) follows the Curie-Weiss law and the fit resulted Weiss constant θ = 120 K and effective paramagnetic moment μ_{eff} = 4.68 μ_B. The positive Weiss constant reflects that the interaction between Fe^{3+} and Mn^{4+} is weakly ferromagnetic. The calculated magnetic moment is slightly higher than the theoretical spin only value of 4.42 μ_B for Fe^{3+} - Mn^{4+} configuration. The ZFC-FC curves at 100 Oe for BLFMO shows that the system orders antiferromagnetically at 220

K (inset in figure 5.9) which is consistent with earlier report [205].

Magnetic isotherms of BSFMO recorded at different temperatures are shown in figure 5.10. At 5 K, the curve is slanted S-shaped with small coercive field of 400 Oe. At lower fields, the shape of the isotherm is related to the glassiness and is similar to that of observed similar compounds. At high fields, the curve shape changes to that of antiferromagnetic systems. This indicates that at high field the glassy feature disappears as all the frozen moments are forced to align towards the applied field. At 75 K, the isotherm shape changes with a higher coercive field value of 700 Oe which indicates a weak ferromagnetic behavior arising due to the canting of antiferromagnetic spins. The difference in the shape is related to the weak anomaly at 30 K in the ZFC data. At room temperature, a linear hysteresis curve is observed confirming the paramagnetic state. Magnetic isotherm (not shown) of BLFMO at low temperature (at 5 K) shows weak ferromagnetic behavior which does not saturate but has a much higher coercive field (3100 Oe) than that of the Sr doped compound (400 Oe).

In order to understand the nature of magnetic interactions associated with three anomalies in BSFMO, we have performed AC susceptibility measurements and the results are shown in figure 5.11. Weak frequency dependence in the anomaly of real part of the AC susceptibility χ' is observed in the vicinity of 40 and 105 K. The peak positions shift to higher temperature with increasing frequency. The imaginary part, χ'' on the other hand, shows frequency dependent peaks near the magnetic anomalies. At the N$\acute{e}$el temperature, χ'' shows sharp peak which are frequency independent. These features along with the DC magnetization data confirm the glassy nature of this system in which the competing magnetic interactions are present below a characteristic temper-

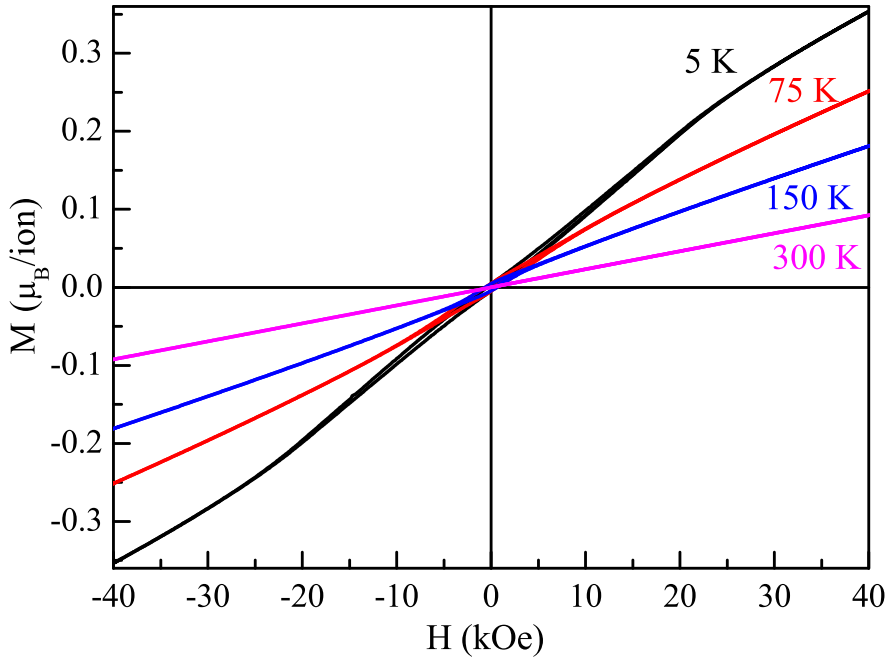

Figure 5.10: Magnetic isotherms of $Bi_{0.5}Sr_{0.5})(Fe_{0.5}Mn_{0.5})O_3$ at 5, 75, 150 and 300 K.

ature. As the glassy state occurs below T_N, it can either be associated with a reentrant spin glass (RSG) or with a cluster glass (CG) behavior [210, 211]. In a RSG, where the glassy nature persists into a long range ferromagnetic or antiferromagnetic order, the magnetic anomaly lies well below the paramagnetic to ferromagnetic/antiferromagnetic transition temperature. On the other hand, in a CG, where a set of clusters shows short range ordering below a characteristic temperature, a strong irreversibility in the ZFC – FC curves is observed below the magnetic ordering temperature. In the present case, the ZFC – FC in DC magnetization data shows a large irreversibility starting below the Néel temperature and also frequency dependent anomalies in χ' lie closer to the Néel temperature which confirms the cluster glass phenomenon. The peak shift in the low temperature anomaly near 40 K is not very clear with frequency which is due to broad

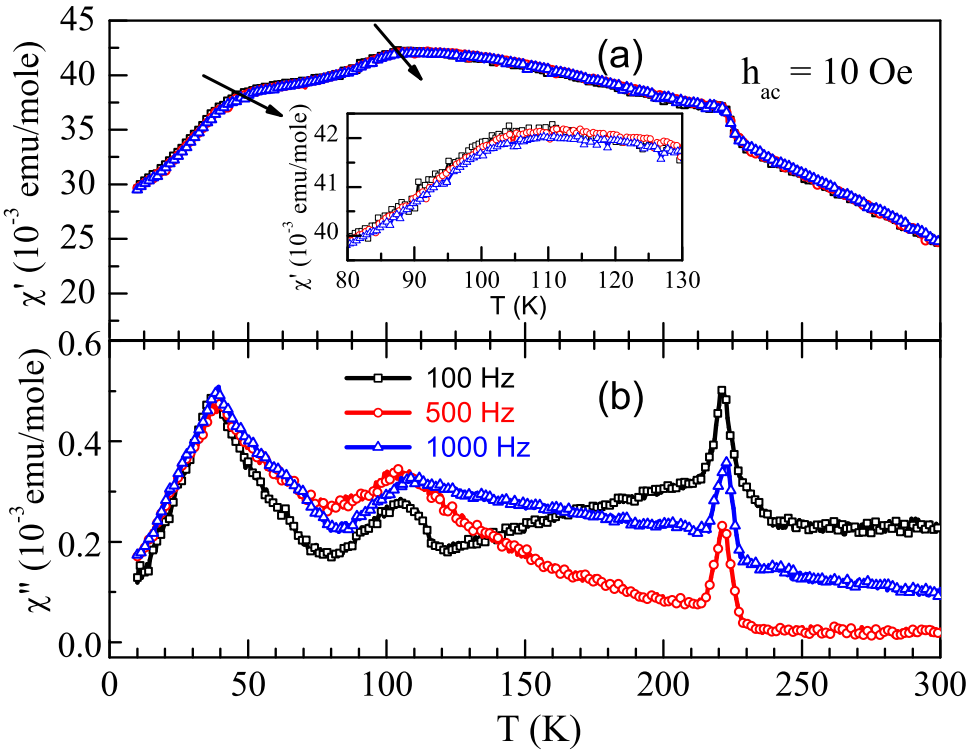

Figure 5.11: Ac susceptibility data of $Bi_{0.5}Sr_{0.5})(Fe_{0.5}Mn_{0.5})O_3$ plotted against temperature for different frequencies

anomalies and existence of cluster glass state above this temperature. Both DC and AC magnetic measurements suggest that the anomaly near 40 K does not represent a long range magnetic ordering, but rather suggests a spin glass transition similar to that of $Bi_{0.5}La_{0.5}Fe_{0.5}Mn_{0.5}O_3$ [205]. Glassy features in a magnetic system results from the competing magnetic interactions due to disorder arrangement of magnetic ions or geometric frustration. In the present compound, three superexchange interactions between Fe and Mn ions exist, Fe^{3+} – O – Fe^{3+}, Fe^{3+} – O – Mn^{4+} and Mn^{4+} – O – Mn^{4+}. According to Goodenough – Kanamori rule, the Fe – O – Fe and Mn – O – Mn superexchange interactions are antiferromagnetic whereas Fe – O – Mn is ferromagnetic. Thus, the glassy features might be arising from competing magnetic interactions due to

the disordered magnetic ions in the same crystallographic site (6*b*). The spin glass and cluster glass states, induced by disorder at the A or B-site are well known in few doped manganites [212–214]. The glassy state in BSFMO more complex than BLFMO possibly due to increased disorder due to size difference between the magnetic ions. Also, the possibility of oxygen non – stoichiometry in the compound cannot be neglected which can lead to the presence of Mn^{3+} ions and contribute to the complex glassy nature.

5.4 Conclusions

$BiFe_{0.5}Mn_{0.5}O_3$ belonging to the multiferroic family of Bi perovskites could be stabilized in the orthorhombic structure by high pressure synthesis technique. The compound orders antiferromagnetically at T_N = 270 K and below compensation temperature (T^*), temperature induced magnetization reversal is observed. The high pressure phase could be stabilized at the ambient pressure by 50% La and Sr substitution at the Bi-site. These compounds form with rhombohedral structure ($R\bar{3}c$) and do not exhibit the reversal phenomenon which may indicate important role of orthorhombic distortion. The reversal is understood in terms of ferrimagnetic ground state arising from the canted moments of Fe – Fe and Fe – Mn coupled antiferromagnetically.

CHAPTER 6

Magnetization Reversal in $YFe_{1-x}M_xO_3$ (M = Cr and Mn)[§]

6.1 Introduction

As discussed in the previous chapter, the orthorhombic $BiFe_{0.5}Mn_{0.5}O_3$ exhibits temperature induced magnetization reversal below a compensation temperature. In order to understand the origin of temperature induced magnetization reversal, we have made an attempt to explore this phenomenon in similar systems. The drawback with the Bi-based compound is the requirement of high pressure synthesis which is not readily available to us. Based on the structural as well as chemical similarity, we found that rare earth orthoferrites, $RFeO_3$ (R = rare earth or yttrium) would be an ideal system, which can be synthesized at ambient pressure and have perovskite type structure with orthorhombic distortion (space group: P*nma*). Depending on the rare-earth, these compounds undergo antiferromagnetic ordering at temperature ranging from 620 to 750 K [123, 197, 215]. Below Néel temperature, the orthoferrites show a canted antiferromagnetic behavior due to antisymmetric Dzyaloshinskii-Moriya interaction [197]. Interestingly, a temperature induced spin-reorientation is observed when the R ion is magnetic and the antiferromagnetic easy axis changes from one crystallographic direction to another [112]. On the other hand the orthoferrites containing non-magnetic A-site cation undergo spin-reorientation transition upon application of magnetic field, pressure and

[§]Based on this chapter work, two manuscripts have been submitted. P. Mandal, C. R. Serrao, N. Dasari, N. S. Vidhyadhiraja, A. Sundaresan and C. N. R. Rao *Communicated*

substitution of Fe with other trivalent magnetic transition metal ions such as Mn, Cr ans Co [112, 216–219]. To avoid complication due to magnetic interaction between the rare earth and the B-site ions, we have purposefully chosen the non-magnetic Y^{3+} ions and investigated the systems $YFe_{1-x}Cr_xO_3$ and $YFe_{1-x}Mn_xO_3$ extensively.

In this chapter, we have focused the study on two systems $YFe_{1-x}M_xO_3$ (M = Cr and Mn) of canted antiferromagnetic oxides where the magnetic ions Fe and Cr (or Mn) are randomly mixed at the B-site. The close ionic radii of the trivalent magnetic ions prevent the system to order in a rock-salt manner. Single phase compounds with orthorhombic structure (Space group: P*nma*) are obtained in the full range $0 \leq x \leq 1.0$ for Cr substitution. The magnetization measurements and neutron diffraction results show that upon Cr substitution, the system undergo a broad spin-reorientation transition from $\Gamma 4(G_zF_y)$ spin structure to a mixed phase of $\Gamma 4$ and $\Gamma 2(G_yF_z)$. The partial spin-reorientation from $\Gamma 4$ to $\Gamma 2$ is second-order. As expected, negative magnetization is observed below 180 and 240 K for the compounds with x= 0.4 and 0.5 respectively. The reversal phenomenon is best explained based on the ferrimagnetic ground state resulting from the antiferromagnetic coupling of canted moments of Fe – O – Fe, Fe - O - Cr and Cr - O - Cr. On the other hand, solid solution in the Mn substituted compounds could be formed up to x = 0.45. In these compounds, magnetization was observed to drop sharply from the canted state ($\Gamma 4$) to a collinear state ($\Gamma 1$). In this first-order spin reorientation transition, the easy axis rotates abruptly from z to x-direction. Similar to the $YFe_{1-x}Cr_xO_3$ samples, magnetization reversal is observed for x = 0.4 and 0.45 but at relatively low temperatures of 90 and 125 K respectively. Another interesting aspect of $YFe_{1-x}Mn_xO_3$ system is the observation of inverse magnetocaloric effect (MCE)

across the spin-reorientation and positive magnetocaloric effect at the antiferromagnetic transitions. As these transition temperatures are dependent on Mn concentration, the magnetocaloric effect is tunable over a broad temperature range.

6.2 Experiments

The compounds $YFe_{1-x}Cr_xO_3$ and $YFe_{1-x}Mn_xO_3$ were prepared by solid state reaction route. Stoichiometric amounts of Y_2O_3 (preheated at 1073 K), Fe_2O_3 and Mn_2O_3 (or Cr_2O_3 in case of Cr substitution) were mixed thoroughly and heated at 1273, 1373 and 1473 K with several intermittent grindings. At the final step, the powder was pressed into pellets and sintered at 1743 K for 24 hours. Phase purity was confirmed by Rietveld refinement on the X-ray powder diffraction data collected with Bruker D8 Advance diffractometer. Neutron diffraction data were collected using wavelength of 2.40 and 1.60 Å in high resolution powder diffractometer D2B at ILL (Institut Laue-Langevin). Magnetic measurements were carried out with a vibrating sample magnetometer in a physical property measurement system (PPMS), Quantum Design, USA. To calculate entropy change in magnetocaloric study, magnetic isotherms were collected in a wide range of temperature at an interval of 4 K and magnetic field step of 500 Oe.

6.3 Result and discussion

For clarity, the results are discussed separately for the Cr and Mn substituted compounds.

6.3.1 Structure and Magnetic Properties of $YFe_{1-x}Cr_xO_3$

6.3.1.1 Structure

Rare earth orthochromites are known to be isostructural with rare earth orthoferrites having $GdFeO_3$ type orthorhombic structure (SG:P*nma*) [123]. The isostructural nature of both end members and close ionic sizes of Fe^{3+} (0.65 Å) and Cr^{3+} (0.62 Å) allow to form solid solution in the complete range $0 \leq x \leq 1.0$. Rietveld refinements on room temperature X-ray data showed orthorhombic symmetry with space group P*nma* for all the compounds (refinements are not shown). Unit cell parameters *a*, *b*, *c* and cell volume *V*, as extracted from the refinement, are plotted against *x* as shown in figure 6.1.

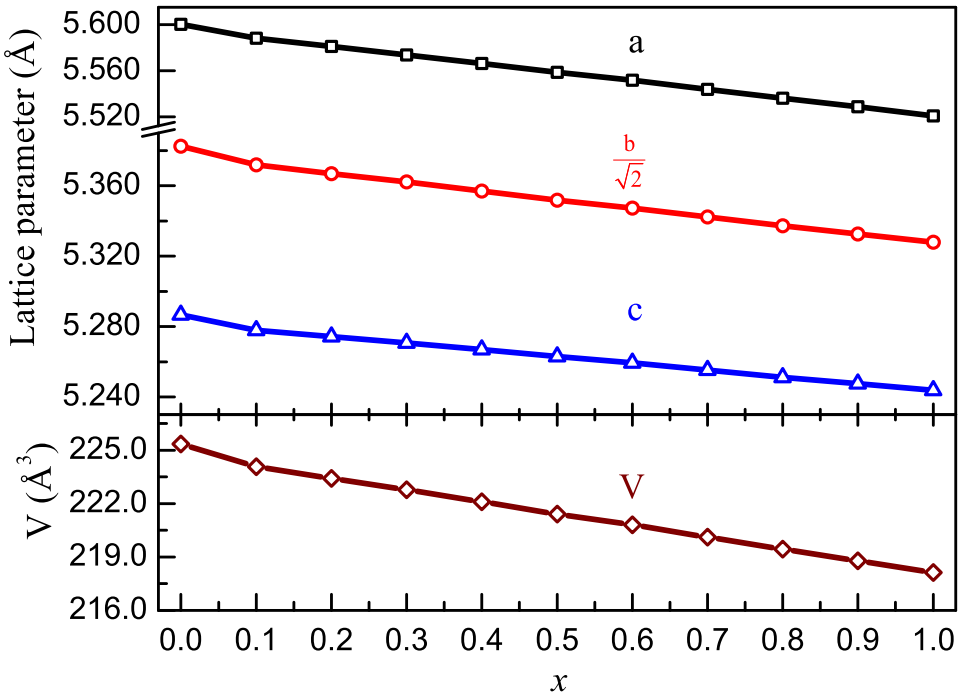

Figure 6.1: Variation of unit cell parameters and volume against Cr substitution in $YFe_{1-x}Cr_xO_3$.

Table 6.1: Atomic position (*x*, *y*, *z*) and isotropic thermal parameters (B) for selected compositions of $YFe_{1-x}Cr_xO_3$ obtained from the Rietveld refinements of X-ray data collected at room temperature.

$\mathbf{YFe_{1-x}Cr_xO_3}$						
Site	Wyckoff Position	Cr level	*x*	*y*	*z*	B(Å^2)
Y	4*c*	0	0.0684(1)	0.2500	0.9826(2)	0.92(2)
		0.1	0.0685(1)	0.2500	0.9823(2)	1.75(3)
		0.3	0.0682(1)	0.2500	0.9821(2)	1.09(2)
		0.4	0.0681(1)	0.2500	0.9824(2)	1.44(2)
		0.5	0.0675(1)	0.2500	0.9818(2)	1.13(2)
		0.8	0.0666(1)	0.2500	0.9833(2)	1.51(2)
		1.0	0.0659(1)	0.2500	0.9839(2)	1.64(2)
O1	4*c*	0	0.4597(8)	0.2500	0.1092(8)	1.00
		0.1	0.4608(9)	0.2500	0.1074(9)	1.00
		0.3	0.4625(8)	0.2500	0.1055(8)	1.00
		0.4	0.4636(9)	0.2500	0.1045(9)	1.00
		0.5	0.4630(8)	0.2500	0.1058(8)	1.00
		0.8	0.4616(8)	0.2500	0.1068(8)	1.00
		1.0	0.4607(8)	0.2500	0.1060(9)	1.00
O2	8*d*	0	0.6935(6)	-0.0574(4)	0.3087(6)	1.00
		0.1	0.6915(7)	-0.0584(5)	0.3089(7)	1.00
		0.3	0.6936(7)	-0.0578(4)	0.3083(7)	1.00
		0.4	0.6920(7)	-0.0578(5)	0.3074(0)	1.00
		0.5	0.6954(6)	-0.0574(4)	0.3061(6)	1.00
		0.8	0.6963(6)	-0.0564(4)	0.3054(6)	1.00
		1.0	0.6970(7)	-0.0558(5)	0.3044(7)	1.00

These parameters decrease with increasing *x* following Vegard's law as expected from the difference in ionic radii between Fe^{3+} and Cr^{3+}. The atomic positions and isotropic thermal parameters as obtained from Rietveld refinements are given in the table 6.1.

6.3.1.2 Weak ferromagnetism and spin-reorientation in $YFe_{1-x}Cr_xO_3$

Field-cooled magnetization curves of $YFe_{1-x}Cr_xO_3$ at an applied magnetic field of 100 Oe in the temperature interval 10 – 400 K are shown in figures 6.2, 6.3, 6.4 and 6.5. It should be mentioned here that in the field cooled process, the field must be applied above the magnetic ordering temperature but due to the limitation with the magnetometer, we applied the magnetic field at 400 K though the magnetic ordering temperatures in samples with x= 0 - 0.3 are well above 400 K. Field cooled magnetization curve of the parent compound is consistent with the weak ferromagnetic behavior expected for a canted antiferromagnet. For $x = 0.1$, magnetization increases with decreasing temperature showing a broad maximum and then decreases to a constant value. Below T_N, the increase of magnetization represents a weak ferromagnetic or canted antiferromagnetic behavior due to spin-canting similar to the parent compound $YFeO_3$. The canted state in these orthoferrites will be referred as AFM1. The decrease in magnetization at low temperature, might indicate a spin-reorientation transition (T_{SR}) where the magnetic easy axis rotates from one to another crystallographic direction. Depending on the magnetic anisotropy constants of Fe and Cr ions, spin reorientation in $YFe_{1-x}Cr_xO_3$ compounds was predicted to be be complete or partial by Kadomtseva *et al*[166]. As seen in figure 6.2, this spin reorientation transition is broad, in agreement with theoretical prediction [166]. This also indicates a second order nature of the transition. With increasing Cr concentration, T_{SR} increases whereas the Néel temperature decreases, as expected due to the dilution of Fe^{3+} (S = 5/2) with Cr^{3+} ions (S = 3/2). This is shown in DC magnetization data collected with high temperature VSM as shown in figure 6.3a. As shown in

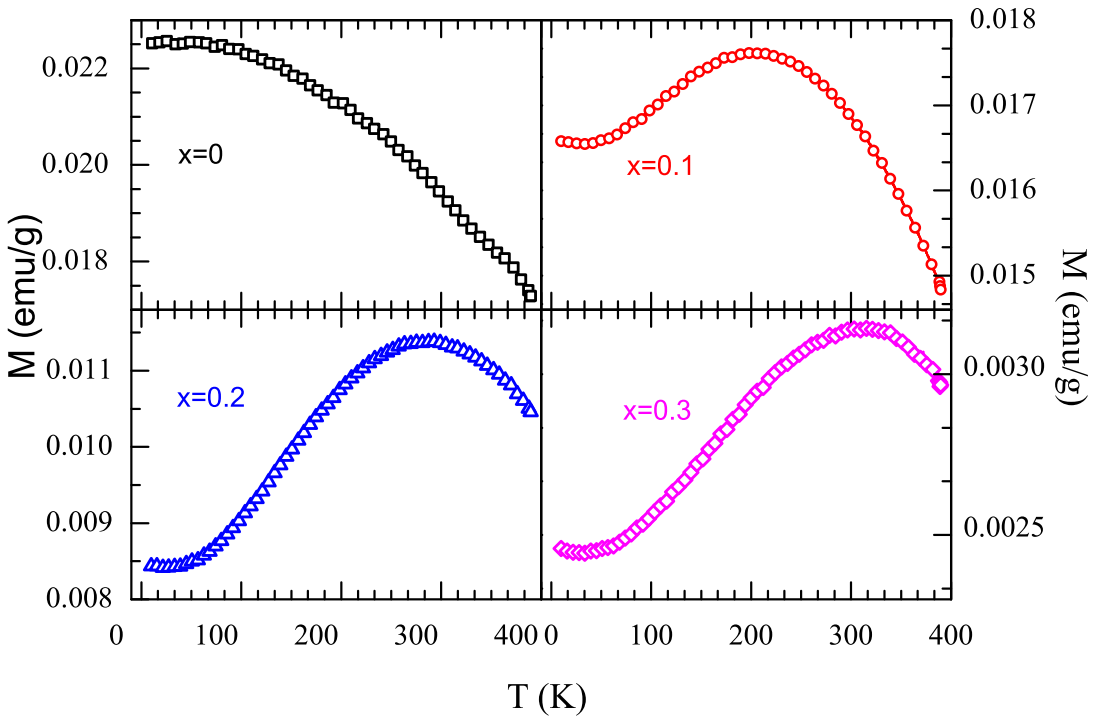

Figure 6.2: Field cooled magnetization curves of $YFe_{1-x}Cr_xO_3$ (x = 0 to 0.3) under 100 Oe showing second order spin reorientation transition.

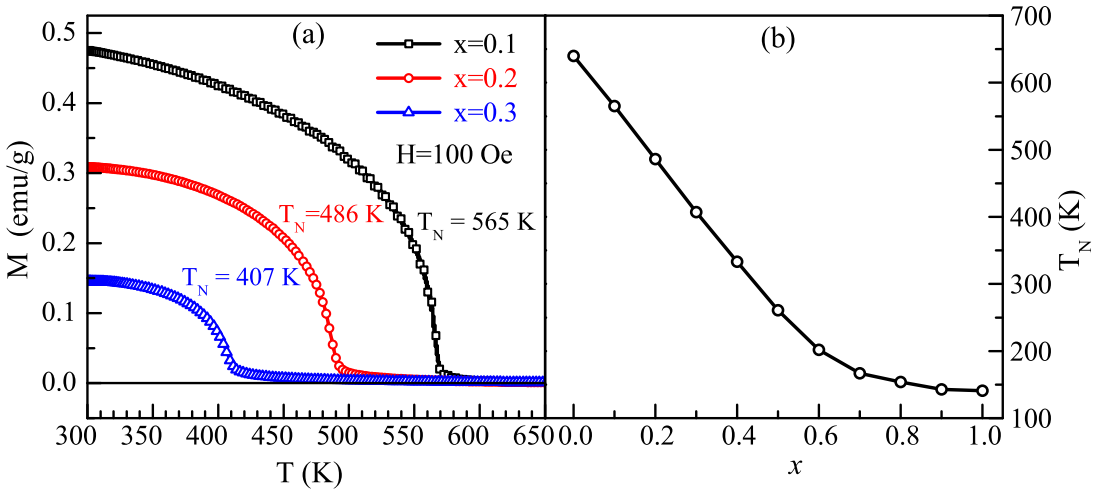

Figure 6.3: (a) Field cooled magnetization data of $YFe_{1-x}Cr_xO_3$ (x = 0.1 to 0.3) collected at high temperature. (b) Néel temperature (T_N) plotted against Cr concentration.

figure 6.3b, the Néel temperature shows a linear behavior with Cr concentration till x = 0.6, beyond which it drops slowly. Such behavior may be due to disordered arrangement of Fe and Cr ions.

6.3.1.3 Temperature induced magnetization reversal

Most interesting aspect of $YFe_{1-x}Cr_xO_3$ compounds is the observation of negative magnetization for x = 0.4 and 0.5 as shown in figure 6.4. For $x = 0.4$, T_N is decreased to 333 K and T_{SR} increased to $\sim$ 300 K. More importantly, the magnetization becomes zero at the compensation temperature $T^* = 184$ K below which it is negative. At further low temperature, the negative magnetization value saturates and remain almost constant. For $x = 0.5$, there is no indication of spin-reorientation transition and the magnetization value decreases below T_N = 260 K. The magnetization value becomes negative below T^* = 240 K. This is consistent with other reports [171, 220].

For $x > 0.5$, all the samples (except for x = 0.8) show a canted antiferromagnetic behavior as shown in figure 6.5. It is worth mentioning here that $YCrO_3$ is also a canted antiferromagnet due to DM interaction similar to the orthoferrites [221]. Surprisingly, $YFe_{0.2}Cr_{0.8}O_3$ which orders at $T_N = 154$ K and exhibits a double compensation. At 150 K, magnetization shows a sudden decrease and below $T_1^* = 140$ K magnetization value becomes negative. Below 105 K, the magnetization value starts increasing and at $T_2^* = 62$ K crosses zero again as shown in figure 6.6. The double compensation effect mentioned above has previously been reported for a Prussian blue compound where simultaneous presence of antiferromagnetic and ferromagnetic interactions resulted such behavior [175, 178]. To our knowledge, this is the first compound known to exhibit two

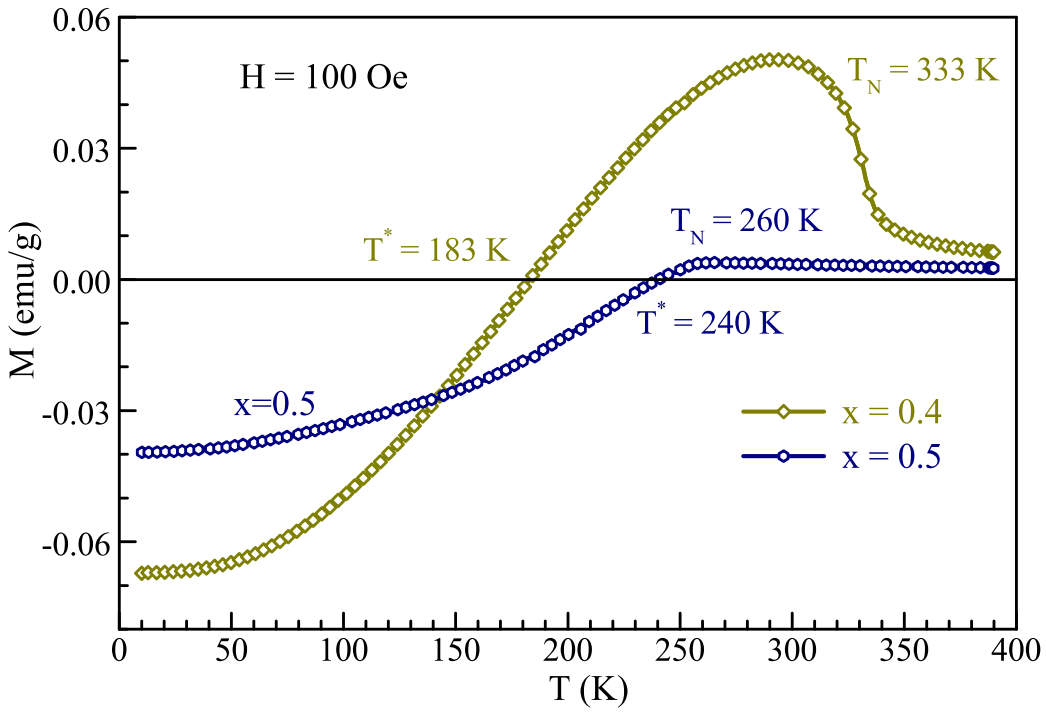

Figure 6.4: Magnetization reversal in $YFe_{1-x}Cr_xO_3$ (x = 0.4 and 0.5).

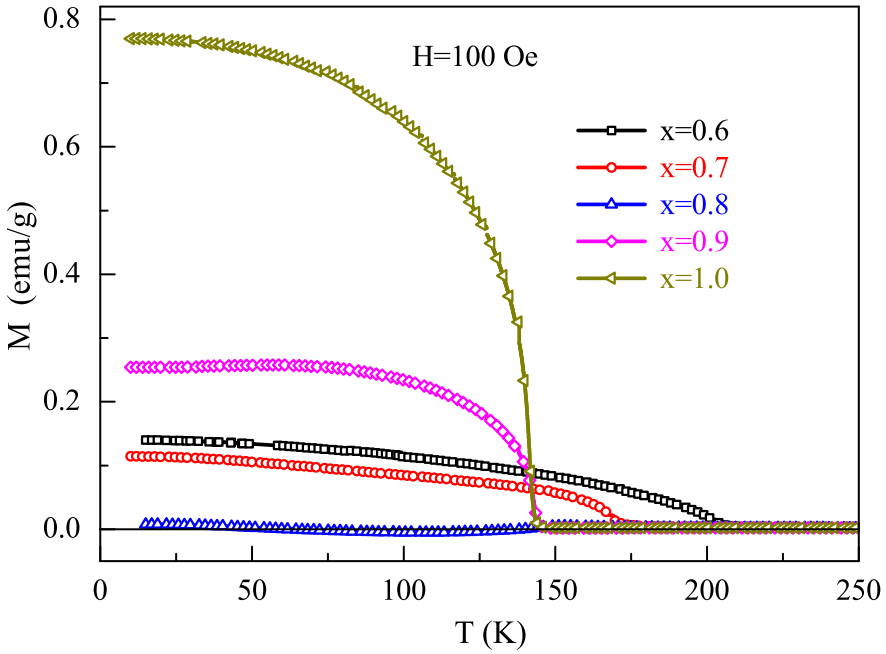

Figure 6.5: Field cooled magnetization curves of $YFe_{1-x}Cr_xO_3$ under 100 Oe for $x =$ 0.6 – 1.0

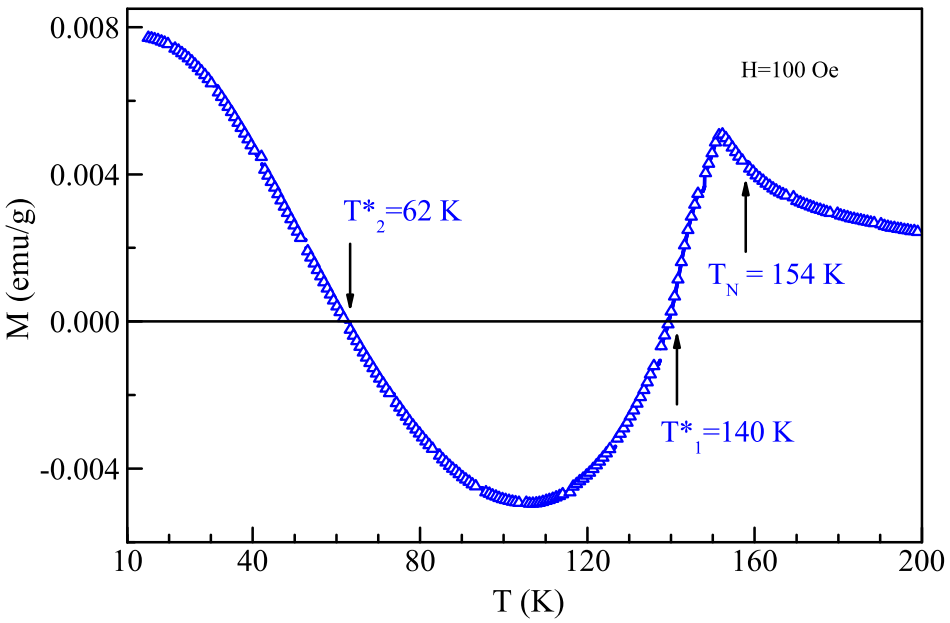

Figure 6.6: Field cooled magnetization curves of $YFe_{0.2}Cr_{0.8}O_3$ under 100 Oe showing two compensation temperature.

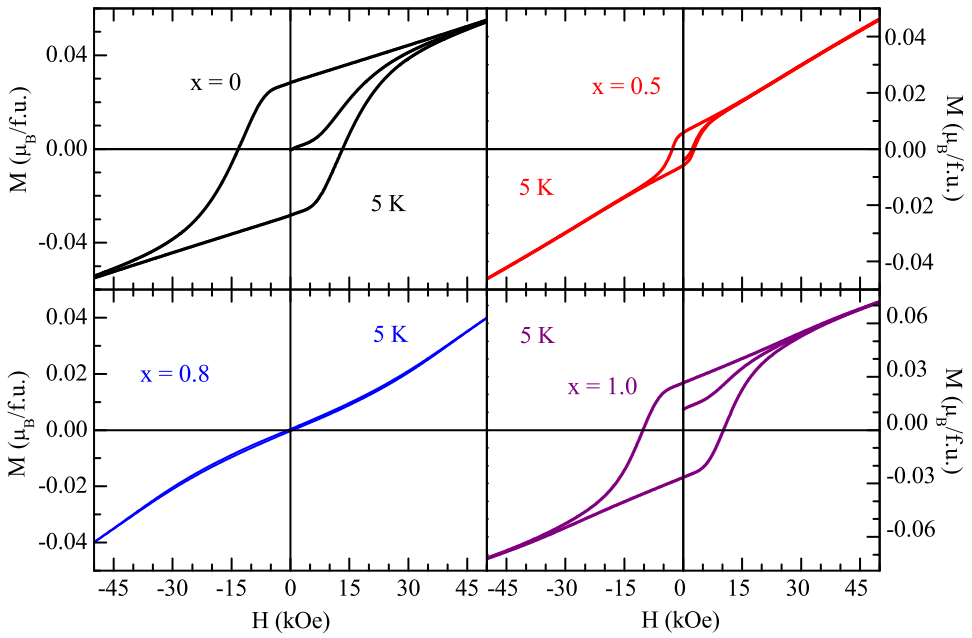

Figure 6.7: Magnetic isotherms of $YFe_{1-x}Cr_xO_3$ collected at 5 K.

compensation temperatures where only two magnetic ions are distributed in a single crystallographic site (4*b*). The magnetic isotherms collected at 5 K for selected compounds (x = 0, 0.5, 0.8 and 1) are shown in figure 6.7. All the compounds showed a ferromagnetic like feature with a saturation magnetization $\sim$ 0.04 μ_B/f.u.. Such a low value indicates that these compounds are canted antiferromagnet.

6.3.1.4 Neutron diffraction study on $YFe_{0.5}Cr_{0.5}O_3$

In order to understand the nature of spin-reorientation transition and magnetization reversal we carried out the neutron diffraction studies on $YFe_{0.5}Cr_{0.5}O_3$. Neutron diffraction data were collected at different temperatures and the results are shown in figure 6.8. A wavelength of 1.60 Å was used to determine nuclear structure whereas below

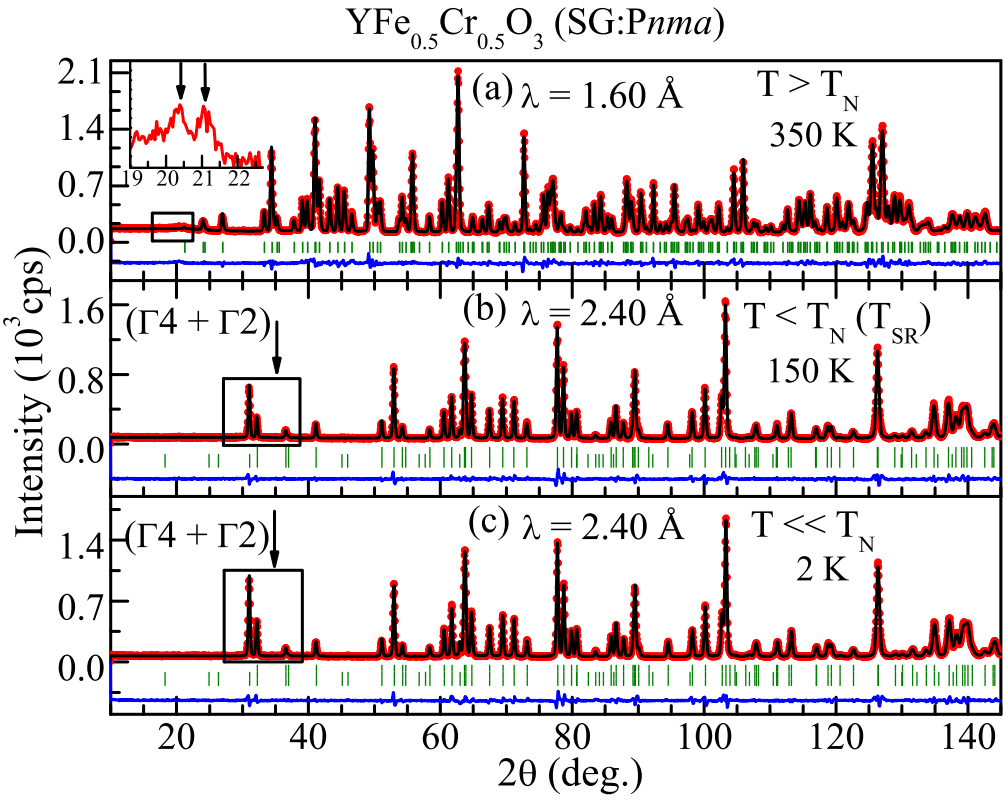

Figure 6.8: Rietveld refinement on the neutron diffraction data of $YFe_{0.5}Cr_{0.5}O_3$ collected at (a) 350, (b) 150 and 2 K.

T_N, a higher wavelength of 2.4 Å was chosen to study magnetic structures. Surprisingly, the neutron diffraction data collected at 350 K (T_N = 260 K) shows two small peaks over a broad hump like feature near $2\theta \sim 20^\circ$ (inset of figure 6.8a). These two reflections can not be accounted for the nuclear contribution. It is noteworthy that this feature appears at the same position (*d*-value) where magnetic reflections appear below T_N. The broad hump is usually described as a short range ordering but the two well defined peaks clearly confirm magnetic ordering in the system. The magnetic reflections at 350 K can be understood in terms of the disorderness at the B-site of the perovskite. As the Fe^{3+} and Cr^{3+} ions are randomly distributed at the 4*b* site of orthorhombic cell in $YFe_{1-x}Cr_xO_3$, there can be three superexchange interactions Fe – O – Fe, Fe - O - Cr and Cr - O - Cr. It is well known that in such disordered compounds, the Fe - Fe and Cr - Cr impurity ions in the host Fe - Cr matrix retain the properties of parent compound $YFeO_3$ and $YCrO_3$ respectively [166]. As the perovskite orthoferrites are known to order antiferromagnetically at very high temperatures ($\sim$ 640 K), we suggest that these reflections are due to the ordering of Fe - Fe near neighours. The Fe - O - Cr would order at the Néel temperature ($\sim$ 260 K) whereas the Cr - O - Cr clusters would order at much lower temperature ($\sim$ 140 K).

As the temperature is decreased below T_N, we observe intense magnetic reflections near $2\theta \sim 31^\circ$. As the Fe and Cr ions are present at the same crystallographic site (4*b*), the magnetic reflections due to Fe - O - Cr ordering appears at the same position as in Fe – O – Fe ordering. To represent the magnetic structure, we have followed Bertaut's notations [222, 223]. In the orthorhombic structure (SG P*nma*), the B-site magnetic ions are present at 4*b* sites and spins present at the 4*b* positions 1 (0, 0, 1/2), 2 (1/2, 0,

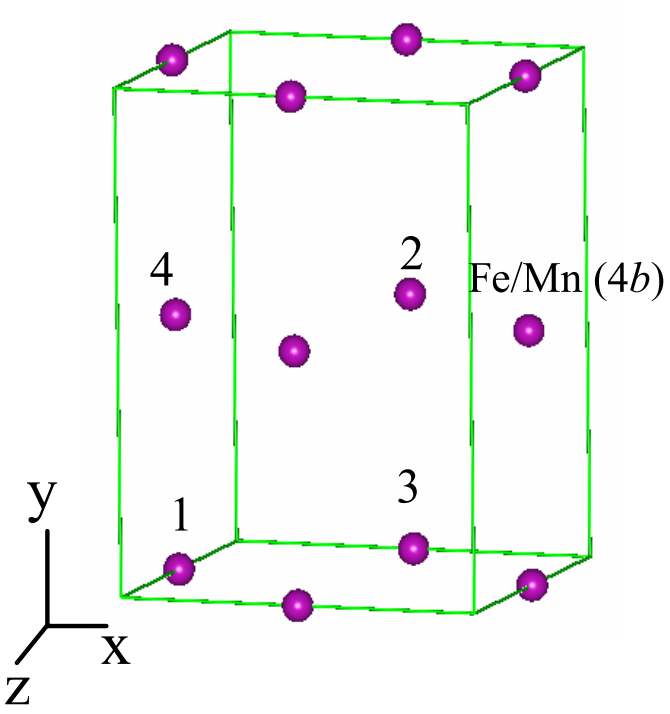

Figure 6.9: Orthorhombic (P*nma*) unit cell showing the four positions (4*b*) defined as 1, 2, 3 and 4 occupied by the B-site cations i.e., Fe and Mn ions.

0), 3 (0, 1/2, 1/2) and 4 (1/2, 1/2, 0) are denoted by S_1, S_2, S_3 and S_4 as shown in figure 6.9. Depending on the relative spin directions at the four positions, there can be four basis vectors possible represented as **F**, **G**, **C** and **A**. Depending on whether these spins are aligned along or opposite to a crystallographic directions, these are represented as + or -. The vectors **F**, **G**, **C** and **A** (space group P*nma*)are defined as,

$$\begin{aligned} F &= +S_1 + S_2 + S_3 + S_4 \\ G &= +S_1 - S_2 - S_3 + S_4 \\ C &= +S_1 - S_2 + S_3 - S_4 \\ A &= +S_1 + S_2 - S_3 - S_4 \end{aligned} \tag{6.1}$$

It should be pointed out that the definition of these vectors are different for the other

setting i.e., space group P*bnm* where c is considered as the long axis. As clear from the above relations, while **G**, **C**, **A** represents antiferromagnetic coupling, the vector **F** represents a ferromagnetic behavior. For example, the basis vector G_x indicates that S_1 and S_4 are directed along *x* axis whereas S_2 and S_3 are directed opposite to S_1 and S_4.

The four irreducible representations known for ferrites or chromites can be represented in terms of vector components **F**, **G**, **C** and **A** along three crystallographic direction. According to Bertaut's notations, these are defined as,

$$\begin{aligned} \Gamma 1 &= G_x\, C_y\, A_z \\ \Gamma 2 &= C_x\, G_y\, F_z \\ \Gamma 3 &= F_x\, A_y\, C_z \\ \Gamma 4 &= A_x\, F_y\, G_z \end{aligned} \tag{6.2}$$

The spin structure $\Gamma\,4$ represents a G-type antiferromagnet with easy axis along the z- direction coupled with a ferromagnetic component (F) along *y*-direction and an antiferromagnetic (A) along *x*-direction. The magnetic structure of few rare earth orthoferrites are represented by $\Gamma 4$ ($G_z\, F_y$) where spins are in G-type configuration along *z*-direction and canted towards *y*-direction [224]. The canting along *y*-direction gives rise to the weak ferromagnetic component F_y whereas A_x is found to be negligible.

Orthoferrites and orthochromites are known to change the magnetic structures upon change in temperature, pressure, magnetic field or chemical doping. The spin reorientation is characterized by an angle (θ) altered from the crystallographic easy axis. The transition can be of several types depending on the magnetic ion at the A-site and the interaction between Fe (or Cr) and the A-site magnetic rare earth. When the rare earth

(R) is nonmagnetic, it has been observed that RMO_3 (M = Fe or Cr) retains $\Gamma 4$ structure at all temperatures [224].

The low temperature neutron diffraction patterns of $YFe_{0.5}Cr_{0.5}O_3$ are shown in figure 6.8*b* and *c*. For low Cr concentration (0.1 to 0.3), the AFM1 state is similar to the canted antiferromagnetic state of parent compounds $YFeO_3$ and $YCrO_3$. These compounds are known to possess $\Gamma 4$ (G_zF_y) spin configuration at all temperature below T_N [224]. The magnetic reflections at 150 K could not be described either by $\Gamma 4$ or $\Gamma 2$ solely. The possibility of $\Gamma 1$ configuration which does not allow any **F** component was ignored due to the fact that a large canted moment is observed below T_N in the magnetization measurements. We rather find that the magnetic structure is best explained with the combination of irreducible representations $\Gamma 4$ (G_zF_y) and $\Gamma 2$ (G_yF_z). The four strong magnetic reflections observed correspond to (1 1 0), (0 1 1), (1 0 1) and (0 2 0) planes. It is noticeable from the aforementioned relations that ferromagnetic

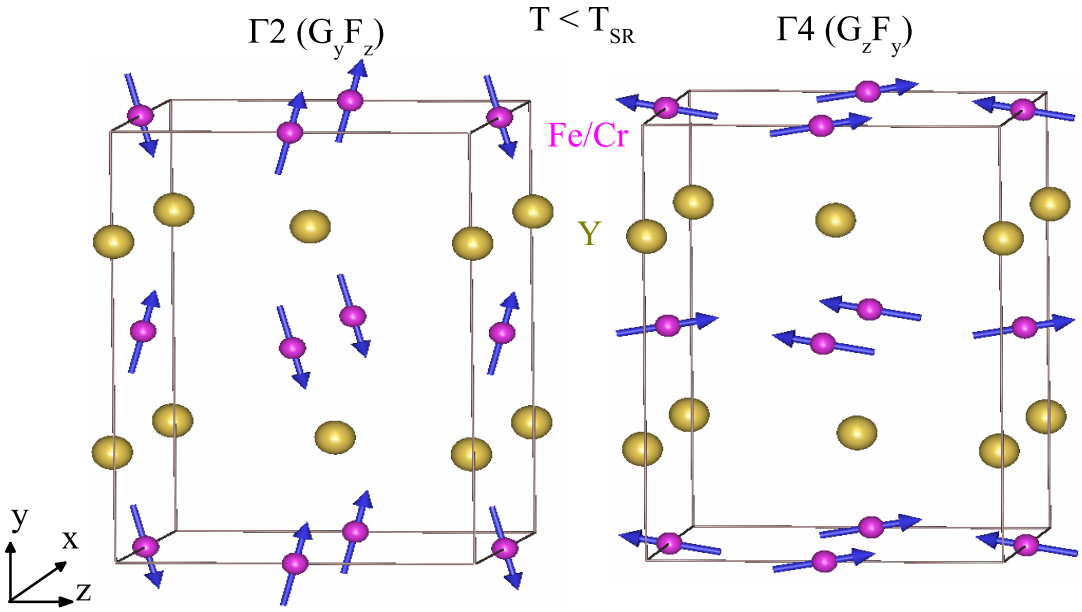

Figure 6.10: Magnetic structure of $YFe_{0.5}Cr_{0.5}O_3$ below T_N. The spin structure below T_N is a mixed phase of $\Gamma 4$ (G_zF_y) and $\Gamma 2$ (G_yF_z).

components are allowed in both $\Gamma 4$ (F_y) and $\Gamma 2$ (F_z) structures thus consistent with experimentally observed canted antiferromagnetic behavior. At 2 K, the coexistence of $\Gamma 4$ and $\Gamma 2$ is still observed. The $\Gamma 4$ phase is the dominant spin structure at all temperatures and the moment values corresponding to G_zF_y and G_yF_z components are seen to increase with decreasing temperature. Magnetic structure below T_N is represented in figure 6.10 where $\Gamma 4$ and $\Gamma 2$ are displayed in the orthorhombic unit cells. The structural parameters and magnetic moments are summarized in table 6.2. The spin-reorientation in this compound is similar to the orthoferrite and orthochromite systems $RFeO_3$ (R = Nd, Sm, Tb, Ho, Er, Tm and Yb) and $RCrO_3$ (R = Sm, Gd) where the easy axis in $\Gamma 4$ configuration starts rotating from z direction at T_2 and the spin configuration changes to $\Gamma 2$ at temperature T_1 where the easy axis is along the *y* direction [112]. The smooth rotation of the easy axis defines this transition to be of second order. In the present compound, the coexistence of $\Gamma 4$ and $\Gamma 2$ confirms a partial spin-reorientation where the high temperature AFM1 phase ($\Gamma 4$) does not completely convert to $\Gamma 2$. It can also be speculated that for low Cr substitution of $0.1 \leq x \leq 0.4$, the high temperature AFM1 phase has $\Gamma 4$ structure partially converts to $\Gamma 2$ below the second order spin reorientation. The spin-reorientation transition in $RFeO_3$ was explained microscopically by Levinson [225] considering Fe^{3+} contribution to the free energy F, written as

$$F = A_0(T) + A_2(T).\sin^2\theta + A_4(T).\sin^4\theta \tag{6.3}$$

where, θ is the rotation angle, A_2 and A_4 are the constants involving second and fourth order anisotropic constants and pseudodipolar spin interactions of Fe^{3+} ions. Based on the ratio's of the anisotropy constants, he predicted spin reorientations to be either

Table 6.2: Atomic position (*x, y, z*), isotropic thermal parameters (B), Magnetic moments (μ), lattice parameters and other reliability factors of $YFe_{0.5}Cr_{0.5}O_3$ at 350, 150 and 2 K as obtained from Rietveld refinements on neutron data.

$YFe_{0.5}Cr_{0.5}O_3$					
Site	Wyckoff Position	*x*	*y*	*z*	B(Å^2)
Y	4*c*	0.0671(1)	0.2500	0.9831(2)	0.42(2)
		0.0679(2)	0.2500	0.9826(3)	0.51(5)
		0.0683(2)	0.2500	0.9824(3)	0.33(5)
Fe/Cr	4*b*	0.00000	0.0000	0.50000	0.32(2)
		0.00000	0.0000	0.50000	0.26(4)
		0.00000	0.0000	0.50000	0.05(4)
O1	4*c*	0.4630(2)	0.2500	0.1079(3)	0.37(2)
		0.4620(3)	0.2500	0.1075(3)	0.14(4)
		0.4619(3)	0.2500	0.1072(4)	0.06(4)
O2	8*d*	0.6967(2)	-0.0555(1)	0.3080(2)	0.44(1)
		0.6965(2)	-0.0560(2)	0.3074(3)	0.45(4)
		0.6966(2)	-0.0562(2)	0.3074(3)	0.23(4)

T(K)	Magnetic Structure	Magnetic moment, μ (μ_B)		
		μ_x	μ_y	μ_z
150	$\Gamma4(A_x\,F_y\,G_z) + \Gamma2(C_x\,G_y\,F_z)$	0.00, 0.00	0.09(46), 1.07(6)	2.35(3), 0.25(20)
2	$\Gamma4(A_x\,F_y\,G_z) + \Gamma2(C_x\,G_y\,F_z)$	0.00, 0.00	0.19(23), 1.83(5)	2.74(3), 0.46(12)

T (K)	*a*	*b*	*c*	χ^2	R_p	R_{wp}	R_B	R_f factor
350	5.5608(1)	7.5770(1)	5.2692(1)	9.76	7.68	8.46	3.21	2.27
150	5.5627(1)	7.5720(1)	5.2652(1)	5.21	10.2	10.5	1.95	1.67
2	5.5621(1)	7.5684(1)	5.2625(1)	5.59	9.98	10.5	1.85	1.41

abrupt or smooth [225]. In this theory, the interaction between the rare earth and the Fe were neglected which later was confirmed not to be true [226]. Later, the anisotropic contribution due to magnetic interaction between the rare earth and Fe (or Cr) ions, antisymmetric and anisotropic-symmetric exchange interaction were suggested to be responsible for the first or second order spin-reorientation [112]. In rare-earth orthoferrites/orthochromites where the A-site ion is nonmagnetic, the magnetic structure retains to be $\Gamma4$. The presence of spin reorientation in the doped system $YFe_{1-x}Cr_xO_3$ may

suggest a role of different single ion anisotropy of Fe^{3+} and Cr^{3+} ions. Considering the different anisotropy and canted antiferromagnetism due solely to the antisymmetric DM interaction second order spin reorientation in Cr substituted $YFeO_3$ was described by Kadomtseva *et al* [166]. The anisotropy contribution to the free energy is written as

$$F = \frac{1}{2}k_u \, cos\, 2\theta + k_b \, cos\, 4\theta \tag{6.4}$$

Here k_u is first anisotropic constant which is dependent on the single ion anisotropy of Fe and Cr ions, DM interaction and magnetic dipole Fe - Fe and Cr - Cr interaction whereas k_b is the second order or the cubic anisotropy. It was shown [166] that the spin reorientation is complete if

$$k_u(T_{sat}) \geq 8k_b(T_{sat})$$

or partial for

$$k_u(T_{sat}) < 8k_b(T_{sat})$$

The temperature T_{sat} denotes the temperature below which the magnetization becomes almost constant.

6.3.1.5 Reversal mechanism

As discussed previously, the parent compound $YFeO_3$ exhibits a weak ferromagnetic behavior arising from a spin canting below $T_N = 640$ K similar to that observed in compounds α-Fe_2O_3 and few transition metal carbonates. This behavior was explained in terms of symmetry grounds by Dzyaloshinskii [193]. Later, Moriya explained this based on antisymmetric superexchange interaction which includes spin-orbit coupling [194]. In antiferromagnets, thus the weak ferromagnetism can result either from DM in-

teraction or from the single-ion magnetic anisotropy (also known as magnetocrystalline anisotropy). In orthoferrites, though both of these mechanisms may simultaneously operate, it has been shown that the antisymmetric exchange interaction (DM interaction) to be the dominant mechanism responsible for the observed weak ferromagnetism [197, 227]. Neutron diffraction studies have shown that magnetic structure of $YFeO_3$ is $\Gamma 4$ (G_zF_y) where easy axis is along the z direction [228, 229]. In these weakly ferromagnetic orthoferrites, the spontaneous moment orient along the *y* direction whereas Dzyaloshinskii vector **D** points along the *x* direction [197, 230]. The Dzyaloshinskii-Moriya (DM) antisymmetric superexchange interaction is mathematically represented as $D_{12}\cdot(S_1\times S_2)$ where **D** is the Dzyaloshinskii field and S_1, S_2 are the sublattice magnetizations. The Dzyaloshinskii vector is proportional to the spin-orbit coupling constant, λ and vertical shift of oxygen ion from the S_1-S_2 line as well as the unit vector along the line connecting the spins S_1 and S_2 and can be formulated as $\mathbf{D}_{12} \propto \lambda\,\mathbf{x}\times\mathbf{r}_{12}$. The single-ion magnetocrystalline anisotropy on the other hand is determined by the interaction between the orbital state of magnetic ion and the surrounding strong crystalline field. The anisotropy originates from quenching of the orbital moment by the crystalline field and the spin-orbit coupling mediates this interaction to the spin moments.

As already pointed out, the magnetic ions are disordered at the B-site of the perovskite. This leads us to consider the $YFe_{1-x}Cr_xO_3$ system as Fe - Cr matrix in which Fe - Fe and Cr - Cr can be treated as impurity clusters retaining their properties as $YFeO_3$ and $YCrO_3$ respectively. A previous report also suggested that antiferromagnetically coupled clusters of iron and chromium in antiferromagnetic collinear matrix of Fe - Cr may be responsible for zero magnetization in $La_{1-x/2}Bi_{x/2}Fe_{0.5}Cr_{0.5}O_3$ [191].

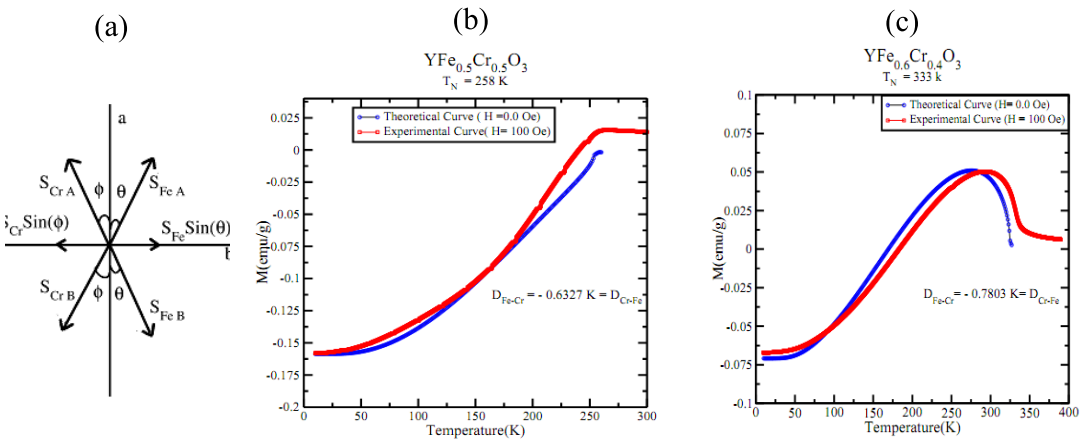

Figure 6.11: Fit to the experimental data of $YFe_{0.6}Cr_{0.4}O_3$ and $YFe_{0.5}Cr_{0.5}O_3$ to the model as discussed in the text. Figure is taken from ref [199].

Due to the disordered nature of the system, the origin of reversal is related to the the weak ferromagnetism where the net canted moments aligned opposite to the applied magnetic field gives rise to the negative magnetization below T^*. The magnetization reversal in $YFe_{1-x}Cr_xO_3$ ($x = 0.4$ and 0.5) could be explained based on the semiclassical model considering superexchange and the DM interaction acting on the Fe – O – Fe, Fe – O – Cr and Cr – O – Cr pathways [166, 199]. In this model the free energy of the system was accounted only for Heisenberg superexchange ($JS_1.S_2$)and DM interactions $D_{12} \cdot (S_1 \times S_2)$ while ignoring the single ion anisotropy contribution. The DM interactions acting on the various superexchange paths D_{Fe-Fe}, D_{Cr-Cr} and D_{Fe-Cr} were obtained from the temperature dependence of magnetization data using the J values for Fe - Fe, Fe - Cr and Cr - Cr interactions. Interestingly, it was observed that D_{Fe-Fe}, D_{Cr-Cr} are positive whereas D_{Fe-Cr} is negative. The negative sign of D_{Fe-Cr} implies that the canting of Fe - O - Cr occurs opposite to that of Fe – O – Fe and Cr - O - Cr. As the Cr - O - Cr clusters orders at low temperature (T_N = 140 K for $YCrO_3$),

a competition arises due to DM interaction operating on Fe – O – Fe and Fe - O - Cr interactions. Though the single ion anisotropy was not considered, the negative value of D_{Fe-Cr} may be a consequence of different anisotropy factor of Fe^{3+} and Cr^{3+} ions. At high temperature (above T_N), Fe – O – Fe orders and the easy direction is determined by the Fe^{3+} anisotropy direction. Below T_N, the role of magnetocrystalline anisotropy of Cr^{3+} ions which is different compared to Fe^{3+} ions comes into play which would fix the easy direction of Fe - O - Cr. EPR experiments on Fe and Cr substituted $LaAlO_3$ compounds has shown the sign of second order anisotropy terms for Fe^{3+} and Cr^{3+} are opposite which suggest that sign of anisotropy Fe and Cr would also be different in matrix of Fe - Cr having $YFeO_3$ type structure [166, 231]. This also leads to a conclusion that the easy axis of matrix i.e., Fe - Cr is may be hard axis for the impurity ion Fe - Fe and vice versa. The different anisotropy factors seems to be defining factor which forces Fe – O – Fe and Fe - O - Cr moments to cant in opposite directions. These two canted moments compete each other resulting negative magnetization below T^*. Above discussion thus leads us to consider the ground state of $YFe_{1-x}Cr_xO_3$ system to be like ferrimagnetic where the canted antiferromagnetic moments of Fe - Cr and Fe - Fe act as two sublattice magnetizations. The net moment observed experimentally will be determined by the sum of the canted moments of impurity (Fe - Fe and Cr - Cr) and the matrix (Fe - Cr). Thus a compensation occurs when the canted moment of Fe - Cr becomes equal and opposite to the Fe - Fe moments as realized for the compound with x = 0.4. In case of compound x = 0.5, the contribution of Fe - Cr exceeds the Fe - Fe contribution immediately below T_N. Following the model described above, a good fit is obtained to the experimental data (taken from ref [199]) as shown in figure 6.11.

The origin of double compensation is $YFe_{0.2}Cr_{0.8}O_3$ is difficult to understand. Although, it should be noticed that this compound orders at 154 K. In this temperature range, the canted moments due to Cr - Cr clusters will also contribute and the system will behave like a ferrimagnet having three sublattices due to canted moments of Fe - Fe, Fe - Cr and Cr - Cr. The competing effect might result in such a double compensation though microscopic understanding would require further studies and theoretical support.

6.3.2 Structure and magnetic properties of $YFe_{1-x}Mn_xO_3$

6.3.2.1 Structure of $YFe_{1-x}Mn_xO_3$

Unlike $YFe_{1-x}Cr_xO_3$, the end members of $YFe_{1-x}Mn_xO_3$ have different structures. The compound $YFeO_3$ is orthorhombic as already mentioned whereas the ambient

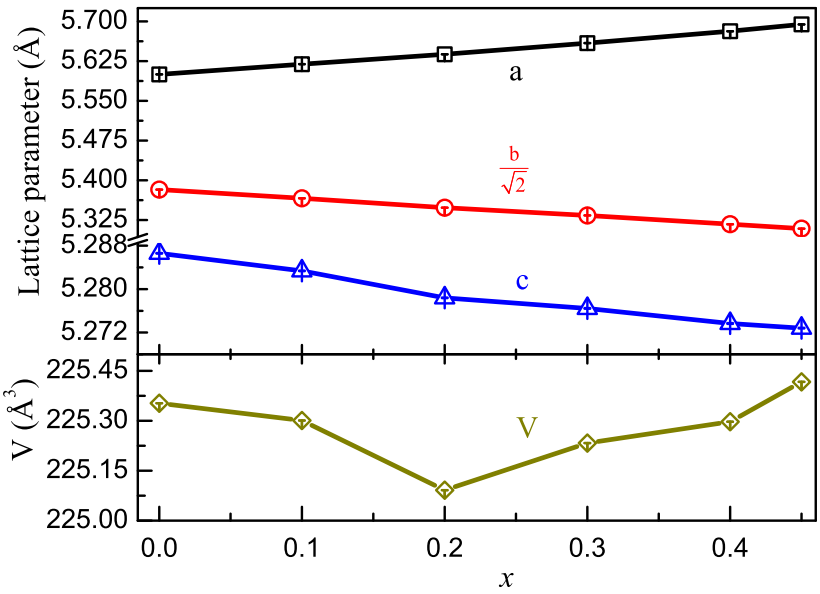

Figure 6.12: Unit cell parameters (a, $b/\sqrt{2}$, c) and cell volume (V), obtained from Rietveld refinements of room temperature X-ray diffraction data, plotted as a function of Mn concentration x in $YFe_{1-x}Mn_xO_3$.

Table 6.3: Atomic position (*x*, *y*, *z*) and isotropic thermal parameters (B) of $YFe_{1-x}Mn_xO_3$. Fe/Mn occupy 4*b* site (0, 0, 0.5).

$YFe_{1-x}Mn_xO_3$						
Site	Wyckoff Position	Mn level	*x*	*y*	*z*	B(Å^2)
Y	4*c*	0	0.0684(1)	0.2500	0.9826(2)	0.92(2)
		0.1	0.0700(1)	0.2500	0.9819(2)	0.78(2)
		0.2	0.0723(1)	0.2500	0.9818(2)	1.42(2)
		0.3	0.0732(1)	0.2500	0.9826(2)	1.21(2)
		0.4	0.0753(1)	0.2500	0.9822(2)	1.27(2)
		0.45	0.0764(1)	0.2500	0.9817(2)	1.26(2)
O1	4*c*	0	0.4597(8)	0.2500	0.1092(8)	1.00
		0.1	0.4602(7)	0.2500	0.1068(7)	1.00
		0.2	0.4636(7)	0.2500	0.1092(7)	1.00
		0.3	0.4610(8)	0.2500	0.1107(8)	1.00
		0.4	0.4599(7)	0.2500	0.1142(8)	1.00
		0.45	0.4575(8)	0.2500	0.1202(8)	1.00
O2	8*d*	0	0.6935(6)	-0.0574(4)	0.3087(6)	1.00
		0.1	0.6908(6)	-0.0592(4)	0.3072(6)	1.00
		0.2	0.6907(5)	-0.0570(4)	0.3057(6)	1.00
		0.3	0.6892(6)	-0.0570(5)	0.3055(6)	1.00
		0.4	0.6855(6)	-0.0558(5)	0.3038(6)	1.00
		0.45	0.6870(6)	-0.0576(5)	0.3011(7)	1.00

pressure phase of $YMnO_3$ has hexagonal structure (SG P6_3cm). Due to the different crystal structure of the parent compounds, a solid solution of $YFe_{1-x}Mn_xO_3$ can be obtained up to 45 % of Mn substitution. Above this limit, the structure is a mixture of orthorhombic and hexagonal phases and finally leads to the hexagonal structure. Rietveld refinements carried out on the room temperature X-ray diffraction data confirms the orthorhombic structure (SG: P*nma*). The obtained cell parameters and calculated volume are plotted against the Mn concentration in figure 6.12. The cell parameter *a* increases with *x* whereas the parameter *b* and *c* decreases with increasing Mn concentration. Thus, calculated cell volume decreases first and then increases. The increase in the *a* parameter with *x* indicates the presence of Jahn - Teller distortion associated

with Mn^{3+} ions, consistent with increasing difference between the equatorial and apical bond distances with *x*. Both Fe^{3+} and Mn^{3+} ions are randomly distributed at the 4*b* site in the P*nma* space group. These results are in accord with the earlier observations on oxides of the $RFe_{1-x}Mn_xO_3$ (R = Pr, Gd, Dy) family [219]. The result of Rietveld refinements are summarized in table 6.3.

6.3.2.2 Weak ferromagnetism and spin-reorientation in $YFe_{1-x}Mn_xO_3$

The field cooled magnetization as a function of temperature recorded at an applied field of 100 Oe is shown in figure 6.13 and figure 6.14. As seen in figure 6.13, the parent compound $YFeO_3$ (right axis) exhibits a weak ferromagnetic behavior in agreement

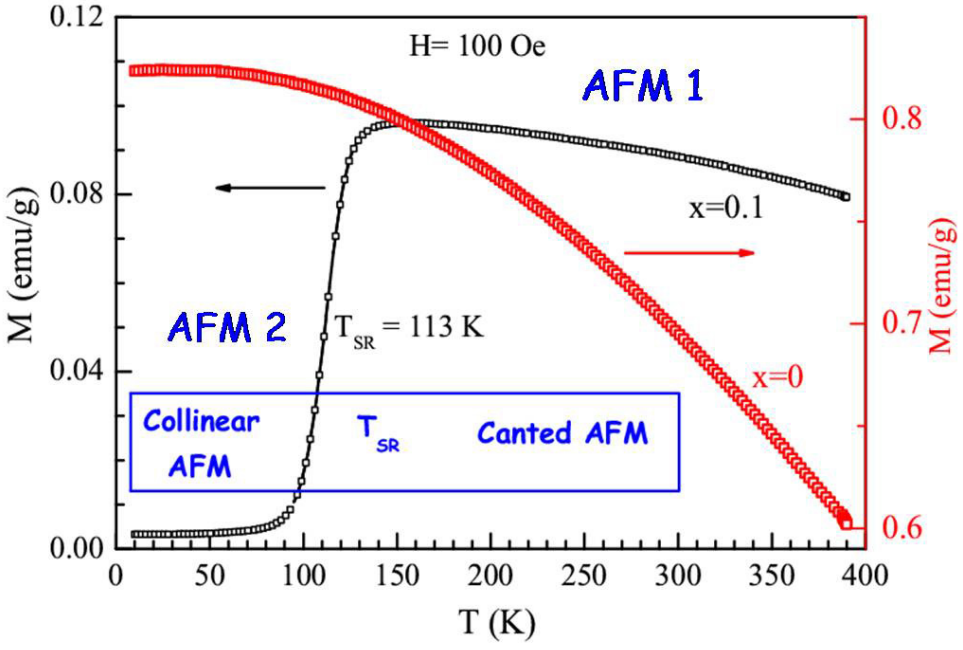

Figure 6.13: Field cooled magnetization curves of $YFe_{1-x}Mn_xO_3$ for *x*= 0 and 0.1 showing spin reorientation transition.

with earlier reports [227]. For x = 0.1, the canted antiferromagnetic state (AFM1) is retained down to 113 K (T_{SR}) below which magnetization drops sharply to nearly zero and does not change appreciably with further decrease of temperature. The transition from the canted antiferromagnetic (AFM1) to nearly collinear antiferromagnetic state (AFM2) is the spin – reorientation transition similar to Morin transition observed in hematite and orthoferrites [112, 232]. This transition is similar to the Cr substituted $YFeO_3$ systems as discussed in the previous section. In contrast to Cr substituted compounds, the present system shows a sharper transition indicating first-order nature of spin-reorientation. This is probably due to the large anisotropy associated with Mn^{3+} ions [195, 196, 233]. With increasing Mn concentration, T_{SR} increases whereas the T_N decreases as seen in the inset of figure 6.14, where T_N values for x= 0.1 – 0.3 are taken from reference [234]. For x= 0.4, both T_{SR} and T_N lies between 300 and 400 K. For x= 0.45, only one magnetic transition is observed at 330 K suggesting that the spin reorientation occurs at the Néel temperature. On the other hand, the substitution of Mn causes the spin – reorientation transition due to its large magnetic anisotropy which accounts for the increase in T_{SR} with increasing Mn concentration x [233]. The first – order nature of spin – reorientation transition is also evidenced from the hysteresis in the field – cooled warming (FCW) and field – cooled cooling (FCC) magnetization data (figure not shown). It is interesting to note the temperature dependence of magnetization in the low temperature AFM2 state. For x= 0.1, the magnetization is close to zero and remains almost unchanged with decreasing temperature. For x= 0.15, 0.2 and 0.3, the magnetization increases at very low temperatures indicating a weak spin canting in the AFM2 state as well. This is supported by magnetic isotherm data of $YFe_{0.6}Mn_{0.4}O_3$ at 5

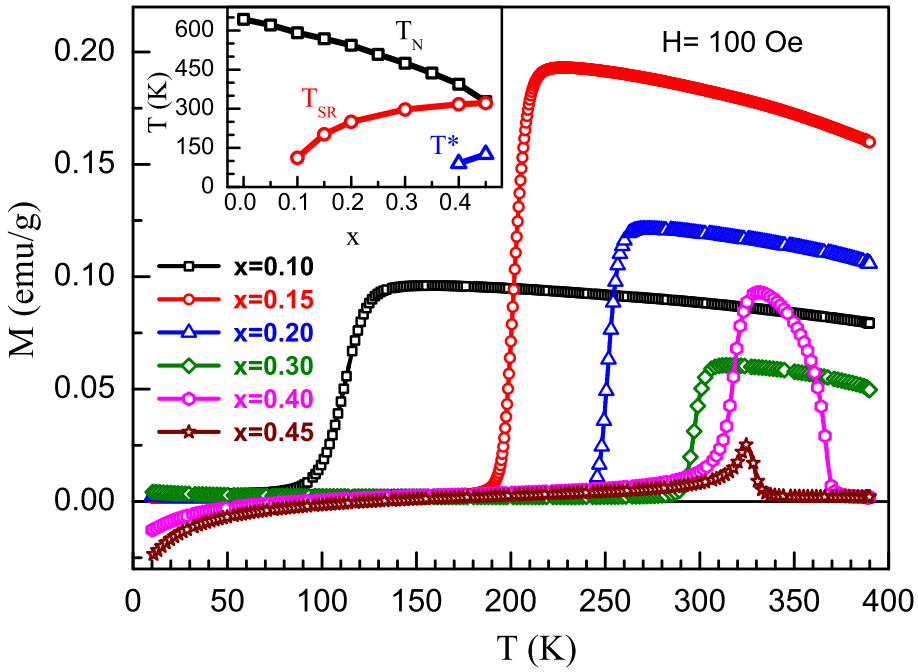

Figure 6.14: Field cooled magnetization curves of $YFe_{1-x}Mn_xO_3$ at an applied field of 100 Oe. Inset shows variation of T_N, T_{SR} and T^* (at 100 Oe) against the Mn concentration.

K where a weak hysteresis could be seen (figure 6.15). At an intermediate temperature (240 K) in the AFM2 state, where magnetization is almost temperature independent, a linear hysteresis loop suggests absence of spin canting. At 340 K, the hysteresis is consistent with spin canting in the AFM1 state.

6.3.2.3 Magnetization reversal

The novel aspect here is the temperature-induced magnetization reversal observed for x= 0.4 and 0.45. For x= 0.4, the magnetization becomes zero at a compensation temperature, $T^* = 90$ K (at 100 Oe) below which it is negative down to the lowest temperature measured as shown in figure 6.15. The other compound, $YFe_{0.55}Mn_{0.45}O_3$ shows nega-

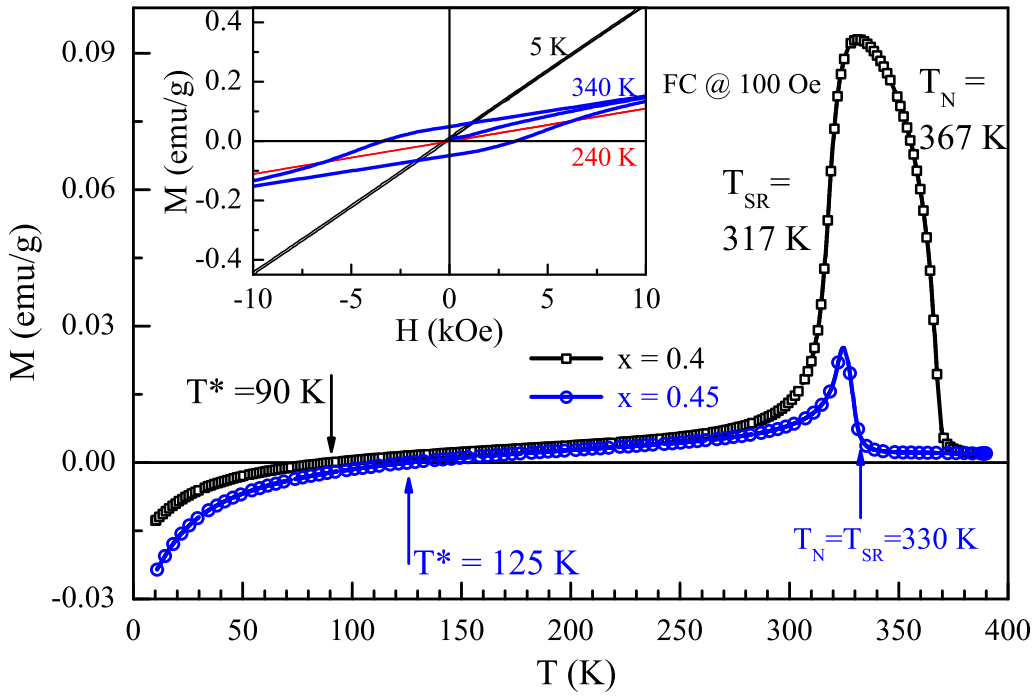

Figure 6.15: Field cooled data of $YFe_{0.6}Mn_{0.4}O_3$ and $YFe_{0.55}Mn_{0.45}O_3$ showing magnetization reversal at low temperatures. Magnetic isotherms collected at different magnetic states (canted, collinear and weakly canted) for x = 0.4 sample are shown in the inset.

tive magnetization below $T^* = 125$ K. With increasing Mn concentration, T^* increases, though it was not possible to go above $x = 0.45$ and would need high pressure synthesis. Further, with increase in magnetic field strength, T^* decreases and above a critical field strength the magnetization value becomes positive similar to $BiFe_{0.5}Mn_{0.5}O_3$ (figure 5.3).

6.3.2.4 Neutron diffraction studies on $YFe_{0.6}Mn_{0.4}O_3$

Similar to Cr compounds, the neutron diffraction data of $YFe_{0.6}Mn_{0.4}O_3$ collected at 400 K shows the presence of small peaks at $2\theta \sim 21^\circ$ as shown in figure 6.16. As the Fe^{3+} and Mn^{3+} ions are disordered at the 4*b* site of $YFe_{1-x}Mn_xO_3$, Fe – O – Fe, Fe – O

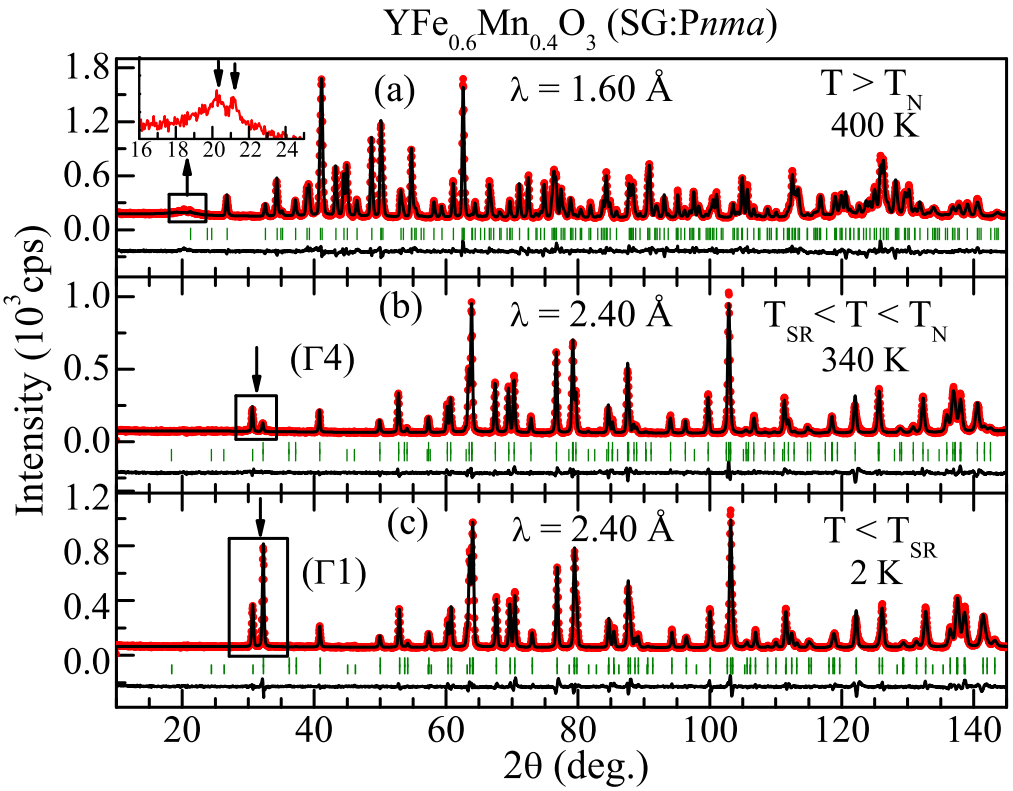

Figure 6.16: Rietveld refinement on the neutron diffraction data of $YFe_{0.6}Mn_{0.4}O_3$ collected at (a) 400, (b) 340 and 2 K. Magnetic reflections are indicated by arrows.

– Mn and Mn – O – Mn would order at the Néel temperatures of their respective parent compounds $YFeO_3$ (640 K), $YFe_{1-x}Mn_xO_3$ (T_N) and $YMnO_3$ (40 K) respectively [198, 229]. As this compound orders at T_N = 367 K, presence of the magnetic peaks at 400 K indicates the ordering of Fe - Fe clusters.

At 340 K, we observe that the most intense magnetic reflections (shown by arrow in figure 6.16b) correspond to the magnetic reflections arising from the ordering of Fe – O – Mn superexchange interactions. The AFM1 state at 340 K in $YFe_{0.6}Mn_{0.4}O_3$ (figure 6.15), has been modelled by the irreducible representation $\Gamma 4$ ($G_z F_y$) which is well known in the family of orthoferrite compounds. The component A_x is very small and thus neglected. The most intense magnetic reflections as indicated by arrow, correspond

to (1 1 0) and (0 1 1) planes which appear near 2θ of 31°. The (1 1 0) reflection is more intense than the second reflection (0 1 1). The reflections near 2θ = 36.5 ° corresponding to (1 0 1) and (0 2 0) planes are weak in the present compound which probably appears in $YFe_{0.5}Cr_{0.5}O_3$ due to presence of $\Gamma 2$ structure below T_N. As shown in top panel of figure 6.17, at 340 K the spins has easy direction along *z*-direction with a canting towards *y*-direction. This canting along *y* direction produces a net moment which is observed in magnetization measurements.

The neutron diffraction data collected at 2 K (figure 6.16*c*) shows that the intensities of (1 1 0) and (0 1 1) is reversed as compared to the 340 K data. This reflects a spin reorientation transition as also indicated in the magnetization showing a change from a canted to collinear states. As the equation 6.2 suggest that the most probable spin configuration would be $\Gamma 1$ which does not allow any ferromagnetic component from spin canting. The magnetic reflections could be described well with the $\Gamma 1$ ($G_x\, C_y$) representation where spins in G-type arrangement along *x*-direction is coupled with the C-type antiferromagnetic component coupled along *y*-direction. At the spin reorientation transition the antiferromagnetic easy axis abruptly changes from *z* to *x*-direction. The magnetic structure at 2 K, is displayed at the bottom panel of figure 6.17. As can be noticed the spins are oriented along *x* direction with a coupled C_y component. The C_y component is difficult to visualize due to small moment value. Unlike F-components, the canting due to C_y does not result in weak ferromagnetic moment. This is consistent with earlier reports which suggested the magnetic structure to change from $\Gamma 4$ to $\Gamma 1$ in $RFe_{1-x}Mn_xO_3$ (R = Y, Pr, Gd and Dy) compounds [219, 234]. Results of the Rietveld refinements on the Neutron data are given in table 6.4.

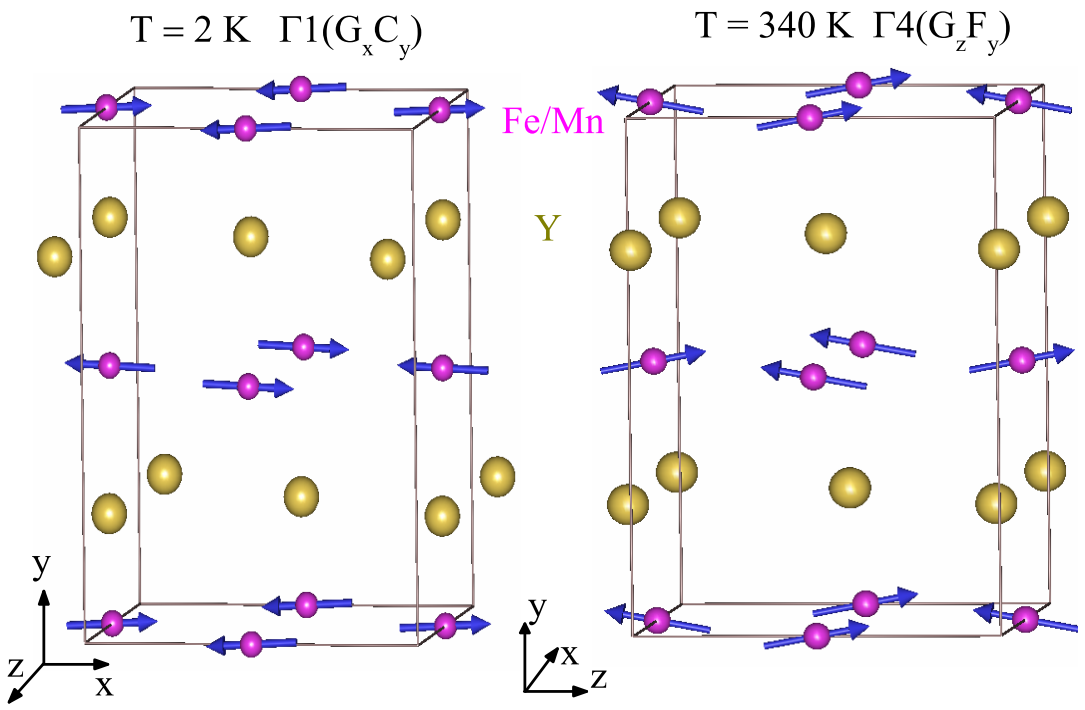

Figure 6.17: Magnetic structure of $YFe_{0.6}Mn_{0.4}O_3$ at 340 (above T_{SR}) and 2 K (below T_{SR}) having $\Gamma 4$ and $\Gamma 1$ configuration respectively.

The spin reorientation transition from $\Gamma 4$ to $\Gamma 1$ in $YFe_{0.6}Mn_{0.4}O_3$ is similar to that observed in $DyFeO_3$ and $ErCrO_3$ [235, 236]. In these orthoferrites/orthochromites, the abrupt spin reorientation was explained in terms of anisotropy of rare earth ions which exceeds the anisotropy of Fe or Cr ions at T_{SR} [112]. In $YFe_{1-x}Mn_xO_3$, the magnetic ions Fe^{3+} and Mn^{3+} have different magnetic anisotropy. In fact the Jahn-Teller distorted Mn^{3+} ions are known to possess large anisotropy as observed in $Fe_{3-x}Mn_xO_4$ and yttrium iron garnet systems [195, 196, 233]. At high temperature the anisotropy contribution of Fe^{3+} is larger and determines the easy direction. With decrease in temperature the anisotropy contribution of Mn^{3+} overcomes to that of Fe^{3+} and this forces the Fe – O – Mn moments to change the easy axis along the *x* direction.

It should be noted that $\Gamma 1$ structure does not contain any **F** component which would

Table 6.4: Atomic position (*x*, *y*, *z*), isotropic thermal parameters (B), Magnetic moments (μ), lattice parameters and other reliability factors at 400, 340 and 2 K as obtained from Rietveld refinements on neutron data.

$YFe_{0.6}Mn_{0.4}O_3$					
Site	Wyckoff Position	*x*	*y*	*z*	B(Å^2)
Y	4*c*	0.0736(2)	0.2500	0.9823(3)	0.68(2)
		0.0746(3)	0.2500	0.9819(3)	0.84(6)
		0.0757(3)	0.2500	0.9812(4)	0.45(7)
Fe/Mn	4*b*	0.00000	0.0000	0.50000	0.41(3)
		0.00000	0.0000	0.50000	0.11(7)
		0.00000	0.0000	0.50000	0.04(7)
O1	4*c*	0.4638(3)	0.2500	0.1100(4)	0.75(3)
		0.4621(4)	0.2500	0.1118(5)	0.84(6)
		0.4637(4)	0.2500	0.1130(5)	0.46(7)
O2	8*d*	0.6860(2)	-0.0554(2)	0.3045(2)	0.74(2)
		0.6862(3)	-0.0557(3)	0.3041(3)	0.82(4)
		0.6869(4)	-0.0553(3)	0.3037(3)	0.73(5)

Temperature (K)	Magnetic Structure	Magnetic moment, μ (μ_B)		
		μ_x	μ_y	μ_z
340 K	$\Gamma4(A_x\,F_y\,G_z)$	0.00	0.29(9)	1.51(2)
2 K	$\Gamma1(G_x\,C_y\,A_z)$	3.43(2)	0.16(10)	0.00

T (K)	*a*	*b*	*c*	χ^2	R_p	R_{wp}	R_B	R_f factor
400	5.6780(1)	7.5302(1)	5.2777(1)	7.43	11.0	11.4	4.98	4.14
340	5.6820(1)	7.5304(1)	5.2787(1)	4.01	14.0	13.0	2.86	2.26
2	5.6791(1)	7.5080(1)	5.2679(1)	5.46	13.3	13.2	3.24	2.40

restrict the system to exhibit canted antiferromagnetic behavior. The magnetic behavior in AFM2 state is difficult to understand and correlate to the neutron diffraction results. In contrast to the collinear magnetic state $\Gamma1$ observed in neutron experiment, magnetization measurement rather showed a spin canting at low temperature. The weak ferromagnetic behavior at low temperature ($< T^*$) is small compared to the magnetization value in the AFM1 state as shown in the magnetic isotherms in figure 6.15. Our efforts to model the low temperature (2 K) magnetic structure with either ($\Gamma1$ + $\Gamma4$) or ($\Gamma1$ + $\Gamma2$) phases, which would allow a weak ferromagnetism, were not successful. The

canted antiferromagnetic behavior may arise due to the presence of $\Gamma 4$ spin structure of AFM1 state or the $\Gamma 4$ phase of Fe - Fe impurity clusters. As the contribution is significantly less compared to the dominant $\Gamma 1$ phase and also the magnetic reflections appear at the same 2θ position, it is indeed difficult to identify this in neutron diffraction. The other possibility can be a magnetic field induced transition where the spin structure $\Gamma 1$ may change to a different structure allowing weak ferromagnetism. Neutron diffraction experiments under a magnetic field would be required to confirm this speculation.

6.3.2.5 Origin of magnetization reversal in $YFe_{1-x}Mn_xO_3$

Assuming the existence of weak ferromagnetism in AFM2 state, the semiclassical model described in case of $YFe_{1-x}Cr_xO_3$ still can not explain the reversal. This reflects the importance of anisotropy of Mn^{3+} which needs to be accounted with the DM interaction. Although, it is expected that in a polycrystalline material the anisotropy would be averaged out to zero, under some preparative conditions anisotropy can exist. The role of anisotropy has been confirmed by aligning the powder sample in a static magnetic field of 5 kOe. For this experiment, powder samples was mixed in a semi-viscous epoxy resin (GE varnish) and heated above T_N and a magnetic field of 5 kOe applied using a permanent magnet. This was allowed to solidify slowly at room temperature in presence of magnetic field. The solid piece was then used to measure the field cooled magnetization while applying the magnetic field parallel and perpendicular to the direction of alignment as shown in figure 6.18. As seen in figure the transition temperatures remain same but there is large change in the magnetization value as well as in the compensation temperature. Different behavior in the magnetization measurements

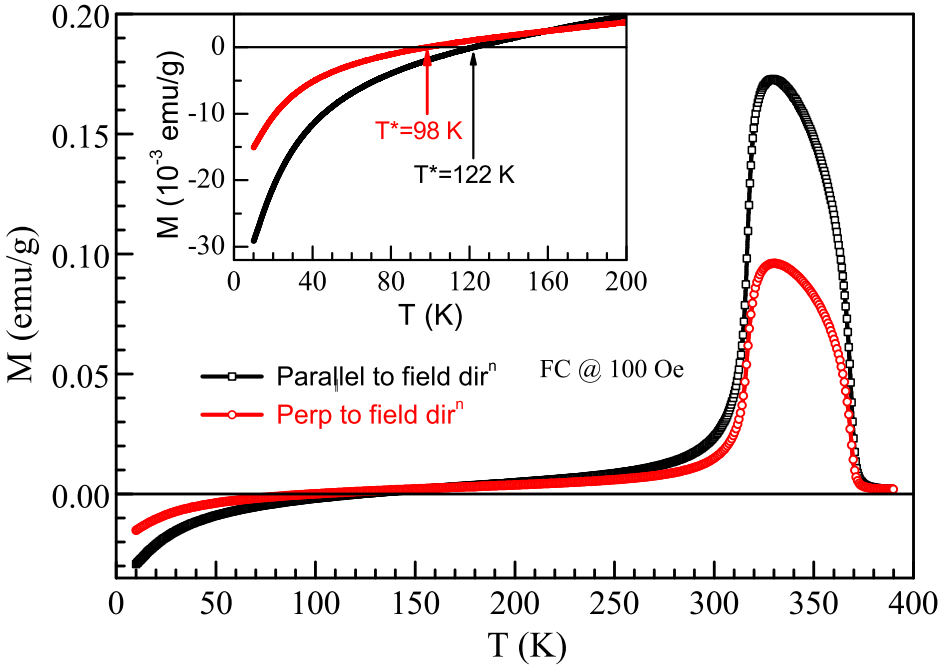

Figure 6.18: Field cooled magnetization curves of $YFe_{0.6}Mn_{0.4}O_3$ under 100 Oe of aligned powder sample measured in parallel and perpendicular to the magnetic field.

supports the existence of anisotropy in the powder sample.

In AFM2 state, the present system can also be considered to hold a ferrimagnetic ground state arising from the coupling of canted moments of Fe - Fe and Mn - Mn as the Fe - Mn forms a collinear spin structure $\Gamma 1$ as indicated from the neutron diffraction. The competition of these sublattices (Fe - Fe and Mn - Mn) thus can result a compensation temperature. As indicated in the neutron diffraction data at 400 K, the canted Fe - Fe clusters would still be present at low temperature. The Mn - Mn clusters which order at $\sim$ 42 K [198], are not expected to show canted antiferromagnetism at high temperature ($\sim T^*$). Although, there is a possibility that Mn - Mn moments are polarized by Fe - Mn or Fe - Fe moments which might contribute to net canted moments. As Fe - Mn moments give a net zero moment, the negative magnetization may arise due to the

polarized Mn - Mn cluster moments opposite to the canted moment of Fe - Fe.

Other than the results presented here, the reversal phenomenon has also been observed in compounds with mixed magnetic ions at the B-site such as $La_{1-x/2}Bi_{x/2}Fe_{0.5}Cr_{0.5}O_3$ [191, 201] and $YCr_{1-x}Mn_xO_3$ ($x = 0.1$ and 0.2) [200]. These distorted perovskites constitute a class of materials where magnetization reversal might have a similar origin. The present studies suggest that temperature-induced magnetization reversal may be a common phenomenon in canted antiferromagnetic system with mixed magnetic ions having different anisotropy.

6.3.2.6 Magnetocaloric effect in $YFe_{1-x}Mn_xO_3$

As discussed previously, in the Mn substituted $YFeO_3$ compounds, the antiferromagnetic ordering is second-order whereas the spin-reorientation is a first order transition. We shall now discuss magnetocaloric effect (MCE) across the two magnetic transitions in $YFe_{1-x}Mn_xO_3$. The entropy change (ΔS) can be calculated from magnetic isotherms data employing Maxwell's equation $(\delta S/\delta H) = (\delta M/\delta T)$ which follows to

$$\Delta S(T, H) = \int (\frac{\delta M}{\delta T}) dH \tag{6.5}$$

Experimentally, if the isotherm data are collected at constant steps of field and temperature, the above equation is approximated by,

$$\Delta S_M = \sum_i \frac{1}{T_{i+1} - T_i} (M_i - M_{i+1})_H \, \Delta H_i \tag{6.6}$$

where M_i and M_{i+1} are the magnetization values collected at the temperatures T_i and T_{i+1} at the constant field value of H [237]. Figure 6.19 shows entropy change ($-\Delta S$)

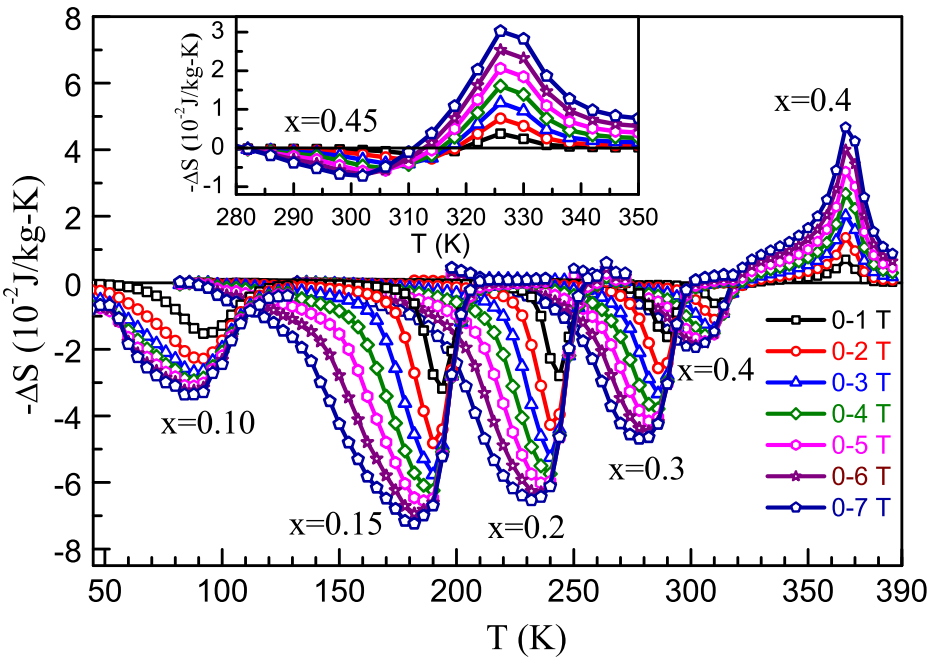

Figure 6.19: Entropy change, $-\Delta S$ against temperature for $YFe_{1-x}Mn_xO_3$. Inset shows the same for compound with x= 0.45

as a function of temperature at different magnetic field calculated from isothermal magnetization data using the above equation. For all the compounds, entropy change shows a negative peak or inverse MCE at the first – order spin – reorientation transition. For a given sample, the peak in $-\Delta S$ shifts towards lower temperature with increasing magnetic field strength which is consistent with the magnetic field dependence of spin – reorientation transition temperature. Above T_{SR}, the entropy change becomes positive and shows a normal MCE at the antiferromagnetic to paramagnetic transition where the peak is independent of magnetic field as this transition is second – order. It is evident from the figure 6.19 that the MCE can be tuned to above room temperature by varying Mn concentration. Further, for a given magnetic field and with increasing Mn concentration, the change in entropy ($-\Delta S$) shows a maximum at x= 0.15 which correlates

well with the corresponding magnetization value (not shown). For x= 0.45, though we do not see a clear separation of T_{SR} and T_N in magnetization data, our magnetocaloric measurements (inset in figure 6.19) clearly show a negative and positive MCE at 300 K and 327 K respectively at 7 T. The most interesting points to note here is the tunable MCE over a broad range of temperature (100 to 320 K for inverse MCE and 330 to 640 K for positive MCE) and presence of positive as well as inverse MCE in the same material. Having both types of MCE in the same system allows the material to be used as a refrigerant during magnetization (in case of inverse MCE) or demagnetization (in case of positive MCE) processes as observed in few systems [238, 239]. Unfortunately, the entropy change in the present case is two orders lower compared to Gd, [240] because the change in magnetization is small as the transitions involved are collinear to canted antiferromagnetic and canted antiferromagnetic to paramagnetic states. In the case of large magnetocaloric materials, the change in magnetization is large because of ferro- to para or ferro- to antiferromagnetic transitions [240, 241].

6.4 Conclusions

The compounds $YFe_{1-x}Cr_xO_3$ and $YFe_{1-x}Mn_xO_3$ crystallize in the orthorhombic structure (P*nma*). The chromium and manganese substituted compounds show second and first order spin-reorientation transitions below the Néel temperature. In case of Cr substituted compounds, the canted spin structure $\Gamma 4$ changes partially to $\Gamma 2$ state whereas in Mn compounds the spin structure changes from $\Gamma 4$ completely to $\Gamma 1$ at the spin reorientation transition. Most interestingly, negative magnetization is observed near equal mixing of Fe and Cr (or Mn). In these disordered oxides, the canted moments

due to DM interaction give rise to a ferrimagnetic like ground state and the competition of which results in compensation. Present study also suggest that magnetization reversal may be a common phenomenon in distorted perovskites containing mixed magnetic ions of different anisotropy. The observation of positive and negative tunable magnetocaloric effect in $YFe_{1-x}Mn_xO_3$ at the antiferromagnetic and spin – reorientation transitions respectively, is another interesting aspect.

CHAPTER 7

Ferroelectricity and Magneto(di)electric Effect in Centrosymmetric $YFe_{1-x}Mn_xO_3$[**]

7.1 Introduction

Magnetoelectric multiferroics are the materials which not only exhibit coexistence of ferroelectricity and ferromagnetism but also show a coupling between the order parameters i.e., the electric polarization can be altered or even switched with magnetic field and vice versa [13]. The cross-coupling between ferroelectric and ferro- or antiferromagnetic orders give rise to an extra degree freedom in device operation and has been suggested demonstrated to be useful for new device applications [78, 79]. Unfortunately, in most of the magnetoelectric multiferroic materials, the coupling is either weak or realized far below room temperature, which makes most of them inapplicable for practical usage. In magnetically induced multiferroic materials, ferroelectricity originates from a complex magnetic ordering and thus the cross coupling is quite strong. Magnetoelectric effect in these compounds is manifested in terms of the occurrence of a magnetically tunable polar state [34–36]. The magnetoelectric coupling inevitably leads to a magnetodielectric effect where the dielectric behavior can be changed with an external magnetic field. In several systems, however, magnetodielectric effect occurs without the presence of any polar state [242, 243]. Such magnetodielectric materials can also have potential applications in microwave tunable filters, miniaturization

[**]This work has appeared in *Phys. Rev. Lett.* **107**, 137202 (2011).

of antenna, magnetic sensors and spin-charge transducers [244]. The isostructural compounds $SeCuO_3$ and $TeCuO_3$ exhibit magnetodielectric effect at ferromagnetic (T_{CE} = 25 K) and antiferromagnetic (T_N = 9 K) transitions, respectively, due to spin-phonon coupling [242]. The strength of the magnetodielectric coupling is quantified in terms of the capacitance change upon application of magnetic field. The observed change in the capacitance is termed as magnetocapacitance and signifies a coupling between electric and magnetic orders. However, magnetocapacitance can originate from extrinsic effects in a Maxwell-Wagner effect due to a finite magnetoresistance[245, 246]. The magnetocapacitance is therefore not a confirmative signature of magneto(di)electric effect and it is necessary to identify and separate out the intrinsic magnetocapacitance from the interfacial magnetocapacitance [245].

In the previous chapter, we have discussed that spin reorientation in $YFe_{-x}Mn_xO_3$ is a first order transition whereas the antiferromagnetic ordering is second order. During the spin reorientation, the magnetic structure changes from $\Gamma 4$ to $\Gamma 1$ and so the transition is termed as a order - order type. We speculate that the first order transition might involve a change in the the local lattice structure that couples with the magnetic structure change. This motivated us to examine the coupling between electric order and magnetization by means of dielectric study. In this chapter, we discuss magneto(di)electric effect across the magnetic transitions in Mn substituted $YFeO_3$. The parent compound $YFeO_3$ is a canted antiferromagnet below the Néel temperature (T_N = 640 K), due to the antisymmetric Dzyaloshinskii-Moriya interaction [197]. The Mn substituted compounds show three magnetic states, canted antiferromagnetic state ($T_{SR} < T < T_N$), collinear state ($T^* < T < T_{SR}$) and weakly canted antiferromagnetic state ($T < T^*$).

With increase of x in $YFe_{1-x}Mn_xO_3$, T_N decreases whereas T_{SR} increases and these two transitions occur close to 330 K for x = 0.45. Interestingly, we found magnetodielectric effect at the spin-reorientation as well as at the antiferromagnetic transition. A large magnetocapacitance of 18% (50 kOe) is observed for x = 0.4 near T_{SR}. Furthermore, ferroelectricity appears at low temperatures (115 - 160 K) and the transition temperature (T_{CE}) decreases with increasing Mn concentration. Below T_{CE}, the electric polarization could be modified by an external magnetic field confirming a magnetoelectric coupling in these compounds. Anomalies in the temperature dependent phonon modes associated with the Jahn-Teller distorted MnO_6 octahedra, as probed by Raman spectroscopy, indicated a spin-phonon coupling at T_N, T_{SR} and T_{CE}. This could be the underlying mechanism for the magnetodielectric effect whereas the origin of ferroelectricity is related to the spin disorder at the B-site of the perovskite.

7.2 Experiments

Phase pure polycrystalline samples of $YFe_{1-x}Mn_xO_3$ (x = 0.1, 0.2, 0.3, 0.4) were prepared by solid state reaction route and details are described in the previous chapter. Magnetic measurements were carried out with a Vibrating Sample Magnetometer (VSM) in a Physical Property Measurement System (PPMS). Silver paint was applied on both sides of pellet and the capacitor was mounted in a custom made sample probe assembly which was then inserted in a 14 T cryo-cooled magnet system to collect temperature and magnetic field dependent data. Agilent 4294A impedance analyzer was used to study dielectric properties in the frequency range 100 Hz to 1 MHz by applying a small AC bias of 20 mV. Pyroelectric measurements were carried out using a Keithley

6517A electrometer. During this measurement the sample was poled down to lowest temperature and then shorted after removing the field to discharge any stray current. Pyroelectric current was then measured while heating the sample at the rate of 4 K/min. Raman experiments were carried out in the backscattering geometry using custom built Raman equipment [247] with a 532 nm laser excitation from a frequency doubled Nd-YAG laser with the laser power of 8 mW at the sample. Temperature dependent studies were performed using a temperature-controller (Linkam TMS 94) equipped with a heating stage unit (Linkam THMS 600).

7.3 Result and discussions

7.3.1 Magnetodielectric effect

The compounds were single phase with the orthorhombic structure (space group: P*nma*) as discussed in the previous chapter [200]. In this space group, Fe and Mn ions are randomly distributed at the same crystallographic (4*b*) site and therefore rules out the ordering of Fe and Mn ions. Mössbauer study has shown that Fe ions are present in trivalent state [248]. The local Jahn-Teller distortion inferred from different Fe/Mn – O bond lengths and change in lattice parameters with x confirm that Mn ions are also present in trivalent state. Figure 7.1 shows the variation of dielectric constant (left axis) and field cooled (FC) magnetization data (right axis) with temperature for compounds with x = 0.2 and 0.3. As clear from the figure, we observe anomalies in dielectric constant behavior near the magnetic transitions. This is a signature of coupling between dielectric and magnetic properties known as the magnetodielectric effect. The dielectric constant and magnetization data for x = 0.4 sample are displayed in figure 7.2. It can

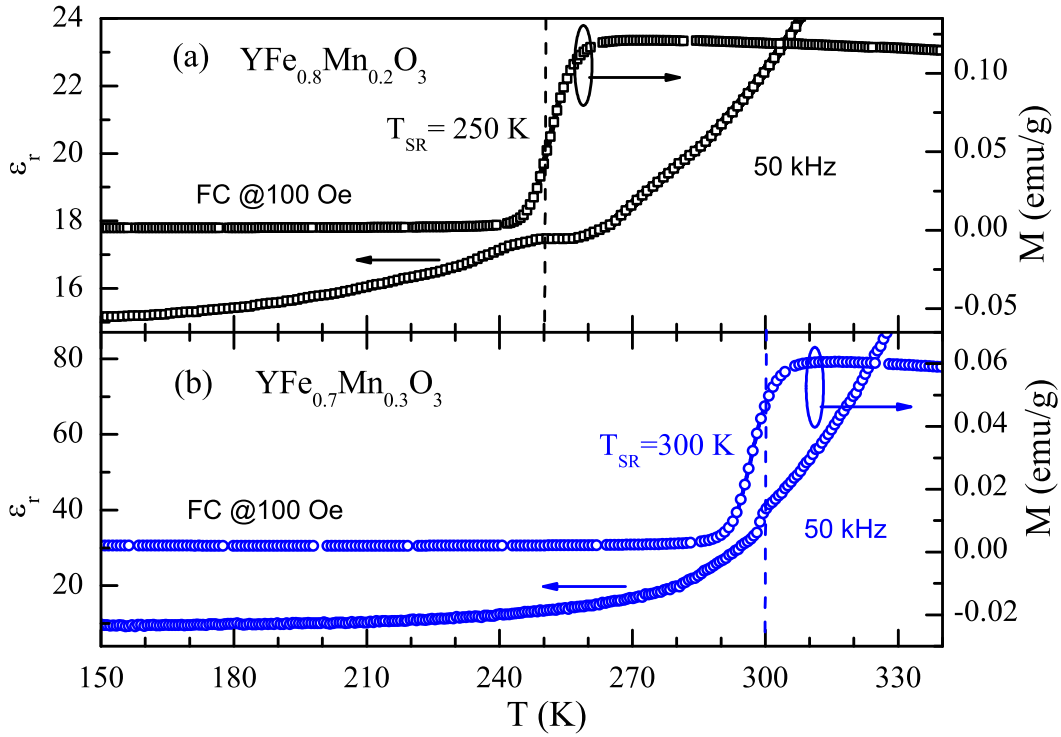

Figure 7.1: Magnetodielectric effect in $YFe_{1-x}Mn_xO_3$. Dielectric constant (left axis) shows an anomaly near the reorientation transition in field cooled magnetization data (right axis) in compounds $YFe_{0.8}Mn_{0.2}O_3$ (upper panel a) and $YFe_{0.7}Mn_{0.3}O_3$ (lower panel b).

be noticed that the dielectric anomaly is pronounced at higher Mn-concentration. For x = 0.1, we could not detect any anomaly at T_{SR} using our impedance analyzer indicating the important role of Mn in inducing magnetodielectric effect.

For a detailed investigation of magnetodielectric effect at the magnetic transitions, we chose the composition with maximum Mn content (x = 0.4), exhibiting spin reorientation close to room temperature. Figure 7.2a shows magnetization data for x = 0.4 recorded in field cooled warming (FCW) and field cooled cooling (FCC) modes (shown by arrows) under an applied field of 100 Oe. It can be seen that there is an irreversibility between the curves at T_{SR} = 317 K (100 Oe) confirming that the spin reorientation

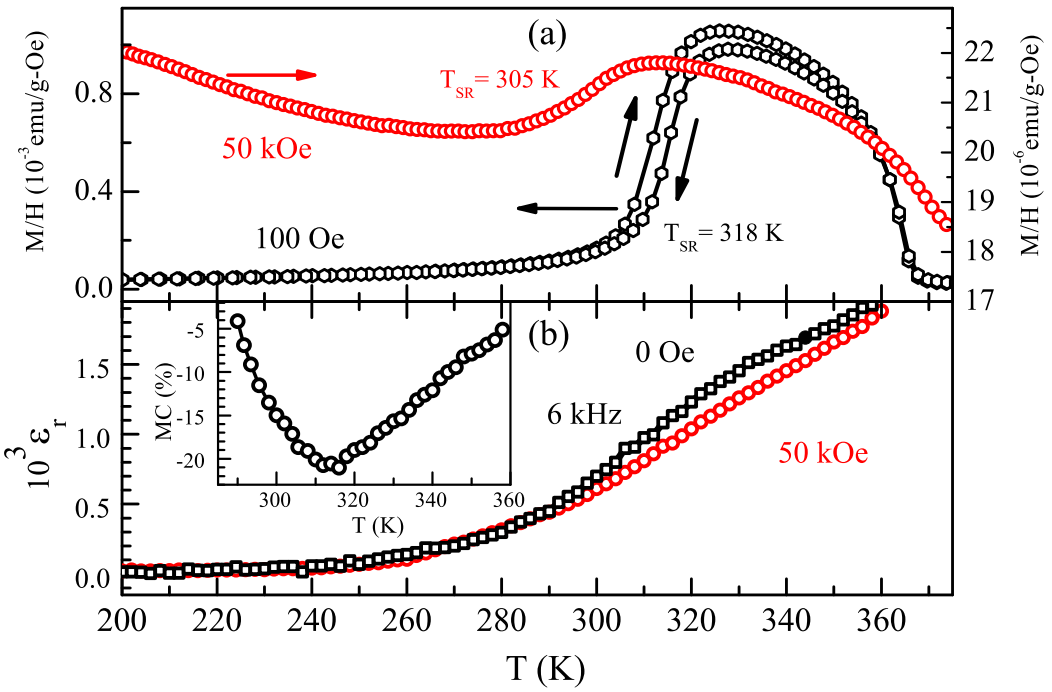

Figure 7.2: Temperature dependence of (a) field cooled magnetization data under applied field of 100 Oe and 50 kOe showing change in the spin reorientation temperature and (b) dielectric constant at 0 and 50 kOe revealing a magnetocapacitance effect in $YFe_{0.6}Mn_{0.4}O_3$. The inset shows magnetocapacitance which is maximum around T_{SR}.

is a first-order transition whereas the antiferromagnetic transition at $T_N = 367$ K is of second order. Dielectric measurements show a step-like increase in dielectric constant above 250 K and anomalies at T_{SR} (figure 7.3a) and T_N (figure 7.3b). Origin of the large value of dielectric constant at room temperature (2500 at 1 kHz) and step-like increase will be discussed later. A dielectric anomaly is also seen at T_N (figure 7.3b), confirming the magnetodielectric effect at both the magnetic transitions at T_{SR} and T_N. To explore the magnetodielectric effect further, we have investigated the effect of magnetic field on the spin reorientation transition and dielectric constant. Increase of magnetic field not only reduces T_{SR} but suppresses the spin reorientation as it is induced by strong

anisotropy of Mn^{3+} ions. As figure 7.2a demonstrates, on application of high magnetic field (50 kOe) T_{SR} is reduced to 305 K from 317 K (at 100 Oe), indicating that the dielectric constant might be affected by the applied magnetic field. We, indeed, observe large effect near 317 K at 50 kOe with no significant shift in the dielectric constant (figure 7.2b). The change in the capacitance i.e., magnetocapacitance ($\frac{C(H)-C(H=0)}{C(H=0)} \times 100$) is found to be $\sim 25\%$ at 6 kHz near T_{SR}. This magnetocapacitance value is quite large and more importantly appears near room temperature. Due to limitation of magnetic field at high temperature, we could not measure magnetocapacitance at T_N. However, a magnetocapacitance of $\sim 5\%$ at 50 kOe is observed at 360 K.

7.3.2 Maxwell-Wagner relaxation and intrinsic magnetocapacitance

As mentioned before, the measured magnetocapacitance has both intrinsic and extrinsic origin. In order to estimate the intrinsic contribution to magnetocapacitance near T_{SR}, we have carried out temperature and frequency dependence of capacitance and loss. Before we discuss about magnetocapacitance, it is important to understand the step-like increase of dielectric constant and its high value. A large dielectric constant is observed in ferroelectric materials near the Curie temperature. In non-ferroelectric materials, large dielectric constant values are observed due to polarization at grain boundaries or at the material-electrode interface known as Maxwell-Wagner effect [113]. As there is no magnetic anomaly at 250 K, the large value of dielectric constant in the present case may arise from Maxwell-Wagner effect. This was confirmed from the loss data which showed two peaks corresponding to different relaxations. The low temperature peak that corresponds to the step-like increase in dielectric constant, shifts towards high tem-

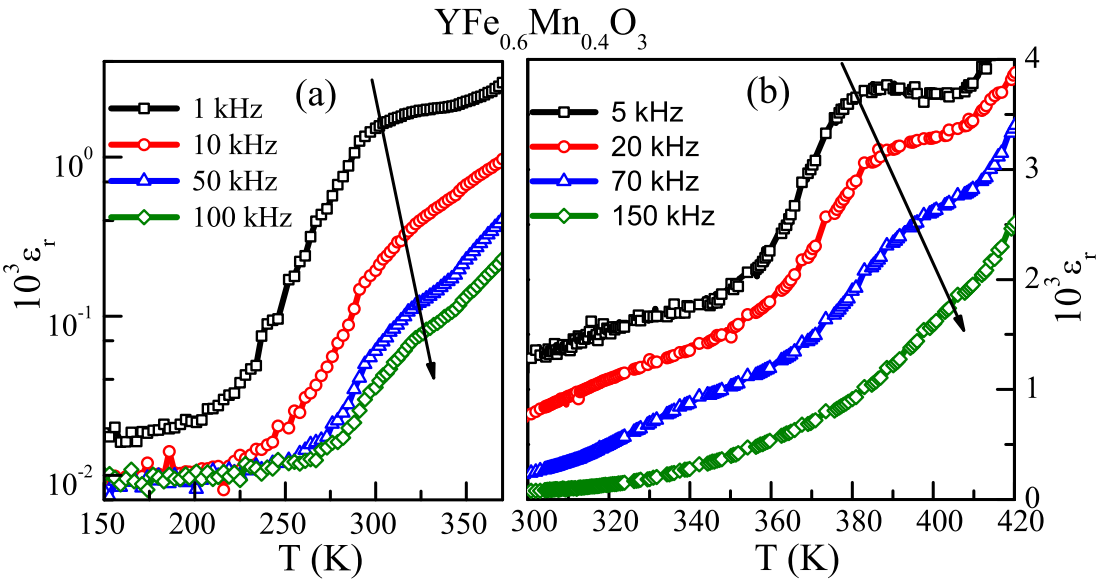

Figure 7.3: Temperature dependence of dielectric constant (ϵ_r) of $YFe_{0.6}Mn_{0.4}O_3$ at different frequency showing relaxation near (a) spin reorientation and (b) Néel temperature

.

perature with increasing frequency, thus confirming the presence of Maxwell-Wagner relaxation. Clearly, there is a contribution from the Maxwell-Wagner effect to the observed magnetocapacitance effect. The second peak at high temperature, corresponds to the dielectric constant anomaly at 320 K, follows Debye relaxation. To estimate the extrinsic contribution due to Maxwell-Wagner effect to the magnetocapacitance, we have analyzed magnetoresistance and the frequency dependence of magnetocapacitance and magnetoloss. In the Maxwell-Wagner model, the material under test can be considered as two parallel capacitance-resistance (C-R) circuits connected in series with one of the resistance in C-R circuits possibly having magnetically tunable resistance. Consequently, a finite magnetoresistance can induce a magnetocapacitance which should not be attributed to magnetodielectric coupling [245]. Intrinsic behavior can be observed at frequencies greater than the corresponding relaxation time ($f_0 = \tau_0^{-1} = RC^{-1}$) below

which the slow resistive processes contribute significantly to the dielectric response. Four-probe resistivity data showed a high value ($> 10^5$ Ohm-cm) near room temperature indicating insulating behavior of the compound. A negligible magnetoresistance ($\leq 0.3\%$) was observed near the magnetic transitions even at a high field of 50 kOe whereas the corresponding magnetocapacitance value is 18% as shown in the inset of figure 7.4. Thus, the large magnetocapacitance observed here cannot be explained in terms of small magnetoresistance.

We have estimated the extrinsic and intrinsic contributions by analyzing the frequency dependence of magnetocapacitance and magnetoloss. As shown in figure 7.4a,

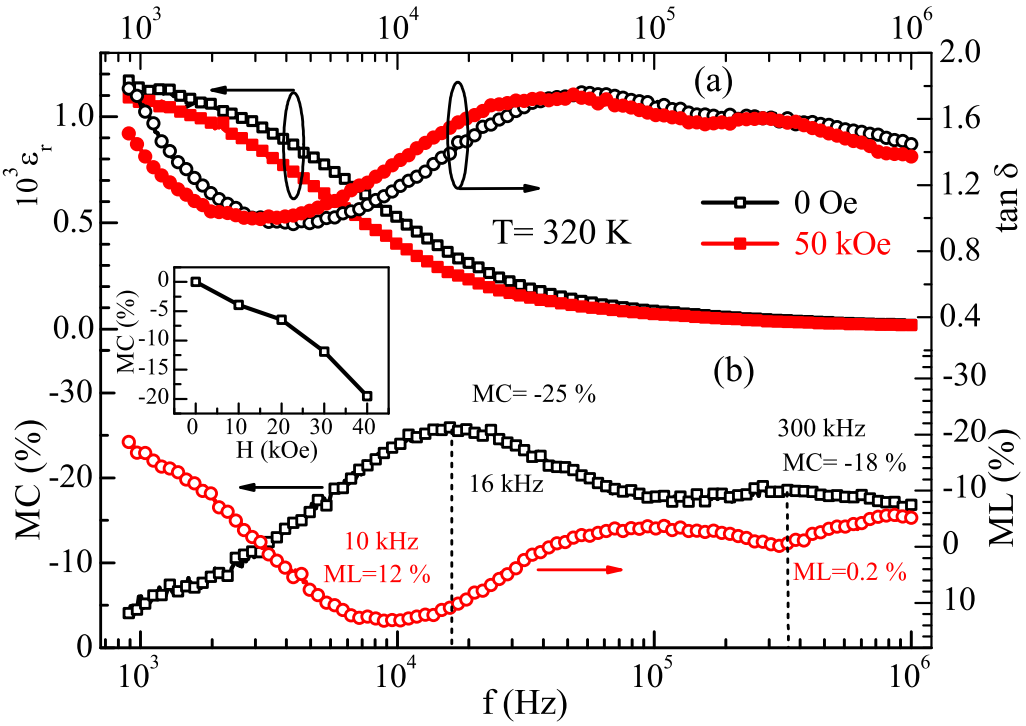

Figure 7.4: (a) Top panel shows frequency dependence of dielectric constant (left axis) and loss (right axis) under magnetic fields of 0 and 50 kOe at 320 K. Bottom panel (b) shows magnetocapacitance (MC) and magnetoloss (ML) against frequency. Inset shows field dependence of magnetocapacitance. Large MC and low ML values at high frequency indicate intrinsic magnetodielectric behavior.

the real part of dielectric constant shows a fall with increasing frequency, which coincides with the peak in loss spectra (at 55 kHz). This behavior is indicative of a Debye-like relaxation process in a Maxwell-Wagner system. At 50 kOe of magnetic field, the dielectric constant value decreases with a corresponding shift in the loss peak to 44 kHz. Magnetocapacitance value increases at low frequency taking a peak at 16 kHz and remains almost constant at high frequency ($f > \tau_0^{-1}$). On the other hand, magnetoloss changes from high negative value (-20 %) at low frequency to a positive maximum value of 12 % at 10 kHz whereas at very high frequency the magnetoloss value is small. An important feature to note that at low frequency the maximum of magnetocapacitance and magnetoloss curves do not exactly coincide with each other which would be expected in the case where magnetocapacitance is completely driven by extrinsic effects. On the other hand, high frequency magnetocapacitance value is quite high (18 % at 300 kHz) where the corresponding magnetoloss is low (0.2 %). At high frequency, Maxwell-Wagner relaxation related resistive processes do not respond and therefore the magnetocapacitance of 18% is intrinsic. The large magnetocapacitance arises due to the field dependent spin-reorientation transition where there is a change in the magnetic structure that couples with the local lattice structure [217].

7.3.3 Ferroelectricity and magnetoelectric coupling

In order to explore whether the observed magnetodielectric effect at the magnetic transitions is accompanied by a ferroelectric order, we performed pyroelectric current measurements. Initial pyroelectric experiments where the poling voltage was applied at high temperature (300 K), indicated the ferroelectric transition to be below 160 K. For

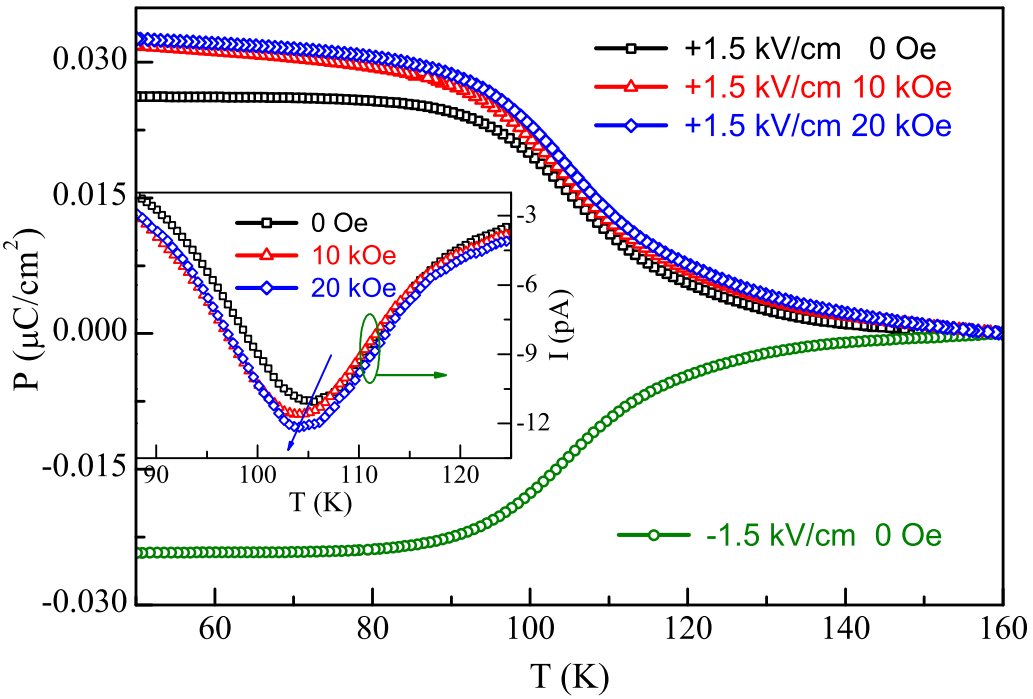

Figure 7.5: Temperature dependence of ferroelectric polarization, P in $YFe_{0.6}Mn_{0.4}O_3$ at positive and negative poling fields confirming bipolar nature. Polarization is observed to increase with magnetic field with a corresponding decrease in the the Curie temperature

all the results discussed, the poling voltage was applied at 200 K. Interestingly, the pyroelectric current shows a peak ranging from 105 to 150 K for the compounds with x = 0 to 0.4 both at the negative and positive poling fields. The polarization, obtained from integration of current data with respect to time, shows a ferroelectric to paraelectric transition (T_{CE}). The transition temperature shifts to higher temperature with decreasing Mn concentration and the transition was observed at 150 K for the compound with x = 0.1. Temperature dependence of electric polarization (P) for x = 0.2 and 0.4 samples are shown in figure 7.5 and figure 7.6 both at positive and negative poling fields. Though the polarization values observed in this system are small (0.02 $\mu C/cm^2$) they

are comparable to those reported for related materials [34–36]. To confirms whether the polarization is switchable, the following experiment has been performed on the sample $YFe_{0.8}Mn_{0.2}O_3$ shown in figure 7.6. As seen in the figure, the polarization shows ferroelectric to paraelectric transition for positive and negative poling fields. The capacitor was again poled down to the lowest temperature with a bias of +1.66 kV/cm. After shorting both ends, the capacitor was subjected to a negative field (E_{max} = -4.4 kV/cm) and shorted again. After removing the shorting, pyroelectric current was measured in usual way. This reduced the polarization value but could not switch the polarization to opposite polarity suggesting either the applied bias is low or the polarization is not switchable. The same procedure is repeated where the reverse bias was applied at slightly high temperature at 100 K. Indeed, the polarization is reversed as shown in figure 7.6. This proves the bipolar nature of these compounds. Variation of T_N, T_{SR} and T_{CE} are summarized in figure 7.7.

To further study the magnetoelectric nature of these compounds, it is important to note the effect of magnetic field on the ferroelectric polarization. As seen in figure 7.5, the polarization increases with applied filed, indicating a substantial magnetoelectric coupling. Further, with increasing field the ferroelectric transition shifts to low temperature, which might indicate a relevance of spin-phonon coupling to the physical origin of ferroelectricity. It should be noticed that although magnetodielectric effect occurs at the magnetic transition, the polarization appears much below. This might imply that ferroelectricity and magnetodielectric effect may not have a common origin. In magnetically induced multiferroic materials, the ferroelectric transition is reflected as an anomaly in magnetization, dielectric constant and heat capacity data. In the present

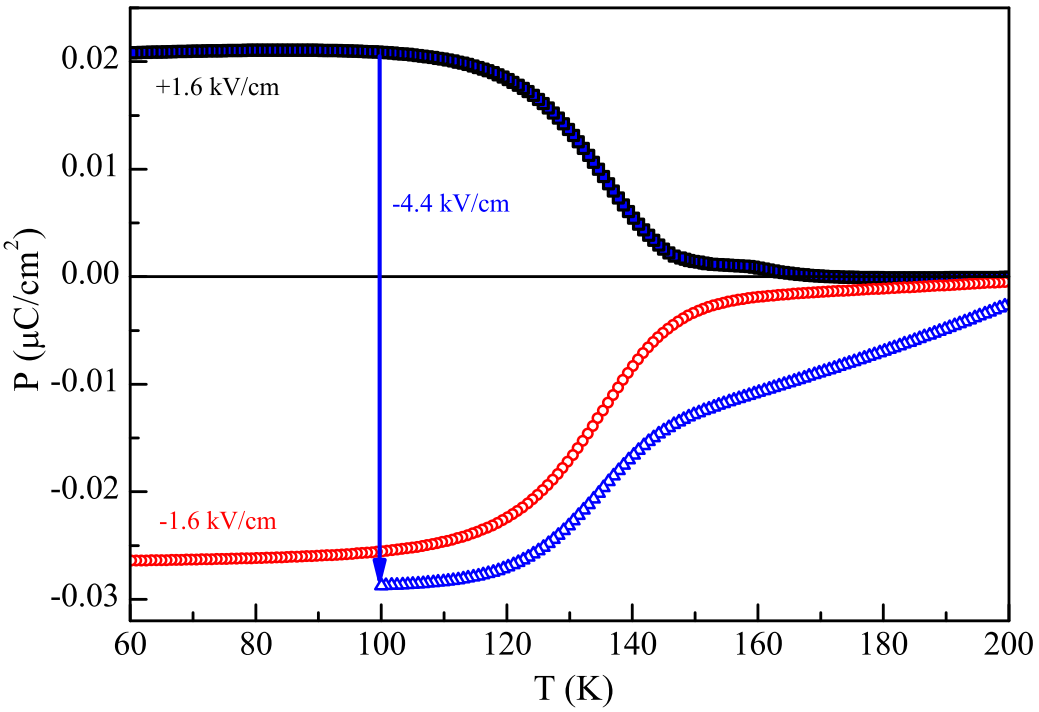

Figure 7.6: Reversal of ferroelectric polarization, P in $YFe_{0.8}Mn_{0.2}O_3$ confirming bipolar nature.

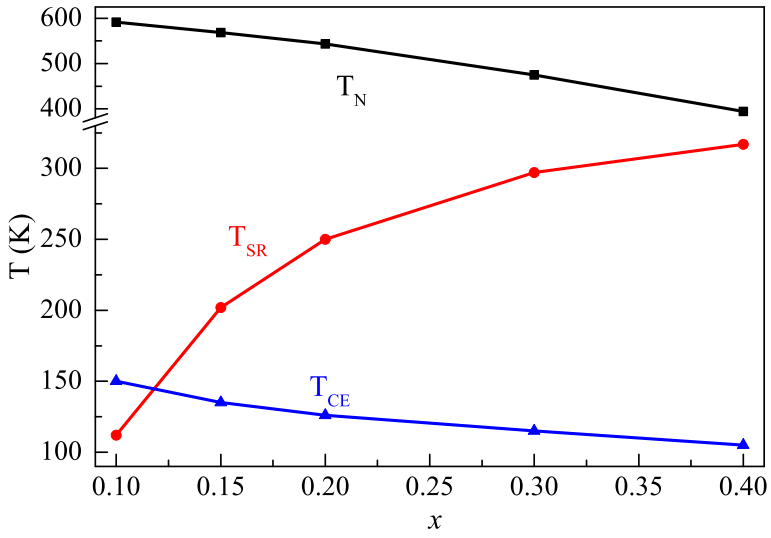

Figure 7.7: Variation of T_N, T_{SR} and T_{CE} with Mn concentration.

system, we did not observe any anomaly which makes the magnetoelectric nature difficult to understand. However, as there is no structural transition, we believe that the

ferroelectricity is magnetism induced.

7.3.4 Origin of ferroelectricity and magneto(di)electric effect

7.3.4.1 Spin-phonon Coupling

Raman spectroscopic measurements have been carried out across the magnetic and ferroelectric transitions in $YFe_{0.6}Mn_{0.4}O_3$. Unpolarized Raman spectrum recorded at room-temperature is shown in figure 7.8. Lattice dynamical calculations have predicted 24 Raman active modes in the orthorhombic perovskites [249]. The mode assignment corresponding to various vibrational symmetries is shown in figure 7.8. Deconvolution of the strongest Raman feature centered at 640 cm^{-1} shows two prominent bands at 624 and 648 cm^{-1} corresponding to B_{3g} and B_{2g} symmetries. Since, it is observed that these modes are weak in $YFeO_3$ and are intense in $RMnO_3$ systems [249, 250], we attribute these modes to the out-of-phase and in-phase stretching of Jahn-Teller distorted MnO_6 octahedra respectively. The temperature dependence of the frequencies of modes at 624 and 648 cm^{-1} around the ferroelectric and magnetic transitions are shown in figure 7.8 *b* and *c*, respectively. For a general case, the temperature dependence of phonon frequency ω(T), follows the relation $\omega(T) = \omega_0 - C(1 + (2/e^{(\hbar\omega_0/2k_BT)} - 1))$ which describes solely the anharmonic phonon-phonon scattering [251]. In the present case, the temperature dependence of both B_{2g} and B_{3g} modes deviates from the above relation at T_{CE}, T_N and T_{SR}. These modes display subtle hardening at T_N, softening across T_{SR} and a sudden increase in phonon frequency at T_{CE}. These anomalous behavior is attributed to spin-phonon coupling caused by the phonon modulation of spin exchange integral [252]. Furthermore, the FWHM (full width half maxima) of the phonon modes

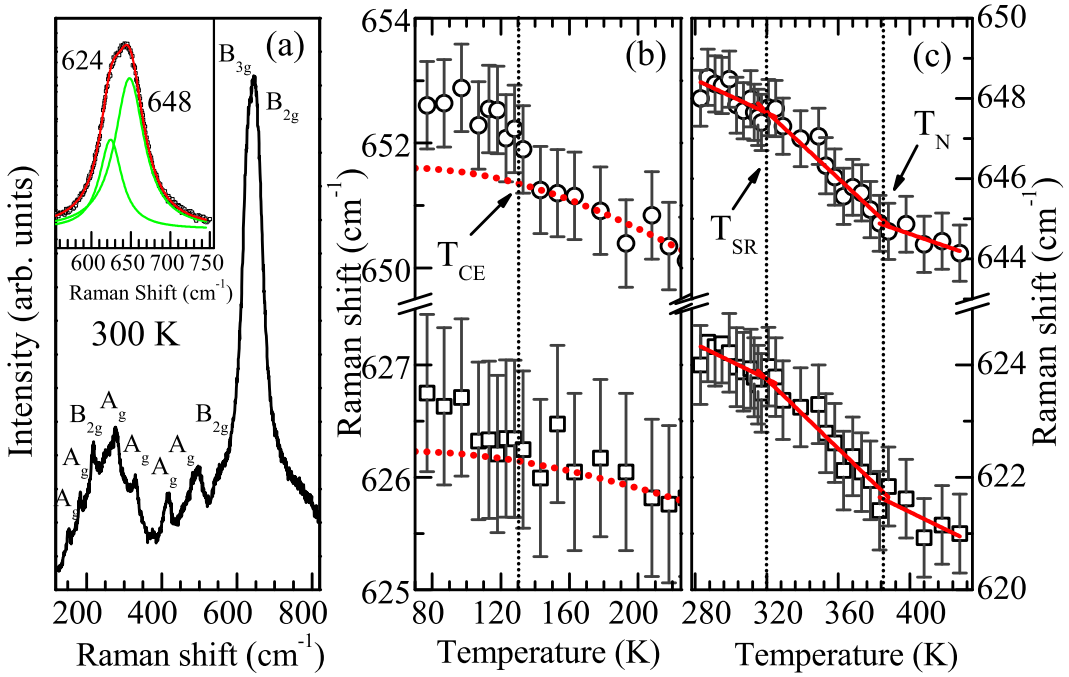

Figure 7.8: (a) Raman spectrum of $YFe_{0.6}Mn_{0.4}O_3$ recorded at room temperature. Inset shows the deconvoluted peak centered around 640 cm^{-1} into B_{2g} and B_{3g} modes. Temperature dependence of frequency corresponding to B_{2g} and B_{3g} phonon modes across the (b) ferroelectric and (c) magnetic transitions. Solid lines in (c) are guide to eye and dotted lines in (b) represent the anharmonic contributions.

increases below T_{SR} and T_{CE} (data is not shown), which indicates that there is a decrease in the lifetime of the phonons due to spin-phonon coupling. Thus, these results suggest that the spin-phonon coupling is responsible for the magnetodielectric effect at the magnetic transitions.

7.3.4.2 Spin disorder

Ferroelectricity in magnetism induced multiferroics has been observed to appear from cycloidal and conical spin structure [34–36]. Neutron diffraction studies as discussed in Chapter 6, did not confirm presence of any complex magnetic ordering at low tem-

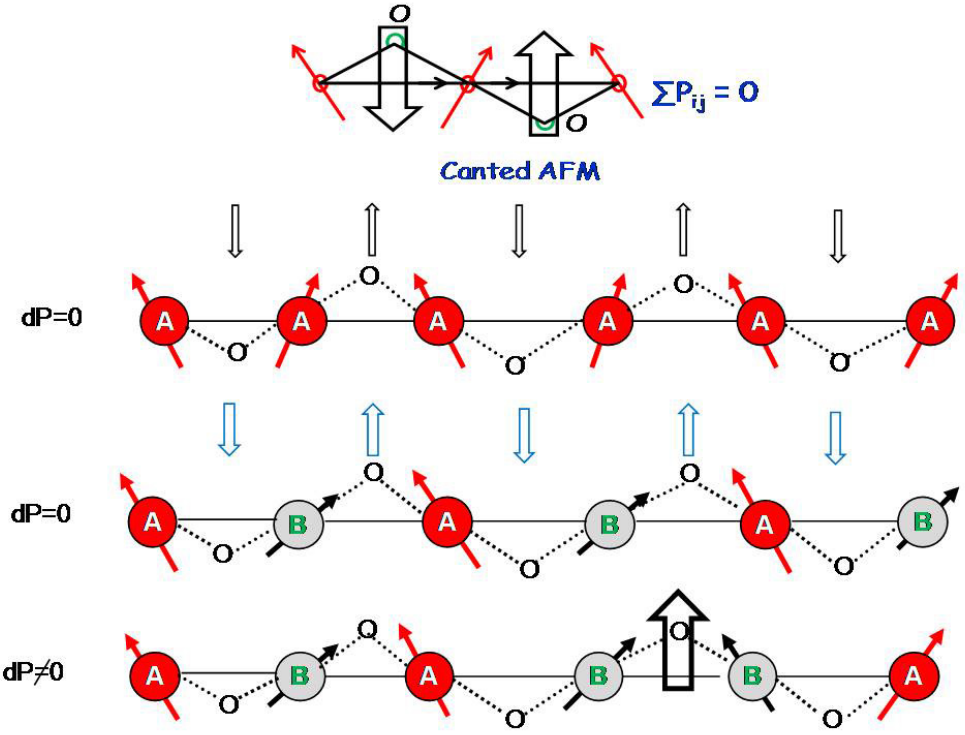

Figure 7.9: Spin-disorder model [71] showing a net polarization induced when magnetic ions are disorder randomly.

perature. For the present compound, the ferroelectricity can be understood in terms of spin-disorder model proposed by Bharath *et al* [71]. In this scenario, each adjacent spins (S_i and S_j) pair produces a local polarization and net polarization can be expressed as

$$\mathbf{P} = a \sum_{<i,j>} \mathbf{e}_{ij} \times (\mathbf{S}_i \times \mathbf{S}_j)$$

where, $\mathbf{e}_{ij}$ is unit vector along the direction connecting the adjacent spins and a is a constant involving spinorbit and spin-exchange interactions as well as the possible spin-lattice coupling terms [63–65]. In a canted antiferromagnet although a polarization is produced locally between two adjacent spins but next neighbour spins produces exactly opposite polarization giving rise to a net zero polarization as shown in figure 7.9. In

the situation, where the different magnetic ions are ordered, the net polarization is still zero. It can be seen that when the canted antiferromagnetic moments are disordered randomly, there is net polarization which is not canceled out (shown by thick arrow). It is also noticed that the ferroelectricity appears nearly at temperature below which the compounds show canted antiferromagnetic behavior in AFM2 state. According to this explanation, the ferroelectricity should appear at the Néel temperature. Although, due to instrument limitation and high leakage current in these samples, the poling field could not be applied above T_N. Very recently, few canted antiferromagnets with spin-disorder have also been shown to exhibit magnetoelectric behavior [71, 72].

7.4 Conclusion

We have demonstrated the occurrence of the magnetodielectric and magnetoelectric effect at different temperature scales in perovskite Mn-substituted yttrium orthoferrite. Magnetodielectric effect and large magnetocapacitance observed near room temperature is proven to be intrinsic and induced by spin-phonon coupling. The ferroelectricity at low temperature is induced by the disorder of magnetic ions at the B-site.

CHAPTER 8

Summary

Multiferroic properties and temperature induced magnetization reversal in Bi and Y based perovskite oxides have been investigated.

The perovskite, $BiFeO_3$ is a room temperature multiferroic which does not show any macroscopic magnetization due to a spiral magnetic ordering. Substitution of non magnetic ions such Al and Sc at the Fe-site have been found to induce finite magnetization which might be due to suppression of spiral magnetic ordering. Further, Sc substitution is proven to improve dielectric and ferroelectric properties compared to Al substitutions.

Bi based double perovskite is another candidate for multiferroics where the superexhange interaction between the ordered B-site ions can give rise to a ferromagnetic ground state similar to Bi_2NiMnO_6. Contrary to the anticipation, the high pressure synthesized compound $BiCr_{0.5}Mn_{0.5}O_3$ has a centrosymmetric structure where Cr and Mn are disordered. This compound exhibits unusually giant dielectric constant similar to $CaCu_3Ti_4O_{12}$. Using dielectric and impedance spectroscopy it is demonstrated that the behavior is extrinsic and arises due to Maxwell-Wagner relaxation at the grain boundary and material-electrode interface.

$BiFe_{0.5}Mn_{0.5}O_3$ was synthesized at high pressure and high temperature to obtain coexistence of ferroelectricity and ferromagnetism. The trivalent Fe and Mn ions are disordered at the B-site of orthorhombic structure. Surprisingly, the compound

shows a negative magnetization below a compensation temperature. Substitution by Sr and La at the Bi-site using ambient pressure solid state reaction changes the structure to rhombohedral. Absence of the magnetization reversal in these compounds indicates important role of orthorhombic distortion.

To understand the reversal phenomenon, $YFe_{1-x}M_xO_3$ (M = Cr and Mn) were synthesized at ambient pressure. These compounds crystallize in orthorhombic structure (P*nma*) and undergo a spin reorientation transition below Néel temperature. The transition is second order for Cr and first order for Mn substitutions. Temperature induced magnetization reversal is observed in compounds near equal mixing of Fe and Mn/Cr ions. It is observed that the reversal is common in many canted antiferromagnetic oxides with magnetic ions disordered at the B-site. The reversal is understood based on the ferrimagnetic like ground state arising from the antiferromagnetic coupling of various superexchange interactions.

The centrosymmetric $YFe_{1-x}Mn_xO_3$ shows a first order spin-reorientation transition below the Néel temperature. A magnetodielectric effect is observed at the magnetic transitions whereas ferroelectricity appears at a much lower temperatures. For x = 0.4 sample, a large intrinsic magnetocapacitance is observed near room temperature. Further, electric polarization could be altered by magnetic field confirming the material to be a new magnetoelectric multiferroic. Magnetodielectric effect is attributed to the spin-phonon coupling whereas the polar state may arise due to spin-disorder.

References

1. V. K. Wadhawan. *Introduction to Ferroic Materials*.

2. Charles Kittel. *Introduction to Solid-State Physics*. WILEY-INDIA.

3. J. Valasek. Piezo-Electric and Allied Phenomena in Rochelle Salt, *Phys. Rev.* **17**, 475–481 (1921).

4. B. M. Wul and I. M. Goldman. Dielectric Constants of Titanates of Metals of the Second Group, *Dokl. Akad. Nauk SSSR* **46**, 154 157 (1945).

5. A. von Hippel, R. G. Breckenridge, F. G. Chesley and L. Tisza. High Dielectric Constant Ceramics, *Ind. Eng. Chem.* **38**, 1097 (1946).

6. P. Weiss. *J. Phys.* **6**, 661 (1907).

7. W. Heisenberg. Zeitschrift für Physik A Hadrons and Nuclei, *Mehrkörperproblem und Resonanz in der Quantenmechanik* **38**, 411 – 426 (1926).

8. P. A. M. Dirac. On the Theory of Quantum Mechanics,, *Proceedings of the Royal Society of London, Series A 112* **762**, 661 – 677. (1926).

9. P. W. Anderson. Antiferromagnetism. Theory of Superexchange Interaction, *Phys. Rev.* **79**, 350 – 356 (1950).

10. John B. Goodenough. Theory of the Role of Covalence in the Perovskite-Type Manganites [La, M(II)]MnO_3, *Phys. Rev.* **100**, 564 (1955).

11. Junjiro Kanamori. Superexchange interaction and symmetry properties of electron orbitals, *J. Phys. Chem. Solids* **10**, 87 – 98 (1959).

12. Manfred Fiebig. Revival of the magnetoelectric effect, *J. Phys. D: Appl. Phys.* **31**, R1 – R30 (2005).

13. W. Eerenstein, N.D. Mathur and J.F. Scott. Multiferroic and magnetoelectric materials, *Nature* **442**, 759 – 765 (2006).

14. W. C. Röntgen. Ueber die durch Bewegung eines im homogenen electrischen Felde befindlichen Dielectricums hervorgerufene electrodynamische Kraft, *Ann. Phys.* **271**, 264–270 (1888).

15. P. Curie. *J. Physique* **3**, 393 (1894).

16. I. E. Dzyaloshinshkii. *Sov. Phys. JETP* **10**, 628 (1960).

17. D. N. Astrov. *Sov. Phys. JETP* **11**, 708 (1960).

18. V. J. Folen, G. T. Rado and E. W. Stalder. Anisotropy of the Magnetoelectric Effect in Cr_2O_3, *Phys. Rev. Lett.* **6**, 607 – 608 (1961).

19. G.T. Rado and V.J. Folen. Observation of the Magnetically Induced Magnetoelectric Effect and Evidence for Antiferromagnetic Domains, *Phys. Rev. Lett.* **7**, 310 – 311 (1961).

20. Hans Schmid. Introduction to the proceedings of the 2nd international conference on magnetoelectric interaction phenomena in crystals, MEIPIC-2, *Ferroelectrics* **161**, 1 – 28 (1994).

21. M. Bichurin. Short introduction to the proceedings of the 3rd International Conference on Magnetoelectric Interaction Phenomena in Crystals, MEIPIC-3., *Ferroelectrics* **204**, XVII – XX (1997).

22. van J. Suchtelen. *Philips Res. Rep.* **27**, 28 (1972).

23. van den J. Boomgaard, van A. M. J. G. Run and van J. Suchtelen. Magnetoelectricity in piezoelectric-magnetostrictive composites, *Ferroelectrics* **10**, 295 – 298 (1976).

24. J. Ryu, A. V. Carazo, K. Uchino and H. Kim. Magnetoelectric Properties in Piezoelectric and Magnetostrictive Laminate Composites, *Jpn. J. Appl. Phys.* **40**, 4948 – 4951 (2001).

25. G. Srinivasan, E. T. Rasmussen, J. Gallegos, R. Srinivasan, Yu. I. Bokhan and V. M. Laletin. Magnetoelectric bilayer and multilayer structures of magnetostrictive and piezoelectric oxides, *Phys. Rev. B* **64**, 214408 (2001).

26. U. Laletsin, N. Padubnaya, G. Srinivasan and C. P. DeVreugd. Frequency dependence of magnetoelectric interactions in layered structures of ferromagnetic alloys and piezoelectric oxides, *Appl. Phys. A* **78**, 33 – 36 (2004).

27. M. K. Lee, T. K. Nath, C. B. Eom, M. C. Smoak and F. Tsui. Strain modification of epitaxial perovskite oxide thin films using structural transitions of ferroelectric $BaTiO_3$ substrate, *Appl. Phys. Lett.* **77**, 3547 – 3549 (2000).

28. H. Zheng, J. Wang, S.E. Lofland, Z. Ma, L. Mohaddes-Ardabili, T. Zhao, L. Salamanca-Riba, S.R. Shinde, S.B. Ogale, F. Bai, D. Viehland, Y. Jia, D.G. Schlom, M. Wuttig, A. Roytburd and R. Ramesh. Multiferroic $BaTiO_3$-$CoFe_2O_4$ Nanostructures, *Science* **303**, 661 – 663 (2004).

29. Mahesh M. Kumar, A. Srinivas, S. V. Suryanarayana, G. S. Kumar and T. Bhimasankaram. An experimental setup for dynamic measurement of magnetoelectric effect, *Bull. Mater. Sci.* **21**, 251 – 255 (1998).

30. G. V. Duonga, R. Groessinger, M. Schoenhart and D. Bueno-Basques. The lock-in technique for studying magnetoelectric effect, *J. Magn. Magn. Mater.* **316**, 390 – 393 (2007).

31. Ronald E. Cohen. Origin of ferroelectricity in perovskite oxides, *Nature* **358**, 136 – 138 (1992).

32. G.A. Smolenskii and I.E. Chupis. Ferroelectromagnets, *Sov. Phys. Usp.* **25**, 475 – 493 (1982).

33. Nicola A. Hill. Why Are There so Few Magnetic Ferroelectrics?, *J. Phys. Chem. B* **104**, 6694 – 6709 (2000).

34. T. Kimura. Spiral Magnets as Magnetoelectrics, *Annu. Rev. Mater. Res.* **37**, 387 – 413 (2007).

35. Sang Wook Cheong and Maxim Mostovoy. Multiferroics: a magnetic twist for ferroelectricity, *Nat. Mater.* **6**, 13 – 20 (2007).

36. Yoshinori Tokura and Shinichiro Seki. Multiferroics with Spiral Spin Orders, *Adv. Mater.* **22**, 1554 – 1565 (2010).

37. G. A. Smolensky, A. I. Agranovskaya and V. A. Isupov. *Sov. Phys. Solid State* **1**, 149 (1959).

38. Yu. N. Venevtsev, G. S. Zhdanov and S. P. Solov'ev. *Kristallografiya* **4**, 575 (1959).

39. J. F. Scott and R. Blinc. Multiferroic magnetoelectric fluorides: why are there so many magnetic ferroelectrics?, *J. Phys. Cond. Matter* **23**, 113202 (2011).

40. Ram Seshadri and Nicola A. Hill. Visualizing the Role of Bi 6s "Lone Pairs" in the Off-Center Distortion in Ferromagnetic $BiMnO_3$, *Chem. Mater.* **13**, 2892 – 2899 (2001).

41. A. P. Levanyuk and Daniil G. Sannikov. Improper ferroelectrics, *Sov. Phys. Usp.* **17**, 199 – 214 (1974).

42. L. E. Cross, A. Fouskova and S. E. Cummins. Gadolinium Molybdate, a New Type of Ferroelectric Crystal, *Phys. Rev. Lett.* **21**, 812 – 814 (1968).

43. T. Katsufuji, M. Masaki, A. Machida, M. Moritomo, K. Kato, E. Nishibori, M. Takata, M. Sakata, K. Ohoyama, K. Kitazawa and H. Takagi. Crystal structure and magnetic properties of hexagonal $RMnO_3$ (R=Y, Lu, and Sc) and the effect of doping, *Phys. Rev. B* **66**, 134434 (2002).

44. G. A. Smolenskii and V. A. Bokov. Coexistence of Magnetic and Electric Ordering in Crystals, *J. Appl. Phys.* **35**, 915 – 918 (1964).

45. Kazimierz Lukaszewicz and Jaroslawa Karut-Kalicinska. X-Ray investigations of the crystal structure and phase transitions of $YMnO_3$, *Ferroelectrics* **7**, 81 – 82 (1974).

46. Bas B. Van Aken, Thomas T.M. Palstra, Alessio Filippetti and Nicola A. Spaldin. The origin of ferroelectricity in magnetoelectric $YMnO_3$, *Nat. Mater.* **3**, 164 – 170 (2004).

47. P. W. VerweyE. J. W. & Haayman. Electronic conductivity and transition point of magnetite, *Physica* **8**, 979 (1941).

48. G. T. Rado and J. M. Ferrari. Linear and bilinear magnetoelectric effects in magnetically biased magnetite (Fe_3O_4), *Phys. Rev. B* **15**, 290 – 297 (1977).

49. Dmitry V. Efremov, van den Jeroen Brink and Daniel I. Khomskii. Bond- versus site-centred ordering and possible ferroelectricity in manganites, *Nat. Mater.* **3**, 853 – 856 (2004).

50. C. R. Serrao, A. Sundaresan and C. N. R. Rao. Multiferroic nature of charge-ordered rare earth manganites, *J. Phys. Cond. Matt.* **19**, 496217 (2007).

51. T. Kimura, S. Kawamoto, I. Yamada, M. Azuma, M. Takano and Y. Tokura. Magnetocapacitance effect in multiferroic $BiMnO_3$, *Phys. Rev. B* **67**, 180401 (2003).

52. G. Lawes, A. B. Harris, T. Kimura, N. Rogado, R. J. Cava, A. Aharony, O. Entin-Wohlman, T. Yildirim, M. Kenzelmann, C. Broholm and A. P. Ramirez. Magnetically Driven Ferroelectric Order in $Ni_3V_2O_8$, *Phys. Rev. Lett.* **95**, 087205 (2005).

53. K. Taniguchi, N. Abe, T. Takenobu, Y. Iwasa and T. Arima. Ferroelectric Polarization Flop in a Frustrated Magnet $MnWO_4$ Induced by a Magnetic Field, *Phys. Rev. Lett.* **97**, 097203 (2006).

54. T. Kimura, Y. Sekio, H. Nakamura, T. Siegrist and A. P. Ramirez. Cupric oxide as an induced-multiferroic with high-TC, *Nat Mater* **7**, 291 – 294 (2008).

55. S. Park, Y. J. Choi, C. L. Zhang and S-W. Cheong. Ferroelectricity in an S=1/2 Chain Cuprate, *Phys. Rev. Lett.* **98**, 057601 (2007).

56. Y. Yamasaki, S. Miyasaka, Y. Kaneko, J.-P. He, T. Arima and Y. Tokura. Magnetic Reversal of the Ferroelectric Polarization in a Multiferroic Spinel Oxide, *Phys. Rev. Lett.* **96**, 207204 (2006).

57. Y. J. Choi, J. Okamoto, D. J. Huang, K. S. Chao, H. J. Lin, C. T. Chen, van M. Veenendaal, T. A. Kaplan and S-W. Cheong. Thermally or Magnetically Induced Polarization Reversal in the Multiferroic $CoCr_2O_4$, *Phys. Rev. Lett.* **102**, 067601 (2009).

58. T. Kimura, G. Lawes and A. P. Ramirez. Electric Polarization Rotation in a Hexaferrite with Long-Wavelength Magnetic Structures, *Phys. Rev. Lett.* **94**, 137201 (2005).

59. Hiroshi Murakawa, Yoshinori Onose, Kenya Ohgushi, Shintaro Ishiwata and Yoshinori Tokura. Generation of Electric Polarization with Rotating Magnetic Field in Helimagnet $ZnCr_2Se_4$, *J. Phys. Soc. Jpn.* **77**, 043709 (2008).

60. S. Ishiwata, Y. Taguchi, H. Murakawa, Y. Onose and Y. Tokura. Low-Magnetic-Field Control of Electric Polarization Vector in a Helimagnet, *Science* **319**, 1643 – 1646 (2008).

61. T. Kimura, J. C. Lashley and A. P. Ramirez. Inversion-symmetry breaking in the noncollinear magnetic phase of the triangular-lattice antiferromagnet $CuFeO_2$, *Phys. Rev. B* **73**, 220401 (2006).

62. S. Seki, Y. Onose and Y. Tokura. Spin-Driven Ferroelectricity in Triangular Lattice Antiferromagnets $ACrO_2$ (A=Cu, Ag, Li, or Na), *Phys. Rev. Lett.* **101**, 067204 (2008).

63. Hosho Katsura, Naoto Nagaosa and Alexander V. Balatsky. Spin Current and Magnetoelectric Effect in Noncollinear Magnets, *Phys. Rev. Lett.* **95**, 057205 (2005).

64. I.A. Sergienko and E. Dagotto. Role of the Dzyaloshinskii-Moriya interaction in multiferroic perovskites, *Phys. Rev. B* **73**, 094434 (2006).

65. A.B. Harris, T. Yildirim, A. Aharony and O. Entin-Wohlman. Towards a microscopic model of magnetoelectric interactions in $Ni_3V_2O_8$, *Phys. Rev. B* **73**, 184433 (2006).

66. R. D. Johnson, Sunil Nair, L. C. Chapon, A. Bombardi, C. Vecchini, D. Prabhakaran, A. T. Boothroyd and P. G. Radaelli. $Cu_3Nb_2O_8$: A Multiferroic with Chiral Coupling to the Crystal Structure, *Phys. Rev. Lett.* **107**, 137205 (2011).

67. R. D. Johnson, L. C. Chapon, D. D. Khalyavin, P. Manuel, P. G. Radaelli and C. Martin. Giant improper ferroelectricity in the ferroaxial magnet $CaMn_7O_{12}$. (2011).

68. Bernd Lorenz, Ya Qi Wang and Ching Wu Chu. Ferroelectricity in perovskite $HoMnO_3$ and $YMnO_3$, *Phys. Rev. B* **76**, 104405 (2007).

69. Y. J. Choi, H. T. Yi, S. Lee, Q. Huang, V. Kiryukhin and S.-W. Cheong. Ferroelectricity in an Ising Chain Magnet, *Phys. Rev. Lett.* **100**, 047601 (2008).

70. Gianluca Giovannetti, Sanjeev Kumar, Daniel Khomskii, Silvia Picozzi and van den Jeroen Brink. Multiferroicity in Rare-Earth Nickelates $RNiO_3$, *Phys. Rev. Lett.* **103**, 156401 (2009).

71. B. Rajeswaran, P. Mandal, Rana Saha, A. Sundaresan and C. N. R. Rao. An Extensive Family of Multiferroic Perovskite Oxides Exhibiting Ferroelectricity Induced by the Presence of Two Transition Metal Ions, *Communicated* (2011).

72. Jung-Hoon Lee, Young Kyu Jeong, Jung Hwan Park, Min-Ae Oak, Hyun Myung Jang, Jong Yeog Son and James F. Scott. Spin-Canting-Induced Improper Ferroelectricity and Spontaneous Magnetization Reversal in $SmFeO_3$, *Phys. Rev. Lett.* **107**, 117201 (2011).

73. B. Rajeswaran, D. I. Khomskii, A. Sundaresan and C. N. R. Rao. Ferroelectricity at the Néel Temperature of Rare-earth Chromites ($RCrO_3$) arising from the Magnetic Interactions between Cr and R-ions: Magnetic Jahn-Teller Effect, *Communicated* (2011).

74. V. E. Wood and A. E. Austin. *Int. J. Magn.* **5**, 303 (1973).

75. M. I. Bichurin, V. M. Petrov, Yu. V. Kiliba and G. Srinivasan. Magnetic and magnetoelectric susceptibilities of a ferroelectric/ferromagnetic composite at microwave frequencies, *Phys. Rev. B* **66**, 134404 (2002).

76. A. K. Zvezdina, A. S. Logginovb, G. A. Meshkovb and A. P. Pyatakov. Multiferroics: Promising Materials for Microelectronics, Spintronics, and Sensor Technique, *Bull. Russ. Aca. Sci. Phys.* **71**, 1561 1562 (2007).

77. E. Ascher, H. Rieder, H. Schmid and H. Stossel. Some Properties of Ferromagnetoelectric Nickel-Iodine Boracite, $Ni_3B_7O_{13}I$, *J. Appl. Phys.* **37**, 1404 – 1405 (1966).

78. V. Laukhin, V. Skumryev, X. Martí, D. Hrabovsky, F. nchez, M.V. Cuenca, C. Ferrater, M. Varela, U. ders, J.F. Bobo and J. Fontcuberta. Electric-Field Control of Exchange Bias in Multiferroic Epitaxial Heterostructures, *Phys. Rev. Lett.* **97**, 227201 (2006).

79. Ying Hao Chu, Lane W. Martin, Mikel B. Holcomb, Martin Gajek, Shu Jen Han, Qing He, Nina Balke, Chan Ho Yang, Donkoun Lee, Wei Hu, Qian Zhan, Pei Ling Yang, Arantxa Fraile-Rodriguez, Andreas Scholl, Shan X. Wang and R. Ramesh. Electric-field control of local ferromagnetism using a magnetoelectric multiferroic, *Nat. Mater.* **7**, 478 – 482 (2008).

80. C.-H. Yang, J. Seidel, S. Y. Kim, P. B. Rossen, P. Yu, M. Gajek, Y. H. Chu, L. W. Martin, M. B. Holcomb, Q. He, P. Maksymovych, N. Balke, S. V. Kalinin, A. P. Baddorf, S. R. Basu, M. L. Scullin and R. Ramesh. Electric modulation of conduction in multiferroic Ca-doped $BiFeO_3$ films, *Nat. Mater.* **8**, 485 – 493 (2009).

81. G. Blasse. Ferromagnetic interactions in non-metallic perovskites, *J. Phys. Chem. Solids* **26**, 1969 – 1971 (1965).

82. N. S. Rogado, J. Li, A. W. Sleight and M. A. Subramanian. Magnetocapacitance and Magnetoresistance Near Room Temperature in a Ferromagnetic Semiconductor: La_2NiMnO_6, *Adv. Mater.* **17**, 2225 – 2227 (2005).

83. H. Rietveld. A profile refinement method for nuclear and magnetic structures, *J. Appl. Cryst.* **2**, 65 – 71 (1969).

84. D.I. Khomskii. Multiferroics: Different ways to combine magnetism and ferroelectricity, *J. Magn. Magn. Mater.* **306**, 1 – 8 (2006).

85. R. Ramesh and Nicola A. Spaldin. Multiferroics: progress and prospects in thin films, *Nat. Mater.* **6**, 21 – 29 (2007).

86. F. Kubel and H. Schmid. Structure of a ferroelectric and ferroelastic monodomain crystal of the perovskite $BiFeO_3$, *Acta Cryst. B* **46**, 698 – 702 (1990).

87. James R. Teague, Robert Gerson and W.J. James. Dielectric hysteresis in single crystal $BiFeO_3$, *Solid State Commun.* **8**, 1073 – 1074 (1970).

88. J. Wang, J.B. Neaton, H. Zheng, V. Nagarajan, S.B. Ogale, B. Liu, D. Viehland, V. Vaithyanathan, D.G. Schlom, U.V. Waghmare, N.A. Spaldin, K.M. Rabe, M. Wuttig and R. Ramesh. Epitaxial $BiFeO_3$ Multiferroic Thin Film Heterostructures, *Science* **299**, 1719 – 1722 (2003).

89. Kwi Young Yun, Dan Ricinschi, Takeshi Kanashima, Minoru Noda and Masanori Okuyama. Giant Ferroelectric Polarization Beyond 150 μC/cm^2 in $BiFeO_3$ Thin Film, *Jpn. J. Appl. Phys.* **43**, L647 (2004).

90. J. B. Neaton, C. Ederer, U. V. Waghmare, N. A. Spaldin and K. M. Rabe. First-principles study of spontaneous polarization in multiferroic $BiFeO_3$, *Phys. Rev. B* **71**, 014113 (2005).

91. S. V. Kiselev, R. P. Ozerov and G. S. Zhdanov. *Sou. Phys. -Dokl.* **7**, 742 – 744 (1963).

92. Pio Baettig and Nicola A. Spaldin. Ab initio prediction of a multiferroic with large polarization and magnetization, *Appl. Phys. Lett.* **86**, 012505 (2005).

93. I. Sosnowska, T. P. Neumaier and E. Steichele. Spiral magnetic ordering in bismuth ferrite, *J. Phys. C: Solid State Phys.* **15**, 4835 – 4846 (1982).

94. Yu. F. Popov, A. K. Zvezdin, G. P. Vorob'ev, A. M. Kadomtseva, V. A. Murashev and Rakov D. N. Linear magnetoelectric effect and phase transitions in bismuth ferrite, $BiFeO_3$, *JETP Lett.* **57**, 69 – 73 (1993).

95. Claude Ederer and Nicola A. Spaldin. Weak ferromagnetism and magnetoelectric coupling in bismuth ferrite, *Phys. Rev. B* **71**, 060401 (2005).

96. V. R. Palkar, Darshan C. Kundaliya, S. K. Malik and S. Bhattacharya. Magnetoelectricity at room temperature in the $Bi_{0.9-x}Tb_xLa_{0.1}FeO_3$ system, *Phys. Rev. B* **69**, 212102 (2004).

97. Benjamin Ruette, S. Zvyagin, A. P. Pyatakov, A. Bush, J. F. Li, V. I. Belotelov, A. K. Zvezdin and D. Viehland. Magnetic-field-induced phase transition in $BiFeO_3$ observed by high-field electron spin resonance: Cycloidal to homogeneous spin order, *Phys. Rev. B* **69**, 064114 (2004).

98. S. Zhang, Y. Zhang, M. Lu, C. Du, Y. Chen, Z. Liu, Y. Zhu, N. Ming and X. Q. Pan. Substitution-induced phase transition and enhanced multiferroic properties of $Bi_{1-x}La_xFeO_3$ ceramics, *Appl. Phys. Lett.* **88**, 162901 (2006).

99. G. L. Yuan, S. W. Or, J. M. Liu and Z. G. Liu. Structural transformation and ferroelectromagnetic behavior in single-phase $Bi_{1-x}Nd_xFeO_3$ multiferroic ceramics, *Appl. Phys. Lett.* **89**, 052905 (2006).

100. V. A. Khomchenko, D. A. Kiselev, J. M. Vieira, L. Jian, A. L. Kholkin, A. M. Lopes, Y. G. Pogorelov, J. P. Araujo and M. Maglione. Effect of diamagnetic Ca, Sr, Pb, and Ba substitution on the crystal structure and multiferroic properties of the $BiFeO_3$ perovskite, *J. Appl. Phys.* **103**, 024105 (2008).

101. Anar Singh, Vibhav Pandey, R. K. Kotnala and Dhananjai Pandey. Direct Evidence for Multiferroic Magnetoelectric Coupling in $0.9BiFeO_3$ - $0.1BaTiO_3$, *Phys. Rev. Lett.* **101**, 247602 (2008).

102. J. Wei, R. Haumont, R. Jarrier, P. Berhtet and B. Dkhil. Nonmagnetic Fe-site doping of $BiFeO_3$ multiferroic ceramics, *Appl. Phys. Lett.* **96**, 102509 (2010).

103. Y. F. Cui, Y. G. Zhao, L. B. Luo, J. J. Yang, H. Chang, M. H. Zhu, D. Xie and T. L. Ren. Dielectric, magnetic, and magnetoelectric properties of La and Ti codoped $BiFeO_3$, *Appl. Phys. Lett.* **97**, 222904 (2010).

104. R. Shannon. Revised effective ionic radii and systematic studies of interatomic distances in halides and chalcogenides, *Acta Cryst. A* **32**, 751 – 767 (1976).

105. Alexei A. Belik, Satoshi Iikubo, Katsuaki Kodama, Naoki Igawa, Shin ichi Shamoto, Makoto Maie, Takuro Nagai, Yoshio Matsui, Sergey Yu Stefanovich, Bogdan I. Lazoryak and Eiji Takayama-Muromachi. $BiScO_3$: Centrosymmetric $BiMnO_3$-type Oxide, *J. Am. Chem. Soc.* **128**, 706 – 707 (2005).

106. Joel Zylberberg, Alexei A. Belik, Eiji Takayama-Muromachi and Zuo-Guang Ye.

Bismuth Aluminate: A New High-TC Lead-Free Piezo-/ferroelectric, *Chemistry of Materials* **19**, 6385 – 6390 (2007).

107. Y. Wang, L. Zhou, M. F. Zhang, X. Y. Chen, J.-M. Liu and Z. G. Liu. Room-temperature saturated ferroelectric polarization in $BiFeO_3$ ceramics synthesized by rapid liquid phase sintering, *Appl. Phys. Lett.* **84**, 1731 – 1733 (2004).

108. S. T. Zhang, M. H. Lu, D. Wu, Y. F. Chen and N. B. Ming. Larger polarization and weak ferromagnetism in quenched $BiFeO_3$ ceramics with a distorted rhombohedral crystal structure, *Appl. Phys. Lett.* **87**, 262907 (2005).

109. J. Rodriguez Carvajal. abstracts of the Satellite Meeting on Powder Diffraction of the XV IUCr Congress. p127, (1990).

110. Ajmala Shireen, Rana Saha, P. Mandal, A. Sundaresan and C. N. R. Rao. Multiferroic and magnetodielectric properties of the $Al_{1-x}Ga_xFeO_3$ family of oxides, *J. Mater. Chem.* **21**, 57 – 59 (2011).

111. Manoj K. Singh, W. Prellier, M. P. Singh, Ram S. Katiyar and J. F. Scott. Spin-glass transition in single-crystal $BiFeO_3$, *Phys. Rev. B* **77**, 144403 (2008).

112. T. Yamaguchi. Theory of spin reorientation in rare-earth orthochromites and orthoferrites, *J. Phys. Chem. Solids* **35**, 479 – 500 (1974).

113. P. Lunkenheimer, V. Bobnar, A.V. Pronin, A.I. Ritus, A.A. Volkov and A. Loidl. Origin of apparent colossal dielectric constants, *Phys. Rev. B* **66**, 052105 (2002).

114. P. Lunkenheimer, R. Fichtl, S.G. Ebbinghaus and A. Loidl. Nonintrinsic origin of the colossal dielectric constants in $CaCu_3Ti_4O_{12}$, *Phys. Rev. B* **70**, 172102 (2004).

115. Xiaoding Qi, Joonghoe Dho, Rumen Tomov, Mark G. Blamire and Judith L. MacManus-Driscoll. Greatly reduced leakage current and conduction mechanism in aliovalent-ion-doped $BiFeO_3$, *Appl. Phys. Lett.* **86**, 062903 (2005).

116. Zuci Quan, Wei Liu, Hao Hu, Sheng Xu, Bobby Sebo, Guojia Fang, Meiya Li and Xingzhong Zhao. Microstructure, electrical and magnetic properties of Ce-doped $BiFeO_3$ thin films, *J. Appl. Phys.* **104**, 084106 (2008).

117. Matjaz Valant, Anna-Karin Axelsson and Neil Alford. Peculiarities of a Solid-State Synthesis of Multiferroic Polycrystalline $BiFeO_3$, *Chem. Mater.* **19**, 5431 – 5436 (2007).

118. W. N. Su. Large polarization and enhanced magnetic properties in $BiFeO_3$ ceramic prepared by high-pressure synthesis, *Appl. Phys. Lett.* **91**, 092905 (2007).

119. C. N. R. Rao and Claudy Rayan Serrao. New routes to multiferroics, *J. Mater. Chem.* **17**, 4931 – 4938 (2007).

120. Shintaro Ishiwata, Masaki Azuma, Mikio Takano, Eiji Nishibori, Masaki Takata, Makoto Sakata and Kenichi Kato. High pressure synthesis, crystal structure and physical properties of a new Ni(II) perovskite $BiNiO_3$, *J. Mater. Chem.* **12**, 3733 – 3737 (2002).

121. A.A. Belik, N. Tsujii, H. Suzuki and E. Takayama-Muromachi. Magnetic properties of bulk $BiCrO_3$ studied with dc and ac magnetization and specific heat, *Inorg. Chem.* **46**, 8746 – 8751 (2007).

122. A.A. Belik, S. Iikubo, K. Kodama, N. Igawa, S. Shamoto and E. Takayama-Muromachi. Neutron powder diffraction study on the crystal and magnetic structures of $BiCrO_3$, *Chem. Mater.* **20**, 3765 – 3769 (2008).

123. S. Geller and E. A. Wood. Crystallographic studies of perovskite-like compounds. I. Rare earth orthoferrites and $YFeO_3$, $YCrO_3$, $YAlO_3$, *Acta Cryst.* **9**, 563 – 568 (1956).

124. Moreira dos A. Santos, A.K. Cheetham, T. Atou, Y. Syono, Y. Yamaguchi, K. Ohoyama, H. Chiba and C.N.R. Rao. Orbital ordering as the determinant for ferromagnetism in biferroic $BiMnO_3$, *Phys. Rev. B* **66**, 064425 (2002).

125. Moreira dos A. Santos, S. Parashar, A.R. Raju, Y.S. Zhao, A.K. Cheetham and C.N.R. Rao. Evidence for the likely occurrence of magnetoferroelectricity in the simple perovskite, $BiMnO_3$, *Solid State Commun.* **122**, 49 – 52 (2002).

126. T. Atou, H. Chiba, K. Ohoyama, Y. Yamaguchi and Y. Syono. Structure Determination of Ferromagnetic Perovskite $BiMnO_3$, *J. Solid State Chem.* **145**, 639 – 642 (1999).

127. A.A. Belik, S. Iikubo, T. Yokosawa, K. Kodama, N. Igawa, S. Shamoto, M. Azuma, M. Takano, K. Kimoto, Y. Matsui and E. Takayama-Muromachi. Origin of the monoclinic-to-monoclinic phase transition and evidence for the centrosymmetric crystal structure of $BiMnO_3$, *J. Am. Chem. Soc.* **129**, 971 – 977 (2007).

128. T. Yokosawa, A.A. Belik, T. Asaka, K. Kimoto, E. Takayama-Muromachi and Y. Matsui. Crystal symmetry of $BiMnO_3$: Electron diffraction study, *Phys. Rev. B* **77**, 024111 (2008).

129. Pio Baettig, Ram Seshadri and Nicola A. Spaldin. Anti-Polarity in Ideal $BiMnO_3$, *J. Am. Chem. Soc.* **129**, 9854 – 9855 (2007).

130. A. Sundaresan, R.V.K. Mangalam, A. Iyo, Y. Tanaka and C.N.R. Rao. Crucial role of oxygen stoichiometry in determining the structure and properties of $BiMnO_3$, *J. Mater. Chem.* **18**, 2191 – 2193 (2008).

131. A.A. Belik, T. Kolodiazhnyi, K. Kosuda and E. Takayama-Muromachi. Synthesis and properties of oxygen non-stoichiometric $BiMnO_3$, *J. Mater. Chem.* **19**, 1593 – 1600 (2009).

132. S. Niitaka, M. Azuma, M. Takano, E. Nishibori, M. Takata and M. Sakata. Crystal structure and dielectric and magnetic properties of $BiCrO_3$ as a ferroelectromagnet, *Solid State Ionics* **172**, 557 – 559 (2004).

133. Alexei A. Belik, Tuerxun Wuernisha, Takashi Kamiyama, Kazuhiro Mori, Makoto Maie, Takuro Nagai, Yoshio Matsui and Eiji Takayama-Muromachi. High-

Pressure Synthesis, Crystal Structures, and Properties of Perovskite-like $BiAlO_3$ and Pyroxene-like $BiGaO_3$, *Chemistry of Materials* **18**, 133 – 139 (2006).

134. Alexei A. Belik, Satoshi Iikubo, Katsuaki Kodama, Naoki Igawa, Shin-ichi Shamoto, Seiji Niitaka, Masaki Azuma, Yuichi Shimakawa, Mikio Takano, Fujio Izumi and Eiji Takayama-Muromachi. Neutron Powder Diffraction Study on the Crystal and Magnetic Structures of $BiCoO_3$, *Chem. Mater.* **18**, 798 – 803 (2006).

135. M. Azuma, K. Takata, T. Saito, S. Ishiwata, Y. Shimakawa and M. Takano. Designed ferromagnetic, ferroelectric Bi_2NiMnO_6, *J. Am. Chem. Soc.* **127**, 8889 – 8892 (2005).

136. M. Sakai, A. Masuno, D. Kan, M. Hashisaka, K. Takata, M. Azuma, M. Takano and Y. Shimakawa. Multiferroic thin film of Bi_2NiMnO_6 with ordered double-perovskite structure, *Appl. Phys. Lett.* **90**, 072903 (2007).

137. Matthew R. Suchomel, Chris I. Thomas, Mathieu Allix, Matthew J. Rosseinsky, Andrew M. Fogg and Michael F. Thomas. High pressure bulk synthesis and characterization of the predicted multiferroic $Bi(Fe_{1/2}Cr_{1/2})O_3$, *Appl. Phys. Lett.* **90**, 112909 (2007).

138. R. Nechache, C. Harnagea, A. Pignolet, F. Normandin, T. Veres, L. P. Carignan and D. Menard. Growth, structure, and properties of epitaxial thin films of first-principles predicted multiferroic Bi_2FeCrO_6, *Appl. Phys. Lett.* **89**, 102902 – 102903 (2006).

139. R. Nechache, C. Harnagea, L.-P. Carignan, O. Gautreau, L. Pintilie, M. P. Singh, D. Ménard, P. Fournier, M. Alexe and A. Pignolet. Epitaxial thin films of the multiferroic double perovskite Bi_2FeCrO_6 grown on (100)-oriented $SrTiO_3$ substrates: Growth, characterization, and optimization, *J. Appl. Phys.* **105**, 061621 (2009).

140. L. P*álová*, P. Chandra and K. M. Rabe. Magnetostructural Effect in the Multiferroic $BiFeO_3$-$BiMnO_3$ Checkerboard from First Principles, *Phys. Rev. Lett.* **104**, 037202 (2010).

141. P. Mandal, A. Sundaresan, C. N. R. Rao, A. Iyo, P. M. Shirage, Y. Tanaka, Ch Simon, V. Pralong, O.I. Lebedev, V. Caignaert and B. Raveau. Temperature-induced magnetization reversal in $BiFe_{0.5}Mn_{0.5}O_3$ synthesized at high pressure, *Phys. Rev. B* **82**, 100416 (2010).

142. R.J. Cava. Dielectric materials for applications in microwave communications, *J. Mater. Chem.* **11**, 54 – 62 (2001).

143. I.P. Raevski, S.A. Prosandeev, A.S. Bogatin, M.A. Malitskaya and L. Jastrabik. High dielectric permittivity in $AFe_{1/2}B_{1/2}O_3$ nonferroelectric perovskite ceramics (A=Ba, Sr, Ca; B=Nb, Ta, Sb), *J. Appl. Phys.* **93**, 4130 – 4136 (2003).

144. Jianjun Liu, Chun gang Duan, W.N. Mei, R.W. Smith and J.R. Hardy. Dielectric properties and Maxwell-Wagner relaxation of compounds $ACu_3Ti_4O_{12}$ (A = Ca,$Bi_{2/3}$,$Y_{2/3}$,$La_{2/3}$), *J. Appl. Phys.* **98**, 093703 – 093705 (2005).

145. A.P. Ramirez, M.A. Subramanian, M. Gardel, G. Blumberg, D. Li, T. Vogt and S.M. Shapiro. Giant dielectric constant response in a copper-titanate, *Solid State Commun.* **115**, 217 – 220 (2000).

146. C.C. Homes, T. Vogt, S.M. Shapiro, S. Wakimoto and A.P. Ramirez. Optical response of high-dielectric-constant perovskite-related oxide, *Science* **293**, 673 – 676 (2001).

147. Naoshi Ikeda, Hiroyuki Ohsumi, Kenji Ohwada, Kenji Ishii, Toshiya Inami, Kazuhisa Kakurai, Youichi Murakami, Kenji Yoshii, Shigeo Mori, Yoichi Horibe and Hijiri Kito. Ferroelectricity from iron valence ordering in the charge-frustrated system $LuFe_2O_4$, *Nature* **436**, 1136 – 1138 (2005).

148. M. M. Ahmad and K. Yamada. Superionic $PbSnF_4$: A giant dielectric constant material, *Appl. Phys. Lett.* **91**, 052912 (2007).

149. Lixin He, J. B. Neaton, Morrel H. Cohen, David Vanderbilt and C. C. Homes. First-principles study of the structure and lattice dielectric response of $CaCu_3Ti_4O_{12}$, *Phys. Rev. B* **65**, 214112 (2002).

150. Morrel H. Cohen, J.B. Neaton, Lixin He and David Vanderbilt. Extrinsic models for the dielectric response of $CaCu_3Ti_4O_{12}$, *J. Appl. Phys.* **94**, 3299 – 3306 (2003).

151. S. Krohns, P. Lunkenheimer, S.G. Ebbinghaus and A. Loidl. Broadband dielectric spectroscopy on single-crystalline and ceramic $CaCu_3Ti_4O_{12}$, *Appl. Phys. Lett.* **91**, 022910 – 022913 (2007).

152. Derek C. Sinclair, Timothy B. Adams, Finlay D. Morrison and Anthony R. West. $CaCu_3Ti_4O_{12}$: One-step internal barrier layer capacitor, *Appl. Phys. Lett.* **80**, 2153 – 2155 (2002).

153. Peter J. W. Debye. *Polar molecules*. The Chemical Catalog Company, New York, (1929).

154. Kenneth S. Cole and Robert H. Cole. Dispersion and Absorption in Dielectrics I. Alternating Current Characteristics, *J. Chem. Phys.* **9**, 341 – 351 (1941).

155. Y. Q. Lin, Y. J. Wu, X. M. Chen, S. P. Gu, J. Tong and S. Guan. Dielectric relaxation mechanisms of $BiMn_2O_5$ ceramics, *J. Appl. Phys.* **105**, 054109 (2009).

156. C. C. Wang, Y. M. Cui and L. W. Zhang. Dielectric properties of $TbMnO_3$ ceramics, *Appl. Phys. Lett.* **90**, 012904 (2007).

157. John T. S. Irvine, Derek C. Sinclair and Anthony R. West. Electroceramics: Characterization by Impedance Spectroscopy, *Adv. Mater.* **2**, 132 – 138 (1990).

158. E. Barsoukov and J. R. MacDonald. *Impedance Spectroscopy: Theory, Experiment and Applications*. Wiley Interscience, New York, 2005., (2005).

159. Helen Hughes, Mathieu M.B. Allix, Craig A. Bridges, John B. Claridge, Xiaojun Kuang, Hongjun Niu, Stephen Taylor, Wenhai Song and Matthew J. Rosseinsky. A Polar Oxide with a Large Magnetization Synthesized at Ambient Pressure, *J. Am. Chem. Soc.* **127**, 13790 – 13791 (2005).

160. Mark T. Anderson, Kevin B. Greenwood, Gregg A. Taylor and Kenneth R. Poeppelmeier. B-cation arrangements in double perovskites, *Prog. Solid State Chem.* **22**, 197 – 233 (1993).

161. P.K. Davies, H. Wu, A.Y. Borisevich, I.E. Molodetsky and L. Farber. Crystal Chemistry of Complex Perovskites: New Cation-Ordered Dielectric Oxides, *Annu. Rev. Mater. Res.* **38**, 369 – 401 (2008).

162. Kenji Ueda, Hitoshi Tabata and Tomoji Kawai. Ferromagnetism in $LaFeO_3$-$LaCrO_3$ Superlattices, *Science* **280**, 1064 – 1066 (1998).

163. K. Ueda, Y. Muraoka, H. Tabata and T. Kawai. Atomic ordering in the $LaFe_{0.5}Mn_{0.5}O_3$ solid solution film, *Appl. Phys. Lett.* **78**, 512 – 514 (2001).

164. Masaki Azuma, Hironori Kanda, Alexei A. Belik, Yuichi Shimakawa and Mikio Takano. Magnetic and structural properties of $BiFe_{1-x}Mn_xO_3$, *J. Magn. Magn. Mater.* **310**, 1177 – 1179 (2007).

165. N. Y. Vasanthacharya, P. Ganguly, J. B. Goodenough and C. N. R. Rao. Valence states and magnetic properties of $LaNi_{1-x}Mn_xO_3$ (for $0 \leq x \leq 0.2$ and $x = 0.5$), *J. Phys. C: Solid State Phys.* **17**, 2745 – 2760 (1984).

166. A. M. Kadomtseva, A. S. Moskvin, I. G. Bostrem, B. M. Wanklyn and N. A. Khafizova. Nature of the anomalous magnetic properties of yttrium ferrite chromites, *Sov. Phys. JETP* **45**, 1202 (1977).

167. Shekhar D. Bhame, V.L.J. Joly and P.A. Joy. Effect of disorder on the magnetic properties of $LaMn_{0.5}Fe_{0.5}O_3$, *Phys. Rev. B* **72**, 054426 (2005).

168. E.W. Gorter and J.A. Schulkes. Reversal of Spontaneous Magnetization as a Function of Temperature in LiFeCr Spinels, *Phys. Rev.* **90**, 487 – 488 (1953).

169. R. Pauthenet. Spontaneous Magnetization of Some Garnet Ferrites and the Aluminum Substituted Garnet Ferrites, *J. Appl. Phys.* **29**, 253 – 255 (1958).

170. N. Menyuk, K. Dwight and D.G. Wickham. Magnetization Reversal and Asymmetry in Cobalt Vanadate (IV), *Phys. Rev. Lett.* **4**, 119 – 120 (1960).

171. A.M.Kadomtseva, A.S.Moskvin, I.G.Bostrem, B.M.Vanklin and N.A.Hafizova. *Sov. Phys. JETP* **72**, 2286 (1977).

172. N. Shirakawa and M. Ishikawa. Anomalous Diamagnetism of a Perovskite $LaVO_3$, *Jpn. J. Appl. Phys.* **30**, L755 – 756 (1991).

173. Hoan C. Nguyen and John B. Goodenough. Magnetic studies of some orthovanadates, *Phys. Rev. B* **52**, 324 – 334 (1995).

174. Shin ichi Ohkoshi, Tomokazu Iyoda, Akira Fujishima and Kazuhito Hashimoto. Magnetic properties of mixed ferro-ferrimagnets composed of Prussian blue analogs, *Phys. Rev. B* **56**, 11642 – 11652 (1997).

175. Shin ichi Ohkoshi, Yukinori Abe, Akira Fujishima and Kazuhito Hashimoto. Design and Preparation of a Novel Magnet Exhibiting Two Compensation Temperatures Based on Molecular Field Theory, *Phys. Rev. Lett.* **82**, 1285 – 1288 (1999).

176. H. Kageyama, D.I. Khomskii, R.Z. Levitin, M.M. Markina, T. Okuyama, T. Uchimoto and A.N. Vasil'ev. Magnetization reversal in weak ferrimagnets and canted antiferromagnets, *J. Magn. Magn. Mater.* **262**, 445 – 451 (2003).

177. H. Kageyama, D.I. Khomskii, R.Z. Levitin and A.N. Vasil'ev. Weak ferrimagnetism, compensation point, and magnetization reversal in $Ni(HCOO)_2.2H_2O$, *Phys. Rev. B* **67**, 224422 (2003).

178. A. A. Taskin and Y. Ando. Peculiar Ferrimagnetism Associated with Charge Order in Layered Perovskite $GdBaMn_2O_{5.0}$, *Phys. Rev. Lett.* **98**, 207201 (2007).

179. L Neel. PROPRIETES MAGNETIQUES DES FERRITES - FERRIMAGNETISME ET ANTIFERROMAGNETISME, *Ann.Phys.(Leipzig)* **3**, 137 (1948).

180. Amit Kumar, S. M. Yusuf, L. Keller and J. V. Yakhmi. Microscopic Understanding of Negative Magnetization in Cu, Mn, and Fe Based Prussian Blue Analogues, *Phys. Rev. Lett.* **101**, 207206 (2008).

181. S.M. Yusuf, Amit Kumar and J.V. Yakhmi. Temperature- and magnetic-field-controlled magnetic pole reversal in a molecular magnetic compound, *Appl. Phys. Lett.* **95**, 182506 (2009).

182. H. Adachi and H. Ino. A ferromagnet having no net magnetic moment, *Nature* **401**, 148 – 150 (1999).

183. A.V. Mahajan, D.C. Johnston, D.R. Torgeson and F. Borsa. Magnetic-Properties of $LavO_3$, *Phys. Rev. B* **46**, 10966 – 10972 (1992).

184. Y. Kimishima, Y. Ichiyanagi, K. Shimizu and T. Mizuno. N-type ferrimagnetism of $SmVO_3$, *J. Magn. Magn. Mater.* **210**, 244 – 250 (2000).

185. Y. Kimishima, M. Uehara and T. Saitoh. Ca-doping effects on N-type ferrimagnetism of $NdVO_3$, *Solid State Commun.* **133**, 559 – 564 (2005).

186. Y. Ren, T.T.M. Palstra, D.I. Khomskii, E. Pellegrin, A.A. Nugroho, A.A. Menovsky and G.A. Sawatzky. Temperature-induced magnetization reversal in a YVO_3 single crystal, *Nature* **396**, 441 – 444 (1998).

187. Y. Ren, T. T. M. Palstra, D. I. Khomskii, A. A. Nugroho, A. A. Menovsky and G. A. Sawatzky. Magnetic properties of YVO_3 single crystals, *Phys. Rev. B* **62**, 6577 – 6586 (2000).

188. K. Yoshii, A. Nakamura, Y. Ishii and Y. Morii. Magnetic properties of $La_{1-x}Pr_xCrO_3$, *J. Solid State Chem.* **162**, 84 – 89 (2001).

189. K. Yoshii. Magnetic Properties of Perovskite $GdCrO_3$, *J. Solid State Chem.* **159**, 204 – 208 (2001).

190. V.A. Khomchenko, I.O. Troyanchuk, R. Szymczak and H. Szymczak. Negative magnetization in $La_{0.75}Nd_{0.25}CrO_3$ perovskite, *J. Mater. Sci.* **43**, 5662 – 5665 (2008).

191. K. Vijayanandhini, C. Simon, V. Pralong, Y. Breard, V. Caignaert, B. Raveau, P. Mandal, A. Sundaresan and C.N.R. Rao. Zero magnetization in a disordered $(La_{1-x/2}Bi_{x/2})(Fe_{0.5}Cr_{0.5})O_3$ uncompensated weak ferromagnet, *J. Phys. Cond. Matt.* **21**, 486002 (2009).

192. Nitesh Kumar and A. Sundaresan. On the observation of negative magnetization under zero-field-cooled process, *Solid State Commun.* **150**, 1162 – 1164 (2010).

193. I. Dzyaloshinsky. A thermodynamic theory of "weak" ferromagnetism of antiferromagnetics, *J. Phys. Chem. Solids* **4**, 241 – 255 (1958).

194. Tru Moriya. Anisotropic Superexchange Interaction and Weak Ferromagnetism, *Phys. Rev.* **120**, 91 – 98 (1960).

195. P. Novak. The magnetic anisotropy of manganate ferrites, *Czech. J. Phys.* **16**, 723 – 736 (1966).

196. P. Novak, V. Roskovec, Z. Simsa and A. M. BrabersV. Effect of Mn^{3+} ion orbit lattice coupling on magnetic anisotropy of $Mn_xFe_{3-x}O_4$ system, *J. Phys. Colloques* **32**, C1–59 – C1–61 (1971).

197. D. Treves. Magnetic Studies of Some Orthoferrites, *Phys. Rev.* **125**, 1843 – 1853 (1962).

198. B. Lorenz, Y.Q. Wang, Y.Y. Sun and C.W. Chu. Large magnetodielectric effects in orthorhombic $HoMnO_3$ and $YMnO_3$, *Phys. Rev. B* **70**, 212412 (2004).

199. P. Mandal, A. Sundaresan, N. M. Dasari and N. S. Vidhyadhiraja. Weak ferromagnetism and magnetization reversal in $YFe_{1-x}Cr_xO_3$, *Communicated* (2011).

200. P. Mandal, C. R. Serrao, A. Sundaresan and C. N. R. Rao. Tunable inverse and normal magnetocaloric effects and the magnetization reversal in $YFe_{1-x}Mn_xO_3$ ($0.1<x<0.45$), *Communicated* , – (2011).

201. A.K. Azad, A. Mellergsrd, S.G. Eriksson, S.A. Ivanov, S.M. Yunus, F. Lindberg, G. Svensson and R. Mathieu. Structural and magnetic properties of $LaFe_{0.5}Cr_{0.5}O_3$ studied by neutron diffraction, electron diffraction and magnetometry, *Mater. Res. Bull.* **40**, 1633 – 1644 (2005).

202. M. Hervieu, A. Maignan, C. Martin, N. Nguyen and B. Raveau. Double Mn^{3+} Stripes in $Bi_{1-x}Sr_xMnO_3$: New Type of Charge Ordering at Room Temperature, *Chem.Mater.* **13**, 1356 – 1363 (2001).

203. Luis Ortega-San-Martin, Anthony J. Williams, Alistair Storer and J.Paul Attfield. Frustrated Orders in the Perovskite $(Bi_{0.5}Sr_{0.5})CrO_3$, *Chem.Mater.* **21**, 2436 – 2441 (2009).

204. Y. Wu, Y. Lin, S. Gu and X. Chen. Synthesis and dielectric characteristics of $La_{0.5}Bi_{0.5}MnO_3$ ceramics, *Appl. Phys. A: Mater. Science & Processing* **97**, 191–194 (2009).

205. Asish.K. Kundu, R. Ranjith, B. Kundys, N. Nguyen, V. Caignaert, V. Pralong, W. Prellier and B. Raveau. A multiferroic ceramic with perovskite structure: $(La_{0.5}Bi_{0.5})(Mn_{0.5}Fe_{0.5})O_{3.09}$, *Appl. Phys. Lett.* **93**, 052906 (2008).

206. I.O. Troyanchuk, D.V. Karpinskii, M.V. Bushinskii, A.N. Chobot, N.V. Pushkarev, O. Prohnenko, M. Kopcewicz and R. Szymczak. Crystal and magnetic structures

of the $Bi_{1-x}Sr_xFeO_3$ and $Bi_{1-x}A_xFe_{1-x}Mn_xO_3$ (A = Sr, Ca) solid solutions, *Cryst. Reports* **54**, 1172–1178 (2009).

207. E. O. Wollan and W. C. Koehler. Neutron Diffraction Study of the Magnetic Properties of the Series of Perovskite-Type Compounds [(1-x)La,xCa]MnO_3, *Phys. Rev.* **100**, 545 – 563 (1955).

208. L. Ghivelder, I. Abrego Castillo, M.A. Gusmao, J.A. Alonso and L.F. Cohen. Specific heat and magnetic order in $LaMnO_{3+\delta}$, *Phys. Rev. B* **60**, 12184 (1999).

209. da F.M.A. Costa and dos A.J.C. Santos. Iron-57 Mssbauer studies on the $La_{1-x}Eu_xFeO_3$ solid solution system, *Inorg. Chim. Acta* **140**, 105 – 106 (1987).

210. J. A. Mydosh. *Spin glasses: an experimental introduction*. Taylor & Francis, Washington, D.C., (1993).

211. S. Mukherjee, R. Ranganathan, P.S. Anilkumar and P.A. Joy. Static and dynamic response of cluster glass in $La_{0.5}Sr_{0.5}CoO_3$, *Phys. Rev. B* **54**, 9267 – 9274 (1996).

212. Joonghoe Dho, W. S. Kim and N. H. Hur. Reentrant Spin Glass Behavior in Cr-Doped Perovskite Manganite, *Phys. Rev. Lett.* **89**, 027202 (2002).

213. Jian Wang Cai, Cong Wang, Bao Gen Shen, Jian Gao Zhao and Wen Shan Zhan. Colossal magnetoresistance of spin-glass perovskite $La_{0.67}Ca_{0.33}Mn_{0.9}Fe_{0.1}O_3$, *Appl. Phys. Lett.* **71**, 1727 – 1729 (1997).

214. K.F. Wang, Y. Wang, L.F. Wang, S. Dong, D. Li, Z.D. Zhang, H. Yu, Q.C. Li and J.M. Liu. Cluster-glass state in manganites induced by A -site cation-size disorder, *Phys. Rev. B* **73**, 134411 (2006).

215. S. Geller. Crystal Structure of Gadolinium Orthoferrite, $GdFeO_3$, (1956). journal article.

216. I.S. Jacobs, Hugh F. Burne and Lionel M. Levinson. Field-Induced Spin Reorientation in $YFeO_3$ and $YCrO_3$, *J. Appl. Phys.* **42**, 1631 – 1632 (1971).

217. K. P. Belov, A. K. Zvezdin, A. M. Kadomtseva and R. Z. Levitin. Spin-reorientation transitions in rare-earth magnets, *Sov. Phys. Usp.* **19**, 574 (1976).

218. K.A. Krezhov, P.S. Jajdzhiev, A.M. Kadomtseva, I.B. Krinettskii and M.M. Lukina. Magnetic structure and spin reorientation transitions in a system of manganese-substituted thulium orthoferrites, *J. Phys. C: Solid State Phys.* **15**, 6437 – 6447 (1982).

219. Y. Nagata, S. Yashiro, T. Mitsuhashi, A. Koriyama, Y. Kawashima and H. Samata. Magnetic properties of $RFe_{1-x}Mn_xO_3$ (R=Pr,Gd,Dy), *J. Magn. Magn. Mater.* **237**, 250 – 260 (2001).

220. Jinhua Mao, Yu Sui, Xingquan Zhang, Yantao Su, Xianjie Wang, Zhiguo Liu, Yi Wang, Ruibin Zhu, Yang Wang, Wanfa Liu and Jinke Tang. Temperature- and magnetic-field-induced magnetization reversal in perovskite $YFe_{0.5}Cr_{0.5}O_3$, *Appl. Phys. Lett.* **98**, 192510 – 192513 (2011).

221. V. M. Jdin and A. B. Sherman. Weak ferromagnetism of $YCrO_3$, *Solid State Commun.* **4**, 661 – 663 (1966).

222. E. F Bertaut. *Magnetism III*. Academic Press, New York, (1963).

223. F. BertautE. On Ferrites. Theory and Practise, *J. Phys. IV France* **07**, C1–11 – C1–26 (1997).

224. R. L. White. Review of Recent Work on the Magnetic and Spectroscopic Properties of the Rare-Earth Orthoferrites, *J. Appl. Phys.* **40**, 1061 – 1069 (1969).

225. Lionel M. Levinson, Marshall Luban and S. Shtrikman. Microscopic Model for Reorientation of the Easy Axis of Magnetization, *Phys. Rev.* **187**, 715 – 722 (1969).

226. J. Sivardiere. Un modele simple pour la reorientation des moments magnetiques du fer dans les orthoferrites $TFeO_3$, *Solid State Communications* **7**, 1555 – 1559 (1969).

227. G. Gorodetsky and D. Treves. Second-Order Susceptibility Terms in Orthoferrites at Room Temperature, *Phys. Rev.* **135**, A97 – A101 (1964).

228. W.C. Koehler and E.O. Wollan. Neutron-diffraction study of the magnetic properties of perovskite-like compounds $LaBO_3$, *J. Phys. Chem. Solids* **2**, 100 – 106 (1957).

229. V. M. Judin, A. B. Sherman and I. E. Myl'nikova. Magnetic properties of $YFeO_3$, *Phys. Lett.* **22**, 554 – 555 (1966).

230. R.C. Sherwood, J.P. Remeika and H.J. Williams. Domain Behavior in Some Transparent Magnetic Oxides, *J. Appl. Phys.* **30**, 217 – 225 (1959).

231. D. R. Taylor, J. Owen and B. M. Wanklyn. Hyperfine interactions and electron transfer between metal ions in Fe:$LaAlO_3$ and Cr:$LaAlO_3$, *J. Phys. C* , 2592 – 2610 (1973).

232. F.J. Morin. Magnetic Susceptibility of alpha Fe_2O_3 and alpha Fe_2O_3 with Added Titanium, *Phys. Rev.* **78**, 819 – 820 (1950).

233. E. Kratochvilova, P. Novak, I. Veltrusky and B.V. Mill. The Jahn-Teller effect of Mn^{3+} ions in YIG: magnetocrystalline anisotropy, *J. Phys. C* **18**, 1671 – 1676 (1985).

234. Y. Nagata and K. Ohta. Magnetic Transition of Orthoferrites with Compositions $YFe_{1-x}Mn_xO_3$, *J. Phys. Soc. Jpn.* **44**, 1148 – 1151 (1978).

235. G. Gorodetsky, B. Sharon and S. Shtrikman. Magnetic Properties of an Antiferromagnetic Orthoferrite, *J. Appl. Phys.* **39**, 1371 – 1372 (1968).

236. M. Eibschütz, L. Holmes, J.P. Maita and L.G. Van Uitert. Low temperature magnetic phase transition in $ErCrO_3$, *Solid State Commun.* **8**, 1815 – 1817 (1970).

237. M. Foldeaki, R. Chahine and T.K. Bose. Magnetic measurements: A powerful tool in magnetic refrigerator design, *J. Appl. Phys.* **77**, 3528 – 3537 (1995).

238. Xixiang Zhang, Bei Zhang, Shuyun Yu, Zhuhong Liu, Wenjin Xu, Guodong Liu, Jinglan Chen, Zexian Cao and Guangheng Wu. Combined giant inverse and normal magnetocaloric effect for room-temperature magnetic cooling, *Phys. Rev. B* **76**, 132403 (2007).

239. N.S. Bingham, M.H. Phan, H. Srikanth, M.A. Torija and C. Leighton. Magnetocaloric effect and refrigerant capacity in charge-ordered manganites, *J. Appl. Phys.* **106**, 023909 (2009).

240. S.Yu. Dan'kov, A.M. Tishin, V.K. Pecharsky and K.A. Gschneidner. Magnetic phase transitions and the magnetothermal properties of gadolinium, *Phys. Rev. B* **57**, 3478 – 3490 (1998).

241. V.K. Pecharsky and Jr Gschneidner. Giant Magnetocaloric Effect in $Gd_5(Si_2Ge_2)$, *Phys. Rev. Lett.* **78**, 4494 – 4497 (1997).

242. G. Lawes, A.P. Ramirez, C.M. Varma and M.A. Subramanian. Magnetodielectric Effects from Spin Fluctuations in Isostructural Ferromagnetic and Antiferromagnetic Systems, *Phys. Rev. Lett.* **91**, 257208 (2003).

243. R. Tackett, G. Lawes, B.C. Melot, M. Grossman, E.S. Toberer and R. Seshadri. Magnetodielectric coupling in Mn_3O_4, *Phys. Rev. B* **76**, 024409 (2007).

244. Yong Sun Shin and Seong Ook Park. A monopole antenna with a magnetodielectric material and its MIMO application for 700 MHz-LTE-band, *Microw. Opt. Technol. Lett.* **52**, 2364 – 2367 (2010).

245. G. Catalan. Magnetocapacitance without magnetoelectric coupling, *Appl. Phys. Lett.* **88**, 102902 – 102903 (2006).

246. T. Bonaedy, Y. S. Koo, K. D. Sung and J. H. Jung. Resistive magnetodielectric property of polycrystalline gamma-Fe_2O_3, *Appl. Phys. Lett.* **91**, 132901 – 132903 (2007).

247. G. V. P. Kumar and C. Narayana. Adapting a fluorescence microscope to perform surface enhanced Raman spectroscopy, *Curr. Science* **93**, 778 (2007).

248. Y. Sundarayya, P. Mandal, A. Sundaresan and C. N. R. Rao. Mössbauer spectroscopic study of spin reorientation in Mn-substituted yttrium orthoferrite, *J. Phys. Cond. Matter* **23**, 436001 – 436006 (2011).

249. M.N. Iliev, M.V. Abrashev, H.G. Lee, V.N. Popov, Y.Y. Sun, C. Thomsen, R.L. Meng and C.W. Chu. Raman spectroscopy of orthorhombic perovskitelike $YMnO_3$ and $LaMnO_3$, *Phys. Rev. B* **57**, 2872 – 2877 (1998).

250. J. LaverdiŁre, S. Jandl, A.A. Mukhin, V.Yu Ivanov, V.G. Ivanov and M.N. Iliev. Spin-phonon coupling in orthorhombic $RMnO_3$ (R = Pr,Nd,Sm,Eu,Gd,Tb,Dy,Ho,Y) : A Raman study, *Phys. Rev. B* **73**, 214301 (2006).

251. M. Balkanski, R.F. Wallis and E. Haro. Anharmonic effects in light scattering due to optical phonons in silicon, *Phys. Rev. B* **28**, 1928 – 1934 (1983).

252. E. Granado, A. García, J.A. Sanjurjo, C. Rettori, I. Torriani, F. Prado, R.D. nchez, A. Caneiro and S.B. Oseroff. Magnetic ordering effects in the Raman spectra of $La_{1-x}Mn_{1-x}O_3$, *Phys. Rev. B* **60**, 11879 (1999).